Stability of power systems with high penetration of sources interfaced by power electronics

Guilherme Santos Pereira

N° d'ordre : 414

Centrale Lille

THESE

présentée en vue
d'obtenir le grade de

DOCTEUR

en

Spécialité : Génie Électrique

par

Guilherme Santos Pereira

DOCTORAT DELIVRE PAR CENTRALE LILLE

Titre de la thèse :

Stability of power systems with high penetration of sources interfaced by power electronics

Stabilité des systèmes électriques comportant une forte proportion de sources interfacées par électronique de puissance

Soutenue le 23 Novembre 2020 devant le jury d'examen :

Président	Jean-Luc Thomas, Professeur, Conservatoire National des Arts et Métiers
Rapporteur	Marta Molinas, Professeur, Norwegian Univ. of Science and Technology
Rapporteur	Luis Rouco Rodríguez, Professeur, Universidad Pontificia Comillas
Examinateur	Deepak Ramasubramanian, Ingénieur, Electric Power Research Institute
Examinateur	Massimo Bongiorno, Professeur, Chalmers University of Technology
Directeur de thèse	Xavier Guillaud, Professeur, Centrale Lille Institut
Encadrant	Antoine Bruyère, Maître de conférences, Centrale Lille Institut
Encadrant	Valentin Costan, Ingénieur chercheur, EDF R&D

Thèse préparée dans le Laboratoire L2EP
Ecole Doctorale SPI 072

Abstract

The massive insertion of Power Electronics (PE)-based sources into the grid is creating some technical challenges which must be overcome in order to guarantee the stability of the power system. One of the main concerns is due to the characteristics of these sources, which are different to those of Synchronous Machines (SMs).

This research intends to provide a supplementary insight into the massive insertion of PE-based sources into the power system, more specifically the evolution of the frequency behaviour of these systems. For this purpose, a set of methods and tools already used on classical SM-based systems is proposed. Reduced order models of PE-based sources behaving as voltage or current sources are proposed, and, since the obtained representations share the same theoretical approach as that employed for SMs, they can be employed together to analyse any power system, regardless its complexity. The reduced order model of the systems can either be designed by representing each source of the original system or using the concept of synchronous areas, providing flexibility in the analysis.

Using a step-by-step approach, the frequency behaviours observed with academic systems are deeply analysed with the proposed methodology, and validated with those obtained with detailed EMT models. The proposed approach developed in this work can be used to determine the impact of the penetration rate of PE-based sources on the overall frequency behaviour, and on the intra- and inter-area oscillations of different power systems.

Keywords

“Stability of power systems”; “synchronous machines”; “power electronics-based sources”; “Voltage Control mode Inverters (VCIs)”; “Current Control mode Inverters (CCIs)”; “small-signal stability”; “reduced order models”.

Résumé étendu en Français

Contexte de l'étude

Le taux d'insertion des Énergies Renouvelables Variables (EnRVs) — i.e. éolien et solaire photovoltaïque — augment rapidement et tous les pays préparent leur transition énergétique. Par exemple, pour l'année de 2040, l'ENTSO-E prévoit des scénarios prospectifs où le part de la production d'électricité d'EnRVs atteindra 51% du total Européen [1]. Le Gouvernement Français a décrété que, jusqu'à 2023, les sources d'EnRVs en Corse et à La Réunion représenteront respectivement 40 et 53% de leur puissance installée [2], [3].

La connexion de ces EnRVs est faite majoritairement via des dispositifs d'Électronique de Puissance (EP) [4]. En Figure 1, ces sources interfacées par EP peuvent être connectées à différents niveaux du réseau, soit pour les topologies plus centralisées sur le réseau de transport, soit dans des structures plus distribuées sur le réseau de distribution. L'insertion massive de ces sources à base d'EP modifie considérablement les caractéristiques du système électrique. Par conséquent, la faisabilité et l'exploitation de ces réseaux électriques sont actuellement un sujet de recherche principal [5]–[10]. Le projet Européen MIGRATE a identifié en [6] les principaux défis techniques liés à l'insertion massive des sources interfacées par EP dans le système électrique. Ces défis sont résumés en Tableau 1.

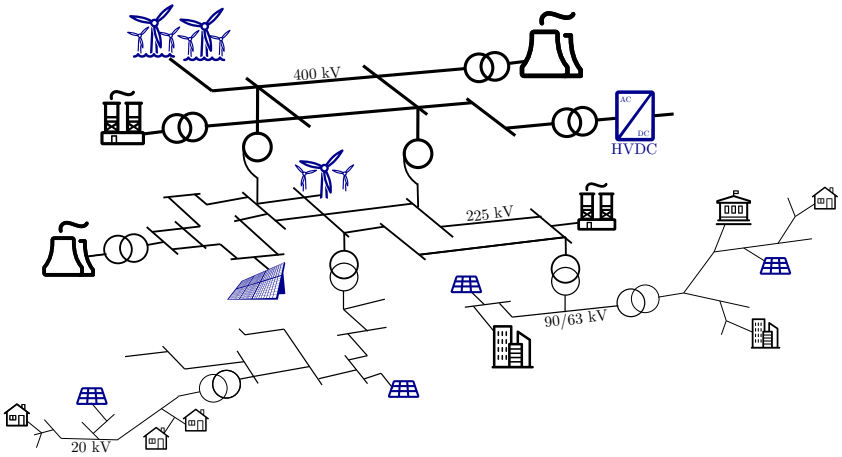

Figure 1 – Sources interfacées par EP connectées à différents niveaux du système électrique.

Table 1 – Résumé des principaux défis techniques liés à l'insertion massive des sources interfacées par EP dans le système électrique (reproduction de [6]).

Rank	**Issue**
1	Réduction de l'inertie du système
2	Résonances liées aux câbles et aux dispositifs d'EP
3	Réduction des marges de stabilité transitoire
4	Manque ou mauvaise participation au réglage de la fréquence par des sources d'EP
5	Interactions entre les contrôleurs d'EP et autres composants passifs ac
6	Îlotage des sources dans le contexte d'alimentation sans panne
7	Réduction de la puissance réactive
8	Introduction des nouvelles oscillations de puissance et/ou réduction de leur amortissement
9	Excès de puissance réactive
10	Chute de fréquence induite par chute de tension
11	Modification de la dépendance statique et dynamique en tension des charges

La réduction de l'inertie totale du système est probablement la plus grande préoccupation liée à l'insertion massive des sources d'EP dans le système électrique [11]–[16]. À ce jour, le coefficient d'inertie du système — ou simplement, inertie (H) — est l'image de l'énergie cinétique emmagasiné dans les masses tournantes du système. Après une perturbation, les machines synchrones réagissent naturellement en modulant cette énergie cumulée, ce que limite la pente de la variation de fréquence (*Rate of Change of Frequency*, RoCoF) du système, jusqu'à ce que les régulateurs réagissent. Dans le cas des sources d'EP, l'énergie correspondante est stockée du côté dc du système, ce qui dans la plupart des cas est négligeable par rapport à l'énergie cinétique des masses tournantes. Par conséquent, le remplacement des machines synchrones par des sources d'EP tend à diminuer l'inertie totale du système. En Figure 2, avec la diminution de l'inertie du système, le RoCoF augmente, aggravant la fréquence nadir. La dégradation de fréquence peut se traduire par une augmentation du nombre de déclenchements des dispositifs de protection afin de préserver l'intégrité des générateurs et autres éléments du réseau [17], [18].

L'utilisation de solutions classiques comme des compensateurs synchrones [12], [13], [19] ou plus flexibles comme la mise en œuvre de nouvelles stratégies de contrôle de sources d'EP pour fournir un effet inertiel [20]–[22] sont proposées dans la littérature pour maintenir l'inertie équivalente du système et surmonter les problèmes connexes.

Du fait de l'augmentation du taux de pénétration des sources d'EP, la dynamique globale des systèmes électriques a tendance à être largement modifiée, et l'introduction de nouvelles et/ou l'évolution des oscillations de fréquence sont également un sujet d'intérêt [6], [10]. Le déplacement des SM et de leurs stabilisatrices associées est cité par [6], [23] comme l'une des principales raisons du changement de l'amortissement des oscillations électromécaniques. La référence [24] souligne que l'augmentation de la production d'énergie par des éoliennes en

Europe continentale sera suivie de nouveaux défis pour amortir les oscillations interzones. L'augmentation de la fréquence de ces oscillations est observée dans [25]. Références [5], [26] proposent l'utilisation de liaisons HVDC pour atténuer d'éventuelles oscillations non amorties.

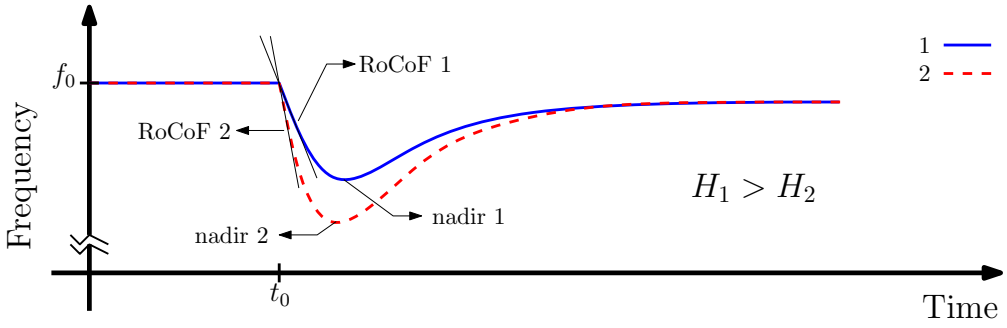

Figure 2 – Illustration du comportement de la fréquence du système après un déséquilibre entre la production et la consommation pour des différentes valeurs d'inertie H (avec système de régulation équivalent).

De plus, l'insertion massive de sources d'EP pourrait entraîner des limitations techniques en raison de la stratégie de contrôle actuelle des onduleurs, dans laquelle ces sources se comportent comme des sources de courant, injectant le maximum de puissance produite dans le réseau. Le fonctionnement de ces sources est assuré par une unité de synchronisation basée sur une boucle à verrouillage de phase (*Phase-Locked Loop*, PLL), qui estime la fréquence du réseau à partir de la mesure de la tension du point de synchronisation [4], [27]. Par conséquent, des réseaux forts avec des tensions stables sont nécessaires pour le bon fonctionnement de ces sources, sinon, dans des conditions de réseau faible, la stabilité de la source est compromise [28]–[31]. Les scénarios prospectifs du système électrique Irlandais ont montré que le taux de pénétration maximal accessible des onduleurs dans le mode de fonctionnement actuel est de 70% [16], [32]. Cependant, il n'est pas possible de déterminer une limite précise pour le taux de pénétration des sources d'EP en mode source de courant, car la force du réseau dépend de plusieurs variables, e.g. topologie du réseau, flux d'énergie, etc.

Étant donné que la dynamique de la fréquence des systèmes comportant une forte proportion de sources interfacées par EP n'est toujours pas bien comprise, l'applicabilité des méthodes et des outils classiques utilisés pour l'évaluation de la dynamique de la fréquence des systèmes dominés par des machines synchrones dans des systèmes dominés par des convertisseurs — en particulier ceux avec une très faible proportion de ou sans machines synchrones — est inconnue. Par conséquent, les études de stabilité de ces systèmes sont jusqu'à présent réalisées à l'aide de modèles représentant tous les phénomènes transitoires électromagnétiques (*electromagnetic transient*, EMT), ce qui pourrait ne pas être idéal pour les grands systèmes comme le réseau Européen. De plus, en raison de l'absence d'une interprétation analytique des phénomènes, les résultats obtenus avec un système spécifique pourraient ne pas être applicables à toutes les configurations. La nécessité de méthodes

et d'outils adaptés pour l'analyse de la stabilité des systèmes électriques avec pénétration massive des sources interfacées par EP est soulignée dans [8], [13], [45]–[49].

Objectifs de la thèse

L'insertion massive de sources interfacées par EP dans le réseau va induire de grands défis techniques à surmonter pour garantir la stabilité du système électrique. L'une des principales préoccupations tient aux caractéristiques de ces sources, qui sont différentes de celles des générateurs classiques. Ce travail apporte un éclairage supplémentaire sur l'effet de l'insertion massive de sources interfacées par EP dans le système électrique. L'objectif principal de ce travail est d'étudier l'évolution du comportement de la fréquence du système en raison du remplacement massif des groupes de production classiques, i.e. des machines synchrones, par des sources d'EP, jusqu'à ce que le taux de pénétration des premiers devienne marginal. Afin de comprendre en profondeur l'impact de l'insertion massive de sources d'EP dans le système électrique, des systèmes à complexité incrémentale sont utilisés. Avec une approche cohérente, les méthodes et outils classiques utilisés pour l'évaluation de la dynamique de la fréquence des systèmes dominés par des machines synchrones sont réévalués et adaptés pour être opérationnels pour l'analyse des réseaux électriques avec des convertisseurs. Les changements du comportement de la fréquence du système dû à la stratégie de contrôle adoptée et aux paramètres des sources d'EP, et la structure du réseau ont été analysés, proposant des interprétations analytiques sur les phénomènes impliqués.

Liste des publications issues de cette thèse

Pendant cette thèse de doctorat, plusieurs contributions scientifiques ont été publiées:

- **G. S. Pereira**, V. Costan, A. Bruyère, and X. Guillaud, "Impact of synchronous machine dynamics on the stability of a power grid with high penetration of variable renewable energies," in *15th IET International Conference on AC and DC Power Transmission (ACDC 2019)*, 2019, vol. 2019, no. CP751, pp. 87 (6 pp.)-87 (6 pp.).
- **G. S. Pereira**, V. Costan, A. Bruyère, and X. Guillaud,"Synchronous Machine Representations for Stability Studies of Power Systems with Inverters," in *2019 IEEE Milan PowerTech*, 2019, vol. 1, pp. 1–6.
- **G. S. Pereira**, V. Costan, A. Bruyère, and X. Guillaud, "Simplified approach for frequency dynamics assessment of 100% power electronics-based systems," in *21st Power Systems Computation Conference (PSCC 2020)*, 2020, p. 8.

- **G. S. Pereira**, V. Costan, A. Bruyère, and X. Guillaud,"Simplified approach for frequency dynamics assessment of 100% power electronics-based systems," *Electr. Power Syst. Res.*, vol. 188, no. September 2019, p. 106551, Nov. 2020.
- **G. Pereira**, V. Costan, A. Bruyère, and X. Guillaud, "Review of the classical power system dynamics concepts," in *Converter-Based Dynamics and Control of Modern Power Systems*, Elsevier, 2021, pp. 7–30.

Les conclusions de la thèse

Cette thèse a traité de l'évolution des caractéristiques des systèmes de puissance due au remplacement massif des groupes de production classiques — i.e. des machines synchrones — par des sources interfacées par EP fonctionnant soit comme des sources de tension (*Voltage Control mode Inverters*, VCIs), soit comme des sources de courant (*Current Control mode Inverters*, CCIs) jusqu'à ce que le taux de pénétration du premier devienne marginal. Ce travail s'est concentré sur l'évolution du comportement de la fréquence en fonctionnement normal du système. Les grands transitoires — e.g. court-circuit — ne sont pas analysés dans ce travail.

Plusieurs défis liés à l'insertion massive de sources d'EP ont été détectés dans la littérature, notamment ceux liés à l'évolution du comportement dominant de la fréquence du système et de l'amortissement des oscillations interzones. Dans le scénario actuel dans lequel les sources d'EP fonctionnent en mode CCI, on s'attend à ce que l'absence d'effet d'inertie augmente le RoCoF et le creux de la fréquence. De plus, en raison du déplacement des machines synchrones et de leurs stabilisatrices, les oscillations interzones devraient être moins amorties. Les deux phénomènes dégradent la stabilité du système, nécessitant une autre stratégie de contrôle commande — i.e. le mode VCI — pour atténuer ces problèmes.

La littérature a suggéré que, étant donné que la dynamique de fréquence des systèmes avec un taux de pénétration élevé des sources d'EP n'est pas bien comprise, l'applicabilité des méthodes et des outils classiques utilisés pour l'évaluation de la dynamique de la fréquence des systèmes dominés par des machines synchrones dans des systèmes dominés par des convertisseurs est inconnue, et par conséquent, les modèles EMT devraient être privilégiés pour effectuer des études de stabilité. Cependant, la conception des modèles EMT pourrait être peu pratique pour les grands systèmes électriques comme le réseau Européen, et, en raison du manque d'interprétation analytique des phénomènes, les résultats obtenus avec un système spécifique pourraient ne pas être applicables à toutes les configurations.

Dans cette recherche, afin de comprendre en profondeur l'impact de l'insertion massive de sources d'EP dans le système électrique, l'approche suivante a été adoptée. En utilisant des systèmes à complexité incrémentale, les changements sur le comportement de la

fréquence dus à la stratégie de contrôle adoptée et aux paramètres des sources d'EP, ainsi que la structure de du réseau ont été analysés, proposant des interprétations analytiques sur les phénomènes impliqués. A cet effet, les méthodes et outils classiques ont été réévalués et adaptés pour être opérationnels pour l'analyse des systèmes électriques avec des convertisseurs, en établissant des modèles d'ordre réduit représentatifs des systèmes étudiés. Avec la méthodologie proposée, il a été possible d'estimer les valeurs propres liées au comportement de la fréquence du système, et par conséquent, d'obtenir une représentation juste de la dynamique de la fréquence du système. En raison de la bonne représentativité des modèles d'ordre réduit (par rapport aux modèles EMTs), il a été possible de relever une série de tendances sur l'évolution du comportement possible de la fréquence des systèmes électriques.

En général, en raison de la flexibilité des sources d'EP, le comportement de la fréquence du système est amélioré avec l'insertion de ces sources. En raison de la dynamique plus rapide de la chaîne de régulation de puissance/fréquence des sources d'EP par rapport à celle des machines synchrones, le comportement dominant de la fréquence du système est plus amorti, améliorant les pics et les creux de fréquence. Avec une contribution massive des sources à base d'EP au réglage primaire de fréquence, le comportement fréquentiel dominant du système peut ressembler à une dynamique de premier ordre. Les oscillations du système — à la fois intra et interzones — deviennent plus amorties. Il a été observé que la fréquence des oscillations interzones reste à l'intérieur de la plage de fréquences connue de ces oscillations, alors que celle des oscillations intrazones a tendance à augmenter.

Les tendances susmentionnées sont obtenues lorsque les sources d'EP en mode VCI ou CCI, et il a été démontré que, malgré les différents comportements inhérents à ces stratégies, les comportements de la fréquence obtenus sont équivalents si les paramètres des deux stratégies sont comparables. Cependant, il est souligné qu'en raison du comportement inhérent des CCIs en tant que sources de courant, le remplacement des machines synchrones par des sources d'EP fonctionnant avec cette stratégie peut modifier la répartition des zones du système. De plus, la stabilité des CCIs étant fortement dépendante des paramètres du réseau, les systèmes avec insertion massive de ces sources peuvent présenter des problèmes de stabilité, compromettant l'utilisation de modèles d'ordre réduit, et donc nécessitant une analyse de stabilité détaillée. Par conséquent, il est suggéré, lorsque cela est possible, de privilégier la stratégie VCI.

Bien que les résultats aient été observés à l'aide de petits systèmes, l'approche adoptée étant cohérente avec celle précédemment utilisée pour l'analyse de systèmes comportant que des machines synchrones, l'auteur de cette thèse est convaincu de son applicabilité à des grands systèmes avec insertion massive de sources interfacées par EP.

Les contributions de la thèse

À partir des paragraphes précédents, la principale contribution de cette recherche à l'état de l'art peut être résumée comme suit :

Comprendre le comportement de la fréquence des systèmes électriques avec forte pénétration de sources interfacées par EP en utilisant une approche orientée qui permet la réévaluation des méthodes et outils classiques utilisés pour les systèmes basés sur des machines synchrones.

Les contributions de chaque chapitre à l'ensemble de cette recherche sont résumées dans les paragraphes suivants :

- **Chapitre 1 :** Présentation des fondamentaux et développement des modèles de référence et simplifiés des sources qui ont été utilisées dans cette thèse. Une comparaison directe entre la structure mécanique des machines synchrones et les commandes des VCIs a été établie, mettant en évidence la flexibilité des VCIs, puisque leurs paramètres peuvent être configurables avec n'importe les valeurs souhaitées. Il a été démontré que les CCIs se comportent différemment des autres sources, agissant comme des injecteurs de puissance.

- **Chapitre 2 :** Étude du comportement de la fréquence des systèmes à deux sources à fréquence variable. Adaptation de la méthodologie classique utilisée pour les systèmes basés à 100% de synchrones basés en assurant la compatibilité avec les systèmes avec des sources d'EP. Avec des modèles d'ordre réduit de ces systèmes, il a été possible d'interpréter analytiquement l'impact du remplacement des machines synchrones par des sources d'EP en mode VCI ou CCI sur le comportement de la fréquence du système. Analyse des tendances sur l'évolution des valeurs propres liées à comportement de la fréquence selon les variations de paramètres importantes vis-à-vis du système électrique.

- **Chapitre 3 :** Le comportement de la fréquence obtenu avec des systèmes multi-zones multi-sources a été comparé aux tendances attendues observées dans le chapitre précédent. Il a été démontré qu'il est possible de concevoir des modèles d'ordre réduit de systèmes avec des sources mixtes en utilisant la même méthodologie qui était précédemment employée en considérant des modifications minimes. Le comportement de la fréquence obtenu avec ces modèles s'est avéré représentatif des modèles de référence des systèmes, justifiant leur utilisation dans des études préliminaires sur l'évolution du comportement de la fréquence des systèmes avec insertion massive de sources interfacées par EP.

Acknowledgements

This thesis is the result of a fruitful three-year research collaboration between the *Laboratoire d'Électrotechnique et d'Électronique de Puissance de Lille* (L2EP) and the department of research and development of *Électricité de France* (EDF). Many people have directly or indirectly contributed to this thesis, and I would like to acknowledge everyone whose assistance was a milestone in completing this work.

First of all, I would like to express my deepest gratitude to my supervisors Dr. Valentin Costan, Dr. Antoine Bruyère and Prof. Xavier Guillaud. Their expertise on the subject and professional experience have been essential for the development of this work, and also in my personal development as a researcher.

I also would like to thank the members of my PhD.'s committee, Prof. Jean-Luc Thomas, Prof. Marta Molinas, Prof. Luis Rouco, Prof. Massimo Bongiorno, and Dr. Deepak Ramasubramanian for their interest in my work, enriching my understanding with significant questions and discussions during my PhD. defence.

To the R12 EDF R&D group — Power System Dynamics and Grid Connection — whose members are more than colleagues, they are friends. I am thankful for all our moments together, from learning experiences to the emotional support that was sometimes necessary during this thesis. A very special thanks to Gilles "*Le Directeur*" Malarange for sharing his wisdom first thing in the morning, and "*aux Justes*" Antoine Rossé and Antoine Breton for all our adventures in the latest bus to Paris followed by the finest gastronomic experience at *Porte d'Orléans*.

To Dr. Stéphanie Muller and Ms. Marianne Entem, on behalf of EDF group, for giving me the opportunity and the privilege to continue my carrier working at EDF R&D.

Last but not least, I am extremely thankful to family who always supports me unconditionally in the pursuit of my dreams.

Para minha família...

Contents

List of Figures

List of Tables

General Introduction

Background and motivations

The penetration rate of Variable Renewable Energies (VREs) — i.e. wind and photovoltaic — is rapidly increasing, and all countries are preparing their energy transition. For example, for future scenarios, ENTSO-E expects that, in 2040, the generation share of VREs will reach up to 51% of the European total [1]. The French Government decreed that, in 2023, VRE sources in Corsica and La Réunion must represent, respectively, 40 and 53% of their total capacity [2], [3].

The connection of these sources with the grid is mostly made via Power Electronics (PE) devices [4]. As illustrated in Figure 3, PE-based sources can be connected to different levels of the grid, in either more centralised topologies in the transmission system or more distributed structures in the distribution system. The massive insertion of these PE-based sources significantly modifies the characteristics of the power system. Therefore, the feasibility and operation of these power grids are currently main research subjects [5]–[10]. The European project MIGRATE has identified in [6] the main technical issues related to the massive insertion of PE-based sources into the grid. These issues are summarised in Table 2.

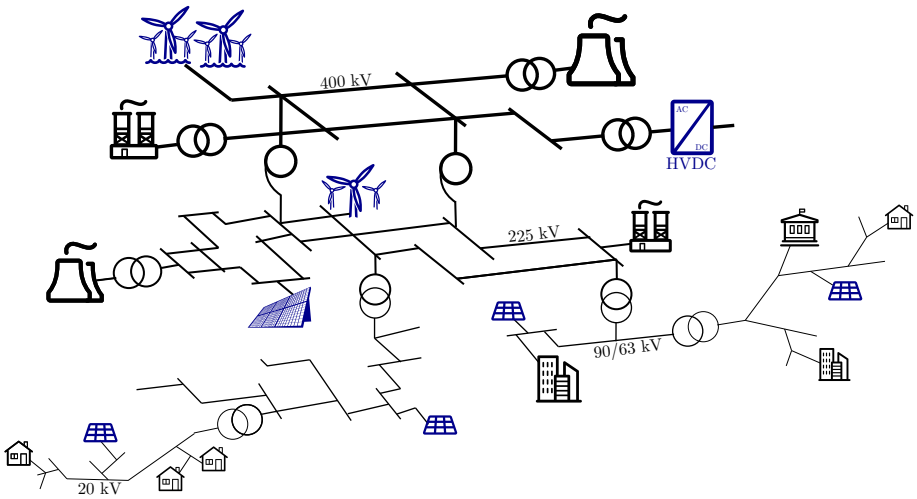

Figure 3 – PE-based sources connected to different levels of the power system.

Table 2 – Summary of the principal technical issues related to the massive insertion of PE-based sources into the grid (reproduction from [6]).

Rank	**Issue**
1	Decrease of inertia
2	Resonances due to cables and PE
3	Reduction of transient stability margins
4	Missing or wrong participation of PE-connected generators and loads in frequency containment
5	PE Controller interaction with each other and passive AC components
6	Loss of devices in the context of fault-ride-through capability
7	Lack of reactive power
8	Introduction of new power oscillations and/or reduced damping of existing power oscillations
9	Excess of reactive power
10	Voltage dip-induced frequency dip
11	Altered static and dynamic voltage dependence of loads

The decrease of the total inertia of the system is probably the main concern related to the massive insertion of PE-based sources in the power system [11]–[16]. Hitherto, the coefficient of inertia of the system — or simply, inertia (H) — is the image of the kinetic energy stored in the rotating masses of the system. Following a system disturbance, synchronous machines naturally react to it modulating the stored energy, which limits the Rate of Change of Frequency (RoCoF) of the system until the controllers react. In the case of PE-based sources, the corresponding energy is stored in the dc-side of the system, which in most cases is negligible compared with the kinetic energy of rotating masses. Therefore, replacement of synchronous machines with PE-based sources tends to decrease the total inertia of the system. As illustrated in Figure 4, with the decrease of the inertia of the system, the RoCoF increases, worsening the frequency nadir. The frequency degradation can result in an increase of the number of times that protection devices are triggered in order to preserve the integrity of the generators and other elements of the grid [17], [18].

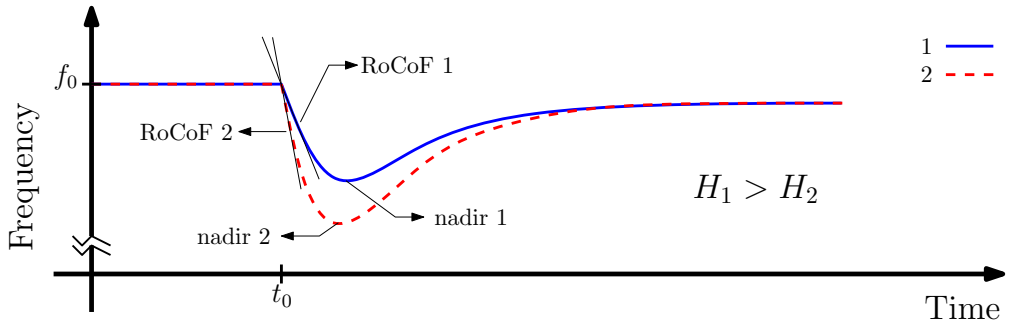

Figure 4 – Illustration of the frequency behaviour of the system after a generation consumption unbalance obtained with different values of H (considering equivalent control system).

The employment of classical solutions such as synchronous compensators [12], [13], [19] or more flexible ones such as the implementation of new control strategies of PE-based sources to provide inertial effect [20]–[22] are proposed in the literature to maintain the amount of inertia within the system and overcome related issues.

Due to the increase of the penetration rate of PE-based sources, the overall dynamics of large power systems tend to be modified, and the introduction of new and/or the evolution of frequency oscillations is also a subject of interest [6], [10]. The displacement of SMs and their associated stabilisation units is cited by [6], [23] as one of the main reasons causing change of the damping of electromechanical oscillations. Reference [24] highlights that the increase of wind power generation in Continental Europe will be followed by new challenges in the damping of inter-area oscillations. The increase of the frequency of these oscillations is observed in [25]. References [5], [26] propose the utilisation of HVDC links to mitigate possible undamped oscillations.

Also, the massive insertion of PE-based sources could entail technical limitations due to the current control strategy of inverters, in which these sources behave as current sources, injecting the maximum available power into the grid. The operation of these sources is ensured by a synchronisation unit based on a Phase-Locked Loop (PLL), which estimates the frequency of the grid using the measurement of the voltage at the synchronisation point [4], [27]. Therefore, strong grids with steady voltages are required to ensure the proper operation of these sources, otherwise, in weak grid conditions, the stability of the source may be compromised [28]–[31]. Prospective scenarios of the Ireland power system have shown that the maximal reachable penetration rate of inverters in the current operating mode is 70% [16], [32]. However, it is not possible to determine a concrete limit for the penetration rate of PE-based sources operating as current source, since the strength of the grid depends on multiple variables, e.g. grid topology, power flow, etc.

New control strategies where the PE-based sources behave as voltage sources are proposed in the literature in order to overcome the technical limits related to the current control strategy [21], [22], [33]–[41]. When an inverter behaves as a voltage source, it generates its own frequency and controls the magnitude and phase of the voltage at the coupling point, and therefore, the active power management is achieved by modifying the phase of the voltage wave [42]–[44]. Unlike inverters behaving as current sources, inverters operating as voltage sources are able to self-synchronise to the grid, being more robust to the variation of the parameters of the grid.

Since the frequency dynamics of systems with high penetration rate of PE-based sources are still not well comprehended, the applicability of the classical methods and tools used for frequency dynamics assessment of systems dominated by synchronous machines in systems dominated by inverters — especially those with a very low proportion of or without synchronous machines — is unknown. Therefore, the stability studies of these systems are

hitherto performed using models representing all electromagnetic transient (EMT) phenomena, which might not be practical for the analysis of large systems such as the European network. Furthermore, due to the lack of an analytical interpretation of the phenomena, the findings obtained with a specific system might not be applicable to all configurations. The necessity of adapted methods and tools for the analysis of the stability of power systems with massive penetration of PE-based sources is emphasised in [8], [13], [45]–[49].

Thesis scope & objectives

The massive insertion of PE-based sources into the grid is creating technical challenges which must be overcome in order to guarantee the stability of the power system. One of the main concerns is due to the characteristics of the PE-based sources, which are different to those of classic generators. This research intends to provide a supplementary insight into the massive insertion of PE-based sources into the power system. The main objective of this work is to study the evolution of the dynamic behaviour of the system due to the massive replacement of classic generating units, i.e. synchronous machines, with PE-based sources, until the penetration rate of the former becomes marginal. In order to deeply understand the impact of the massive insertion of PE-based sources in the power system, systems with incremental complexity are studied. Using a step-by-step approach in which the complexity of the analysed systems gradually increases, the classical methods and tools used for frequency dynamics assessment of systems dominated by synchronous machines are re-evaluated and adapted to be operational for the analysis of power systems with inverters. The changes in the frequency behaviour due to the adopted control strategy and parameters of the PE-based sources, and structure of the grid have been analysed, proposing analytical interpretations of the involved phenomena.

Outline of chapters

In Chapter 1, the fundamentals of the different sources which are used in this work are presented. It can demonstrated that, depending on the operating strategy implemented in the controls of PE-based sources, it is whether or not possible to establish similarities to synchronous machines. Indeed, when a PE-based source behaves as a voltage source, its control structure can be designed to partially mimic the behaviour of synchronous machines (i.e. the way in which it synchronises with the system). On the contrary, it is not possible to establish any comparison between synchronous machines and PE-based sources behaving as current sources. In Chapter 2, using a two-source system, the classical methods and tools used in the analysis of systems dominated with synchronous machines are recalled, and, with minimal adaptations, employed when the synchronous machines are replaced with

PE-based sources. The frequency behaviour of the system is analysed, providing analytical interpretations and tendencies about its evolution as a function of important parametric variations *vis-à-vis* the power system. In Chapter 3, the analysis is expanded for multi-source multi-area systems, investigating whether or not the principal tendencies of the evolution of the frequency behaviour observed in the previous chapter can be applied to multi-area systems. The equivalence of the structure of the reduced order models of a two-area system and a two-source system is demonstrated, and consequently, the findings obtained in the previous chapter can be transposed to multi-area system. Finally, conclusions, contributions and proposals for future work are presented in Chapter 4.

List of publications derived from this work

Within this PhD. thesis, several scientific contributions have been published:

- **G. S. Pereira**, V. Costan, A. Bruyère, and X. Guillaud, "Impact of synchronous machine dynamics on the stability of a power grid with high penetration of variable renewable energies," in *15th IET International Conference on AC and DC Power Transmission (ACDC 2019)*, 2019, vol. 2019, no. CP751, pp. 87 (6 pp.)-87 (6 pp.).
- **G. S. Pereira**, V. Costan, A. Bruyère, and X. Guillaud, "Synchronous Machine Representations for Stability Studies of Power Systems with Inverters," in *2019 IEEE Milan PowerTech*, 2019, vol. 1, pp. 1–6.
- **G. S. Pereira**, V. Costan, A. Bruyère, and X. Guillaud, "Simplified approach for frequency dynamics assessment of 100% power electronics-based systems," in *21st Power Systems Computation Conference (PSCC 2020)*, 2020, p. 8.
- **G. S. Pereira**, V. Costan, A. Bruyère, and X. Guillaud, "Simplified approach for frequency dynamics assessment of 100% power electronics-based systems," *Electr. Power Syst. Res.*, vol. 188, no. September 2019, p. 106551, Nov. 2020.
- **G. Pereira**, V. Costan, A. Bruyère, and X. Guillaud, "Review of the classical power system dynamics concepts," in *Converter-Based Dynamics and Control of Modern Power Systems*, Elsevier, 2021, pp. 7–30.

Chapter 1

Fundamental behaviour of grid sources

Contents

1.1 Introduction

In order to analyse the impact of PE-based sources in the transmission system, this work adopts generic models of the principal sources connected to the grid. The objective of this chapter is to introduce the sources used in this work, as well as the two different levels of detail adopted for each source, which can be exploited in both time and frequency domains. The reference model of each source is designed considering a level of detail capable of representing the electromagnetic phenomena, and with a timescale sufficiently small to evaluate possible interactions between the sources and the elements of the grid, and between sources. A more simplified model is also proposed with the purpose to focus on the evolution of the frequency behaviour of the interconnected power system. The employment of these models depends on the objective of the study.

1.2 Synchronous Machines

Even with the fast increase of the renewable energy, synchronous machines are still the key element in electricity production. Developed in the late 19th century, its operation is based on the electromechanical phenomena which have emerged in those years. These machines are very reliable and efficient part of the conversion of the energy coming from the primary source to the electrical energy delivered to the grid. Even though the concept has not evolved much since their appearance, their sizes have grown, reaching significant power levels (e.g. each synchronous machine of the Taishan nuclear power plant commissioned in 2018/2019 has a nominal capacity of 1750 MW). The power of a primary source drives a turbine system mounted in the same shaft of the rotor, and an excitation system is used provide dc power to the rotor windings, producing a dc flux. This rotating dc flux generates induced voltages in the stator windings, guaranteeing the electromechanical conversion.

Synchronous machine theory and modelling are vastly addressed in the literature [50]–[55]. Depending on the required analysis to be carried out, a specific representation is more suitable than others. The turbine-generator shaft is a very complex mechanical system composed of the rotor of the synchronous machine and the different stages of the turbine. The multimass shaft model can be used to calculate its natural frequencies and inherent mechanical damping [56]. On the contrary, for steady-state studies such as transmission network planning, just the electric circuits are considered. For the analysis of the stability of power systems — which is the focus of this work — both mechanical and electric representations are required [52], [55]. Furthermore, according to the desired trade-off between accuracy and computation costs, different levels of detail can be adopted in the representation of synchronous machines.

In this chapter, the foundations of the classic electromagnetic (EMT) representation of the synchronous machine are reviewed and compared with a simplified model used to describe its power frequency dynamic behaviour. The different elements of the power conversion chain are gradually described and added to the synchronous machine model. It is proposed a short overview of the speed governor and steam turbines, the different types of excitation systems and the power system stabiliser. For each added element, a dynamic analysis is provided, and the oscillating electromechanical eigenvalues of the EMT system are compared with those obtained with the simplified representation of the synchronous machine.

1.2.1 Reference model of Synchronous Machines

One of the objectives of this work is to investigate possible interactions between synchronous machines and Power Electronics (PE)-based sources. For this purpose, a minimum level of detail is required to reliably represent the sources used in the study. Regarding the electric representation of the synchronous machine, according to [51], a model including two rotor circuits in each axis — one field circuit and one damper in the d-axis and two dampers in the q-axis — is recommended for use in more critical stability studies, and therefore, it is adopted as reference model in this work. The following paragraphs summarises the foundations used to establish the reference model, although, if necessary, detailed development can be found in [52], [54], [55], [57].

Figure 1.1a illustrates the equivalent circuit of the synchronous machine using the adopted as reference in this work. As mentioned previously, the rotor circuit is composed of four windings, whereas the stator circuit is composed of one winding for each phase of the system. The terminal voltage of each winding is expressed as the combined effect of an induced voltage and a voltage drop, considering the adopted convention. According to Faraday's law, the former is due to the variation of the linkage flux across the winding over time. From Figure 1.1a, it can be observed the presence of two reference frames, where one is static and the other rotates over time. The major challenge related to that is the complexity of the equations describing the physical phenomena, which present multiple trigonometric terms.

In order to circumvent this issue, Blondel has proposed an elegant solution in [58], applying a rotating transformation on the quantities related to the stator. Because this transformation rotates at the angular frequency of the rotor at all times, in the rotor frame, all windings are stationary, simplifying the problem. This transformation is known in the literature as "abc to dq0 transformation" or even, "the Park transformation" after R. H. Park, who has generalised the method in [50]. The winding distribution after the application of the Park transformation is illustrated in Figure 1.1b. It should be highlighted that, under balanced sinusoidal conditions, the component "0" is null and, since only balanced operations are treated within this work, this component is not represented.

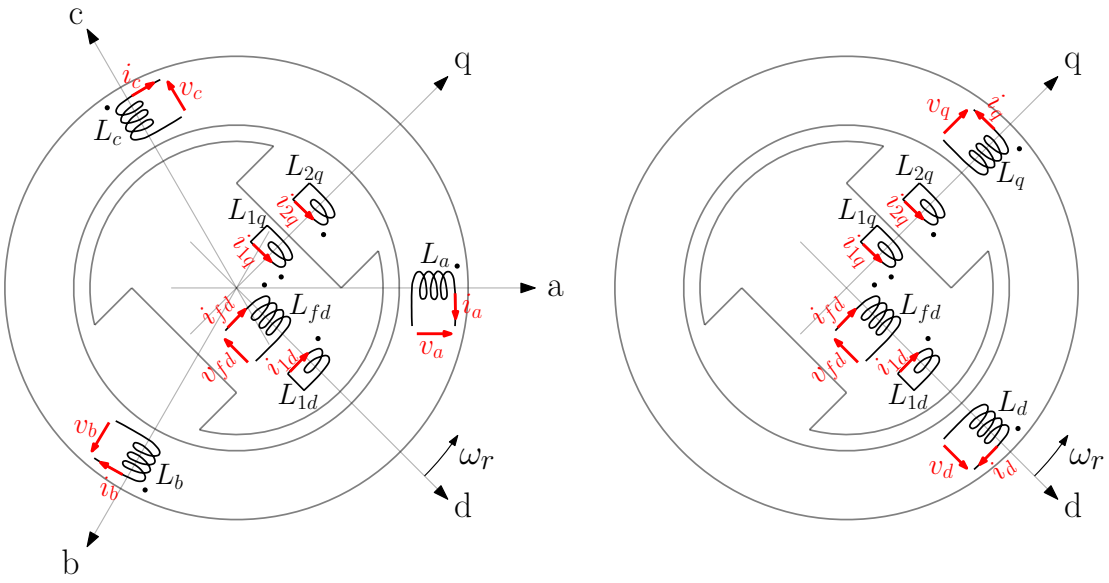

(a) abc-frame (b) dq-frame

Figure 1.1 – Equivalent circuit of the reference model of the synchronous machine.

Therefore, eqs. (1.1) to (1.6) express the terminal voltage of each winding of the synchronous machine considering the equivalent circuit illustrated in Figure 1.1b. *Nota bene:* since the dampers of the synchronous machine are short-circuited, the terminal voltage of these windings are equal to zero. It should be highlighted that all electric equations of the synchronous machine are expressed in *per unit* using the conventions of Appendix A.

$$v_d = -R_s i_d + \frac{1}{\omega_b}\frac{d\psi_d}{dt} - \omega_r \psi_q \tag{1.1}$$

$$v_q = -R_s i_q + \frac{1}{\omega_b}\frac{d\psi_q}{dt} + \omega_r \psi_d \tag{1.2}$$

$$v_{fd} = R_{fd} i_{fd} + \frac{1}{\omega_b}\frac{d\psi_{fd}}{dt} \tag{1.3}$$

$$0 = \frac{1}{\omega_b}\frac{d\psi_{1d}}{dt} + R_{1d} i_{1d} \tag{1.4}$$

$$0 = \frac{1}{\omega_b}\frac{d\psi_{1q}}{dt} + R_{1q} i_{1q} \tag{1.5}$$

$$0 = \frac{1}{\omega_b}\frac{d\psi_{2q}}{dt} + R_{2q} i_{2q} \tag{1.6}$$

where v_d, v_q and v_{fd} are the terminal voltages of the stator and field windings, R_s, R_{fd}, R_{1d}, R_{1q}, R_{2q} are the resistances of the windings, i_d, i_q, i_{fd}, i_{1d}, i_{1q}, i_{2q} and ψ_d, ψ_q, ψ_{fd}, ψ_{1d}, ψ_{1q}, ψ_{2q} are the currents and linkage fluxes across the stator, field and dampers windings, ω_r and ω_b are the angular frequency and base angular frequency of the rotor.

The linkage fluxes are expressed in eqs. (1.7) to (1.12). Since all windings along one axis are magnetically coupled, the linkage flux across one winding is composed both of the leakage flux induced by its self-inductance and of the mutual flux linking all inductances along the axis. Because d and q-axes are perpendicular, there is no linkage between the windings of the axes.

$$\psi_d = -L_{ld} i_d + L_{ad} \left(-i_d + i_{fd} + i_{1d}\right) \tag{1.7}$$

$$\psi_q = -L_{lq} i_q + L_{aq} \left(-i_q + i_{1q} + i_{2q}\right) \tag{1.8}$$

$$\psi_{fd} = L_{lfd} i_{fd} + L_{ad} \left(-i_d + i_{fd} + i_{1d}\right) \tag{1.9}$$

$$\psi_{1d} = L_{l1d} i_{1d} + L_{ad} \left(-i_d + i_{fd} + i_{1d}\right) \tag{1.10}$$

$$\psi_{1q} = L_{l1q} i_{1q} + L_{aq} \left(-i_q + i_{1q} + i_{2q}\right) \tag{1.11}$$

$$\psi_{2q} = L_{l2q} i_{2q} + L_{aq} \left(-i_q + i_{1q} + i_{2q}\right) \tag{1.12}$$

where L_{ld}, L_{lq}, L_{lfd} L_{l1d}, L_{l1q}, L_{l2q} are the leakage inductances of the stator, field and the dampers and L_{ad}, L_{aq} are the mutual inductances of d and q-axes.

Figure 1.2 illustrates a visual description of the equivalent circuits of the synchronous machine proposed from eqs. (1.1) to (1.12). From this representation it is possible to determine the expressions of the so-called standard parameters of the synchronous machines, which "translate" their behaviours during transients, in which, the linkage fluxes are forced into high-reluctance paths by different induced currents, which decay in different periods of time [52], [54]. Depending on the decaying velocity of these components, the parameters associated to the phenomena are called — from the fastest to the slowest — sub-transient, transient and synchronous, where the last one represents the steady-state of the synchronous machine [52]. These parameters can be determined from experimental data obtained from short-circuit tests on unloaded machines [52], [59]. Most of the aforementioned expressions are not indispensable for the analyses carried out in this work, and therefore, they will be developed if necessary and opportune, otherwise, and they will not be developed; If desired, the reader can find all expressions in [52].

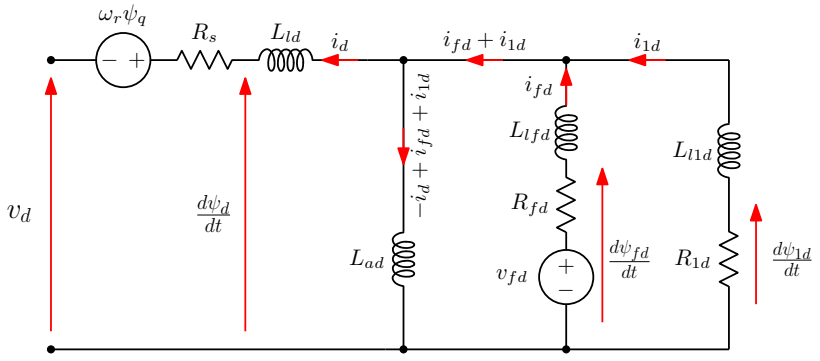

(a) d-axis

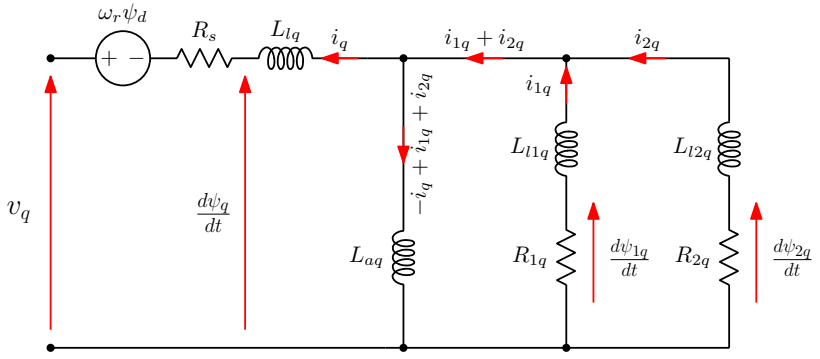

(b) q-axis

Figure 1.2 – Equivalent circuits of the dq-axes of the synchronous machine.

Regarding the mechanical modelling of the synchronous machine, since the analysis of the impact of PE-based sources on torsional modes of rotating masses is out of the scope of this work, the turbine-generator shaft is represented with a lumped single mass model, not displaying any torsional effect. Therefore, the variation of angular frequency of the shaft is caused by the unbalance between the mechanical and electromagnetic torques applied to it. In *per unit*, the motion of the synchronous machine can be expressed as a function of the power unbalance. In the literature, eq. (1.13) is also known as the swing equation.

$$\begin{cases} \dfrac{d\omega_r}{dt} = \dfrac{1}{2H}\left(P_m - P_e - K_d\Delta\omega\right) \\ \dfrac{d\delta}{dt} = \omega_b\omega_r \end{cases} \tag{1.13}$$

where $\Delta\omega$ is the angular frequency deviation of the rotor in relation to the grid frequency (ω_g), H and K_d are the coefficient of inertia and the damping factor of the rotating mass, P_m and P_e are the mechanical and electric powers at the shaft level, and δ is the internal angle of the synchronous machine rotor. The coefficient of inertia (H) represents the amount of kinetic energy per rated power (MWs/MVA) stored into the turbine-generator shaft, and it is

inherent to the physical construction of the machinery. Typical values of H are between 2.5 and 10 s, depending on the type of generating unit [52]. The damping factor (K_d) represents the damping related to the mechanics of the system (i.e. mechanical losses), and it can often be neglected for practical considerations [54]. In order to deduce P_e, the electric power at the stator level (P_t) is given in eq. (1.14).

$$P_t = v_d i_d + v_q i_q \tag{1.14}$$

Replacing eqs. (1.1) and (1.2) in eq. (1.14):

$$P_t = \left(-R_s i_d + \frac{1}{\omega_b}\frac{d\psi_d}{dt} - \omega_r \psi_q\right) i_d + \left(-R_s i_q + \frac{1}{\omega_b}\frac{d\psi_q}{dt} + \omega_r \psi_d\right) i_q \tag{1.15}$$

Rearranging the right side of eq. (1.15):

$$\begin{aligned} P_t = & \frac{i_d}{\omega_b}\frac{d\psi_d}{dt} + \frac{i_q}{\omega_b}\frac{d\psi_q}{dt} \\ & + \omega_r \left(\psi_d i_q - \psi_q i_d\right) \\ & - R_s \left({i_d}^2 + {i_q}^2\right) \end{aligned} \tag{1.16}$$

The right side terms of eq. (1.16) correspond, respectively, to the rate of change of the magnetic energy stored in the armature, the electric power at the shaft level (P_e), which is also known as the power transferred across the air gap between the rotor and the stator of the synchronous machine, and the resistive losses at the stator level [50], [52].

1.2.2 $E'X'H$ SM model

According to [52], [53], despite the fact that simplified models of synchronous machines may conceal critical phenomena, they can still be considered acceptable for determined studies. In the case of this work, a simplified model of the synchronous machine is proposed to determine the dominant dynamic of the system composed of a synchronous machine connected to an infinite bus. It is based on the simplest model used to represent synchronous machines during transients, usually called "constant voltage behind a single reactance", associated with the swing equation. This model is hereinafter referred to as $E'X'H$, referring

to its electric and mechanical representations, where $E'X'$ and H are the main parameters of these models, respectively. The hypotheses considered to establish this model are listed below [52], [54], [55]:

- Considering that the variations of the angular frequency of the rotor are sufficiently small, ω_r is assumed approximately equal to its nominal value (ω_0), it does not presenting any impact on the stator voltages.
- The variations of the linkage fluxes of the stator (ψ_d and ψ_q) are also neglected. This neglects the electromagnetic transients of the stator of the synchronous machine, and, according to [52], the overlook of these phenomena can only be made if the same is applied to the network equations, otherwise, the assumption is inconsistent.
- As mentioned previously, the armature flux is forced into high-reluctance paths outside the field winding by induced currents during transients. Since the sub-transient stage decays much faster than the transient stage, the former (and its associated circuit) will be neglected. Furthermore, since the decay of the transient stage is slow — order of several seconds — the linkage fluxes are considered constant during all the transient period.

From these hypotheses, eqs. (1.1) to (1.6) can be rewritten as given in eqs. (1.17) to (1.19). The equivalent circuit illustrating the relationship between fluxes and currents are given in Figure 1.3.

$$v_d = -R_s i_d - \omega_0 \psi_q \tag{1.17}$$

$$v_q = -R_s i_q + \omega_0 \psi_d \tag{1.18}$$

$$v_{fd} = R_{fd} i_{fd} \tag{1.19}$$

From Figure 1.3a, it is possible to determine the expressions of the fluxes:

$$\psi_d = -L_{ld} i_d + \psi_{ad} \tag{1.20}$$

$$\begin{aligned} \psi_{ad} &= L_{ad}\left(-i_d + i_{fd}\right) \\ &= \psi_{fd} - L_{lfd} i_{fd} \end{aligned} \tag{1.21}$$

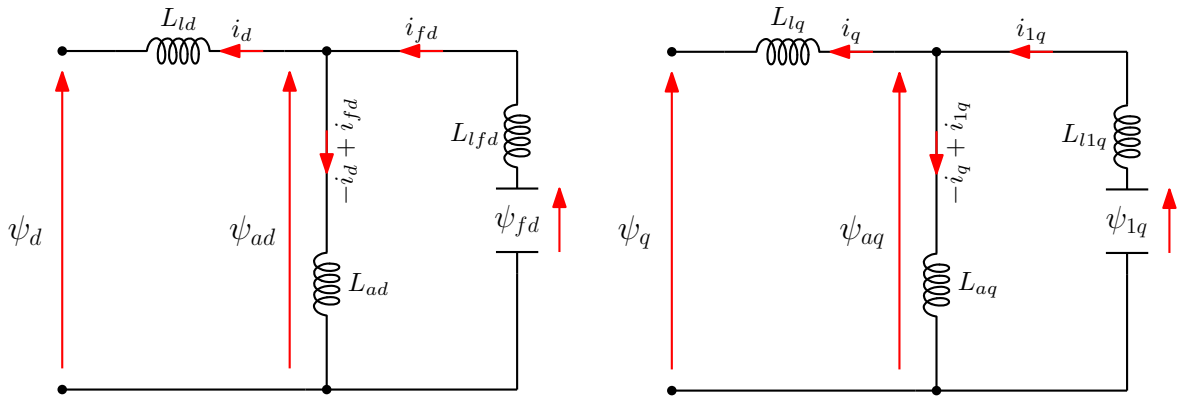

(a) d-axis (b) q-axis

Figure 1.3 – Equivalent circuits of the dq-axes of the synchronous machine illustrating the relationship between fluxes and currents after considering the simplifying hypotheses.

Isolating i_{fd} in the second line of eq. (1.21) and replacing in the first line, it is possible to rewrite ψ_{ad} as:

$$\psi_{ad} = \frac{L_{ad}L_{lfd}}{L_{ad} + L_{lfd}} \left(-i_d + \frac{\psi_{fd}}{L_{lfd}} \right) \tag{1.22}$$

Also, from Figure 1.3a, the equivalent inductance of the circuit, measured at the stator level, represents the transient inductance of d-axis of the synchronous machine (L'_d):

$$L'_d = L_{ld} + \frac{L_{ad}L_{lfd}}{L_{ad} + L_{lfd}} \tag{1.23}$$

Combining eqs. (1.22) and (1.23) and replacing ψ_{ad} at eq. (1.20):

$$\psi_d = -L_{ld}i_d + (L'_d - L_{ld}) \left(-i_d + \frac{\psi_{fd}}{L_{lfd}} \right) \tag{1.24}$$

The same can be deduced for the q-axis, *mutatis-mutandis*:

$$\psi_q = -L_{lq}i_q + \left(L'_q - L_{lq}\right) \left(-i_q + \frac{\psi_{1q}}{L_{l1q}} \right) \tag{1.25}$$

Replacing eq. (1.25) and (1.24) in eqs. (1.17) and (1.18), respectively:

$$\begin{cases} v_d = -R_s i_d + \omega_0 L'_q i_q - \omega_0 \left(L'_q - L_{lq}\right) \dfrac{\psi_{1q}}{L_{l1q}} \\ v_q = -R_s i_q - \omega_0 L'_d i_d + \omega_0 \left(L'_d - L_{ld}\right) \dfrac{\psi_{fd}}{L_{lfd}} \end{cases} \tag{1.26}$$

Defining the transient electromotive force (e'_d and e'_q) as:

$$\begin{cases} e'_d = -\omega_0 \left(L'_q - L_{lq}\right) \dfrac{\psi_{1q}}{L_{l1q}} \\ e'_q = +\omega_0 \left(L'_d - L_{ld}\right) \dfrac{\psi_{fd}}{L_{lfd}} \end{cases} \tag{1.27}$$

The stator voltage of the synchronous machine ($\vec{v}_{sm}$) can be rewritten as in eq. (1.28). For this purpose, the transient saliency of the synchronous machine is neglected, and therefore $L'_q = L'_d$.

$$(v_d + jv_q) = \left(e'_d + je'_q\right) - \left(R_s + j\omega_0 L'_d\right)(i_d + ji_q) \tag{1.28}$$

Therefore, from eq. (1.28), it can be observed that the transient model of the synchronous machine is represented as an ideal voltage source (transient electromotive force, $\vec{e'}$) behind a transient reactance ($X'_d = \omega_0 L'_d$) and, for this reason, this model may present steady-state errors at post disturbance conditions. The stator resistance can also be neglected due to its small value compared to X'_d. Figure 1.4 illustrates the simplified transient model of the synchronous machine connected to an infinite bus bar, where X_t and X_l represent the inductances of a coupling transformer and an inductive transmission line[1], respectively.

For the $E'X'H$ model, the mechanicals of the synchronous machine are also represented with eq. (1.13). The electric power at the shaft level of the synchronous machine (P_e) is equal to the active power flow between the synchronous machine and the infinite bus, computed at the synchronisation point of the synchronous machine, which is $\vec{e'}$. Therefore:

$$P_e = \frac{E'V_g}{X_{eq}} \sin\left(\delta - \delta_g\right) \tag{1.29}$$

[1] According to [52], when a full network is reduced to a two-bus system, the resulting impedance is essentially inductive.

where E' and δ are the magnitude and phase of the transient electromotive force ($\vec{e'}$), and V_g and δ_g are the magnitude and phase of the infinite bus voltage ($\vec{v}_g$).

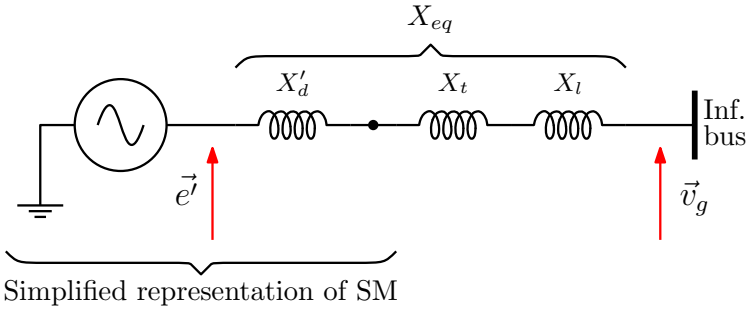

Figure 1.4 – Transient model of the synchronous machine ($E'X'H$, resistance of the stator neglected) vs infinite bus.

Furthermore, in the $E'X'H$ model, the damping factor (K_d) does not have the exact same meaning of that from the reference model. While in the latter, K_d represents a damping purely related to the mechanics (i.e. mechanical losses) which can generally be neglected for all practical considerations [54], in the former, on the other hand, it represents a combination of different damping effects of the system, which is used to compensate the lack of damping due to simplifying hypotheses. According to [60], the equivalent value of K_d composing the damping provided by generators and loads is a function of the parameters of the synchronous machine and the grid. According to [54], a rigorous derivation of the damping power is long and complicated, and therefore, from simplifying assumptions, it is proposed a simplified expression of it, providing an average value of K_d. References [52], [57] only consider the load damping (typical value 1 or 2%). Normally, for large systems, these parameters are estimated using Phasor Measurement Units (PMUs) at specific buses of the system [61].

With eqs. (1.13) and (1.29), it is possible to determine a state-space representation of the system as demonstrated in Appendix B.2:

$$\frac{d}{dt}\begin{bmatrix}\Delta\omega_r\\ \Delta\delta\end{bmatrix} = \underbrace{\begin{bmatrix}-\frac{K_d}{2H} & -\frac{K_s}{2H}\\ \omega_b & 0\end{bmatrix}}_{\mathbf{A}}\begin{bmatrix}\Delta\omega_r\\ \Delta\delta\end{bmatrix} + \underbrace{\begin{bmatrix}\frac{1}{2H}\\ 0\end{bmatrix}}_{\mathbf{B}}\Delta P_m \tag{1.30}$$

where K_s is the synchronising torque between the synchronous machine and the infinite bus, which is given in eq. (1.31). The synchronising torque is a restoring torque acting on the shaft of a synchronous machine to keep the synchronism when its angular frequency is different from the nominal frequency [57].

$$\begin{aligned} K_s &= \left.\frac{\partial P_e}{\partial \delta}\right|_{(\delta,\delta_g)=(\delta_0,\delta_{g,0})} \\ &= \frac{E'V_g}{X_{eq}}\cos\left(\delta_0 - \delta_{g,0}\right) \end{aligned} \tag{1.31}$$

As illustrated in Figure 1.5, this system can also be displayed using a more tangible representation. Block diagrams are very flexible to represent small systems, providing visual interpretations of the propagation of actions through the parts of the system.

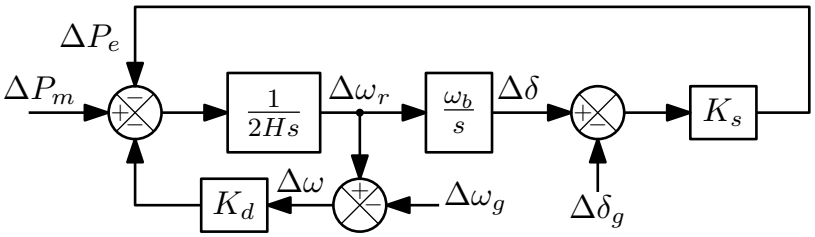

Figure 1.5 – Block diagram of the synchronous machine vs infinite bus system.

The characteristic polynomial of the system is found solving $\det(\mathbf{A} - \lambda\mathbf{I}) = 0$:

$$\lambda^2 + \frac{K_d}{2H}\lambda + \frac{\omega_b K_s}{2H} = 0 \tag{1.32}$$

From eq. (1.32), it is possible to determine the undamped natural frequency (ω_n) and the damping ratio (ξ) of the oscillating eigenvalues of the system as a function of its parameters. It should be highlighted that, in time-domain simulations and eigenvalues analysis, the observed frequency is the damped frequency (ω_d), which is, as given in eq. (1.35), a combination of ω_n and ξ.

$$\omega_n = \sqrt{\frac{\omega_b K_s}{2H}} \tag{1.33}$$

$$\xi = \frac{K_d}{2\sqrt{2H\omega_b K_s}} \tag{1.34}$$

$$\omega_d = \omega_n\sqrt{1-\xi^2} \tag{1.35}$$

From eqs. (1.33) and (1.34), it is observed that, with the increase of K_d, the oscillations becomes continuously more damped. Otherwise, with the increase of K_s, the oscillations becomes continuously less damped and the faster. The increase of H decreases both the damping and the frequency of the oscillations.

1.2.3 Comparison between SM models

Two different levels of detail of the synchronous machine are proposed in this work. The reference model represents the electric circuits of the synchronous machine with six windings, being two of the stator and four of the rotor circuit. The $E'X'H$ model proposes a simplified representation of the synchronous machine considering many simplifying hypotheses. Depending on the application, one, other or both models will be used. Therefore, in order to be capable of providing a critical look when the $E'X'H$ model can be applied, or to be able to explain possible divergences between both models, a first analysis is performed in this section to observe the expected deviations in these applications.

For this purpose, the synchronous machine vs infinite bus of Figure 1.6 is adopted as case study, and the parameters of the grid are given in Table 1.1. For this scenario, the adopted length for the transmission line L_{12} is 25 km, and, since it is a short line, its shunt susceptance is neglected [52]. Therefore, the simplified representation of the system is similar to that from Figure 1.4. Regarding the synchronous machine, despite not being realistic, initially, its regulators are not taken into account, and therefore, its inputs — mechanical power (P_m) and field voltage (v_{fd}) — are constant and calculated from the power flow. The controls of the synchronous machine are added progressively over this section. The parameters of the synchronous machine are given in Table 1.2.

The power flow of the system is presented in Table 1.3 and, from the given tables, it is possible to compute $\vec{e'}$ and, subsequently, K_s. *Nota bene:* all quantities and parameters should be expressed in the same *per unit* base to compute the right value of K_s and, depending on the chosen base, H should also be adapted. Considering the rated power of the synchronous machine as base power, $X_{eq} = 0.825$ pu, and $\vec{e'} = 1.07\angle 0.64$ pu. Therefore, applying eq. (1.31), $K_s = 1.04$ pu torque/rad.

Using a similar method to that introduced in [61], the value of K_d of the $E'X'H$ model is estimated in order to reasonably represent the damping of the system. In this example, $K_d = 7.78$ pu torque/pu speed. Figure 1.7 illustrates a comparison of the behaviours of frequency oscillations obtained with the reference and the $E'X'H$ model of the synchronous machine after a phase shift on the voltage of the infinite bus. The dynamics obtained with both models are similar for the first swing and, after that, the mismatch between them increases over time. This behaviour is stated in the specialised literature and it is due to the aforementioned hypotheses related to the simplified model [52]–[54].

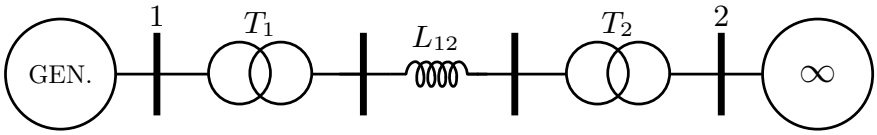

Figure 1.6 – Adopted case study for Chapter 1.

Table 1.1 – Dynamic model data for transformers and transmission lines.

Transformers parameters	**Value**
Rated frequency (f_n, Hz)	60
Rated power ($S_{3\phi}$, MVA)	900
Rated voltage (V_n, kV)	20/230
Winding resistance (R_t, pu)	0
Winding reactance (X_t, pu)	0.15
Π-lines parameters	**Value**
Base frequency (f_b, Hz)	60
Base power (S_b, MVA)	100
Base voltage (V_b, kV)	230
Direct resistance (r_d, pu/km)	0.0001
Direct reactance (x_d, pu/km)	0.001
Direct susceptance (b_d, pu/km)	0.00175

Table 1.2 – Dynamic model data for synchronous machines (SMs).

SM parameters	**Value**
Rated frequency (f_n, Hz)	60
Rated power ($S_{3\phi}$, MVA)	900
Rated voltage (V_n, kV)	20
Stator resistance (R_a, pu)	0.0025
Leakage reactance (X_l, pu)	0.02
Synchronous reactance d (X_d, pu)	1.80
Transient reactance d ($X_d^{'}$, pu)	0.30
Sub-transient reactance d ($X_d^{''}$, pu)	0.25
Synchronous reactance q (X_q, pu)	1.70
Transient reactance q ($X_q^{'}$, pu)	0.55
Sub-transient reactance q ($X_q^{''}$, pu)	0.25
Coefficient of inertia (H, s)	6.5
Damping factor (K_d, pu)	0

Table 1.3 – Power flow of the system.

Bus n°	**V (pu)**	**θ (rad)**	**P (MW)**	**Q (MVAr)**
1	1.0	0.417	700.00	117.19
2	1.0	0	-687.41	176.65

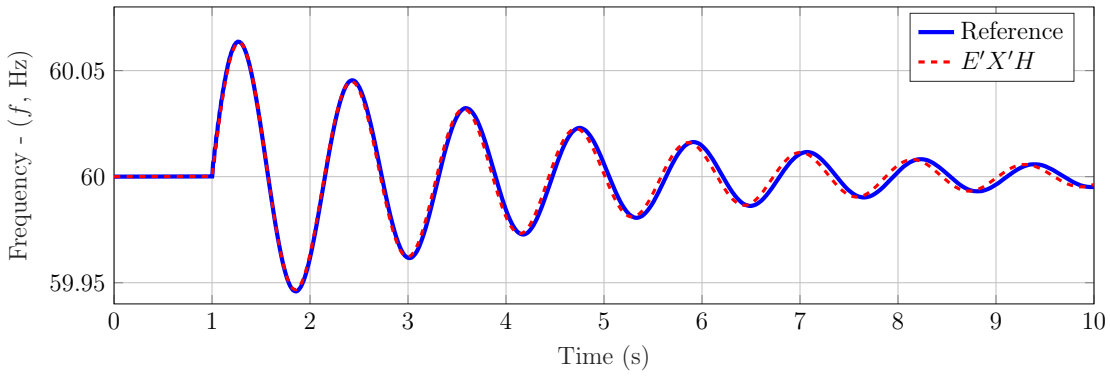

Figure 1.7 – Frequency oscillation behaviour of the synchronous machine vs infinite bus system after a phase shift on the voltage of infinite bus ($\Delta\delta_g = \pi/40$ rad).

Since the electric frequency of the synchronous machine is an image of the angular frequency of its rotating mass, the analysis of the electromechanical eigenvalues can provide more information about the frequency and the damping of the oscillations observed in Figure 1.7. The eigenvalues of the system are found from the linearised representation of system using the the methodology introduced in Appendix B.3. The participation factor matrix [52], [54] is employed to identify the electromechanical eigenvalues of the system using the reference model of the synchronous machine. The same is not necessary for the system using the $E'X'H$ model, since the system has only one pair of eigenvalues, which are the electromechanical ones. The comparison between the electromechanical eigenvalues of the synchronous machine considering both models is given in Table 1.4.

Table 1.4 – Electromechanical eigenvalues of the synchronous machine.

	Reference model	$E'X'H$ **model**
Eigenvalues ($\sigma \pm j\omega_d$)	$-0.28 \pm j5.46$	$-0.30 \pm j5.48$
Damping ratio (ξ, %)	5.14	5.45
Damped frequency (f_d, **Hz**)	0.869	0.872

Figure 1.7 and Table 1.4 provide substantial information about the consistency of the $E'X'H$ model with the reference model to represent the behaviour of the frequency of a synchronous machine without regulators.

1.2.4 Prime movers and governor

When operating in generator mode, the kinetic power developed on the shaft of synchronous machines is converted into electric power. In these applications, the rotors of synchronous machines are driven by turbines which in turn are driven by the energy provided by a primary source (i.e. hydro, fossil or nuclear). Considering that the nature and the conversion chain of each primary source are irrelevant to the studies carried out in this work, they are not detailed. Although, it is important to take notice that the dynamics of the conversion chain of each primary source are different [52], [56], [62]. This work adopts a generic model of nuclear prime movers representing the dynamics of steam valves and a three-stage steam turbine [62].

In order to maintain the proper functioning of the grid, the mismatch between generation and consumption must constantly be adjusted to maintain the frequency of the grid the closest to its nominal value. For this purpose, Transmission System Operators (TSOs) require that the generating units contribute to a series of ancillary services to the grid. At the European level, there are three main services to support the frequency of the grid [63]:

- Frequency Containment Reserve (FCR) is the active power reserve available to compensate the mismatch between generation and consumption. This service does not restore the frequency of the grid to its nominal value after the disturbance. This automatic service is ensured by all FCR providing units at the European level, although, not all connected units are qualified to provide FCR. The scheduled cross-frontier power flows are affected by FCR contribution.
- Frequency Restoration Reserve (FRR) is the reserve available to restore the frequency of the system to its nominal value. The FRR is an automatic centralised service handled by the TSO responsible for the area where the disturbance took place, and provided only by the generating units of this area, re-establishing the scheduled cross-frontier power flows.
- Replacement Reserve (RR) is the power reserve which is activated to restore or support the required level of FRR, preparing the system for additional imbalances. This service is manual and centralised by the local TSO.

These services have different timescales, FCR being the fastest and RR the slowest between the three. In France, these timescales are between 15 and 30 s, 133 and 800 s, and 30 min and 8 h, for FCR, FRR and RR, respectively [18]. A comparison between the grid codes of some countries can be found in [64]. Due to the timescale analysed in this work, only FCR is considered. The FCR — and other frequency related ancillary services — is realised by the speed governor, and implemented using a power frequency droop, where the operating point of mechanical power (P_{m0}) is proportionally adjusted as a function of the mismatch between the reference and the instantaneous angular frequency of the shaft of the synchronous machine, as given in eq. (1.36).

$$P_m^* = P_{m0} - K_{pf} \left(\omega_0 - \omega_r\right) \tag{1.36}$$

where P_m^* is the adjusted operating point of mechanical power of the synchronous machine, K_{pf} is the power frequency characteristic of the governor and ω_0 is the setpoint of angular frequency of the synchronous machine (which is, in general, equal to its nominal value, ω^*). In France, the French TSO determines that K_{pf} must be comprised between 6.25 and 33 pu power/pu frequency [18]. Typical values of K_p for steam turbine governors are between 16.66 and 25 pu power/pu frequency.

Figure 1.8 illustrates the generic frequency control chain of synchronous machines adopted in this work, the IEESGO [62]. It can be observed that this model has both a control piece and a power interface. It can be observed that the governor is composed of a power frequency droop function and two low-pass filters representing its dynamics. The power structure represents the dynamics of steam valves and a three-stage steam turbine. Standard models of turbines for power system simulation are presented [62].

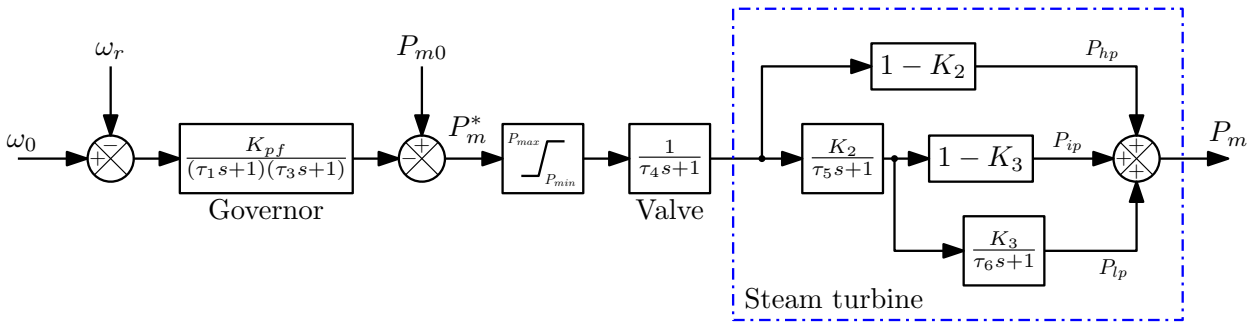

Figure 1.8 – IEESGO governor and steam turbine representation (simplified).

The frequency control chain presented in Figure 1.8 can be implemented in both the reference and $E'X'H$ models of the synchronous machine. For the same scenario and parameters given in Section 1.2.3, the impact of the frequency control chain on the electromechanical eigenvalues of the synchronous machine is compared in Table 1.6 considering both models of the synchronous machine. The parameters adopted for the control chain are given in Table 1.5. In this case study, since the infinite bus imposes the frequency of the system, the synchronous machine, *a priori*, does not need to contribute to FCR, and therefore, the impact of prime movers and the governor can be separately observed.

Table 1.5 – Dynamic model data for governor and steam turbine model IEESGO.

IEESGO parameters	**Value**
Power frequency characteristic (K_{pf}, pu)	-25
Lag time constant (τ_1, s)	0.1
Lag time constant (τ_3, s)	0.2
Steam flow time constant (τ_4, s)	0.05
Reheater time constant (τ_5, s)	7.0
IP-LP time constant (τ_6, s)	0.4
Reheater power fraction (K_2, pu)	0.7
IP-LP power fraction (K_3, pu)	0.4

Table 1.6 – Impact of the frequency control chain on the electromechanical eigenvalues of the synchronous machine.

	Reference model		$E'X'H$ **model**	
	FCR off	**FCR on**	**FCR off**	**FCR on**
Eigenvalues ($\sigma \pm j\omega_d$)	$-0.28 \pm j5.46$	$-0.25 \pm j5.63$	$-0.30 \pm j5.48$	$-0.28 \pm j5.67$
Damping ratio (ξ, %)	5.14	4.49	5.45	4.93
Damped frequency (f_d, **Hz**)	0.869	0.896	0.872	0.902

When just prime movers are considered (FCR off), the behaviour of frequency oscillations is the same as that of the system without the prime movers (refer to Table 1.4). The phenomenon can be easily understood from the analysis of the block diagram of Figure 1.9. When the FCR contribution is off, $K_{pf} = 0$, and therefore, the feedback of ω_r does not have any effect on the transfer function $\omega_r(s)/\theta_g(s)$, justifying the findings. On the contrary, when the FCR activated, it is observed a slight negative damping effect on the damping of the electromechanical eigenvalues, which is also stated by [62], [65]. This small impact can be explained by the fact that the frequency oscillations are filtered by the control chain, especially by the intermediate stage of the turbine which presents slow dynamics — dynamics of the reheater — reducing the bandwidth of the feedback signal. Therefore, the impact of the frequency oscillations on the closed-loop system is minor. Moreover, it should be highlighted that, in both cases, when equipped with the frequency control chain, the $E'X'H$ model is still representative of the reference model of the synchronous machine.

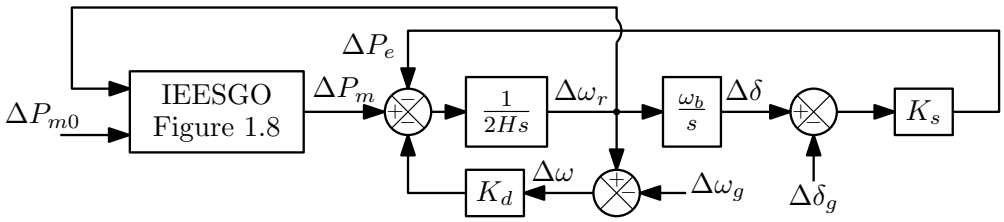

Figure 1.9 – Block diagram of the synchronous machine vs infinite bus system considering $E'X'H$ model and IEESGO.

1.2.5 Excitation system

In generator mode, the electromechanical energy conversion can only be ensured in the presence of an existing field flux (ψ_{fd}) which, in turn, is established when a dc field voltage (v_{fd}) is applied to the terminals of the field winding of the rotor of the synchronous machine. The excitation system supplies and automatically adjusts the field voltage of the synchronous machine to maintain the output voltage of the stator within the acceptable range [52], [66]. Excitation systems are classified in three categories based on the excitation power source [52], [66], [67]:

- The dc excitation system uses dc generators as the source of excitation power, injecting the field current via slip rings. The exciter may be driven by the shaft of the synchronous machine or by a motor. The exciter itself can be self or separately excited. The application of dc excitation system is continuously being replaced by ac or static excitation systems.

- The ac excitation system uses alternators as the source of excitation power, which usually shares the same shaft of the main generator. The conversion of the ac voltage of

the exciter to dc voltage of the field is ensured by controlled or non-controlled rectifiers. The power electronics switches can be static or rotating, where, in the former, the field current is injected via slip rings. The latter is known as brushless excitation system.

- The static excitation system does not possess any turning device. The excitation system is composed of static power electronics switches and provides the field current to the synchronous machine via slip rings. The excitation power is supplied to the rectifiers by the synchronous machine itself.

Voltage ancillary services to the grid are also required by the TSOs in order to maintain the voltages of the grid buses in acceptable values, and therefore, to maintain the proper functioning of the grid. At the European level, the regulations can be found in [63]. In France, there are two levels of voltage control required of the generating units by the French TSO [18]:

- The primary voltage control is an automatic service to control the local quantities of voltage and/or reactive power. There are three different types of primary voltage control: the supply of a fixed amount of reactive power; an adaptive output voltage following a reactive power voltage droop function; or the control of output voltage of the synchronous machine following a fixed operating point. The latter is the most used for synchronous machines.

- The secondary voltage control is an automatic centralised service deployed to expand the efficacy of the primary control and expand it to more global level. This service is coordinated by the TSO to control either the reactive level of a "geographical" area of the system, or the reference voltage of this area.

A third level of voltage control can be used to adapt, manually, the output voltage of the generating unit in order to respect the contractual reactive power voltage diagram. The timescale of primary and secondary voltage control are between hundreds of milliseconds and a few seconds, and 10 and 30 s, respectively. As for frequency ancillary services, only primary voltage control is considered in this work.

Figure 1.10 illustrates the simplified block diagrams of three different excitation systems adopted in the first part of this work: the DC1C, the AC1C and the ST1C [67]. All three models are composed of an Automatic Voltage Regulator (AVR) which, in turn, is composed of a voltage sensor and a low-pass filter, a main voltage regulator, and an input for a stabilisation signal (v_{stab}) provided by a power system stabiliser, which is discussed further in this section. The dc and ac excitation systems also present the dynamics of the exciter and a supplementary feedback stabilisation signal. Considering the ST1C, since the dynamics of the static exciter are very fast, they are not represented in the block diagram of the model. More details about these models can be found in [52], [67].

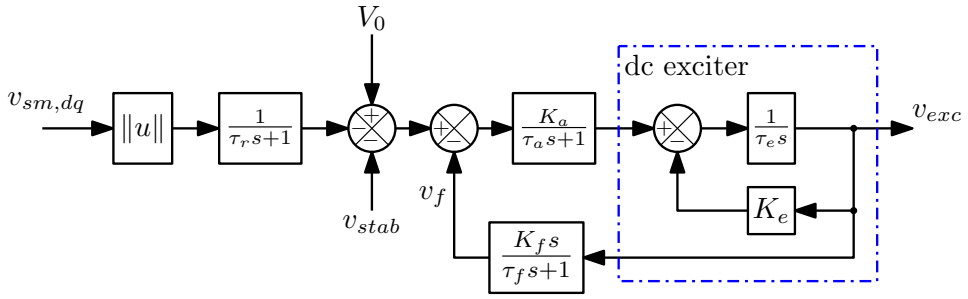

(a) DC1C

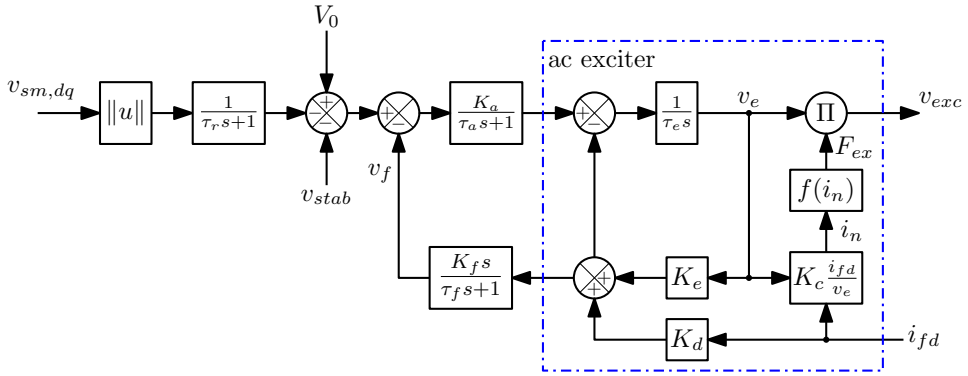

(b) AC1C

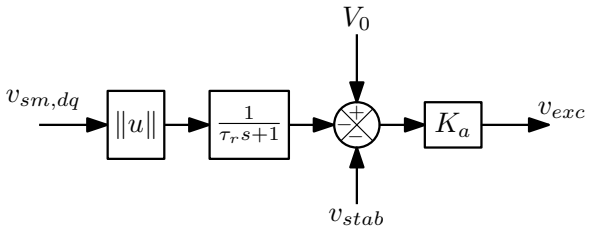

(c) ST1C

Figure 1.10 – Block diagram of dc, ac and static excitation systems (simplified).

From Figure 1.10 it can be observed that the output of the excitation system is the excitation voltage (v_{exc}), yet in the introduction of this section is was explained that the excitation system supplies the field voltage (v_{fd}). Indeed, in volts, these quantities are the same, although, in the *per unit* system, they are usually expressed using two different *per unit* bases to better interface the model of the excitation system with the that of the synchronous machine (both the variables of the field and stator terminals) [52]. The relationship between v_{exc} and v_{fd} is expressed in eq. (1.37) and developed in [52].

$$v_{exc} = \frac{L_{ad}}{R_{fd}} v_{fd} \tag{1.37}$$

Despite the possibility to adapt the $E'X'H$ model of the synchronous machine to take into account the dynamics of the field circuit and that of the excitation system, only the reference model of the synchronous machine is used in the following analysis. The idea is to observe how much the electromechanical eigenvalues estimated with the $E'X'H$ model get further from those found with the reference model of the synchronous machine equipped with the excitation system, evaluating then, how qualitative are the tendencies obtained with the former. If required, the methodology to consider the dynamics of field circuit and excitation system is presented in [52].

The adopted parameters for the different excitation systems are given in Table 1.7. The impact of the excitation system on the electromechanical eigenvalues of the synchronous machine is given in Table 1.8. It should be highlighted that, according to the exciter type, the impact on the damping ratio of the oscillations can be more or less pronounced. In the case of the AC1C, the electromechanical eigenvalues are not impacted by the exciter. On the contrary, for the ST1C, the system is unstable. The impact on the frequency oscillations are slightly negative when the synchronous machine is equipped with the DC1C excitation system. According to [54], if the AVR or the exciter has a large time constant, the AVR will not react during the transient state and the regulated system behaves akin to the unregulated one. On the contrary, fast-acting AVRs with large gains may result in a negative damping, leading to an unstable system [54], [55], consequently requiring additional stabilisation systems.

Table 1.7 – Dynamic model data for ac rotating excitation system model AC1C, dc rotating excitation system model DC1C and static excitation system model ST1C.

Parameters	**DC1C**	**AC1C**	**ST1C**
Filter time constant (τ_r, s)	0.01	0.01	0.01
Main regulator gain (K_a, pu)	20	78.14	200
Main regulator time constant (τ_a, s)	0.055	0.013	—
Regulator stabilising gain (K_f, pu)	0.125	0.143	—
Reg. stabilising time constant (τ_f, s)	1.8	1	—
Exciter gain (K_e, pu)	1	1	—
Exciter time constant (τ_e, s)	0.36	1.75	—
Demagnetising factor (K_d, s)	—	0.17	—
Rectifier loading factor (K_c, s)	—	0.12	—

Table 1.8 – Impact of the excitation system on the electromechanical eigenvalues of the synchronous machine.

	Reference model			
Exciter type	—	**DC1C**	**AC1C**	**ST1C**
Eigenvalues ($\sigma \pm j\omega_d$)	$-0.25 \pm j5.63$	$-0.23 \pm j5.59$	$-0.25 \pm j5.62$	$0.004 \pm j6.12$
Damping ratio (ξ, %)	4.49	4.09	4.50	-0.07
Damped frequency (f_d, Hz)	0.896	0.890	0.894	0.974

1.2.6 The Power System Stabiliser

The electromechanical oscillations of the synchronous machine are negatively impacted by the addition of its regulators [54], [62], [65], especially by the fast AVR and static exciter, where the system is even unstable. Despite the usual absence of specific legislations, recommendations or guidelines about the minimum required damping for these oscillations, 5% is often considered as the minimum accepted value [24], [55]. In order to enhance the damping of these oscillations, the Power System Stabiliser (PSS), a supplementary control unit, is added to the regulators of the synchronous machine [52], [54], [55], [67].

In the transmission system, because the ratio between resistance and reactance (R/X) is low, strong links between frequency and active power, and between voltage and reactive power are observed. Otherwise, cross-links between these quantities are fairly decoupled. Therefore, ideally, the PSS could easily mitigate the electromechanical oscillations by applying power oscillations of same amplitude in the opposite direction (ac component) in order to counteract the former oscillations. According to [54], PSSs can be applied to the governor or to the excitation system, however, despite what could be indicated by common sense, in most cases, the PSS may not be effective when applied to the governor, because, as mentioned previously, the frequency bandwidth of the frequency control chain is very limited due to the slow dynamics of the turbine. Therefore, despite the weak link between power and voltage, the only practical solution is to apply the PSS on the AVR-excitation system.

The PSSs are usually based on the angular frequency of the synchronous machine, the active power, or both signals, and their main elements are: the signal sensor and low-pass filter, a proportional gain, a washout filter to insulate the ac component of the oscillations, and phase compensations to match the stabilisation signal to the ideal phase of the electromechanical oscillations [52], [54], [55], [67]. Figure 1.11 illustrates the block diagram of the PSS1A, which is the model of PSSs adopted for this work. The tuning of the parameters of a PSS is a laborious task, and it is usually accomplished using optimisation routines. The methodology and/or examples can be found in [52], [54], [55], [68]. The adopted parameters are given in Table 1.9.

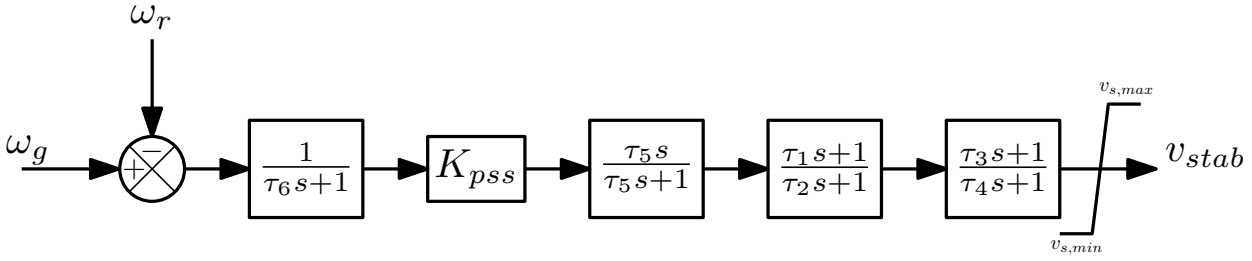

Figure 1.11 – Block diagram of power system stabiliser PSS1A (simplified).

Table 1.9 – Dynamic model data for power system stabiliser model PSS1A.

PSS1A parameters	**Value**
Filter time constant (τ_6, s)	0.01
PSS gain (K_{pss}, pu)	variable
Washout filter (τ_5, s)	0.05
First lead time constant (τ_1, pu)	0.05
First lag time constant (τ_2, pu)	0.02
Second lead time constant (τ_3, pu)	3.0
Second lag time constant (τ_4, pu)	5.4

The analysis of the impact of the PSS on the electromechanical eigenvalues of the system is performed and given in Table 1.10. In order to provide an easy comparison, the eigenvalues of the system without PSS (from Table 1.8) are also displayed. As for the previous analysis, only the reference model of the synchronous machine is considered for the analysis of the impact of the PSS. As for the excitation system, if desired, it is also possible to implement a simplified PSS effect in the $E'X'H$ model [52], [65], [68].

Table 1.10 – Impact of the power system stabiliser on the electromechanical eigenvalues of the synchronous machine.

		Reference model		
	Exciter type	**DC1C**	**AC1C**	**ST1C**
PSS off	**Eigenvalues ($\sigma \pm j\omega_d$)**	$-0.23 \pm j5.59$	$-0.25 \pm j5.62$	$0.004 \pm j6.12$
	Damping ratio (ξ, %)	4.09	4.50	-0.07
	Damped frequency (f_d, Hz)	0.890	0.894	0.974
PSS on	**PSS Gain (K_{pss}, pu)**	100	100	20
	Eigenvalues ($\sigma \pm j\omega_d$)	$-0.60 \pm j5.32$	$-0.47 \pm j5.41$	$-1.04 \pm j6.62$
	Damping ratio (ξ, %)	11.28	8.75	15.55
	Damped frequency (f_d, Hz)	0.847	0.861	1.054

The implementation of the PSS enhances the damping of the electromechanical oscillations for the three excitation systems, overcoming the aforementioned threshold of 5% of damping ratio. From the analysis of Table 1.10, it is observed that the performance of the PSS is more pronounced as the excitation system is faster, which is possibly related to the bandwidth of the exciter. However, it should be highlighted that the set of parameters, excepting K_{pss}, is the same for the three cases, and therefore, the parameters can still be optimised.

1.2.7 Considerations about the $E'X'H$ model

This section has presented the main elements which constitute the classical power conversion chain of a synchronous machine, analysing their impact on the electromechanical eigenvalues of the system. Due to the slow behaviour of the turbine, the governor does not present an important impact on the oscillating electromechanical eigenvalues of the system. The integration of the excitation can however have a larger effect, especially with the static excitation which is the fastest between the three types of excitation. It should be highlighted that even if the excitation system and PSS are implemented in the $E'X'H$ model, it is still possible to adjust the parameters of this model to provide a good estimation of the frequency oscillations. Therefore, it can be concluded that the E'X'H model of the synchronous machine is capable of providing qualitative tendencies about the behaviour of the frequency oscillations of the system.

However, it should be emphasised that the parameters of this model may diverge from the initial physical meaning. For example, Figure 1.12 illustrates the frequency oscillation behaviour of the synchronous machine vs infinite bus system using both representations of the synchronous machine, where the reference model is equipped with the IEESGO, ST1C and PSS, whereas the simplified model is only equipped with the simplified version of the IEESGO. Using a method similar to that presented in [61], from the analysis of eqs. (1.33) and (1.34), the value of K_d of the $E'X'H$ model has to be modified in order to estimate the damping of the frequency oscillations observed with the reference model, and if both K_d and K_s are adjusted, it is even possible to match the frequency of these oscillations.

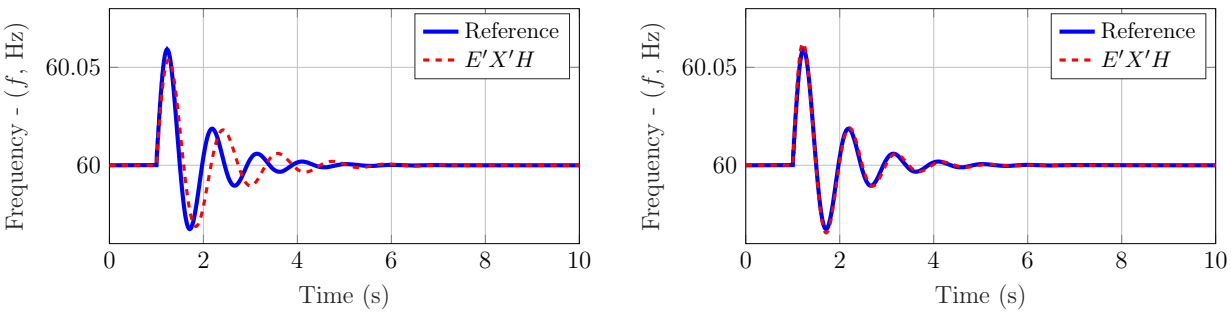

(a) $K_s = 1.04$ pu and $K_d = 24.4$ pu

(b) $K_s = 1.44$ pu and $K_d = 31.1$ pu

Figure 1.12 – Frequency oscillation behaviour of the synchronous machine vs infinite bus system after a phase shift on the voltage of infinite bus ($\Delta\delta_g = \pi/40$ rad). Reference model of synchronous machine equipped with IEESGO (FCR on), ST1C and PSS1A. Simplified model equipped with IEESGO (FCR on).

1.3 Power Electronics (PE)-based sources

Figure 1.13 illustrates the generic topology of a Voltage Source Converter (VSC), a PE-device used to convert dc to ac power and *vice versa*. Despite many different topologies, the operating principle is similar: the ac voltage (v_m) is produced from the modulation of the dc voltage (v_{dc}). The electronic switches used to modulate v_{dc} are driven using on/off pulses by a low level control in a way that the average values of v_m correspond to the reference (v_m^*) generated with a control strategy. Different strategies can be used to generate the switching pulses; if desired, the reader can find more in [69].

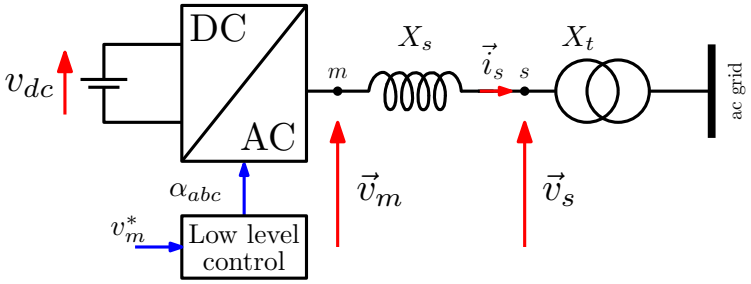

Figure 1.13 – Generic topology of a Voltage Source Converter.

In this work however, the inverter is represented using an ideal average model, neglecting the low level control. For power system analysis, this model is more suitable than detailed model due its simplifications. Average model is a fairly representation of power electronics sources, neglecting just high-frequency harmonics caused by transistors switching [4].

In Figure 1.13 the inverter is interfaced to the ac grid with an inductive filter (X_s) and a transformer (X_t), and the resistances of these elements are neglected. In grid connected applications, the behaviour of the PE-based source depends on how the inverter manages the active power flow with the grid. Inverters, differently than synchronous machines, do not have an inherent synchronisation point, but it is derived from the control strategy. Considering two possible synchronisation points, m and s, the active power flow between the inverter and grid can be expressed as given in eqs. (1.38) and (1.39). The electric equations are expressed in *per unit* using the conventions of Appendix A.

$$\begin{aligned} P &= \Re\left\{\vec{v}_s\left(\frac{\vec{v}_m - \vec{v}_s}{jX_s}\right)^*\right\} \\ &= \frac{V_m V_s}{X_s}\sin(\delta_m - \delta_s) \end{aligned} \tag{1.38}$$

$$\begin{aligned} P &= \Re\left\{\vec{v}_s \vec{i}_s^{\,*}\right\} \\ &= V_s I_s \cos(\varphi) \end{aligned} \tag{1.39}$$

where V_m and δ_m are the magnitude and phase of $\vec{v}_m$, V_s and δ_s are the magnitude and phase of $\vec{v}_s$, I_s is the magnitude of $\vec{i}_s$, and φ phase between $\vec{v}_s$ and $\vec{i}_s$.

From eqs. (1.38) and (1.39), it can be observed that the power flow can be controlled either acting on V_m and δ_m, or on I_s and φ. Therefore, considering the first, the inverter behaves as a voltage source, whereas, regarding the latter, as a current source. In this work, inverters displaying a voltage source behaviour are hereinafter referred to as Voltage Control mode Inverters (VCIs). On the other hand, inverters behaving as a current source are hereinafter referred to as Current Control mode Inverters (CCIs). In the literature, VCI and CCI strategies are also known as grid-forming [16], [33], [45], and grid-feeding [70], [71] or grid-following [44], [47], [72], respectively. It should be highlighted that these control strategies can be implemented conserving the same power electronics interface.

1.3.1 Voltage Control mode Inverters (VCIs)

First applications of inverters operating in voltage control mode were as Uninterruptible Power Supply (UPS), where the inverter operated in standalone mode to supply electric power to critical loads under emergency conditions [4], [73]. Other characteristics of VCIs — such as load sharing and black start capability — also make them very attractive for microgrids applications [70], [71], [74]. In interconnected power systems, the majority of the connected inverters operates hitherto in current control mode, although, theoretical results reported in [45], [75] show that in power system with 100% PE-based sources, 30% of inverters should operates in VCI mode in order to maintain the system stability. Very few inverters operating in VCI mode are hitherto connected to the power grid [76], [77]. To the author's knowledge the 30 MW Battery Energy Storage System (BESS) in South Australia is currently the powerful VCI in operation [77].

1.3.1.1 The principle of the VCI control

The VCI control is related to eq. (1.38), where P is sensitive to V_m and δ_m. In transmission systems, since the equivalent reactance of the system is much bigger than its equivalent resistance, the sensitivity of the active power to angular variations is much stronger than to

voltage variations, and consequently, focus is applied to the P-δ_m link. Therefore, as illustrated in Figure 1.14, the principle of the VCI control relies on the generation of a δ_m^*, which is the image of δ_m, to control the active power flow. The estimation $\tilde{\delta}_s$ is added in feed forward to the control in order to compensate the disturbances in δ_s, providing a better power control. In real applications, the estimation of $\tilde{\delta}_s$ could be provided using a Phase-Locked Loop (PLL) [4] or applying the observability principle [78] on the physical model.

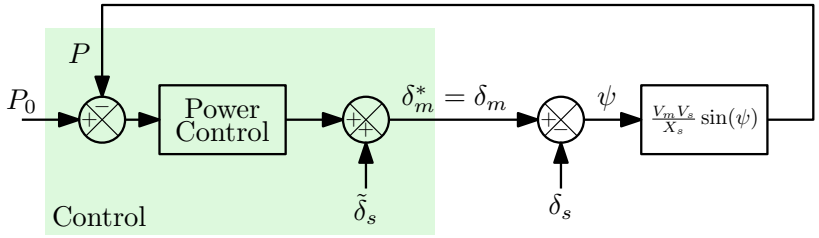

Figure 1.14 – The principle of the VCI control.

Focussing on the control, as illustrated in Figure 1.15, an integral control can be implemented as a viable solution [42], [79]. This control strategy is known as Strategy A in [42], [80]–[82]. The integrator of this structure guarantees a steady-state error null, the gain m_p can modifies the closed loop dynamics, and the low-pass filter mitigates the noise related to the measure and is responsible to provide a supplementary service which is discussed further in this section. Due to the feedforward term δ_s, the power flow across the inductive filter is well managed independent of the strength of the grid, revealing an excellent robustness of the control [42], [79]–[82].

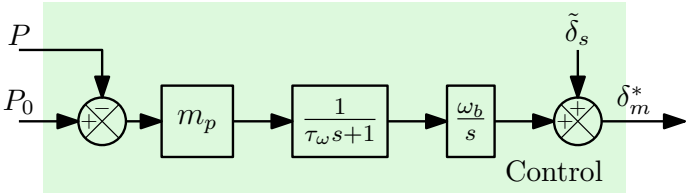

Figure 1.15 – Integral control of the active power (Strategy A).

Several variants can be deduced from the control structure of Figure 1.15. In general, these variants worsen the accuracy of the active power control, however they can provide supplementary functionalities [42], [79], [81], [82]. The rearrangement illustrated in Figure 1.16 proposes the usage of the estimation of the frequency $\tilde{\omega}_s$ instead of $\tilde{\delta}_s$. Due to the similarities with the power frequency droop function, the control strategy of Figure 1.16 is also known as droop control-based in the literature [21], [33], [83]. In this work, strategies employing an estimation of the frequency are referred to as Strategy B. As well as $\tilde{\delta}_s$, $\tilde{\omega}_s$ can be provided using many types of estimators. As given in eq. (1.40), an estimation of $\tilde{\omega}_s$ can be derived from the expression of the active power flow given in eq. (1.38). *Nota bene:* a small filtering element (τ_e) is added to the expression in order to respect the causality of the system.

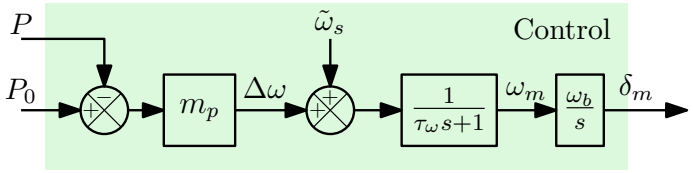

Figure 1.16 – VCI control based on the power frequency droop function (Strategy B).

$$\tilde{\omega}_s = \omega_m - \frac{s}{\tau_e s + 1}\,\frac{P}{\omega_b K_e} \tag{1.40}$$

From Figure 1.16, the derivative of ω_m with respect to the time ($d\omega_m/dt$) is written as given in eq. (1.41). Comparing eq. (1.41) with the first line of eq. (1.13), a relationship between the parameters of the swing equation of synchronous machines and this strategy can be given in eq. (1.42).

$$\frac{d\omega_m}{dt} = \frac{m_p}{\tau_\omega}\left(P_0 - P - \frac{1}{m_p}(\omega_m - \tilde{\omega}_s)\right) \tag{1.41}$$

$$\begin{cases} \tau_\omega = \dfrac{2H}{K_d} \\ m_p = \dfrac{1}{K_d} \end{cases} \tag{1.42}$$

The control structure of Figure 1.16 can therefore be represented in the Virtual Synchronous Machine (VSM) form [22], [41], [84], illustrated in Figure 1.17, without any impact on the performance of the source. The VSM form of the control allows to establish a direct comparison with the simplified mechanical structure of the synchronous machine, highlighting the inertial effect and the damping factor of the VCI, which, differently than synchronous machines, these parameters are configurable with any desired value.

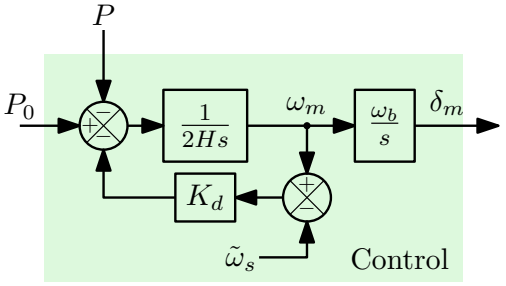

Figure 1.17 – Virtual Synchronous Machine (VSM) control representation (Strategy B).

Considering that the variations of the frequency of the grid are small and around its nominal value, $\tilde{\omega}_s$ can be replaced with a fixed value (ω_0), giving place to the Strategy C of the VCI, illustrated in Figure 1.18. The Strategy C of the VCI also provide an inertial effect.

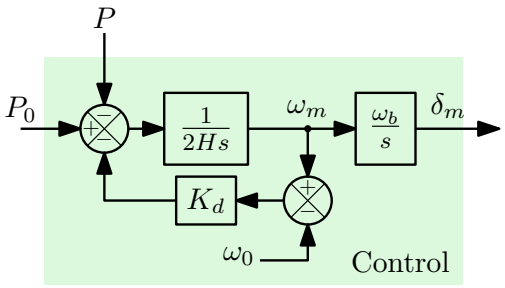

Figure 1.18 – Virtual Synchronous Machine (VSM) control representation (Strategy C).

The choice between strategies B and C presents an impact on the contribution to FCR. In steady-state, Figures 1.17 and 1.18 give:

$$\begin{cases} P = P_0 - K_d\,(\omega_m - \tilde{\omega}_s) & \text{if scheme B} \\ P = P_0 - K_d\,(\omega_m - \omega_0) & \text{if scheme C} \end{cases} \tag{1.43}$$

In the case of Strategy B, even if the frequency of the grid is different from its nominal value, ω_m is always equal to $\tilde{\omega}_s$ in steady-state, and consequently, the injected power is also equal to its setpoint, presenting a steady-state error null. On the contrary, in the case of Strategy C, if ω_m is different from ω_0, the active power injected by the inverter is also different from its setpoint, inherently contributing to FCR.

As illustrated in Figure 1.19a, an additional power frequency droop can be implemented in Strategy B for FCR contribution. In Figure 1.19b, the block diagram of Strategy C is rearranged, highlighting its compulsory contribution to FCR, and providing a comparison with Strategy B with droop control. It is emphasised that, in the case of Strategy C, the value of K_d must be compatible with the range of the power frequency characteristic (K_{pf}). Therefore, in Strategy C, the VCI loses the flexibility in providing damping power to the system, requiring, a supplementary damping action; this subject is discussed further in this section.

1.3.1.2 Reference model of VCIs

Power interface: In this work, all PE-based sources adopt the power interface illustrated in Figure 1.20. The inverter is represented using the aforementioned ideal average model,

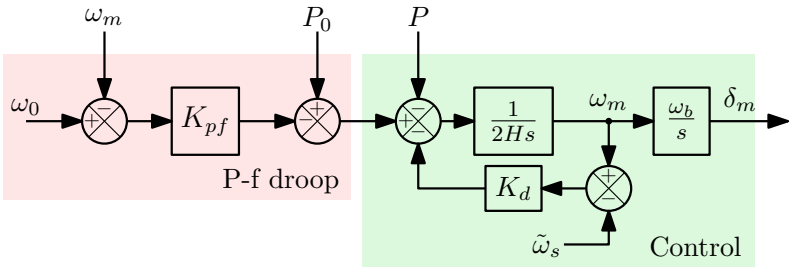

(a) Strategy B with P-f droop control

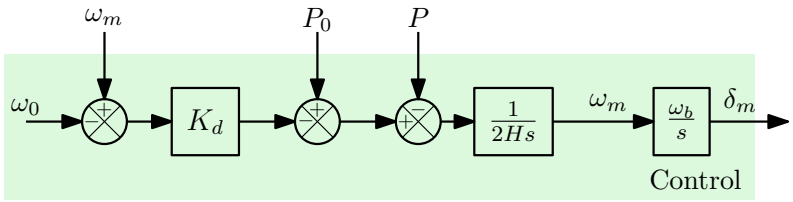

(b) Strategy C, rearranged

Figure 1.19 – Comparison between strategies B and C regarding the FCR contribution.

neglecting the low level control. The dc grid is represented with an ideal dc voltage source, and therefore, the dynamics of the dc side are neglected, hypothesis to circumvent over-modulation issues which can impact on the stability of the ac side. The ac side of the inverter is connected to the grid through an LCL filter composed of a series resistance (R_s) and inductance (L_s) on the inverter side, a transformer on the grid side, and a shunt capacitor (C_s) between these elements. The design procedure of the filter is detailed in Appendix C, considering that the inverter is a two-level VSC.

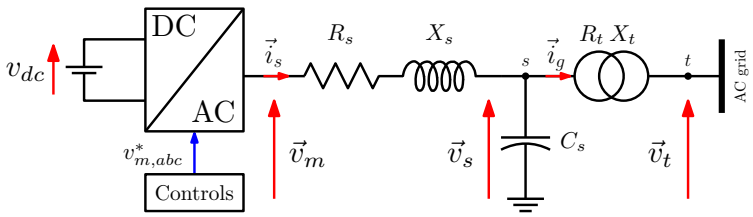

Figure 1.20 – Adopted interface for PE-based sources.

Control structure: The VCI structure proposed in this work is illustrated in Figure 1.21. This architecture aims to control the voltage and the active power flow at the shunt capacitor level, considering therefore, the point s as synchronisation point. The VCI control can either be implemented using strategies B or C, considering the necessary adaptations for the new synchronisation point. In the case of Strategy B, the frequency of the grid is estimated using a PLL.

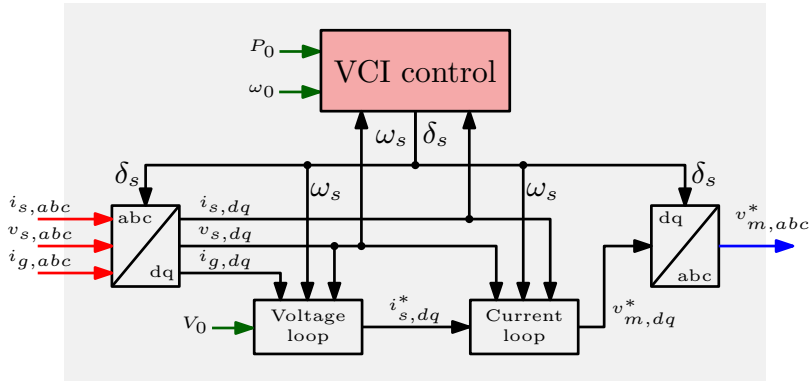

Figure 1.21 – Control structure of the reference model of VCIs.

The voltage of the synchronisation point ($\vec{v}_s$) is controlled using cascaded voltage and current loops of Figure 1.22, which are designed considering the electric equations of the interface of the inverter in the dq-frame given in eq. (1.44). Since the classic tuning of cascaded voltage and current loops employed on standalone applications is not suitable for grid connected operation, the tuning of the controller is made adopting the optimisation strategy described in [33], [85].

A transient feedback compensator using the grid current ($\vec{i}_g$) is added to the input of the voltage controller to mitigate possible electromagnetic oscillations due to the lack of natural damping of the transmission system, which, in turn, is due to the low R/X ratio of the transmission line. The tuning of this compensator is made as described in [33], where it is known as transient virtual resistance.

$$\begin{cases} i_{s,dq} - i_{g,dq} = \dfrac{C_s}{\omega_b}\dfrac{dv_{s,dq}}{dt} \mp \omega_g C_s v_{s,qd} \\ v_{m,dq} - v_{s,dq} = R_s i_{s,dq} + \dfrac{L_s}{\omega_b}\dfrac{di_{s,dq}}{dt} \mp \omega_g L_s i_{s,qd} \end{cases} \tag{1.44}$$

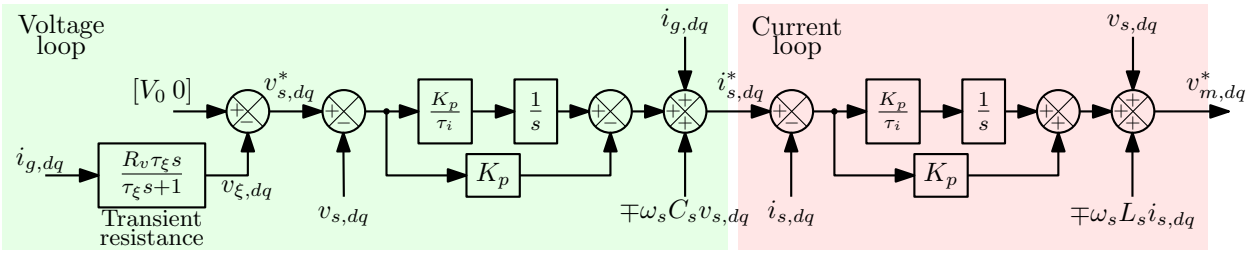

Figure 1.22 – Cascaded voltage and current loops employed on the reference model of the VCI control structure.

1.3.1.3 Simplified model of VCIs

The simplified model of VCIs just considers the power frequency strategy adopted in the controls, neglecting therefore the cascaded voltage and current loops. This model shares the same principle used for the synchronous machines, where the active power flow between the source and the grid is established using the notion of synchronising torque (K_s). Figure 1.23 illustrates a quasi-static model of the VCI vs infinite bus system. Since s is the synchronisation point of the VCI, the equivalent reactance between the VCI and the infinite bus is represented with the addition of the reactances of the transformer and the transmission line, and therefore, K_s is expressed as given in eq. (1.45).

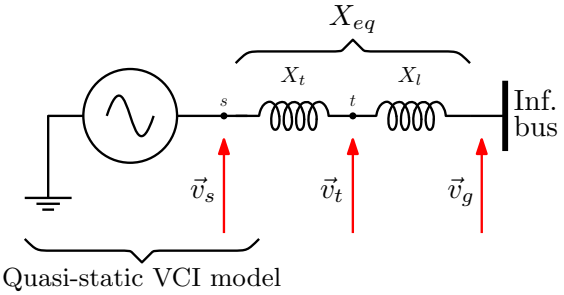

Figure 1.23 – Quasi-static model of the VCI vs infinite bus system.

$$K_s = \frac{V_s V_g}{X_t + X_l} \cos\left(\delta_{s,0} - \delta_{g,0}\right) \tag{1.45}$$

Figure 1.24 illustrates the simplified model of the VCI vs infinite bus system for both strategies B and C. For Strategy B, the $\tilde{\omega}_t$ is estimated using eq. (1.40), *mutatis mutandis*. Since the FCR contribution is not compulsory in Strategy B, and the infinite bus imposes the frequency of the system, a supplementary power frequency droop is not represented in this model; the impact of the FCR contribution of the VCI on the frequency behaviour of a dynamic system is treated in Section 2.3.3.1. It is emphasised that this system is equivalent to that of the synchronous machine vs infinite bus system of Figure 1.4, and therefore, the aforementioned findings are also valid in this case.

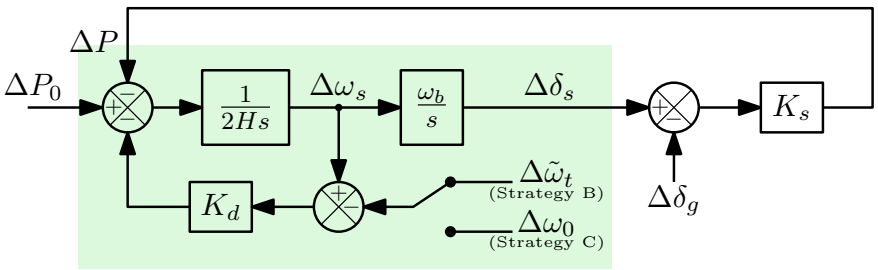

Figure 1.24 – Simplified model of the VCI vs infinite bus system (strategies B and C).

1.3.1.4 Comparison between VCI models

The comparison between the reference and simplified models of the VCI vs infinite bus system is carried out using the same power interface as in Section 1.2.3. The parameters adopted for the power interface of the PE-based sources are given in Table 1.11. Seeking a fair comparison with the synchronous machine vs infinite bus system, the rated power of the inverter is the same as that of the synchronous machine. However, it should be emphasised that there are still not power electronics inverters, especially two-level VSCs, with such rated power and/or current.

Table 1.11 – Dynamic model data for power electronics inverters.

Inverter parameters	**Value**
Rated frequency (f_n, Hz)	60
Rated power (S_n, MVA)	900
Rated AC voltage (V_n, kV)	20.0
Rated DC voltage (V_n, kV)	36.0
Inverter side inductance (L_s, pu)	0.10
Inverter side resistance (R_s, pu)	0.015
Shunt capacitance (C_s, pu)	0.11
Transformer data	refer to Table 1.1

The parameters adopted for the VCI control strategy are given in Table 1.12. The K_d value adopted for strategies B and C are different because in the latter it must be representative of the power frequency characteristic (K_{pf}). The other parameters are the same for both strategies, excepting those of the PLL, which is not part of Strategy C.

Table 1.12 – Dynamic model data for voltage control mode inverters (VCIs).

Parameters	**Strategy B**	**Strategy C**
Inertial effect (H, s)	Variable	
Damping factor (K_d, pu)	400	25
PLL: proportional gain (K_p, pu)	-1.27	—
PLL: integral time constant (τ_i, ms)	8.33	—
PLL: frequency estimator time constant (τ_e, ms)	25	—
V loop: proportional gain (K_p, pu)	0.52	
V loop: integral time constant (τ_i, s)	0.45	
V loop: virtual resistance (R_v, pu)	0.2	
V loop: damping filter time constant (τ_ξ, ms)	10.0	
I loop: proportional gain (K_p, pu)	0.73	
I loop: integral time constant (τ_i, s)	0.61	

The power flow adopted for the comparison is also the same as given in Table 1.3, which is rewritten below ease reading. The power flow of the VCI bus (n° 1) is indicated after the shunt capacitor. Considering the rated power of the inverter as base power, $X_{eq} = 0.525$ pu, and therefore, applying eq. (1.45), $K_s = 1.74$ pu torque/rad.

Table 1.13 – Power flow of the system.

Bus n°	**V (pu)**	θ **(rad)**	**P (MW)**	**Q (MVAr)**
1	1.0	0.417	700.00	117.19
2	1.0	0	-687.41	176.65

Figure 1.25 illustrates the behaviours of frequency oscillations obtained with the reference and the simplified model of the VCI after a phase shift on the voltage of the infinite bus. Since the the inertial effect of the VCI can be parametrised, the comparison is made for two values: 1 and 6.5 s.

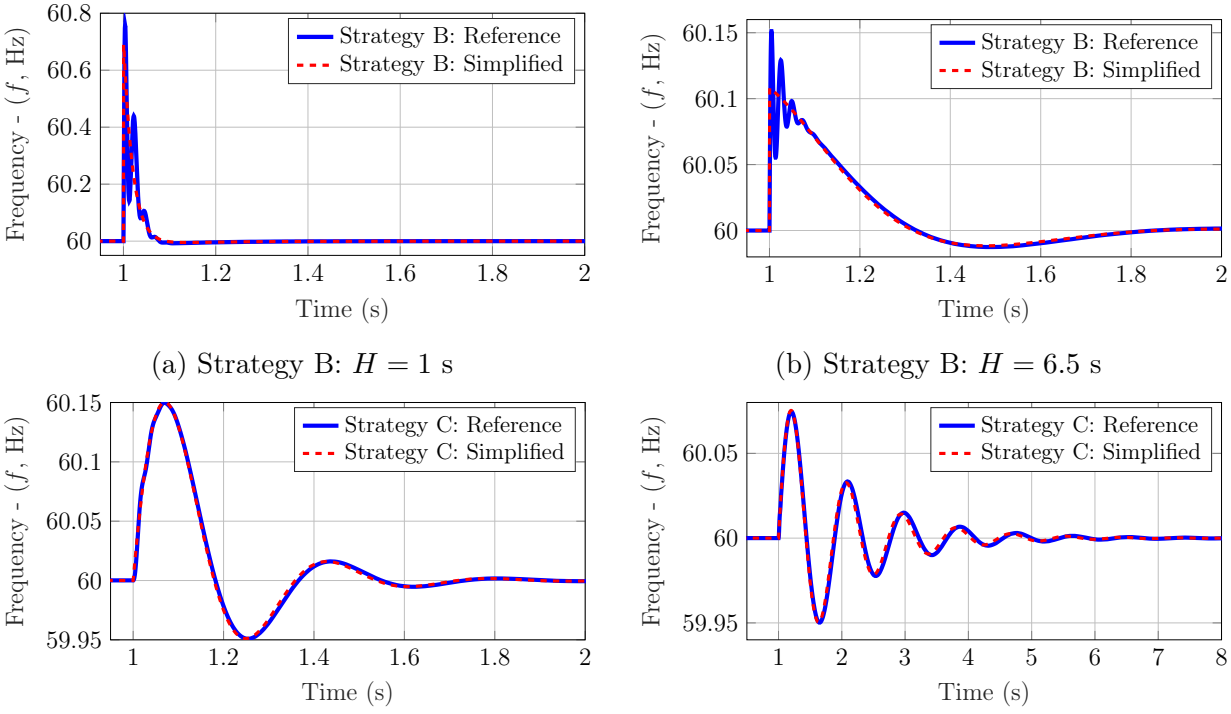

(a) Strategy B: $H = 1$ s

(b) Strategy B: $H = 6.5$ s

(c) Strategy C: $H = 1$ s

(d) Strategy C: $H = 6.5$ s

Figure 1.25 – Frequency oscillation behaviour of the VCI vs infinite bus system after a phase shift on the voltage of infinite bus ($\Delta\theta_g = \pi/40$ rad).

The behaviour of frequency oscillations are in accordance with eqs. (1.33) and (1.34), where the increase of H decreases both the damping and the frequency of the oscillations. As illustrated in Figure 1.25, due to the higher damping factor implemented in Strategy B, the observed frequency oscillations are more damped than those obtained with Strategy C, which,

due to a compulsory FCR contribution, presents a limited K_d value. However, in Strategy B, also due to the high implemented K_d, it is observed some residual electromagnetic noise of the PLL in the VCI frequency. It is emphasised that this transient is pronounced because of the phase shift, which is near to the PLL bus. Since the dynamics of the PLL are neglected in the simplified model of the Strategy B, the residual noise is not observed in its simulation results.

The simplified models of the VCIs are more compliant with their reference models than the equivalent for the synchronous machines. It could be explained by the fact that synchronous machines are very non-linear systems and the effect of dampers is not represented in the proposed simplified model, whereas, the VCI control strategy does not present a high level of non-linearity. Furthermore, the parameters of the simplified model of the VCI do not need to be estimated in order to fit to the response using the reference model.

1.3.1.5 Strategy C: improvement of the damping with a derivative compensation

In the case of Strategy C, due to limited K_d value, the drawbacks related to inertial effect can be easily observed: if the inertial effect provided by the VCI is high, the dynamics of the system become unacceptable for power electronics devices. Similarly to synchronous machines, a stabilisation system must be considered to mitigate the system oscillations. References [21], [33] propose the utilisation of a lead-lag compensator on the feedback of the active power measurement in order to increase the damping of the system. Figure 1.26 illustrates the synchronisation scheme of VCIs with a lead-lag compensator, where τ_1 and τ_2 are, respectively, the lead and the lag time constants of the compensator. This stabilisation system can be implemented in both simplified and reference representations of the VCI control strategy.

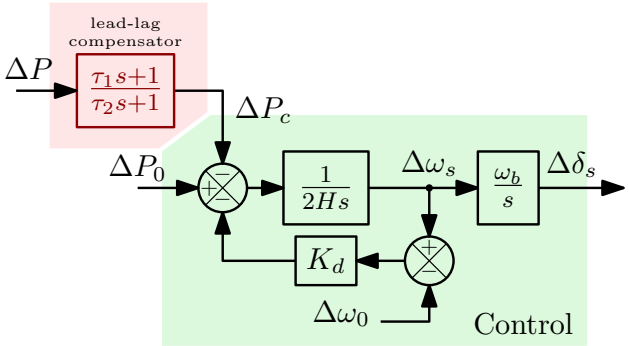

Figure 1.26 – Strategy C of VCI control with lead-lag compensator.

In order to observe the stabilisation effect provided with the lead-lag compensator, the scenario of Section 1.3.1.4 is repeated for Strategy C ($H = 6.5$ s). The values adopted for

τ_1 and τ_2 are, respectively, equal to 125 and 25 ms. Figure 1.27 illustrates a comparison of the frequency behaviours obtained before and after the deployment of the lead-lag feedback compensator, and Table 1.14 summarises the evolution of the oscillating eigenvalues of the system.

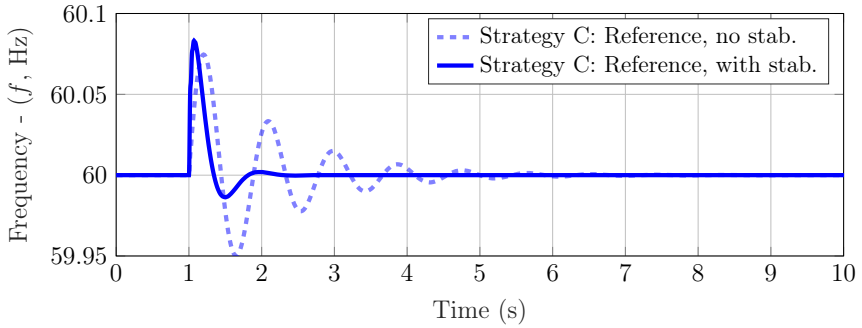

Figure 1.27 – Impact of the lead-lag compensator on the frequency behaviour of the VCI vs infinite bus system (Strategy C, $H = 6.5$ s). Disturbance: phase shift on the voltage of infinite bus ($\Delta\theta_g = \pi/40$ rad).

Table 1.14 – Impact of the lead-lag compensator on the oscillating eigenvalues of the system.

	Without compensator	**With compensator**
Eigenvalues ($\sigma \pm j\omega_d$)	$-0.90 \pm j7.08$	$-4.13 \pm j6.64$
Damping ratio (ξ, %)	12.67	52.82
Damped frequency (f_d, Hz)	1.13	1.06

The stabilisation system used for VCIs is more effective than the PSSs of synchronous machines, since it acts directly on the strong link between active power and frequency, which is just possible due to the fact that, differently than the prime movers of synchronous machines, the synchronisation units of VCIs have high frequency bandwidths. It is emphasised that, as well as a PSS of a synchronous machine, the lead-lag compensator should be tuned to illustrate an acceptable performance for a desired operating range. Reference [78] illustrates an example lead-lag tuning using root-locus techniques, although, for high-complexity systems, optimisation routines may be favoured over other techniques due to its ease of use.

1.3.1.6 Equivalence between Strategies B and C

At first sight, the nature of the damping power in strategies B and C seems to be completely different. Strategy B provides damping similarly to synchronous machines whereas a lead-lag compensator is implemented in the feedback of the active power measurement to provide damping in Strategy C. However, with a simple algebraic manipulation, it is possible to prove the equivalence between both strategies. For the simplified model of Figure 1.24

where the VCI operates with Strategy B, applying the observability principle, the estimated frequency $\Delta\tilde{\omega}_t$ can be expressed as given in eq. (1.46), and therefore, the damping power provided by the VCI can be rewritten as a function of ΔP as given in eq. (1.47).

$$\Delta\tilde{\omega}_t = \Delta\omega_s - \frac{s}{\tau_e s + 1}\,\frac{\Delta P}{\omega_b K_e} \tag{1.46}$$

$$K_d\left(\Delta\omega_s - \Delta\tilde{\omega}_t\right) = \left(\frac{K_d}{\omega_b K_e}\,\frac{s}{\tau_e s + 1}\right)\Delta P \tag{1.47}$$

Considering eq. (1.47), the block diagram of Figure 1.24 can be rearranged as illustrated in Figure 1.28. The transfer function $\Delta P_c(s)/\Delta P(s)$ is expressed as given in eq. (1.48). Similarly to Strategy C, a lead-lag in the feedback of the active power is retrieved on Strategy B, proving the equivalence between these strategies.

$$\begin{aligned}\frac{\Delta P_c(s)}{\Delta P(s)} &= \frac{K_d}{\omega_b K_e}\,\frac{s}{\tau_e s + 1} + 1 \\ &= \frac{\left(\dfrac{K_d}{\omega_b K_e} + \tau_e\right)s + 1}{\tau_e s + 1}\end{aligned} \tag{1.48}$$

It is emphasised that, despite the mathematical proof being realised with a fixed frequency system, the equivalence between strategies B and C is also valid for a variable frequency system. The dynamic behaviours obtained with both strategies in a variable frequency condition are compared in Section 2.3.5.

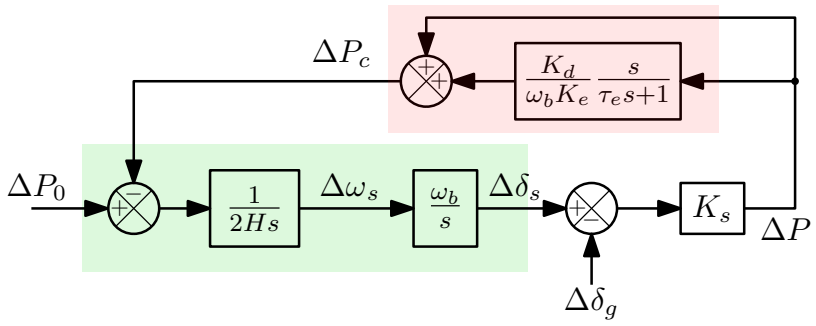

Figure 1.28 – Rearranged block diagram of the VCI vs infinite bus system (Strategy B).

1.3.1.7 Variants of VCI control

In grid connected applications, either in microgrids or in large power systems, a synchronisation unit is mandatory to adapt the power flow of the VCI in accordance with the grid needs guaranteeing the synchronism with the system. This section has introduced the design of VCIs based on the fundamentals of active power flow, presenting three different strategies (A, B and C) with different functionalities. It is emphasised that many other VCI strategies and/or nomenclatures can be found in the literature, where the principal ones are briefly summarised below:

- Synchronverter is a VCI control where the inverter mimic the behaviour of synchronous machines [20], [40], [86]. In this control mode, both electric and mechanical equations of synchronous machines are implemented in the inverter control, displaying all the good and bad properties of the synchronous machine. Therefore, the synchronisation is based on the swing equation, and the modulation signal is equivalent to the electromotive force of the synchronous machine.
- Virtual Synchronous Machine (VSM) is either based on the behaviour of synchronous machines [22], [41], [84]. The synchronisation is also based on the swing equation, and, in many designs, the modulation signal is generated using an internal current loop. For this purpose, the electric equations of the synchronous machine are differently expressed in order to adapt this internal current loop.
- Droop control is the synchronisation strategy based on the power frequency droop function, i.e. the frequency of the inverter is proportionally adapted according the mismatch between the setpoint and the delivered active power [21], [33], [83]. The modulation signal of the inverter can either be generated using a reference of ac voltage or implementing cascaded controls with voltage and current loops.
- Matching control establishes a relationship between the transferred power through the air gap of synchronous machines and that between the dc and ac side of inverters [35]–[37], [43]. In this strategy, the frequency of the VCI is proportional to its dc voltage and the modulation signal is generated considering the setpoint of active and reactive power and the power conservation between dc and ac side.
- The dispatchable Virtual Oscillators (dVOC) is the fully dispatchable version of the control strategy based on the behaviour of Van der Pol oscillators to synchronise and to generate the modulation signal of the inverter [39], [87], [88].

From these five strategies, synchronverter, virtual synchronous machine and matching control are proposed using direct relationships with synchronous machines, and therefore, the can provide an inertial effect to the system. As introduced in Section 1.3.1.1, it is possible to establish an analogy between droop control-based and synchronous machine-based strategies, and therefore, the former can also provide inertial effect. On the contrary, dispatchable

virtual oscillations are outlined using different phenomena, not providing inherent inertial effect.

1.3.2 Current Control mode Inverters (CCIs)

Nowadays, the current control mode is the control strategy employed in the majority of the PE-based sources connected to the grid. Inverters operating in CCI mode manage the active power flow with the grid by controlling the current injection, principle expressed in eq. (1.39), behaving as current sources [4], [33], [89].

1.3.2.1 Synchronisation of CCIs and the Phase-Locked Loop

In order to guarantee the proper current injection in relation to the voltage $\vec{v}_s$, it is used a synchronisation system based on PLL [4]. As illustrated in Figure 1.29a the PLL is composed of three main components: a phase detector based on the dq-frame, a compensator (usually a PI or PID controller), and a Voltage-Controlled Oscillator (VCO). The PLL creates a control frame ($\tilde{dq}$) which is aligned with $\vec{v}_s$ (Figure 1.29b), forcing the component $\tilde{v}_{s,q}$ to zero. In the case where the phase of $\vec{v}_s$ changes, the component $\tilde{v}_{s,q}$ is different from zero, forcing the realignment of the control frame, guaranteeing the synchronisation with the grid.

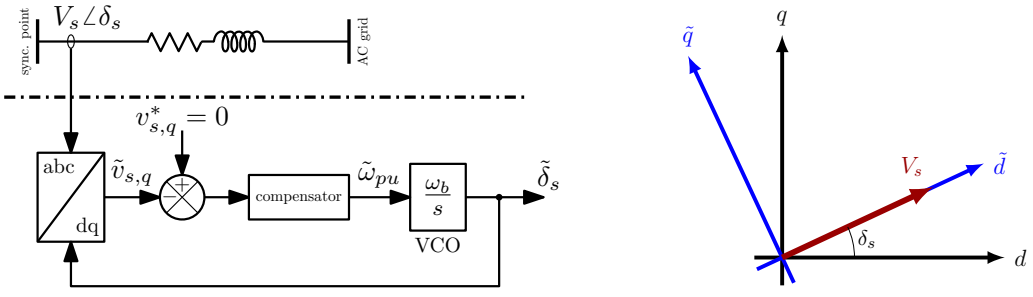

(a) Block diagram (b) dq-frame

Figure 1.29 – Functioning of a Phase-Locked Loop (PLL).

Limitations: The CCI strategy relies on the control frame managed by the PLL, and, since PLLs are based on voltage measurement, two conditions are imposed for their proper operation: the magnitude of the voltage of the synchronisation point must be around 1 pu, and the phase variations should be limited. Both constraints are valid for strong grids, although, weak grids are susceptible to voltage stability issues which can impact or even destabilise the PLL [13], [28]–[31]. References [30], [31] suggest the usage of virtual impedances to virtually change the synchronisation point of the CCI to a more stable location,

extending the stability range of the inverter in weak grid condition. Furthermore, grids with high penetration of CCIs presents general stability issues due to the fact that there are fewer assets "forming" the grid (i.e. generating the three-phase ac voltage of the grid) [90]. As aforementioned, theoretical results reported in [45], [75] show that in power system with 100% PE-based sources, 30% of inverters should operates in VCI mode in order to maintain the system stability.

1.3.2.2 Principle of power flow with CCI control

Thanks to the PLL action, the active power injected into the grid (P_s) can be expressed in dq-frame as given in eq. (1.49), and the control of active power is achieved by acting on the d-axis of the current. Therefore, the principle of active power control with the CCI is illustrated in Figure 1.30. The control of the current is compulsory in the CCI strategy, and therefore, a current loop is mandatory.

$$P_s = v_{s,d} i_{s,d} \tag{1.49}$$

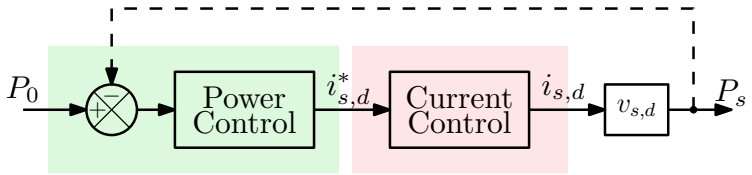

Figure 1.30 – Principle of active power control with CCIs.

The current reference ($i^*_{s,d}$) can be determined using a closed-loop of power, however, since eq. (1.49) is straightforward, it also can be defined using a "direct mode", by dividing of the active power setpoint (P_0) by the voltage estimated by the PLL ($\tilde{v}_{s,d}$). A structure of current loop using PI controller is illustrated in Figure 1.22, and the aforementioned options of power control are illustrated in Figure 1.31. The closed-loop dynamics of the current and the power controllers can be tuned using the classic techniques. In the case of the direct control, the dynamics are imposed by filtering the setpoint of active and reactive power. The reactive power control is similarly implemented.

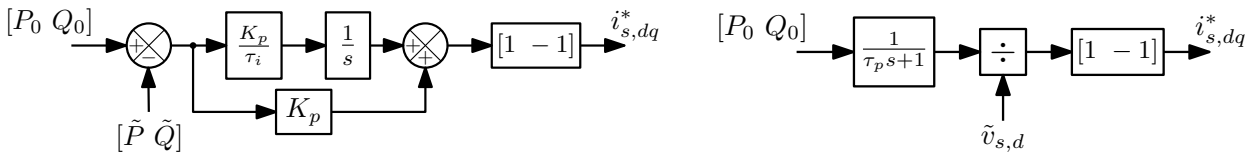

(a) Closed-loop control (b) Direct mode

Figure 1.31 – Possible options the active and reactive power control.

1.3.2.3 Reference model of CCIs

In this work, the power interface of CCIs is the same as that used for VCIs, illustrated in Figure 1.20; refer to Section 1.3.1.2 for description. The control structure of the reference model of the control strategy is illustrated in Figure 1.32.

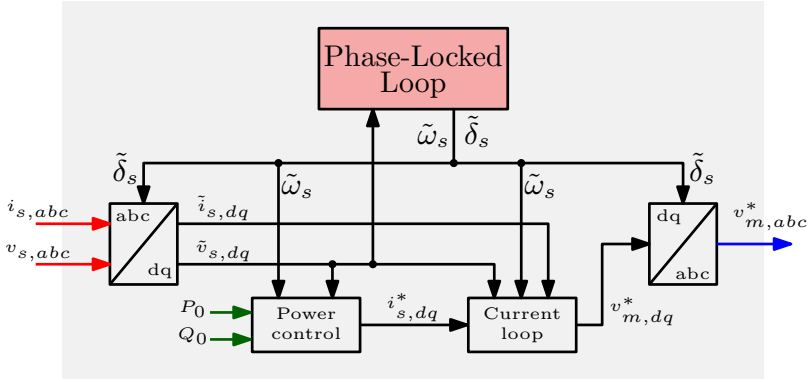

Figure 1.32 – Control structure of the reference model of CCIs.

The synchronisation with the grid is made at the shunt capacitor level using a generic PLL based on PI controller; refer to Figure 1.29a. The CCI operates in PQ direct mode, establishing power injection after the shunt capacitor level. For this purpose, an estimation of the capacitor current is added in feedforward to the power control in order to compensate its reactive power. The inner current loop is similar to that of Figure 1.22, however, it has been stated in [29] that the addition of a low-pass filter in the voltage feedforward can improve the robustness of the CCI. The details of the power control and current loop implemented in the CCI controls are illustrated in Figure 1.33.

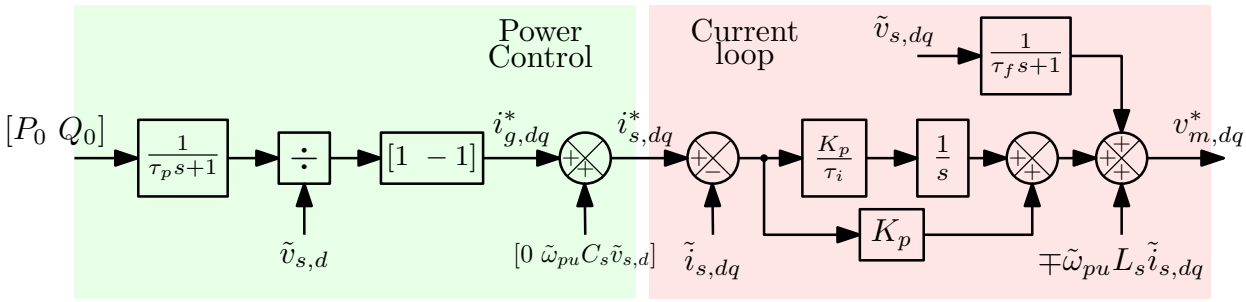

Figure 1.33 – Details of the power control and current loop implemented in the reference model of the CCI controls.

1.3.2.4 Simplified model of CCIs

The simplified model of CCIs is based on the principle of active power control illustrated in Figure 1.30. In order to guarantee the proper functioning of the CCI, the inner current loop should be considerably faster than the outer power control, and therefore, the dynamics of the former can be neglected, meaning that $\tilde{i}_{s,d} = i^*_{s,d}$. Consequently, as illustrated in Figure 1.34, the simplified model of CCIs is just represented with the first order dynamics of active power controller.

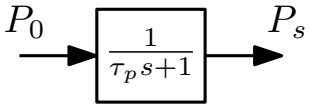

Figure 1.34 – Simplified representation of inverters operating in CCI mode.

It is however emphasised that the simplified model of CCIs can be considered accurate only in strong grid conditions. Otherwise, in weak grid conditions, the complex interactions between the different control loops prevent to obtain consistent dynamics, and therefore, it is not possible to propose a simplified model of these sources.

1.3.2.5 Comparison between CCI models

The comparison between the reference and simplified models of the CCI vs infinite bus system is carried out using the same grid topology and power flow of those made for synchronous machines and VCIs; refer to Section 1.2.3. The parameters adopted for the CCI control strategy are given in Table 1.15.

Table 1.15 – Dynamic model data for current control mode inverters (CCIs).

Parameters	**Value**
PLL: settling time (ms)	200.0
PLL: proportional gain (K_p, pu)	-0.11
PLL: integral time constant (τ_i, ms)	81.0
PQ control: settling time (ms)	100.0
PQ control: time constant (ms)	25.0
I loop: settling time (ms)	10.0
I loop: proportional gain (K_p, pu)	0.14
I loop: integral time constant (τ_i, ms)	2.3
I loop: Feedforward filter time constant (τ_f, ms)	0.3

Figure 1.35 illustrates a comparison of the behaviours of active power injection with the reference and the simplified model of the CCI after multiple changes of the setpoint of active power. It can be observed that, for a strong grid, the dynamics obtained with the simplified model are consistent with those obtained with the reference model fo the CCI, despite the simplicity of the proposed representation.

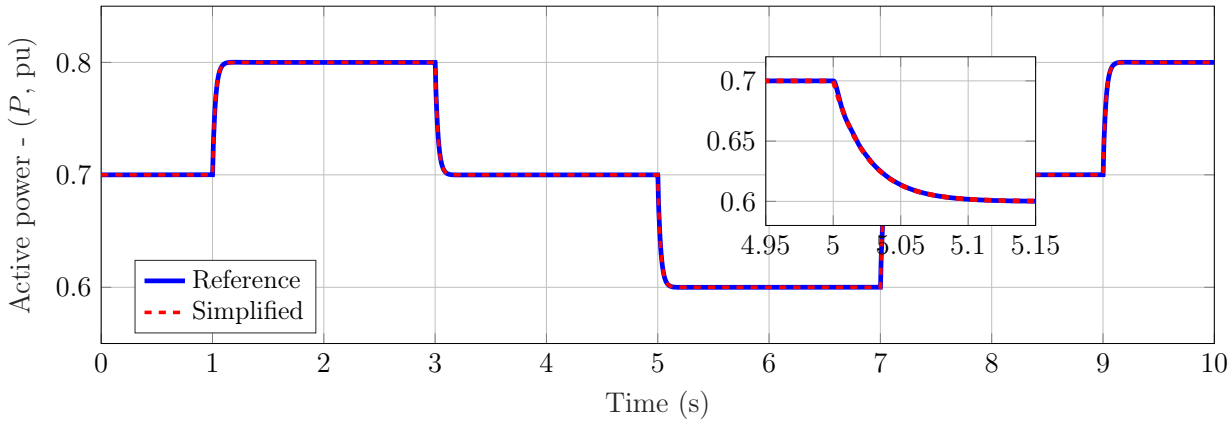

Figure 1.35 – Dynamics of active power injection of a CCI connected to an infinite bus. Power base: $S_b = 1000$ MVA.

1.3.2.6 Ancillary services to the grid

Different ancillary services to the grid — frequency and voltage — can be implemented in the CCI control strategy. Regarding frequency services, an active power frequency droop function can be used in order to modulate the setpoint of active power, and therefore, contribute to Frequency Containment Reserve [90]–[93]. Also, it is possible to provide a fast frequency response, proportionally injecting active power to the RoCoF estimated by the PLL, providing an "inertial control" [91], [93]–[96]. A similar technique to the inertial control, the P-WAF, is proposed in [26], [97] in order to increase the damping of electromechanical oscillations using multi-terminal dc grids. The modulation of the injected active power to provide dc voltage regulation is also a common application [4], [26], [91]. Similarly to the active power channel, the CCI can also provide voltage ancillary services to the grid by modulating its setpoint of reactive power [42], [72].

In this work, only a power frequency droop function of is implemented in the CCI control, allowing the contribution to FCR. As illustrated in Figure 1.36a, in the reference model, a low-pass filter added to the droop strategy in order to mitigate the oscillations linked to the frequency estimation, preventing system destabilisation [13]. On the contrary, as illustrated in Figure 1.36b, since the dynamics of the PLL are neglected, the low-pass filter can also be neglected in the simplified model of the CCI.

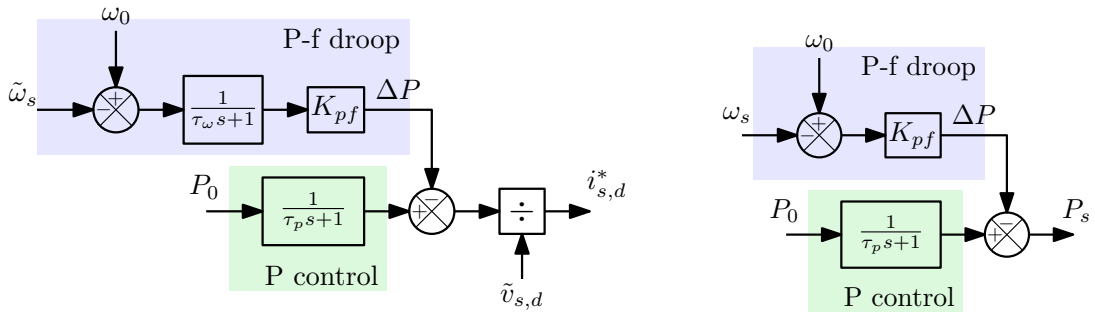

(a) Reference model (b) Simplified model

Figure 1.36 – Implementation of FCR in the CCI strategy.

1.4 Chapter conclusions

This chapter has presented the fundamentals of the principal sources which will be used in the following chapters of this work. For each source, two representations have been proposed with different levels of detail, which will be employed according to the objective of the study to be carried out. The reference models of the sources are designed to represent a detailed version of the control chains, and considering the electromagnetic phenomena of the grid, whereas the simplified models are proposed focusing only on their power frequency behaviours.

Focusing on the simplified models of the sources, from a direct comparison between the mechanicals of the synchronous machines (i.e. the swing equation) and the controls of VCIs, it has been possible to highlight the similarities of these sources. Although, since the parameters of VCIs can be configurable with any desired values, their flexibility is emphasised. It has been demonstrated that the inherent behaviour of PE-based sources operating in CCI mode is different from that of synchronous machines and VCIs, not being possible to establish a comparison between the sources.

In this chapter, the dynamics obtained with both representations of the sources were compared using a fixed frequency system. In the next chapter, the sources will be connected two by two composing a variable frequency grid. The impact of each source on the frequency behaviour of the system will be analysed.

Chapter 2

Frequency behaviour of two-source systems

Contents

2.1 Introduction

The interactions between synchronous machines and power electronics-based sources are not easy to analyse. Seeking to facilitate the understanding of this matter, the key idea of this chapter is to study the interactions between these sources in a very simple system composed of two generators and a load. For this purpose, the analysis relies on simplified models of the sources and other elements of the system, providing analytical interpretations of the interactions between a synchronous machine and a PE-based source either behaving as a voltage or a current source, i.e. VCI or CCI mode.

It has been shown in Chapter 1 that the simplified model of a PE-based source operating in VCI mode presents similarities to that of the synchronous machine. Therefore, considering some adjustments, the classical methodology proposed in the specialised literature [52], [54], [57] can be applied in analysis of interactions between the VCI and the synchronous machine.

In order to recall the classical methodology, the case of a two-synchronous machine system is first analysed. From a highly detailed level representation of the system, it is possible to design a simplified model used to observe the frequency behaviour displayed by each synchronous machine. Considering some simplifying hypotheses, the simplified model can be reduced to observe the main dynamics of the system, which are decomposed into two components: the "dominant behaviour" illustrates the overall frequency dynamics displayed by both synchronous machines, whereas the "oscillating behaviour" illustrates the frequency oscillations between them. The same methodology can be used to analyse the interactions between a VCI and a synchronous machine. However, due to the difference in the magnitude order of both sources, the simulation results show a quite different frequency behaviour.

Regarding the CCI, as also mentioned in Chapter 1, its behaviour is very different to that of the VCI, and the simplification method is not the same. It is still possible to determine the dominant behaviour of a system composed of a CCI and a synchronous machine, however its representativeness is limited since the CCI can easily display stability issues. Therefore, a method based on the linearised representation of the system is proposed in order to determine its stability limits.

In this chapter, multiple scenarios considering the variation of macroscopic parameters of the power system — e.g. electrical distance, inertial effect, power frequency characteristics — are analysed. It is emphasised that the findings from the analyses carried out in this chapter can be considered as the foundations for the study of interconnected power systems further in this work.

2.2 The reference system: association of two synchronous machines

The two-synchronous machine system is considered as reference for the present chapter. The objective of this section is to describe the system and to introduce the different representations which can be employed on the analysis of the frequency behaviour of a two-voltage source system.

2.2.1 Description of the studied system: the reference model

Figure 2.1 illustrates the single line diagram of the Reference Model of the two-source system in which both generators are synchronous machines. The control chain of each synchronous machine is composed of an IEESGO governor and a steam turbine, a ST1C excitation system and a PSS1A power system stabiliser. The modelling of the synchronous machines and their controllers are introduced in Chapter 1, and the parameters adopted for the system are given in Tables 1.2, 1.5, 1.7 and 1.9. The design of the grid elements are described as follows, and their adopted parameters are given in Table 1.1.

- the transmission line is represented as a series impedance,
- the step-up transformers are represented only with their leakage inductance, neglecting the active losses,
- the load is modelled as a composite of a shunt resistance, inductance and capacitance in parallel, with constant impedance.

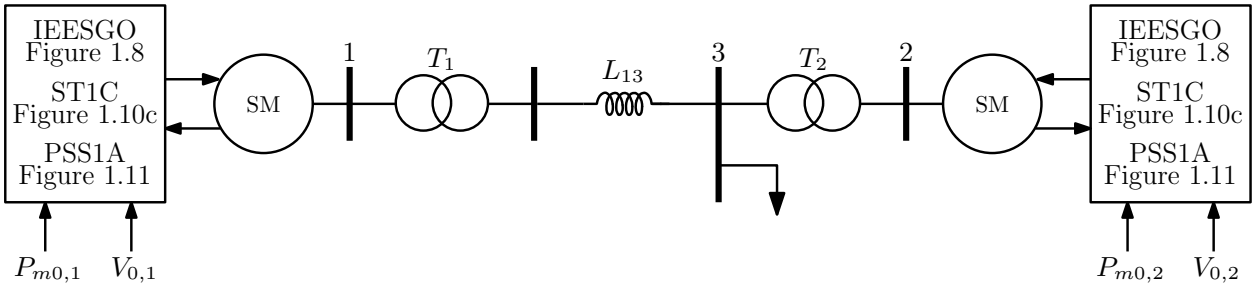

Figure 2.1 – Reference model of the SM vs SM system.

A linearised form of the reference model is proposed to perform the analysis in the frequency domain. Since the dynamics of the reference representation of the system are described with 44 differential equations, the linearised form of the model has 44 differential states:

- eight for the grid:
  - two for the equivalent $T_1 + L_{13}$,
  - two for the transformer T_2,
  - four for the load.
- 18 for each generator:
  - eight for the synchronous machine: eqs. (1.1) to (1.6) and eq. (1.13),
  - five for the IEESGO: Figure 1.8,
  - one for the ST1C: Figure 1.10c,
  - four for the PSS1A: Figure 1.11.

In order to verify the compliance of the linearised form of the reference model, the dynamics obtained with both representations in time domain simulations are compared. For this purpose, the Transmission Line Length (TLL) of L_{13} is 25 km, and the initial operating point of the system is given in Table 2.1.

Table 2.1 – Power flow results of the studied system (TLL = 25 km).

Bus n°	**Bus type**	**V (pu)**	**θ (rad)**	**P (pu)**	**Q (pu)**
SM n°1 (Bus 1)	PV	1.02	0.151	0.700	0.051
SM n°2 (Bus 2)	Slack	1.01	0.000	0.711	−0.021
Load (Bus 3)	PQ	1.02	0.104	−1.400	0.222

Base power: $S_b = 900$ MVA

Figure 2.2 illustrates the dynamics obtained with the reference model of the system and its linearised form after a variation of $P_{m0,1}$. It can be observed that the simulation results are similar, which validates the accuracy of the linearised model.

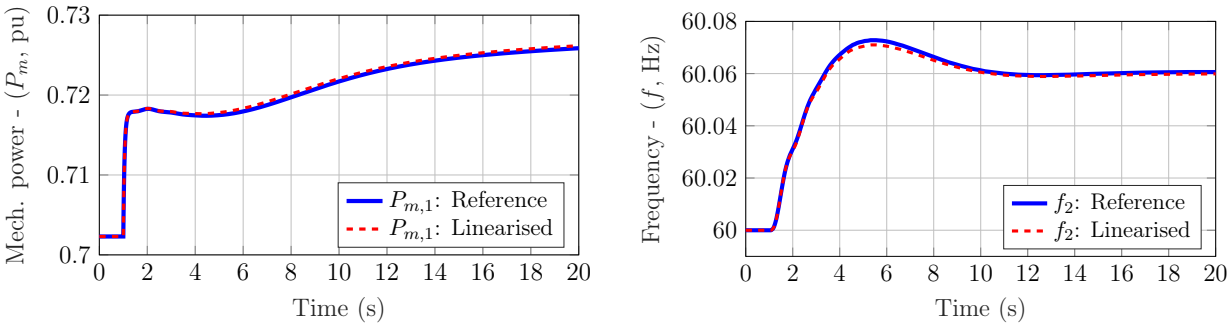

(a) $P_{m,1}$ (pu) (b) f_2 (Hz)

Figure 2.2 – Validation of the linearised form of the reference representation of the SM vs SM system. Stimulus: $\Delta P_{m0,1} = 0.05$ pu.

The following analyses are carried out in time and frequency domains. In further frequency domain analyses, the reference eigenvalues are extracted from the linearised form of the reference model of the system, and therefore, these eigenvalues are hereinafter referred to as Reference Model. An in-depth analysis regarding the dynamics of the system is realised further in this section.

2.2.2 Reduced order representations of the system

It is nearly impossible to draw out any physical meaning using a 44^{th} order model such as that described in Section 2.2.1. Therefore, several levels of simplifications are proposed in order to understand the main dynamics of the system. As described in Chapter 1, the association of $E'X'H$ models of synchronous machines with their power frequency regulators and the grid is employed as a first level of simplification. From this model, it is possible to deduce another representation, the dominant model, which is much more simplified than the reference model, to highlight the dominant behaviour of the frequency. Furthermore, based on the frequency decoupling due to the high time constant of the steam turbines, it is also possible to neglect the dynamics of the regulators from the simplified model in order to analyse the oscillating frequency behaviour of the system.

2.2.2.1 The simplified model of the SM vs SM system

Figure 2.3 illustrates the block diagram of the Simplified Model of the SM vs SM system. As introduced in Chapter 1, each synchronous machine is represented with the $E'X'H$ model associated with an IEESGO as power frequency regulator. In this system, differently than the synchronous machine vs infinite bus system, the frequency of the grid is not constant, but it is a composite of the frequencies of both synchronous machines. This composite frequency displays the behaviour of the Centre of Inertia (COI) of the system, and is computed as given in eq. (2.1) [68], [98]–[100].

$$\omega_{coi} = \frac{H_1\omega_1 + H_2\omega_2}{H_1 + H_2} \tag{2.1}$$

The dynamics of the simplified representation of the system are described with 14 differential equations, being, for each generator, two for the synchronous machine and five for the IEESGO. The parameters adopted for this model are the same as those of the reference model of the synchronous machine, excepting the values of $K_{d,1}$ and $K_{d,2}$ which, as well as in Section 1.2, they are estimated in order to reasonably represent the damping of the system.

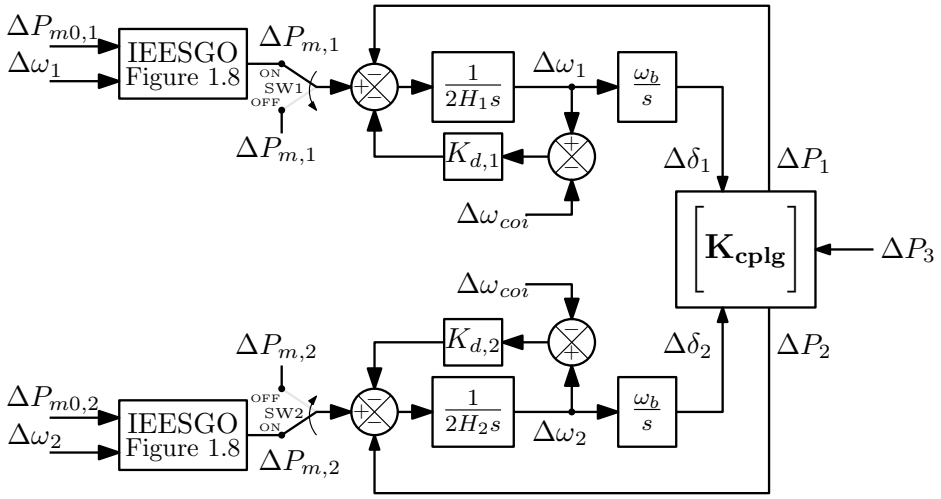

Figure 2.3 – Simplified model of the SM vs SM system.

The network linking the two synchronous machines and the load is represented with a quasi static model ($\mathbf{K_{cplg}}$). The modelling and numerical application to design the grid are presented in Appendix D. The size of $\mathbf{K_{cplg}}$ is 2-by-3, and, for the following analysis, its elements are noted as K_{11} to K_{23}. The principal steps to define $\mathbf{K_{cplg}}$ are summarised as follows:

1. Determination of the admittance matrix of the system ($\mathbf{Y}$);
2. Computation of $\partial P_i/\partial\delta_i$ (Jacobian matrix, $\mathbf{J}$);
3. Reduction of the dependent variable (δ_3).

The eigenvalues maps of both simplified and reference representations of the system are illustrated in Figure 2.4. The eigenvalues of the simplified representation display a good estimation of the corresponding ones of the reference model, and therefore, it might be possible to determine the expected frequency behaviour of the system using the simplified model. However, this representation still has 14 eigenvalues, and not all of them are related to the frequency dynamics. Therefore, in order to identify the eigenvalues which have an influence on the frequency behaviour, their participation factors in the electromechanical states of the system are illustrated in Figure 2.5. The colour intensities indicate the factors according to the sidebar on the right of the figure. The factors smaller than 5% are neglected and represented in grey.

Between the 14 eigenvalues of the simplified representation of the system, only $\lambda_{3,4}$, $\lambda_{5,6}$, λ_8 and λ_9 have influence on $\Delta\omega_1$ and $\Delta\omega_2$, and therefore, focus is applied to these eigenvalues, summarising them in Table 2.2 with their corresponding ones of the reference model for numerical comparison. The eigenvalue λ_1 is overlooked in the analysis, since it corresponds to the null eigenvalue related to the absence of common angle reference [52].

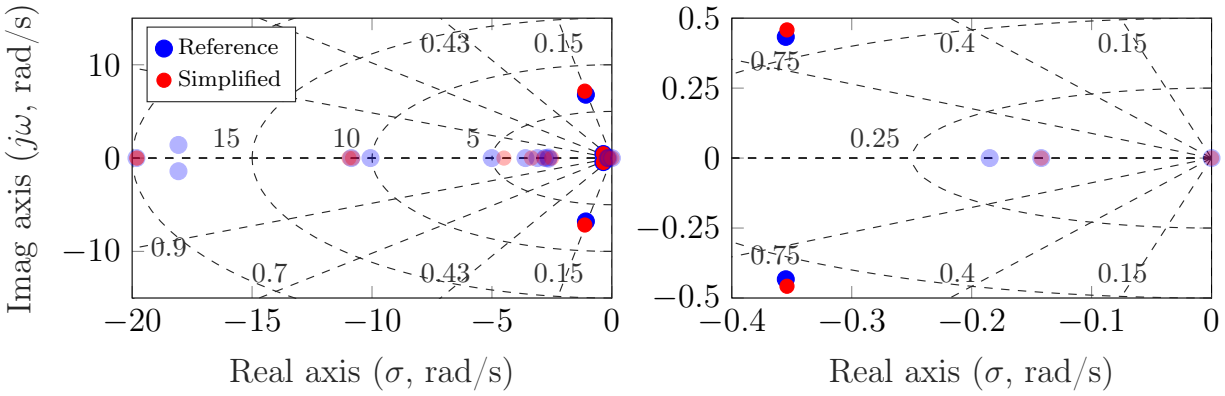

Figure 2.4 – Comparison of the eigenvalues map of the simplified and reference representations of the SM vs SM system (magnified view at the subject of interest).

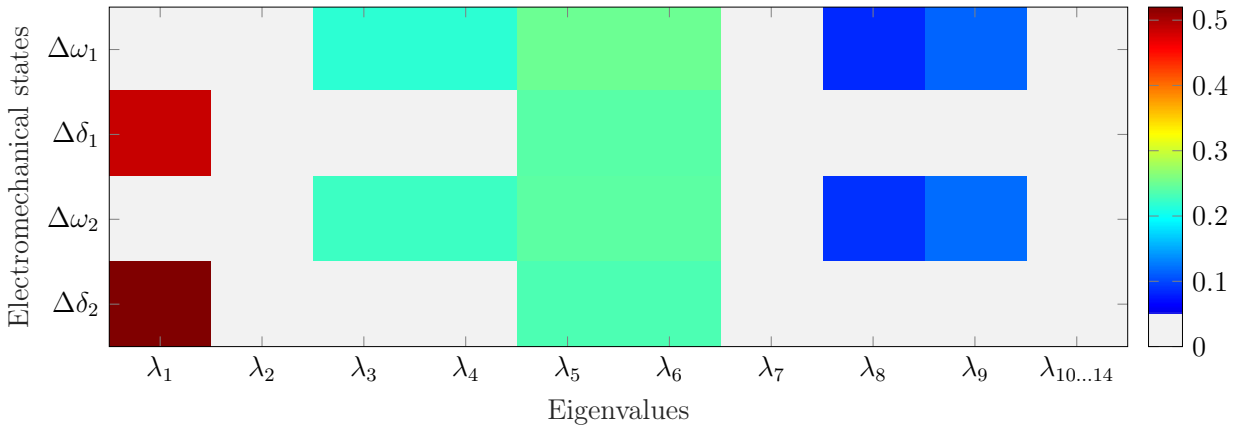

Figure 2.5 – Participation factors of the eigenvalues in the electromechanical states the system (simplified model).

Table 2.2 – Summary of noteworthy eigenvalues.

Simplified		**Reference**	
$\lambda_{\mathbf{3,4}}$	$-0.35 \pm j0.46$	$-0.35 \pm j0.43$	$\lambda_{\mathbf{7,8}}$
$\lambda_{\mathbf{5,6}}$	$-1.13 \pm j7.18$	$-1.08 \pm j6.79$	$\lambda_{\mathbf{9,10}}$
$\lambda_{\mathbf{8}}$	-2.82	-2.79	$\lambda_{\mathbf{13}}$
$\lambda_{\mathbf{9}}$	-3.35	-3.10	$\lambda_{\mathbf{14}}$

Using the eigenvalues of the simplified representation listed in Table 2.2, it is possible to determine the expected frequency behaviour of the system.

- The second order dynamics of $\lambda_{3,4}$ presents the slowest time constant between the aforementioned eigenvalues, decaying in around 11 s. The frequency of the oscillations of $\lambda_{3,4}$ is around 0.07 Hz ($T = 14.29$ s), and since the settling time of these eigenvalues is smaller than the period of the oscillations, it is not possible to visually retrieve the frequency of the oscillations using its time response.

- The eigenvalues $\lambda_{5,6}$ oscillate at 1.14 Hz ($T = 0.88$ s) and completely decay after 3.54 s.

- The time constants of λ_8 and λ_9 are the fastest between the eigenvalues of Table 2.2, completely decaying in less than 1.5 s, and, as illustrated in Figure 2.5, the participation factors of these eigenvalues in $\Delta\omega_1$ and $\Delta\omega_2$ are around 10%, and therefore, they should not present a big influence on the main transient behaviour of the frequency.

The analysis carried out using the numerical values of the eigenvalues of the simplified model allows to determine the expected frequency behaviour of the system, however, it does not physically explain the observed behaviour. In order to explain the origin of these eigenvalues, the frequency dynamics are decomposed into two different components: the dominant and the oscillating behaviours.

2.2.2.2 The dominant model of the SM vs SM system

Based on the classic approach given in [52], the dominant frequency behaviour of the system (ω_{coi}) can be determined using the representation of Figure 2.6, which is hereinafter referred to as Dominant Model, or DM. Since the frequencies of the generators are supposed to be equal to ω_{coi}, this representation considers an aggregated model of the synchronous machines, where the equivalent coefficient of inertia (H_{eq}) is a composite of H_1 and H_2 [52], [54], [57], [100]. Likewise, since the structures and the parameters of the power frequency regulators are equivalent, they also are represented with an aggregated model, where the equivalent power frequency characteristic of the regulator (K_{pf}) is a composite of $K_{pf,1}$ and $K_{pf,2}$.

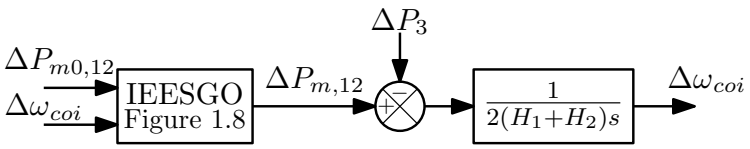

Figure 2.6 – Block diagram representing the dominant frequency behaviour of the SM vs SM system (the dominant model).

Since the grid is completely disregarded in this representation of the system, the equilibrium frequency after the disturbance may be different from those of the simplified and reference representations. This phenomenon can be more flagrant when the active power losses of the system are more important.

The DM illustrated in Figure 2.6 is described with six differential equations, being five from the IEESGO model. Since it still is too difficult to carry out an analytical analysis with this model, a simplified representation of the frequency control chain is proposed in Figure 2.7. In this representation, since the time constant τ_5 of the steam turbine is at least 10 times bigger than the other time constants of the control chain, the dynamics of the governor and the steam turbines are neglected [101]. The model of Figure 2.7 is hereinafter referred to as Dominant Model - Simplified Controls, or DM-SC.

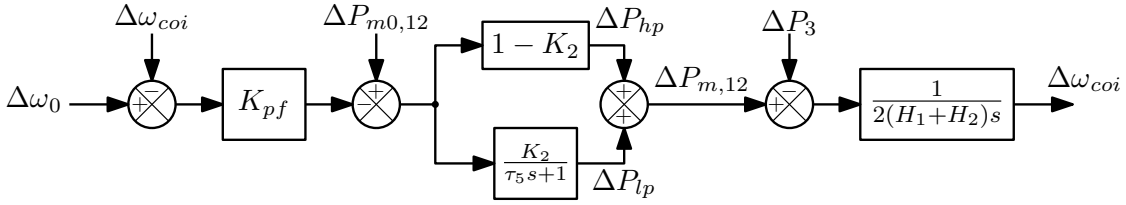

Figure 2.7 – Block diagram representing the dominant frequency behaviour of the SM vs SM system considering a simplified representation of the power frequency control chain (DM-SC).

It is emphasised that, in the DM-SC, the instantaneous action of ΔP_{hp} leads to an increase of the damping of the eigenvalues, overestimating the performance of the system, and therefore, the frequency nadirs/peaks illustrated with this model are expected to be less pronounced than those found with the other models. However, with this model, it is possible to analytically determine the expression of the eigenvalues which describe the dominant frequency behaviour of the system, which in turn, allows to draw conclusions out about the impact of the parameters of the system on the aforementioned behaviour.

The transfer function $H_{coi}(s) = \Delta\omega_{coi}/\Delta P_3$ of the DM-SC is given in eq. (2.2). The characteristic polynomial of $H_{coi}(s)$ indicates that the transient dynamics of $\Delta\omega_{coi}$ behave as a second order system, which depends on both parameters of the synchronous machines and the control chain.

$$\frac{\Delta\omega_{coi}}{\Delta P_3} = \frac{-\dfrac{1}{2\left(H_1+H_2\right)}\left(s+\dfrac{1}{\tau_5}\right)}{s^2+\left(\dfrac{1}{\tau_5}-\dfrac{K_{pf}\left(1-K_2\right)}{2\left(H_1+H_2\right)}\right)s-\dfrac{K_{pf}}{2\left(H_1+H_2\right)\tau_5}} \tag{2.2}$$

Since in eq. (2.2), the characteristic polynomial is expressed in the standard form, the

undamped natural frequency and damping ratio of the dominant eigenvalues of the system are expressed as given in eq. (2.3). It is emphasised that all the parameters, excepting K_{pf} are inherent to the physical construction of the synchronous machines and the turbines. As introduced in Section 1.2.4, the power frequency characteristic for steam turbines is, in absolute values, between 16.66 and 25 pu, however not all synchronous machines must contribute to FCR. In this system, since at least on synchronous machine must contribute to FCR, $16.66 \leq K_{pf} \leq 50$ pu, which, can considerably change the settling time and the value of nadirs/peaks of ω_{coi}.

$$\begin{cases} \omega_n = \sqrt{-\dfrac{K_{pf}}{2\left(H_1+H_2\right)\tau_5}} \\ \\ \xi = \dfrac{\dfrac{1}{\tau_5} - \dfrac{K_{pf}\left(1-K_2\right)}{2\left(H_1+H_2\right)}}{2\omega_n} \end{cases} \tag{2.3}$$

For $K_{pf} = -50$ pu, the eigenvalues of the DM-SC are $\lambda_{1,2} = -0.36 \pm j0.38$, whereas those found with the DM are $\lambda_{1,2} = -0.35 \pm j0.46$. The eigenvalues of the DM are equivalent to those of the simplified and reference models; refer to Table 2.2. As expected, the eigenvalues found with the DM-SC are more damped than the corresponding ones found with the other representations of the system (ξ equal to 68.77 against 60.55%).

From eq. (2.2), considering that ΔP_3 is a step disturbance, the RoCoF and the steady-state value of $\Delta\omega_{coi}$ ($\Delta\omega_{coi}^{ss}$) can be respectively found applying the initial and final value theorems, eqs. (2.4) and (2.5). As expected, the RoCoF does not depend on the control chain, and $\Delta\omega_{coi}^{ss}$ depends exclusively on the power frequency characteristics. The numerical analysis of the RoCoF and $\Delta\omega_{coi}^{ss}$ are postponed to Section 2.2.3.

$$\begin{aligned} \text{RoCoF} &= \mathcal{L}^{-1}\left\{\lim_{s\to\infty} sH_{coi}(s)\right\}\Delta P_3 \\ &= -\frac{\Delta P_3}{2\left(H_1+H_2\right)} \end{aligned} \tag{2.4}$$

$$\begin{aligned} \Delta\omega_{coi}^{ss} &= \mathcal{L}^{-1}\left\{\lim_{s\to 0} sH_{coi}(s)\right\}\Delta P_3 \\ &= K_{pf}\Delta P_3 \end{aligned} \tag{2.5}$$

2.2.2.3 Analysis of the oscillating frequency behaviour

Regarding the oscillating frequency behaviour, the simplified model of the system can be used. For this analysis, the power frequency regulators of the synchronous machines are completely disregarded, considering that they do not react on time, and the interactions are just between the synchronous machines and the grid. A visual representation can be obtained opening the switches SW01 and SW02 in Figure 2.3.

The behaviour of the frequency oscillations between the sources ($\Delta\omega_{12}$) can be determined from the analysis of the transfer function $H_{osc}(s) = \Delta\omega_{12}/\Delta P_3$. The transfer function $\Delta\omega_1/\Delta P_3$ is given in eq. (2.7).

$$\frac{\Delta\omega_{12}}{\Delta P_3} = \frac{\Delta\omega_1}{\Delta P_3} - \frac{\Delta\omega_2}{\Delta P_3} \tag{2.6}$$

$$\frac{\Delta\omega_1}{\Delta P_3} = \frac{\dfrac{-K_{13}\left(4H_2s^3 + K_{d,2}s^2 + 2\omega_b K_{22}s\right) - K_{23}\left(K_{d,1}s^2 - 2\omega_b K_{12}s\right)}{8H_1H_2}}{p(s)} \tag{2.7}$$

where

$$\begin{aligned} p(s) = s^4 &+ \frac{H_1K_{d,2} + H_2K_{d,1}}{4H_1H_2}s^3 + \frac{\omega_b\left(H_1K_{22} + H_2K_{11}\right)}{2H_1H_2}s^2 \\ &+ \frac{\omega_b\left(K_{d,1}K_{21} + K_{d,1}K_{22} + K_{d,2}K_{11} + K_{d,2}K_{12}\right)}{8H_1H_2}s \\ &+ \frac{\omega_b^2\left(K_{11}K_{22} - K_{12}K_{21}\right)}{4H_1H_2} \end{aligned} \tag{2.8}$$

It is emphasised that, from the properties of the matrix $\mathbf{K_{cplg}}$, the elements $K_{11} = -K_{12}$ and $K_{21} = -K_{22}$, and therefore, eq. (2.8) can be rewritten as given in eq. (2.9).

$$p(s) = s^4 + \frac{H_1K_{d,2} + H_2K_{d,1}}{4H_1H_2}s^3 + \frac{\omega_b\left(H_1K_{22} + H_2K_{11}\right)}{2H_1H_2}s^2 \tag{2.9}$$

Likewise, the transfer function $\Delta\omega_2/\Delta P_3$ is given in eq. (2.10).

$$\frac{\Delta\omega_2}{\Delta P_3} = \frac{\dfrac{K_{13}\left(-K_{d,2}s^2 + 2\omega_b K_{21}s\right) - K_{23}\left(4H_1s^3 + K_{d,1}s^2 + 2\omega_b K_{11}s\right)}{8H_1H_2}}{s^4 + \dfrac{H_1K_{d,2} + H_2K_{d,1}}{4H_1H_2}s^3 + \dfrac{\omega_b\left(H_1K_{22} + H_2K_{11}\right)}{2H_1H_2}s^2} \tag{2.10}$$

Substituting eqs. (2.7) and (2.10) into eq. (2.6), and simplifying the null zeros and eigenvalues, transfer function $H_{osc}(s) = \Delta\omega_{12}/\Delta P_3$ is given in eq. (2.11). The natural frequency and damping ratio of the oscillating eigenvalues of the system are expressed as given in eq. (2.12).

$$\frac{\Delta\omega_{12}}{\Delta P_3} = \frac{\dfrac{H_1K_{23} - H_2K_{13}}{2H_1H_2}s}{s^2 + \dfrac{H_1K_{d,2} + H_2K_{d,1}}{4H_1H_2}s + \dfrac{\omega_b\left(H_1K_{22} + H_2K_{11}\right)}{2H_1H_2}} \tag{2.11}$$

$$\begin{cases} \omega_n = \sqrt{\dfrac{\omega_b\left(H_1K_{22} + H_2K_{11}\right)}{2H_1H_2}} \\ \\ \xi = \dfrac{H_1K_{d,2} + H_2K_{d,1}}{4\sqrt{2\omega_b H_1H_2\left(H_1K_{22} + H_2K_{11}\right)}} \end{cases} \tag{2.12}$$

From eq. (2.12), both ω_n and ξ depend on the inertia of the synchronous machines and the synchronising torque between the sources, i.e. K_{11} and K_{22}. The frequency of the oscillations increase as K_{11} and K_{22} get bigger and *vice versa*. Only ξ presents a direct dependency with the damping factor of the synchronous machines, however, since $\omega_d = \omega_n\sqrt{1-\xi^2}$, it is emphasised that the frequency of the oscillations also varies with the variation of $K_{d,1}$ and $K_{d,2}$.

The eigenvalues of the characteristic polynomial of eq. (2.11) are $\lambda_{1,2} = -1.20 \pm j7.03$, representing a good estimation of the eigenvalues obtained with the reference model of the system ($\lambda_{9,10} = -1.08 \pm j6.79$). However, as expected, the damping ratio and the frequency of the oscillations are slightly overestimated, being $\xi = 16.83\%$ and $f = 1.12$ Hz, against $\xi = 15.71\%$ and $f = 1.08$ Hz of the reference model.

2.2.3 Comparison between the models

In order to analyse the performance of the reduced order models and to observe the expected main behaviour of the system, the dynamic responses obtained with all representations are compared. For this purpose, a load step $\Delta P_l = 0.1$ pu is applied in the system, however, due to the characteristics of the load, the effective load step is $\Delta P_l = 0.092$ pu.

Since both synchronous machines contribute to FCR, the total power frequency characteristic of the system is $K_{pf} = -50$ pu. Considering the signal convention of the droop function established in Figure 2.6, after the disturbance, the equilibrium frequency of the system is $f_{coi} = 59.89$ Hz. Since the power frequency characteristics of the sources are equivalent, the variation of active power of both sources is $\Delta P = 0.046$ pu.

The simulations results are given in Figure 2.8. Based on these results, the following can be observed:

- The reference, simplified and dominant (DM) representations display similar transient dynamics. The frequency nadir obtained with these representations are equivalent.

- As expected, due to the simplifying hypothesis made for the frequency regulator, the frequency behaviour obtained with the DM-SC is more damped, presenting a shallower nadir than the other models.

- Contrarily to the nadir, since the control chain does not impact on the system RoCoF, the magnitude order of RoCoF is visually equivalent for all representations of the system.

- The steady-state frequency of the system is the same in all representations. The observed settling time is around 13 s, against the expected 11 s from the numerical analysis given in Section 2.2.2.1.

- The dynamics of the frequency oscillations obtained with the simplified model and with eq. (2.11) are visually equivalent. The frequency of these oscillations are slightly bigger than that of those of the reference model. The oscillations completely decay in around 3.5 s, which is in accordance with the aforementioned numerical analysis.

- The initial load sharing between the synchronous machines observed with the simplified model is consistent with that of the reference model. Since the power frequency characteristics of both synchronous machines are equivalent, the equilibrium point of the active powers after the disturbance are the same.

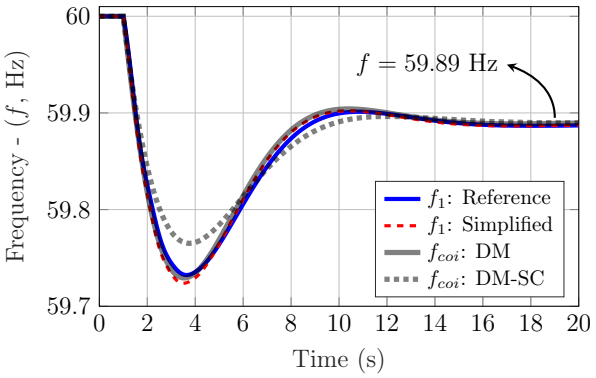

(a) f_1 (Hz)

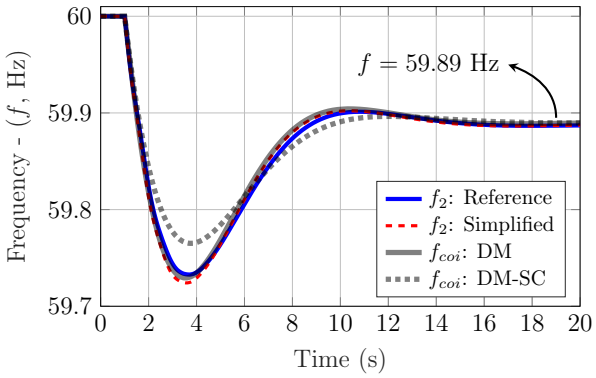

(b) f_2 (Hz)

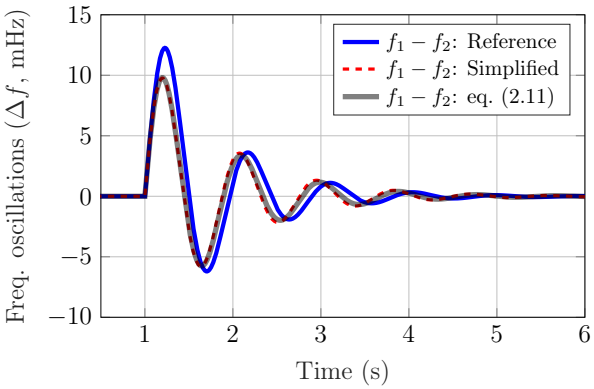

(c) $\Delta f = f_1 - f_2$ (mHz)

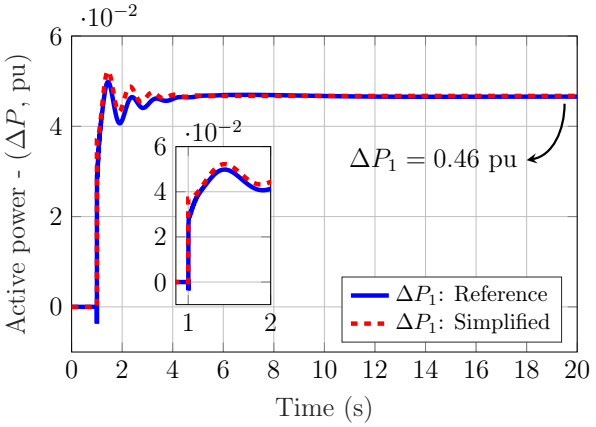

(d) ΔP_1 (pu)

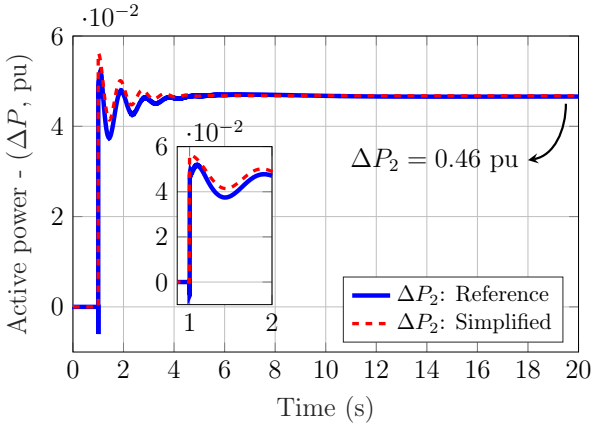

(e) ΔP_2 (pu)

Figure 2.8 – Dynamic behaviour of the SM vs SM system after a load step.

Impact of the electrical distance between the sources The previous analysis has shown that the reference model of the SM vs SM system can fairly be represented using the reduced order models proposed in Section 2.2.2. The impact of the electrical distance between the sources on the frequency behaviour of the system and on the compliance of the reduced order models is analysed as follows. For this scenario, it is assumed that TLL = 125 km. The power flow results are given in Table 2.3.

Table 2.3 – Power flow results of the studied system (TLL = 125 km).

Bus n°	**Bus type**	**V (pu)**	**θ (rad)**	**P (pu)**	**Q (pu)**
SM n°1 (Bus 1)	PV	1.02	0.913	0.700	0.352
SM n°2 (Bus 2)	Slack	1.01	0.000	0.766	0.276
Load (Bus 3)	PQ	0.98	0.117	−1.400	0.222

The dynamic behaviours obtained with all representations of the system after a load step are compared in Figure 2.9. The dominant and the oscillating eigenvalues obtained with the different representations of the system are summarised in Table 2.4 for numerical comparison. Since these eigenvalues have different subscript in each representation, they are denoted in Table 2.4 as λ_{dom} and λ_{osc}, respectively.

From Table 2.4, it can be observed that λ_{dom} all three representations are equivalent, and, furthermore, equal to when the transmission line length is small, indicating that the electrical distance between the sources does not impact on the dominant frequency behaviour of the system. The frequencies of the synchronous machines are illustrated in Figures 2.9a and 2.9b, and indeed, all three representations display the same dominant frequency behaviour. However, in comparison to the reference and the simplified models, the steady-state frequency obtained with the dominant model is higher. It could be explained by the fact that, since the latter completely disregard the grid, the active power losses — which are more pronounced in this scenario due to the length of the transmission line — are not represented, and therefore, the total power imbalance is smaller, increasing the steady-state frequency.

In the frequencies obtained with the reference and the simplified representations of the system, the oscillating frequency behaviour can be observed all around the dominant one, indicating that they have similar time constants ($\approx$ 2.9 s), which can also be observed in Table 2.4. As illustrated in Figure 2.9c, the frequency oscillations between the synchronous machines are similar, displaying the equivalent magnitude orders of damping ratio (between 7.3 and 8%) and frequency (between 0.6 and 0.7 Hz).

To summarise, the simplified representations can satisfactorily illustrate the expected frequency behaviour of the reference model of the SM vs SM system, even for a high electrical distance between the sources.

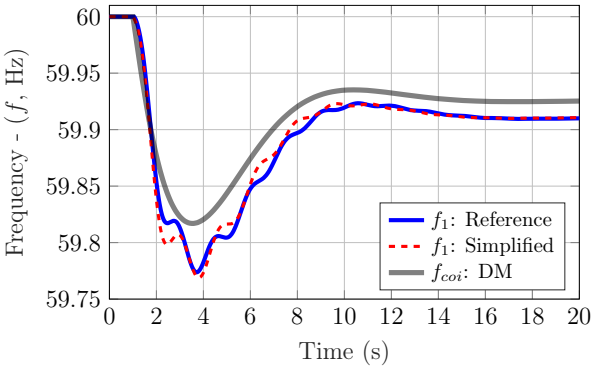

(a) f_1 (Hz)

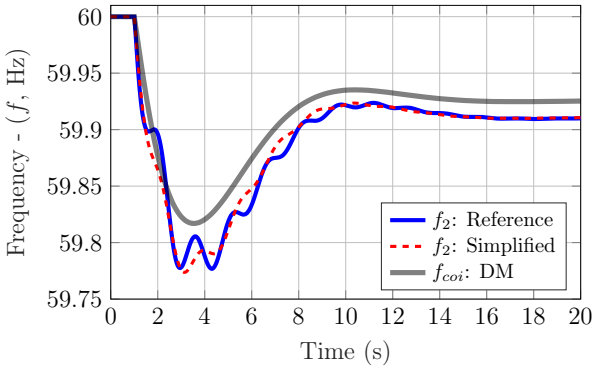

(b) f_2 (Hz)

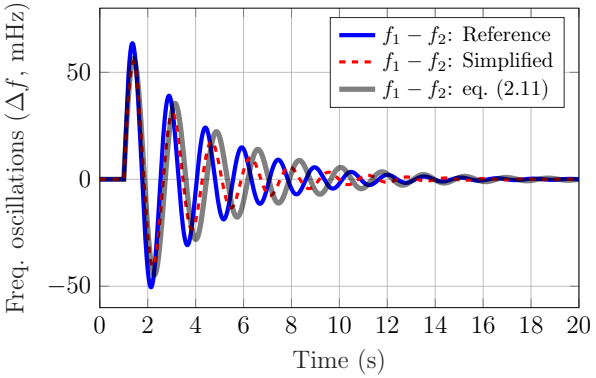

(c) $\Delta f = f_1 - f_2$ (mHz)

Figure 2.9 – Comparison between the simulations results obtained with the reference and simplified model of the SM vs SM system (TLL = 125 km).

Table 2.4 – Summary of the dominant and the oscillating eigenvalues of the SM vs SM system (TLL = 125 km).

	Reference	**Simplified**	**DM**	**eq. (2.11)**
$\lambda_{\mathbf{dom}}$	$-0.35 \pm j0.44$	$-0.35 \pm j0.46$	$-0.36 \pm j0.46$	—
$\lambda_{\mathbf{osc}}$	$-0.35 \pm j4.39$	$-0.34 \pm j3.86$	—	$-0.27 \pm j3.64$

2.3 Replacement of a synchronous machine with a VCI

The second configuration considers that the synchronous machine which was connected to the bus n° 1 is replaced with a PE-based source behaving as a voltage source (VCI). The reduced order models of this configuration are compared with those of the reference system, and the impact of PE-based source on the frequency behaviour of the system is analysed in this section.

2.3.1 Description of the studied system: the reference model

Figure 2.10 illustrates the Reference Model of the VCI vs SM system. In this representation, the inverter is represented with an average model, an ideal voltage source is used to represent the dc side of the source, and an LC filter interfaces it with the ac grid. The controls are implemented using cascaded voltage and current loops, and the synchronisation strategy is based on the swing equation of the synchronous machines, where the frequency of the grid is estimated using a PLL (VCI-B; refer to Section 1.3.1.1). The parameters adopted for the PE-based source operating in VCI-B mode are given in Table 1.11 and Table 1.12.

The modelling and parameters of the synchronous machine and the grid elements are the same as introduced in Section 2.2.1.

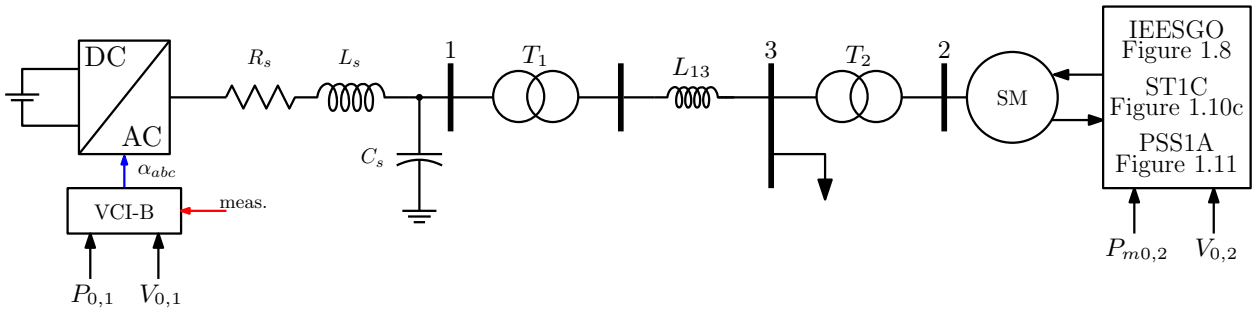

Figure 2.10 – Reference model of the VCI vs SM system.

A linearised form of the reference model is proposed to perform the analysis in the frequency domain. Since the dynamics of the reference representation of the system are described with 40 differential equations, the linearised form of the model has 40 differential states, being:

- eight for the grid,
- four for the inverter filter:
  - two for the inductance L_s,
  - two for the capacitor C_s.
- 10 for the VCI-B control strategy:
  - two for the VSM representation: Figure 1.17,
  - two for the PLL: Figure 1.29a,
  - four for the voltage loop: Figure 1.22,
  - two for the current loop: idem.
- 18 for the synchronous machine and associated controls.

Using the same scenario and operating point as described in Section 2.2.1, the compliance of the linearised form of the VCI vs SM system is verified in Figure 2.11. The dynamics obtained with the reference model and its linearised form are equivalent, validating this representation. Therefore, the eigenvalues of the linearised form of the reference model are considered as reference in further frequency domain analyses.

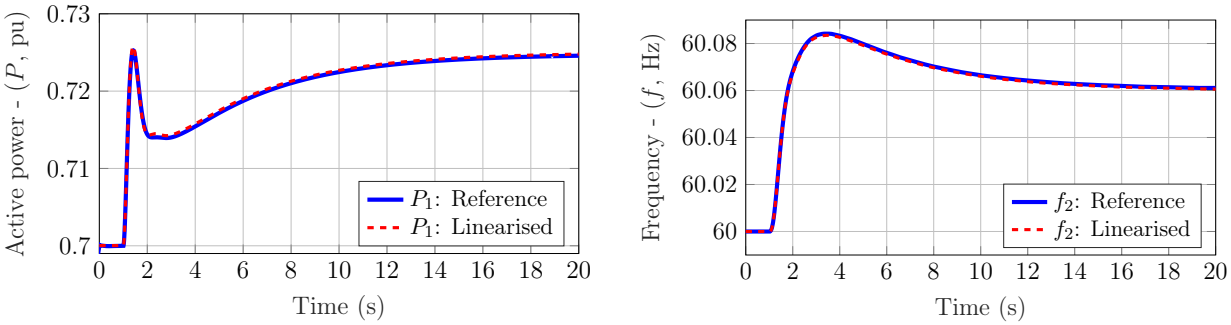

(a) P_1 (pu) (b) f_2 (Hz)

Figure 2.11 – Validation of the linearised form of the reference representation of the VCI vs SM system. Stimulus: $\Delta P_{0,1} = 0.05$ pu.

2.3.2 Reduced order representations of the system

As demonstrated in Section 1.3.1.1, the control structure of VCIs shares the same foundations as the swing equation of synchronous machines. Adopting the same theoretical approach employed in Section 2.2.2, reduced order models of the VCI vs SM system are proposed in order to analyse the frequency behaviour of the system.

2.3.2.1 The simplified model of the VCI vs SM system

Figure 2.12 illustrates the Simplified Model of the VCI vs SM system. In this representation, the simplified model of the synchronous machine is the same as used in Section 2.2.2.1, and the matrix $\mathbf{K_{cplg}}$ is similarly determined as previously described. As introduced in Section 1.3.1.3, the VCI is designed just considering its synchronisation strategy. The parameters adopted for the simplified model are the same as the reference model.

The dynamics of the simplified representation of the system are described with 10 differential equations, being two of the VCI, one of the frequency estimator, two of the synchronous machine and five of the IEESGO.

It is emphasised that the simplified representation of the VCI-B presents an important symmetry when compared with the synchronous machine model. Highlighted in red, the principal differences between these models are:

- Contrarily to the synchronous machine, the inertia and damping factor of the VCI are parameters of the control, and therefore, they are configurable with any desired value.
- Regarding the power frequency control chain, the control signal of the regulator of the synchronous machine displays the dynamics of its governor and turbines, whereas, that of the VCI presents an instantaneous power response to frequency variations.
- In this model, the frequency of the grid which is estimated with a PLL in the reference representation, is obtained using the expression given in eq. (1.46).

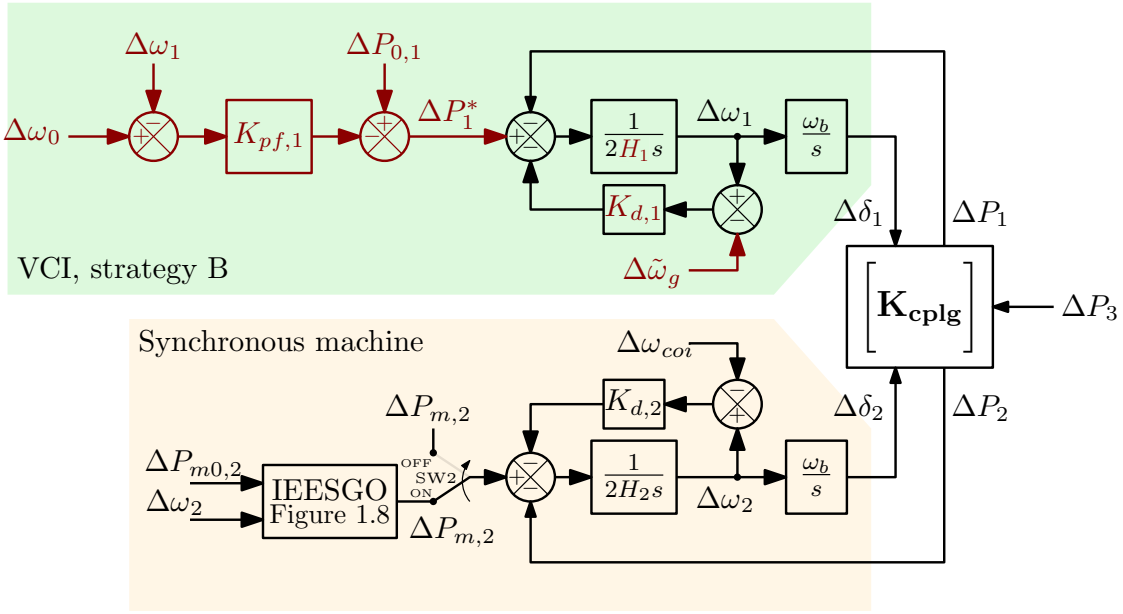

Figure 2.12 – Simplified model of the VCI vs SM system.

2.3.2.2 The dominant model of the VCI vs SM system

For the dominant frequency behaviour of the system, the Dominant Model - Simplified Controls (DM-SC) illustrated in Figure 2.13 is proposed, establishing a direct comparison with that of the SM vs SM system of Figure 2.7. Similarly to the DM-SC of the SM vs SM system, the frequency of both sources are supposed to be equal to ω_{coi}, and the equivalent inertia of the system is represented using a composite of the coefficient of inertia of both sources. However, since the dynamics of the power frequency control chains of the sources are different, the controls are represented using two channels, one of each generator.

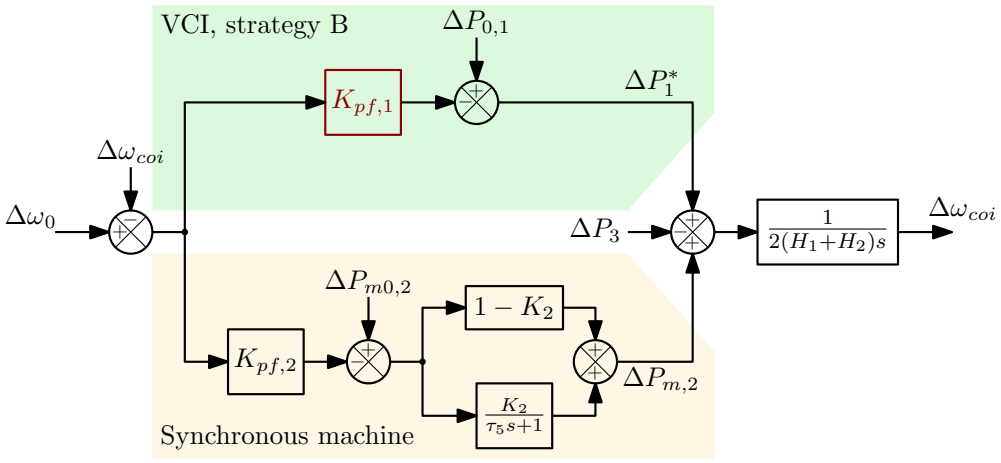

Figure 2.13 – Block diagram representing the dominant frequency behaviour of the VCI vs SM system considering a simplified representation of the power frequency control chain of the synchronous machine (DM-SC).

Despite the simplifying hypothesis for the IEESGO of the synchronous machine proved to overestimate the dynamics of the system, it is interesting to illustrate the impact of the replacement of one synchronous machine with a VCI on the dominant frequency behaviour of the system. In the SM vs SM system, the high pressure fraction of the equivalent turbine is $\Delta P_{hp} = K_{pf}(1-K_2)$. In this system, the droop of the VCI plays the same role as the high pressure stage of the steam turbine. Therefore, replacing $\Delta P_{hp} = K_{pf}(1-K_2)$ in eq. (2.2) with $\Delta P_{hp} = K_{pf,1} + K_{pf,2}(1-K_2)$, the transfer function $H_{coi}(s) = \Delta\omega_{coi}/\Delta P_3$ is expressed as:

$$\frac{\Delta\omega_{coi}}{\Delta P_3} = \frac{-\dfrac{1}{2\left(H_1+H_2\right)}\left(s+\dfrac{1}{\tau_5}\right)}{s^2+\left(\dfrac{1}{\tau_5}-\dfrac{K_{pf,1}+K_{pf,2}\left(1-K_2\right)}{2\left(H_1+H_2\right)}\right)s-\dfrac{K_{pf,1}+K_{pf,2}}{2\left(H_1+H_2\right)\tau_5}} \tag{2.13}$$

In the SM vs SM system, the dominant eigenvalues of the characteristic polynomial of eq. (2.2) are always a complex conjugate pair. On the contrary, in this system, depending on the adopted parameters, the dominant eigenvalues can either be a complex conjugate pair or two purely real eigenvalues.

In the case where $0 < \xi < 1$, the natural frequency and damping ratio of the dominant eigenvalues of the system are given in eq. (2.14), whereas if $\xi = 1$, the analytical expression of the dominant eigenvalues of the system are given in eq. (2.15).

$$\begin{cases} \omega_n = \sqrt{-\dfrac{K_{pf,1}+K_{pf,2}}{2\left(H_1+H_2\right)\tau_5}} \\ \xi = \dfrac{\dfrac{1}{\tau_5} - \dfrac{K_{pf,1}+K_{pf,2}\left(1-K_2\right)}{2\left(H_1+H_2\right)}}{2\omega_n} \end{cases} \tag{2.14}$$

$$\begin{aligned} \lambda_{dom} = & -\frac{1}{2\tau_5} + \frac{K_{pf,1}+K_{pf,2}\left(1-K_2\right)}{4\left(H_1+H_2\right)} \\ & \pm \frac{1}{2}\sqrt{\left(\frac{1}{\tau_5} - \frac{K_{pf,1}+K_{pf,2}\left(1-K_2\right)}{2\left(H_1+H_2\right)}\right)^2 + \frac{2\left(K_{pf,1}+K_{pf,2}\right)}{\left(H_1+H_2\right)\tau_5}} \end{aligned} \tag{2.15}$$

In order to illustrate the impact of the replacement of the synchronous machine with the VCI on the dominant frequency behaviour of the system, the eigenvalues of the DM-SC of both systems are compared in Table 2.5. For the numerical application, it is considered that TLL = 25 km, and that the inertial effect of the VCI is equivalent to the coefficient of inertia of the synchronous machines. For the VCI vs SM system, two different scenarios are considered:

- **First scenario:** only the SM contributes to FCR, $K_{pf,1} = 0$ pu and $K_{pf,2} = -50$ pu;
- **Second scenario:** both sources contribute to FCR, $K_{pf,1} = K_{pf,2} = -25$ pu.

Table 2.5 – Eigenvalues of the DM-SC of the SM vs SM and VCI vs SM systems.

	SM vs SM system	**VCI vs SM system**	
	$K_{pf} = -50$ **pu**	**First scenario**	**Second scenario**
Eigenvalues (λ_{dom})	$-0.36 \pm j0.38$	$-0.36 \pm j0.38$	-0.25 -1.23
Damping ratio (ξ, %)	68.77	68.77	—
Damped frequency (f_d, mHz)	60.48	60.48	—

Nota bene: $f_d = f_n\sqrt{1-\xi^2}$

From Table 2.5, it can be observed that, when the VCI does not contribute to FCR, the dominant eigenvalues of the VCI vs SM system are the same as those of the SM vs SM system, a complex conjugate pair. When the VCI participate to FCR, the dominant eigenvalues of the system becomes purely real. Time domain simulations displaying the impact of the contribution of the VCI to FCR are analysed in Section 2.3.3.1.

2.3.2.3 Analysis of the oscillating frequency behaviour

Similarly to the SM vs SM system, the analysis of the oscillating frequency behaviour is carried out using the simplified model of the system (Figure 2.12). Likewise, due to its dynamics, the power frequency regulator of the synchronous machine is completely disregard (SW2 OFF). On the other hand, since the droop control of the VCI instantaneously react to frequency variations, it cannot be neglected. From the comparison of both configurations, it is possible to draw out a qualitative interpretation about the oscillatory behaviour of the system using two hypotheses:

1. Considering that $K_{pf,1} = 0$ and $\Delta\tilde{\omega}_g \approx \Delta\omega_{coi}$, the model is equivalent to that with two synchronous machines. However, in this case, the value of $K_{d,1}$ is much higher than that of the previous configuration (400 instead of 30 pu). From eq. (2.12), for fixed values of H_1 and H_2, the increase of the $K_{d,1}$ increases the damping ratio and decrease the frequency of $\lambda_{1,2}$. Likewise, the decrease of H_1 have the same impact on the oscillating eigenvalues.

2. Considering that the frequency of the system is around its nominal value, and the frequency oscillations are relatively small, $\Delta\tilde{\omega}_g \approx \Delta\omega_0$. In the case in which $K_{pf,1} \neq 0$, the effect of the droop can be combined with $K_{d,1}$, increasing the damping of the oscillating eigenvalues. However, when analysing the usual numerical values, e.g. $K_{d,1} = 400$ pu and $K_{pf,1} = -25$, the contribution of the droop to the damping of $\lambda_{1,2}$ can be considered as moderate.

In order to observe the impact of the replacement of the synchronous machine with the VCI on the damping of the oscillations between the sources, the eigenvalues of the characteristic polynomial of eq. (2.11) are compared in Table 2.6. Once again, for the numerical application, it is considered that TLL = 25 km, and that the inertial effect of the VCI is equivalent to the coefficient of inertia of the synchronous machine ($H_1 = 6.5$ s). For the VCI vs SM system, two different scenarios are considered:

- **First scenario:** $K_{pf,1} = 0$ pu and $K_{d,1} = 400$ pu;

- **Second scenario:** $K_{pf,1} = -25$ pu and $K_{d,1} = 400$ pu.

From Table 2.6, it can be observed that, since $K_{d,1}$ of the VCI is very high in comparison with that of the synchronous machine, the oscillating eigenvalues of the VCI vs SM system are significantly more damped than those of the SM vs SM system. Furthermore, the oscillating eigenvalues are moderately more damped when the VCI contributes to FCR than when it does not contribute to it.

Table 2.6 – Comparison of the oscillating eigenvalues of the SM vs SM and VCI vs SM systems obtained with the characteristic polynomial of eq. (2.11).

	SM vs SM system	**VCI vs SM system**	
	$K_{d,1} = K_{d,2} = 30$ **pu**	**First scenario**	**Second scenario**
Eigenvalues (λ_{osc})	$-1.20 \pm j7.03$	$-3.36 \pm j7.72$	$-3.81 \pm j7.13$
Damping ratio (ξ, %)	16.83	39.91	47.13
Damped frequency (f_d, **Hz**)	1.12	1.23	1.13

Nota bene: $f_d = f_n\sqrt{1-\xi^2}$

2.3.3 Impact of the frequency support of the VCI on the dynamics of the system

2.3.3.1 Contribution of the VCI to FCR

In Sections 2.3.2.2 and 2.3.2.3, using very simplified analyses, it was observed the evolution of the dominant and oscillating frequency behaviour of the two-voltage source system due to the replacement of a synchronous machine with a VCI. Regarding the contribution of the VCI to FCR, it was observed that it can improve the dynamics of the frequency of the system, especially the dominant frequency behaviour.

In this section the impact of the contribution of the VCI to FCR is observed using time domain simulations. For this purpose, the same configurations adopted in Sections 2.3.2.2 and 2.3.2.3 are used in the analysis. As a reminder, two different scenarios are considered:

- **First scenario:** only the SM contributes to FCR, $K_{pf,1} = 0$ pu and $K_{pf,2} = -50$ pu;
- **Second scenario:** both sources contribute to FCR, $K_{pf,1} = K_{pf,2} = -25$ pu.

The TLL adopted for both scenarios is 25 km, and, in both scenarios, the damping factor of the VCI is $K_{d,1} = 400$ pu. The simulations results obtained with the reference model of the system are illustrated in Figure 2.14. In addition, a comparison between the eigenvalues obtained with both the reference and simplified models of the system is given in Table 2.7.

As illustrated in Figure 2.14a, the dominant frequency behaviour of the system in the first scenario, i.e. when the VCI does not contribute to FCR, is the same as that of the SM vs SM system. In the second scenario, when the VCI contributes to FCR, the dominant

frequency behaviour of the system is significantly improved, reducing the frequency nadir from 59.73 to 59.84 Hz. In Figure 2.14b, even if the dynamics of the frequency oscillations between the sources in the first scenario are already well damped due to the high value of $K_{d,1}$, it can still be observed that this behaviour is improved when the VCI contributes of FCR.

From the comparison between Tables 2.5 to 2.7, it can be observed that tendencies illustrated with the reduced order models introduced in Section 2.3.2 are quite representative of the reference model of the system. The misrepresentation of λ_{dom} in the second scenario is addressed further in this section.

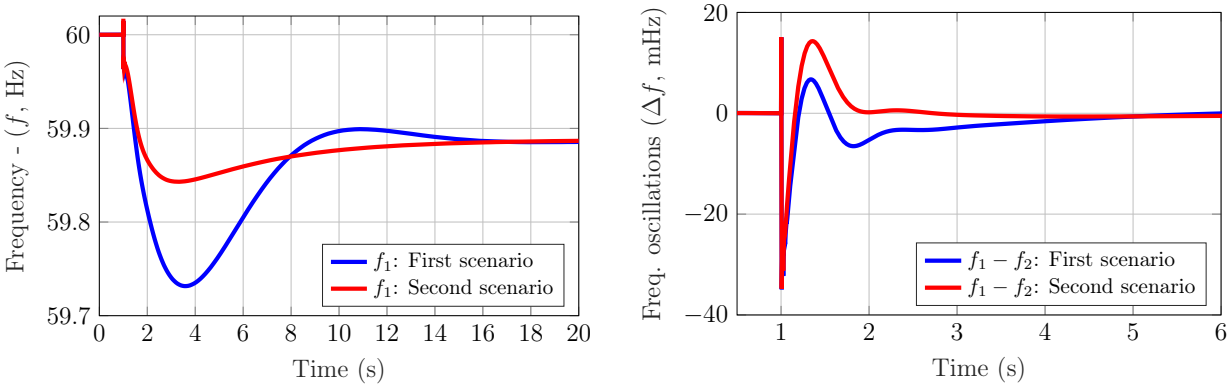

(a) f_1 (Hz) (b) $\Delta f = f_1 - f_2$ (mHz)

Figure 2.14 – Impact of the power frequency characteristic of the VCI on the frequency behaviour of the VCI vs SM system (reference model). In blue: First scenario; In red: Second scenario.

Table 2.7 – Comparison of the dominant and oscillating eigenvalues of the VCI vs SM system obtained with its reference and simplified representations.

	First scenario		**Second scenario**	
	Reference	**Simplified**	**Reference**	**Simplified**
$\lambda_{\mathbf{dom}}$	$-0.34 \pm j0.42$	$-0.35 \pm j0.45$	-0.24 $-1.33 \pm j0.12$	-0.25 -1.30
$\lambda_{\mathbf{osc}}$	$-3.13 \pm j6.83$	$-3.18 \pm j7.78$	$-3.62 \pm j6.18$	$-3.69 \pm j7.14$

2.3.3.2 Impact of inertial effect of the VCI

With the replacement of synchronous machines with PE-based sources, in addition to the damping factor, the inertia (inertial effect) of the generator is not any more an inherent value linked to its physical construction, but a configurable parameter. The following analysis

focuses on the evolution of the dynamic behaviour of the system due to the variation of the inertial effect of the VCI. The eigenvalues trajectories of the reference and simplified models of the VCI vs SM system considering the variation of H_1 are illustrated in Figure 2.15.

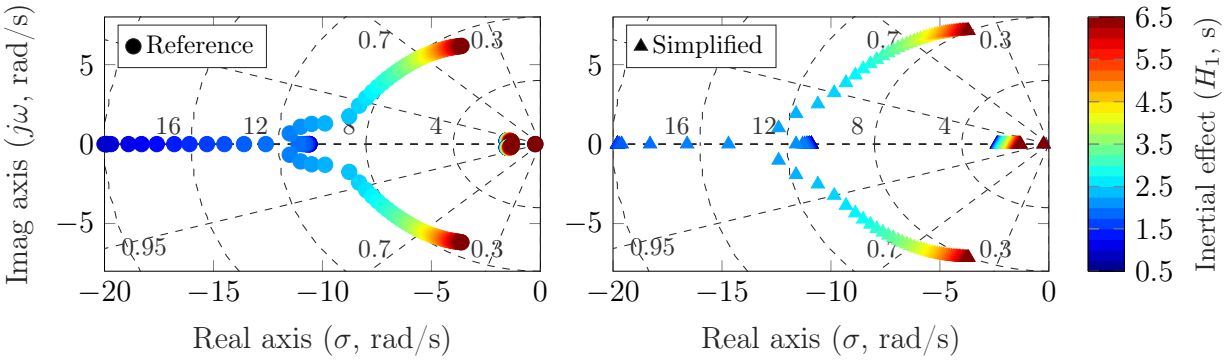

(a) H_1 variation: full view

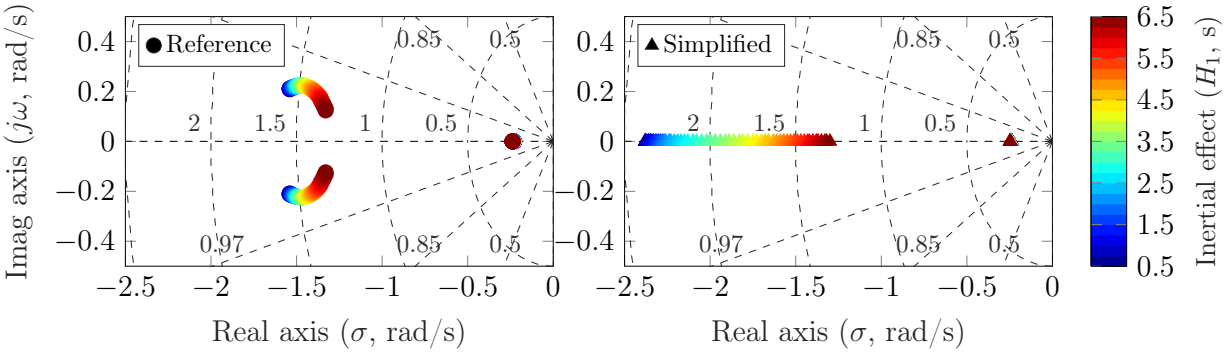

(b) H_1 variation: magnified view

Figure 2.15 – Comparison of the trajectories of the dominant and the oscillating eigenvalues obtained with the reference and simplified models of the VCI vs SM system. Variation of the inertial effect of the VCI.

Figure 2.15a highlights the so-called oscillating eigenvalues of the system. The simplified model is capable of providing the same tendency as that observed with the reference model of the system. For low values of H_1, the oscillating eigenvalues are well damped and much faster than the dominant ones. With the increase of H_1, these eigenvalues move towards the imaginary axis, becoming less damped and slower. However, it can be observed that they always are faster than the dominant eigenvalues of the system.

A focus is applied to the dominant eigenvalues in Figure 2.15b. It can be observed that the slowest eigenvalue is almost insensitive to the variation of H_1, whereas the faster eigenvalues are more sensitive to such variation. For low values of H_1, the eigenvalues on the left are much faster than that on the right, and therefore, their dynamics could even be neglected, reducing the system to a first order.

In Figure 2.15b, comparing the eigenvalues of the reference and simplified models, it can be observed that the complex conjugate pair on the left is not correctly represented with the simplified model. However, as illustrated in Figure 2.16, the time domain response reveals a good compliance between the representations, therefore, the misrepresentation of the aforementioned eigenvalues by the simplified model does not have a major impact on the representativeness of the reference one.

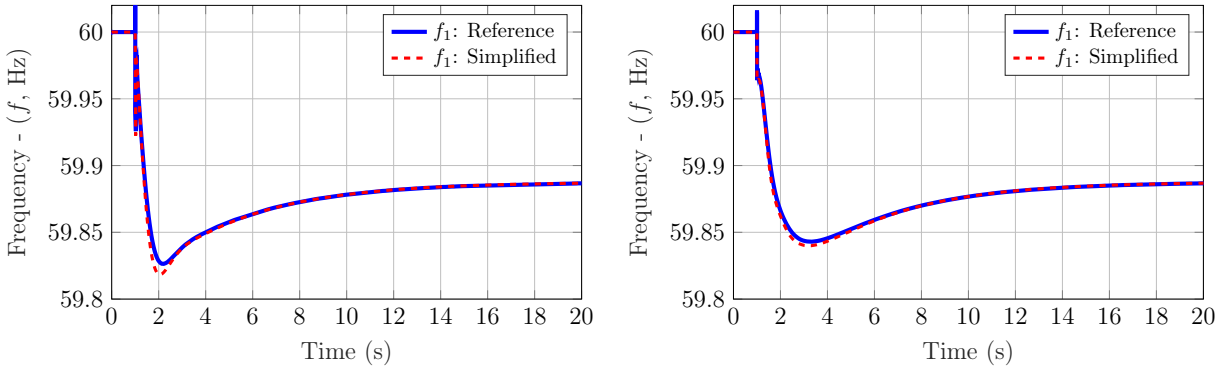

(a) f_1 (Hz); $H_1 = 0.5$ s (b) f_1 (Hz); $H_1 = 6.5$ s

Figure 2.16 – Comparison of the frequency behaviours of the VCI obtained with the reference and simplified representations of the system.

In addition, as illustrated in Figure 2.16, the increase of H_1 decreases the magnitude of the RoCoF of the system, which can also be verified applying the theorem of the initial value on eq. (2.13). Furthermore, since the RoCoF is less pronounced and the dynamics of the control chain are the same, the frequency nadir is shallower.

2.3.4 Impact of power ratio between the sources

Hitherto, the performed analyses have considered that both sources had the same rated power. In order to enlarge the analysis, the impact of the Power Ratio (PR) between the sources is investigated in the following analysis. The PR is computed as given in eq. (2.16).

$$\text{PR} = \frac{\text{VCI rated power } (S_{b,1}, \text{ MVA})}{\text{SM rated power } (S_{b,2}, \text{ MVA})} \tag{2.16}$$

As illustrated in Figure 2.17, in order to account the PR between the sources, the simplified model of the system must be adapted. The matrix $\mathbf{K_{cplg}}$ and the synchronous machine are expressed using $S_{b,2}$ as power base, whereas ΔP_1 is converted to the base $S_{b,1}$ by dividing by the coefficient PR.

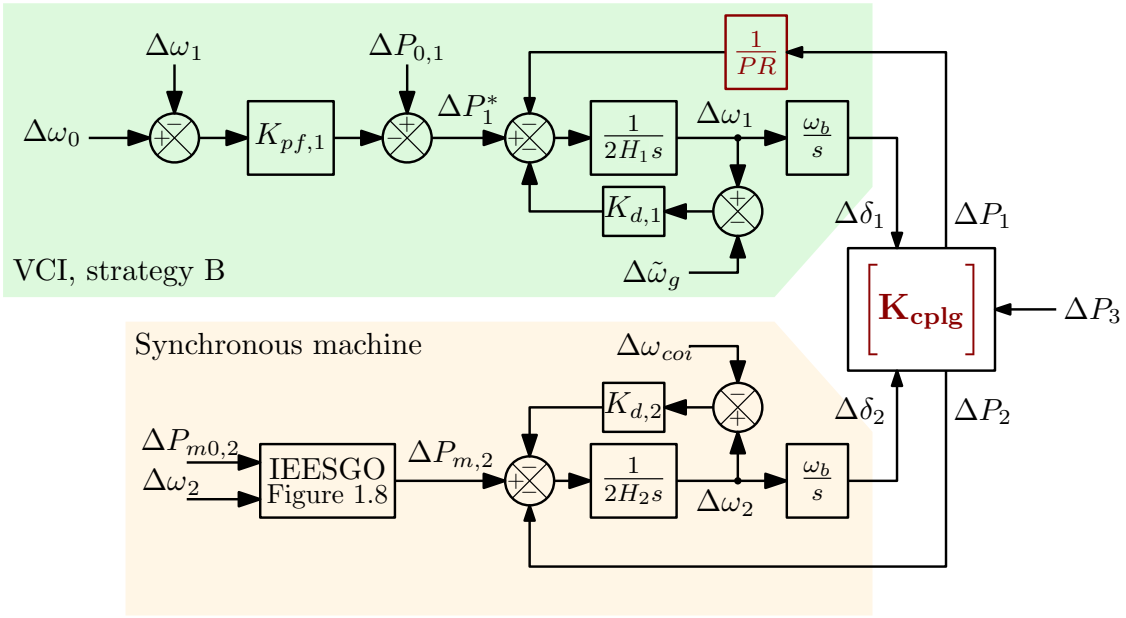

Figure 2.17 – Simplified model of the VCI vs SM system accounting the variation of the PR between the sources.

In order to better observe the phenomenon, the coefficient PR can be spread into the VCI blocks, expressing all parameters as a function of $S_{b,2}$. Therefore, Figure 2.18 illustrates the simplified model of the system highlighting the necessary adaptations to account the variation of the PR between the sources.

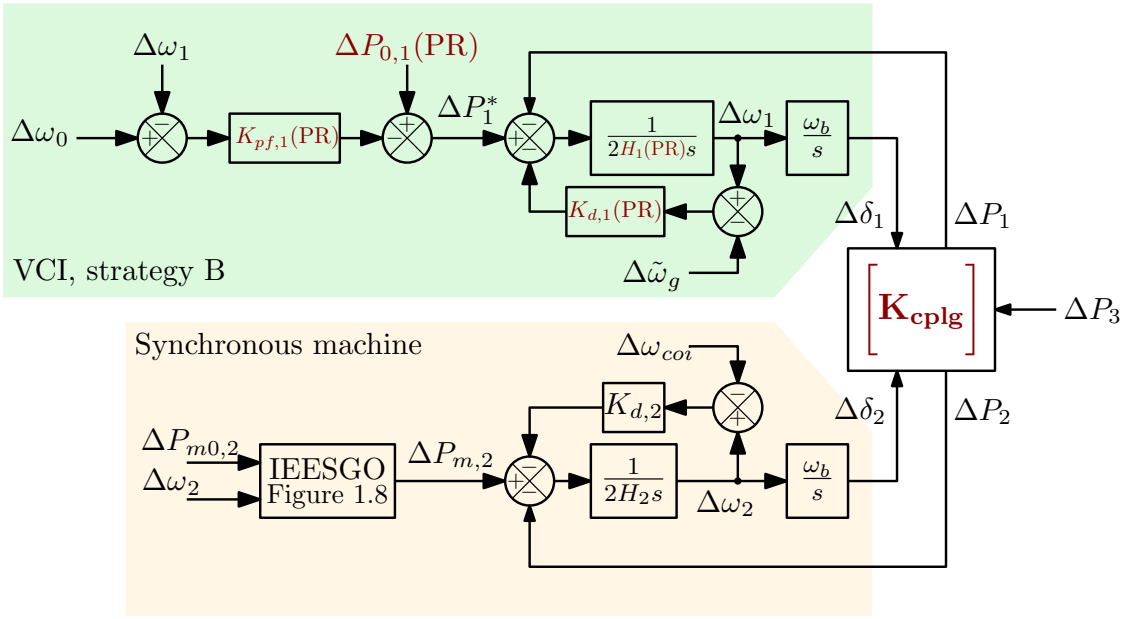

Figure 2.18 – Alternative form of the simplified model of the VCI vs SM system accounting the variation of the PR between the sources.

The coefficient PR can also be considered in the other representations of the system. For example, in order to consider the power ratio between the sources, the transfer function $H_{coi}(s) = \Delta\omega_{coi}/\Delta P_3$ obtained with the dominant model of the system is rewritten as given in eq. (2.17).

$$\frac{\Delta\omega_{coi}}{\Delta P_3} = \frac{-\frac{1}{2\left(H_1\mathrm{PR}+H_2\right)}\left(s+\frac{1}{\tau_5}\right)}{s^2+\left(\frac{1}{\tau_5}-\frac{K_{pf,1}\mathrm{PR}+K_{pf,2}\left(1-K_2\right)}{2\left(H_1\mathrm{PR}+H_2\right)}\right)s-\frac{K_{pf,1}\mathrm{PR}+K_{pf,2}}{2\left(H_1\mathrm{PR}+H_2\right)\tau_5}} \tag{2.17}$$

From Figure 2.18, it can be observed that the power ratio between the sources results on the variation of multiple parameters, notably, the inertial effect, damping factor and the power frequency characteristic of the VCI (H_1, $K_{d,1}$ and $K_{pf,1}$, respectively). In addition, since the LCL filter of the inverter also depends on the rated power of the VCI, the electrical distance between the sources also varies with the PR between the sources (variation of the elements of $\mathbf{K_{cplg}}$).

Figure 2.19 illustrates the trajectories of the dominant and the oscillating eigenvalues of the system as a function of the PR between the sources, expressed in percentage. It is emphasised that, since $S_{b,2} = 900$ MVA, $S_{b,1}$ varies between when 90 and 2700 MVA. It is highlighted that, in this analysis, due to the high rated power of the VCI, a hypothetical inverter is considered.

Figure 2.19a highlights the movement of the oscillating eigenvalues of the system. When the PR is equal to 10%, the oscillations between the sources are very damped. With the increase of the PR, the damping of the oscillating eigenvalues decreases. In addition, it can be observed that the sensibility of these eigenvalues to the PR decreases as it increases, displaying a slightly variation between 200 and 300%.

The trajectory of the dominant eigenvalues of the system is illustrated in Figure 2.19b. When the PR between the sources is equal 10%, the equivalent $\mathrm{PR}K_{pf,1}$ is equal to -2.5 pu. As observed in Section 2.3.3.1, when the $K_{pf,1}$ fraction is small, the dominant frequency behaviour of the system is similar to that of the SM vs SM system, presenting a complex conjugate pair as dominant eigenvalues. As the PR increases, the equivalent $K_{pf,1}$ also increases, and the dominant eigenvalues become two purely real eigenvalues. For high values of PR, the most dominant eigenvalue, i.e. the closest to the imaginary axis, is much slower than that of the eigenvalue(s) on the left. Therefore, the latter can almost be neglected, and, as illustrated in Figure 2.20, the dynamics of the dominant frequency behaviour of the system are very close to a first order. The phenomenon can be explained by the fact that the participation of the synchronous machine becomes marginal in comparison with that of the VCI. The behaviour of a two-VCI system will be observed in Section 2.4.

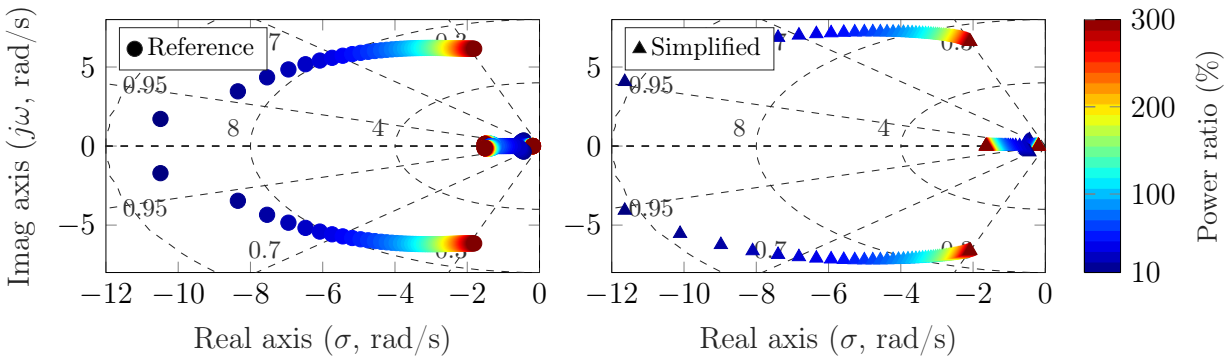

(a) PR variation: full view

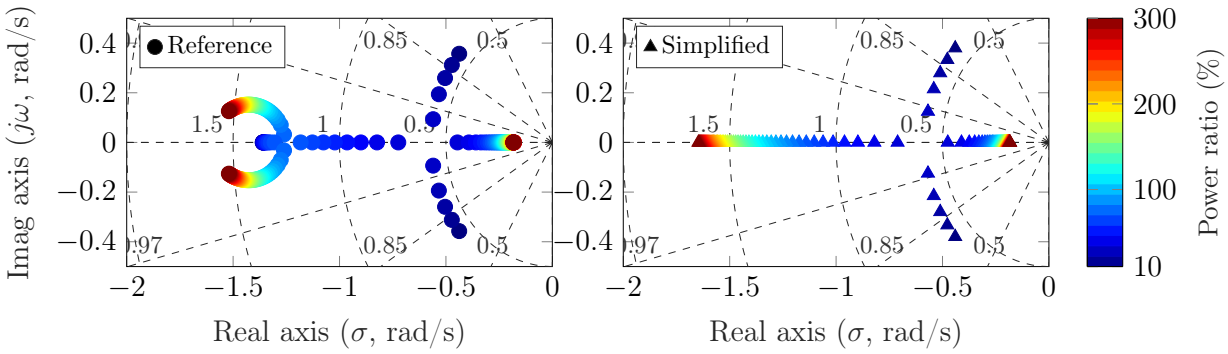

(b) PR variation: magnified view

Figure 2.19 – Comparison of the trajectories of the dominant and the oscillating eigenvalues obtained with the reference and simplified models of the VCI vs SM system. Variation of the Power Ratio between the sources.

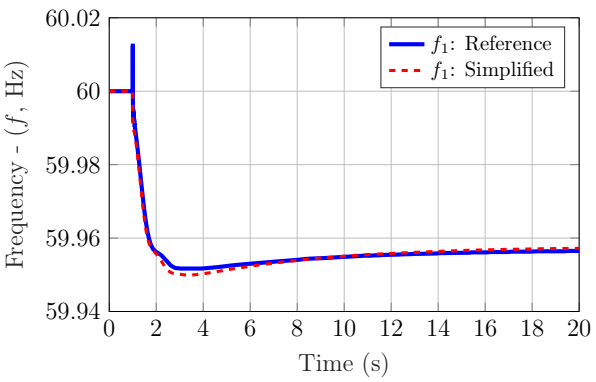

(a) f_1 (Hz)

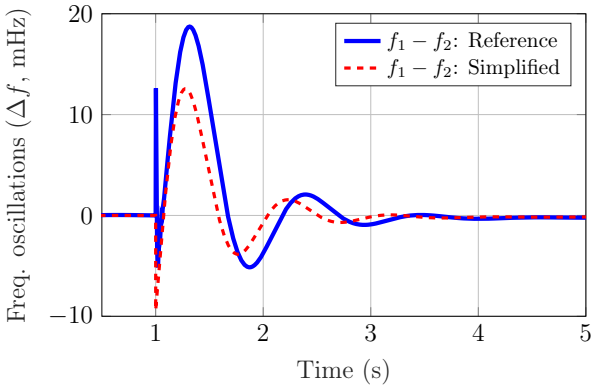

(b) $\Delta f = f_1 - f_2$ (mHz)

Figure 2.20 – Frequency behaviour of a VCI vs SM system considering a power ratio between the sources equal to 300%.

2.3.5 Influence of the VCI control strategy

Hitherto, in the analysis of the frequency behaviour of the VCI vs SM system, the strategy B of the VCI has been employed. In this analysis, the VCI structure is modified, adopting the strategy C, where the estimated frequency of the grid ($\tilde{\omega}_g$) is replaced with a constant value (ω_0). Therefore, the simplified representation of the VCI vs SM system, employing the VCI-C strategy is illustrated in Figure 2.21. In comparison with the representation of Figure 2.12, as introduced in Section 1.3.1.5, the VCI-C strategy lacks of a natural damping power, displaying just the inertial parameter H_1. Therefore, a lead-lag compensator is added to the measure of active power in order to provide damping to the system.

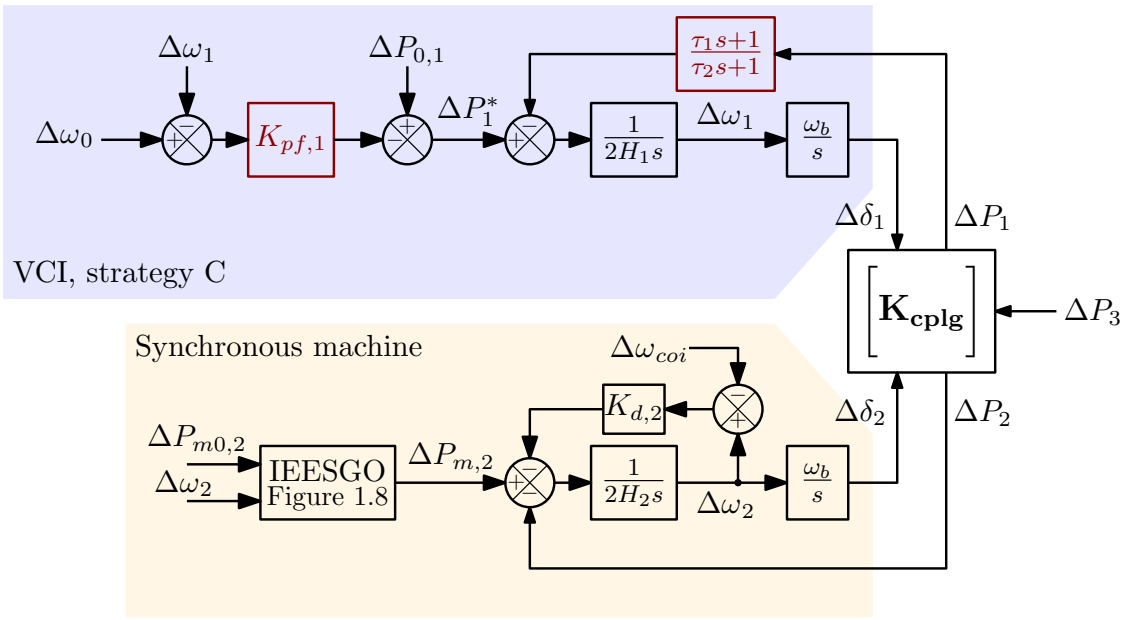

Figure 2.21 – Simplified representation of the VCI vs SM system employing VCI-C strategy.

In Section 1.3.1.6, strategies VCI-B and VCI-C have been proven equivalent for a fixed frequency system, which should also be valid for a variable frequency system. Firstly, the equivalence between the parameters of VCI-B and VCI-C are established applying eq. (1.48). The parameters τ_1 and τ_2 of the lead-lag compensator of the VCI-C equivalent to $K_{d,1}$ of the VCI-B are equal to 204 and 25 ms, respectively.

In order to illustrate the equivalence between these strategies, the dynamic behaviour obtained with both strategies are compared for the scenario where the TLL is equal to 125 km. The frequency of the VCI and the frequency oscillations between the sources are illustrated in Figure 2.22. It can be observed that both the dominant and the oscillating frequency behaviours of the system are the same regardless of the adopted VCI strategy, ratifying the equivalence between them.

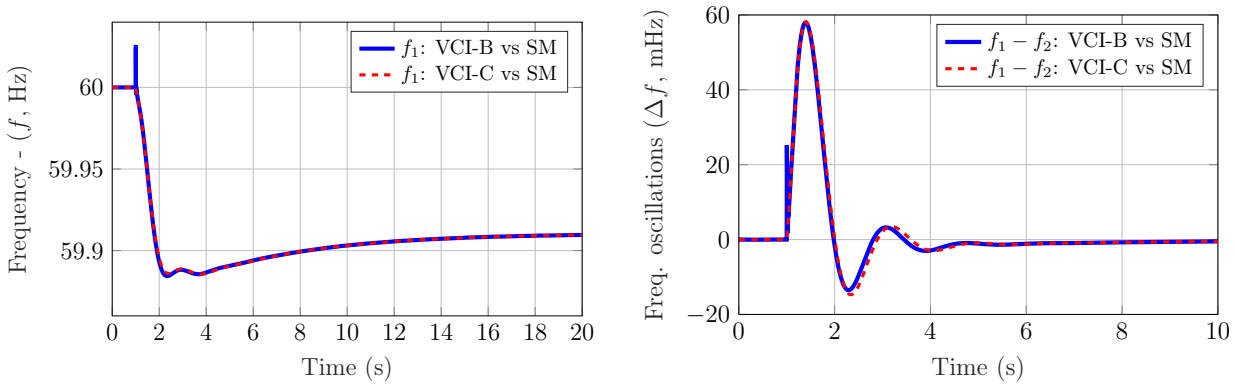

(a) f_1 (Hz) (b) $\Delta f = f_1 - f_2$ (mHz)

Figure 2.22 – Comparison between the dynamic behaviour obtained with VCI-B vs SM and VCI-C vs SM systems (TLL = 125 km).

Therefore, the findings observed with the VCI vs SM system are independent of the VCI strategy transposable, and equivalent results can be obtained using both VCI-B and VCI-C strategies.

2.3.6 Summary of the findings

An in-depth analysis about the frequency dynamics of a system composed of one PE-based source operating in VCI mode and one synchronous machine was performed in this section. The evolution of the frequency behaviour as a function of different parameters has been analysed. The findings obtained from these analyses will extensively be used in the following chapter, and therefore, a summary of the impact of each parametric variation on the dominant and oscillating frequency behaviour of the system are given in Table 2.8.

Table 2.8 – Impact of each parametric variation of the frequency behaviour of the system. Tendencies described considering the increase of the parameters.

	Dominant behaviour		**Oscillating behaviour**	
Parameter	**Impact**	**Tendency**	**Impact**	**Tendency**
Transmission line length (TLL)	Negligible	—	High	Decrease of ξ of the oscillating eigenvalues Frequency oscillations more pronounced
VCI p-f characteristic (K_p)	High	Increase of ξ of the dominant eigenvalues Peaks and nadirs less pronounced	Moderate	Increase of ξ of the oscillating eigenvalues Frequency oscillations less pronounced
VCI Inertial effect (H)	Moderate	Decrease of the RoCoF magnitude Peaks and nadirs less pronounced	High	Decrease of ξ of the oscillating eigenvalues Frequency oscillations more pronounced
VCI Damping factor (K_d)	Negligible	—	High	Increase of ξ of the oscillating eigenvalues Frequency oscillations less pronounced
Power Ratio (PR)	High	Increase of ξ of the dominant eigenvalues Peaks and nadirs less pronounced	High	Decrease of ξ of the oscillating eigenvalues Frequency oscillations more pronounced

2.4 Two-voltage source system composed of VCIs

The main tendencies of the frequency behaviour of a system composed of two voltage sources have already been determined in Section 2.3. In this section, the impact of the replacement of the remaining synchronous machine by a second VCI, resulting in a 100% PE-based system, is verified.

2.4.1 Description of the studied system: the reference model

The Reference Model of the studied system is composed of two identical VCIs. The inverters are represented with average models, ideal voltage sources to represent the dc side of the sources, and LCL filters to interface them with the ac grid. The controls of each VCI are implemented using cascaded voltage and current loops, and the VCI-C synchronisation strategy illustrated in Figure 1.26. The parameters adopted for the system are given in Table 1.11 and Table 1.12.

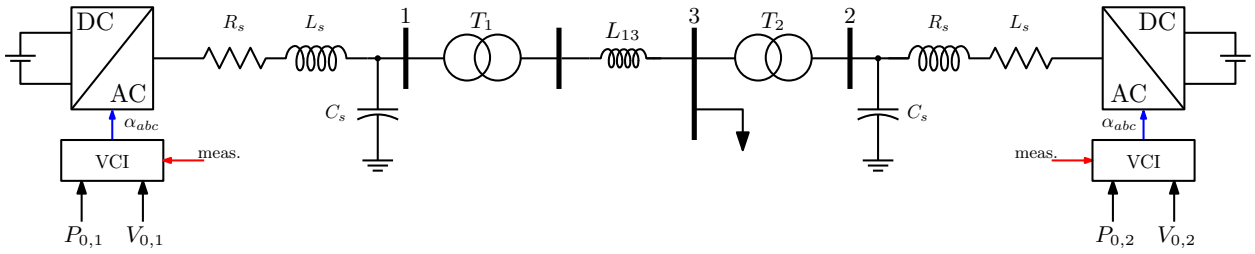

Figure 2.23 – Reference model of the VCI vs VCI system.

A linearised form of the reference model of the system is proposed and validated as in previous sections. The linearised form of the model has 34 differential states, being:

- eight for the grid,
- 2 × four for the inverter filter:
  - two for the inductance L_s,
  - two for the capacitor C_s.
- 2 × 9 for the VCI-C control strategy:
  - (two + one) for the VSM representation: Figure 1.26,
  - four for the voltage loop: Figure 1.22,
  - two for the current loop: idem.

2.4.2 A completely different frequency behaviour

The Simplified Model of the VCI vs VCI system is illustrated in Figure 2.24. It can be observed that, in this representation, both sources instantaneously react to frequency variations.

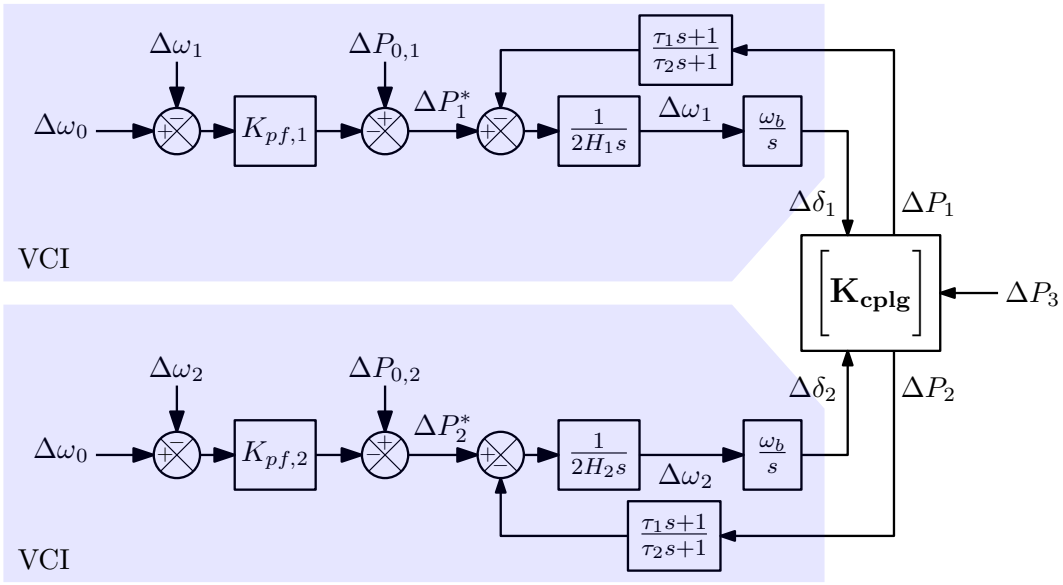

Figure 2.24 – Simplified model of the VCI vs VCI system.

Similarly to other configurations, considering that the frequency of both sources are the same, it is possible to determine a model to illustrate the dominant frequency behaviour of the system. Figure 2.25 illustrates the dominant model of the VCI vs VCI system.

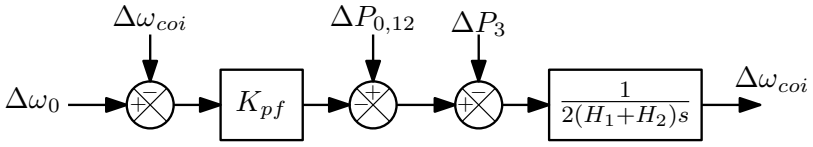

Figure 2.25 – Dominant model of the VCI vs VCI system.

The replacement of the remaining synchronous machine with a second VCI represents a major impact on the dominant frequency behaviour of the system. In allusion to the DM-SC of the VCI vs SM system of Figure 2.13, the power reaction to frequency variations is composed only of a "high pressure fraction", and the transfer function $H_{coi}(s) = \Delta\omega_{coi}/\Delta P_3$, given in eq. (2.18), illustrating first order dynamics, instead of the classic second order dynamics coming from the steam turbine behaviour. The analytical form of the dominant eigenvalue is given in eq. (2.19).

$$\frac{\Delta\omega_{coi}}{\Delta P_3} = \frac{-1}{2\left(H_1 + H_2\right)s - K_{pf}} \tag{2.18}$$

$$\lambda_{dom} = \frac{K_{pf}}{2\left(H_1 + H_2\right)} \tag{2.19}$$

Regarding the oscillating frequency behaviour of the system, since the VCIs instantaneously react to grid disturbances, it is not possible to neglect any dynamics of the simplified model of the system. However, based on the analysis carried out in Section 2.3.2.3, since in this system both VCIs have high equivalent damping factor ($k_{d,1} = k_{d,2} = 400$ pu), it can easily be concluded that the oscillations between the VCIs are still more damped than those observed in the previous configurations.

2.4.3 Comparison with the two-synchronous machine system

The frequency behaviour obtained with the VCI vs VCI system is compared with that of the SM vs SM system. For this purpose, the scenario described in Section 2.2.1 is adopted, and it is considered that the inertial effect of the VCIs are equivalent to the coefficient of inertia of the synchronous machines ($H_1 = H_2 = 6.5$ s). The simulations results are illustrated in Figure 2.26. In addition, a numerical comparison of the dominant and oscillating eigenvalues of both system is given in Table 2.9.

From Figure 2.26a, the VCI vs VCI system displays a first order dynamic behaviour with settling time of $t_s \approx 2$ s. The dynamics of the system meet with the expected performance obtained with the dominant model of the system, in which, from eq. (2.18), for the adopted parameters, $\tau = 0.52$ s ($t_s \approx 4\tau$). Furthermore, the dominant eigenvalue obtained with this model — eq. (2.19), $\lambda_{dom} = 1.92$ — is consistent with those obtained with the reference and simplified representations of the system given in Table 2.9.

The dominant frequency behaviour of the SM vs SM system displays a second order dynamics, which is characteristic of steam turbines; this subject is extensively addressed in Section 2.2.2.2.

From Figure 2.26b, as expected, the frequency oscillations between the VCIs are very damped, being completely mitigated in less than one second after the disturbance. Furthermore, in comparison with the SM vs SM system, the frequency os the oscillations are higher. This phenomenon could be explained by the fact that the electrical distance between the sources decreased, increasing the synchronising torque between them, and consequently, increasing the frequency of the oscillations between the sources; refer to eq. (2.12).

In addition, it can be observed that the compliance between the simplified and reference models of the VCI vs VCI system is visually bigger than that between the models of the SM vs SM system. Differently than simplified models with at least one synchronous machine, in which the damping factor must be estimated, all parameters of the simplified model of the VCIs are derived from their reference model, increasing the representativeness of the system.

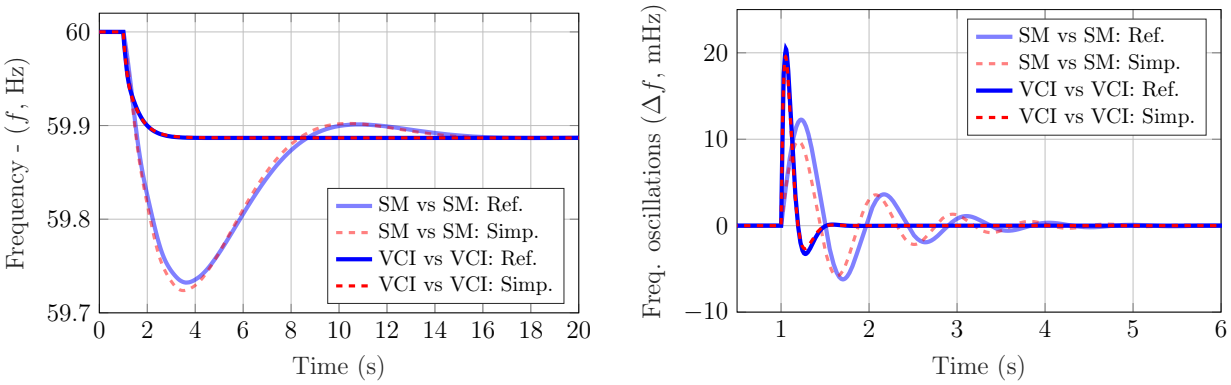

(a) f_1 (Hz) (b) $\Delta f = f_1 - f_2$ (mHz)

Figure 2.26 – Comparison between the frequency behaviour of the SM vs SM and the VCI vs VCI systems.

Table 2.9 – Comparison of the dominant and oscillating eigenvalues of the SM vs SM and the VCI vs VCI systems.

	SM vs SM system		**VCI vs VCI system**	
	Reference	**Simplified**	**Reference**	**Simplified**
$\lambda_{\mathbf{dom}}$	$-0.35 \pm j0.43$	$-0.35 \pm j0.46$	-1.98	-1.92
$\lambda_{\mathbf{osc}}$	$-1.08 \pm j6.79$	$-1.13 \pm j7.18$	$-9.86 \pm j10.51$	$-10.77 \pm j10.17$

2.5 The association of a CCI with a synchronous machine

The previous configurations have addressed the analysis of two-generator systems where both sources behave as voltage sources. In this section, a system composed of one PE-based source behaving as a current source and one synchronous machine is analysed.

2.5.1 Description of the studied system: the reference model

As introduced in Chapter 1, this work adopts the same the power interface for PE-based sources behaving as voltage or current source. Therefore, the reference model of the CCI

vs SM system is equivalent to that of the VCI vs SM system of Figure 2.10, and the only difference is on the control strategy of the inverter. The CCI control is implemented using a power control in direct mode, an inner current loop, and a PLL for the synchronisation with the grid. A power frequency droop strategy is available for the contribution to FCR; refer to Section 1.3.2.3 for details about the control structure. The parameters adopted for the CCI strategy are given in Table 1.15.

2.5.2 The dominant model of the CCI vs SM system

Due to the inherent behaviour of the CCI as a power injector, it is not possible to define a simplified model to the CCI vs SM system as it was proposed for previous configurations. Only models illustrating the dominant frequency behaviour of the system can be derived from this configuration. For the same reason, since the CCI does not generate its own frequency, it should be highlighted that the concept of frequency oscillations between the sources does not exist in this configuration.

The DM-SC model of the system is illustrated in Figure 2.27. It can be observed that this model is similar to that of the VCI vs SM system illustrated in Figure 2.13. However, it should be noticed that the CCI does not contribute to the equivalent inertia of the system, which is composed only of the coefficient of inertia of the synchronous machine (H_2).

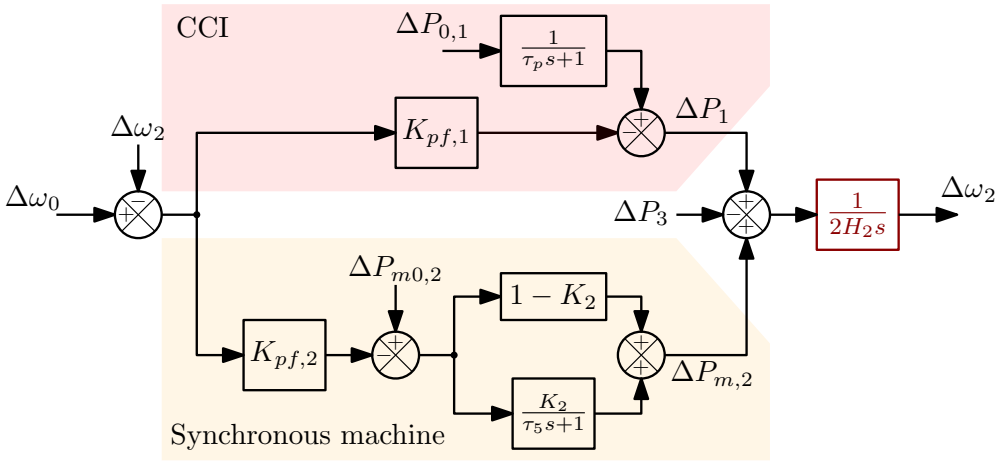

Figure 2.27 – DM-SC representation of the CCI vs SM system.

In Section 2.3.3.1, it has been observed that the contribution of the VCI to FCR is equivalent to a high pressure stage of the steam turbine, and, as illustrated in Figure 2.14, the $K_{pf,1}$ fraction has an important impact on the dominant frequency behaviour of the system. Since the dominant models of both VCI vs SM and CCI vs SM systems are equivalent on this regard, the conclusions about the contribution of the VCI to FCR are transposable to the CCI case.

The case study of Section 2.3.3.1 is repeated to verify the impact of the contribution of the CCI to FCR. As a reminder, two different scenarios are considered, and, for both, it is adopted TLL = 25 km.

- **First scenario:** only the SM contributes to FCR, $K_{pf,1} = 0$ pu and $K_{pf,2} = -50$ pu;
- **Second scenario:** both sources contribute to FCR, $K_{pf,1} = K_{pf,2} = -25$ pu.

The frequency behaviour of the system obtained after a load step ($\Delta P_l = 0.1$ pu) is illustrated in Figure 2.28. Since the CCI operates in PQ mode, the voltage map is not exactly the same in both scenarios, and therefore, a slight difference in the equilibrium frequency after the disturbance can be observed, which is however not an obstacle to the analysis. An enhancement on the frequency dynamics similar to that verified in Figure 2.14a for the VCI vs SM system, is observed when the CCI contribute to FCR, revealing an important impact on the frequency behaviour of the system.

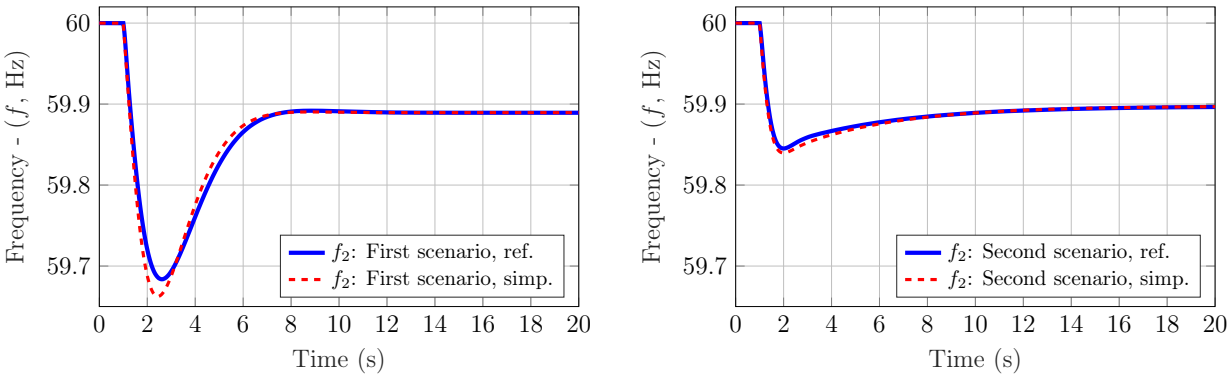

(a) f_2 (Hz); First scenario

(b) f_2 (Hz); Second scenario

Figure 2.28 – Impact of the power frequency characteristic of the CCI on the frequency behaviour of the CCI vs SM system.

2.5.3 Dynamic analysis of a CCI vs SM system

The dominant model of the system allows to predetermine the overall dynamics when no stability problems are encountered. However, it is not suitable to provide any information about the stability limit of the system. Therefore, the analysis of the system stability should be carried out using a more detailed representation of the system.

In this section, a stability analysis based on the observation of the eigenvalues of the linearised form of the reference model of the system is proposed. At first, considering the

scenario described in Section 2.2.1, the linearised representation of the CCI vs SM system is validated in Figure 2.29. The system has 39 differential states:

- eight for the grid,
- four for the inverter filter,
- nine for the CCI control strategy:
  - two for the PLL: Figure 1.29a,
  - one for the FCR droop control: Figure 1.36a,
  - two for the power control: Figure 1.33,
  - four for the current loop: idem.
- 18 for the synchronous machine and associated controls.

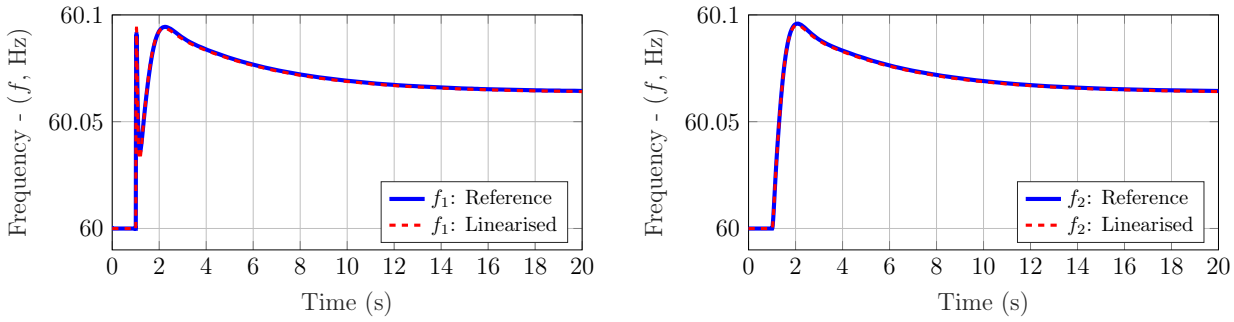

(a) CCI node 1 (b) SM node 2

Figure 2.29 – Validation of the linearised form of the reference representation of the CCI vs SM system. Stimulus: $\Delta P_{0,1} = 0.05$ pu.

The main analysis is carried out using the concept of stability surfaces introduced in Appendix B.5, focusing on the variations of the power ratio and the electrical distance between the sources. The PR is varied from 10 to 100% varying the rated power of the inverter and its interface. The electrical distance between the sources is varied varying the TLL from 25 to 125 km.

In order to illustrate the employed methodology, a preliminary analysis considering the variation of the TLL and a PR equal to 100% is displayed in Figure 2.30. It can be observed that two pairs of complex conjugate eigenvalues, $\lambda_{7,8}$ and $\lambda_{25,26}$, are considered as critical[1]. It is emphasised that the critical eigenvalues of the system are dependent of many variables (e.g. grid topology, operating point, control design, etc.), and therefore, they can be different for different scenarios.

[1]It is defined as critical, the eigenvalues going towards, and eventually crossing, the critical damping ratio (ξ_{cr}) adopted as threshold for the study. For the following analysis, $\xi_{cr} = 10\%$, meaning that, if damping one of any eigenvalue is below the threshold, the system is considered as unacceptable to operate.

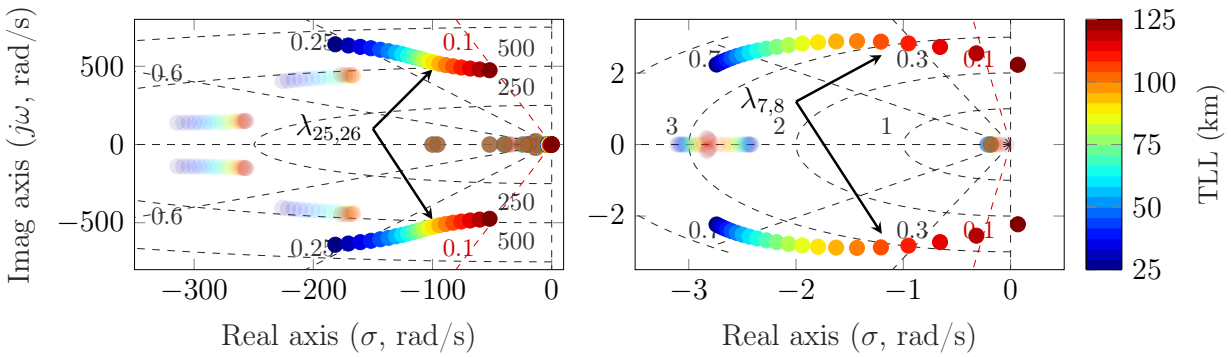

Figure 2.30 – Eigenvalues trajectories of the CCI vs SM system considering the variation of the transmission line length from 25 to 125 km.

Using the participation factor matrix, the main dependencies between the critical eigenvalues and the differential states of the system can be determined. Figure 2.31 illustrates these dependencies considering PR equal to 100% and TLL equal to 125 km. It is emphasised that the participation factor are dependent of the configurations of the system. The eigenvalues $\lambda_{7,8}$ are mainly related to the mechanicals and excitation system of the synchronous machine, whereas $\lambda_{25,26}$ are mainly related to the grid currents and the inner current loop of the CCI (γ variables).

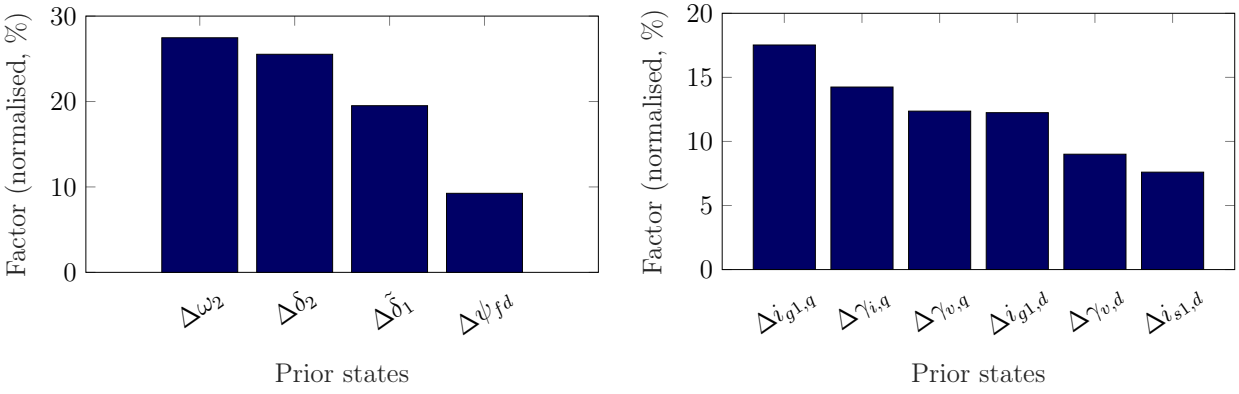

(a) $\lambda_{7,8}$ (b) $\lambda_{25,26}$

Figure 2.31 – Participation factor of the critical eigenvalues of the system, considering PR equal to 100% and TLL equal to 125 km.

In the proposed approach, the given analysis is repeated for the whole range of PR, allowing build surfaces of the damping ratio of the critical eigenvalues as a function of each pair (PR,TLL), as illustrated in Figure 2.32.

On the one hand, the representation of Figure 2.32 is useful to observe the damping ratio of each critical eigenvalues of the system, however, on the other hand, it is not practical to determine the operating limits of the system. Therefore, a second representation projecting

and superposing all pairs (PR, TLL) which does not satisfy the minimal damping is proposed in Figure 2.33. In this work, the representation of Figure 2.33 is known as stability surface. Contrarily to Figure 2.32, the stability surface indicates the operating limits of the system, preventing however to separately observe the evolution of the damping ratio of each critical eigenvalue.

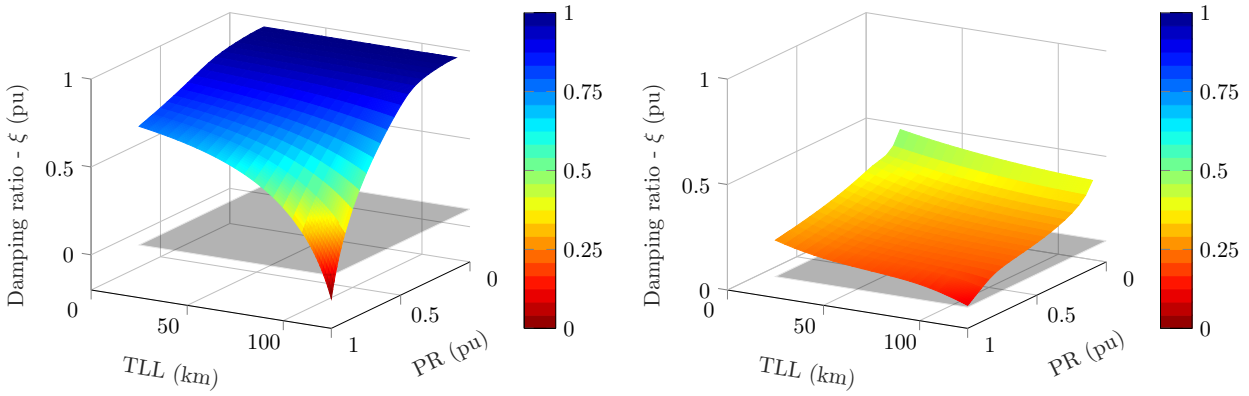

(a) $\lambda_{7,8}$ (b) $\lambda_{25,26}$

Figure 2.32 – Surfaces of damping ratio of the critical eigenvalues as a function of the power ratio between the sources and the transmission line length of the system.

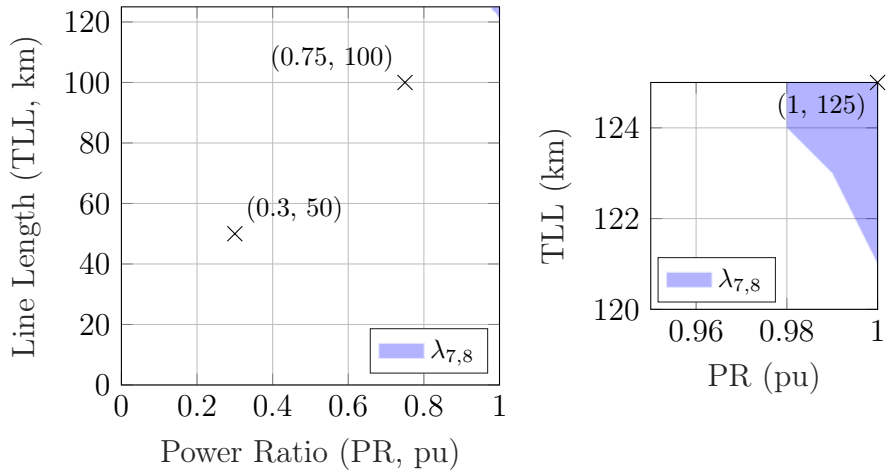

Figure 2.33 – Stability surface of the CCI vs SM system.

Since only $\lambda_{7,8}$ cross ξ_{cr}, the stability surface is only composed of its limits. It can be observed that operating limit on the stability surface is small, indicating that the system cannot properly operates when both the TLL and the PR are increased. However, it is emphasised that this stability study is based on small-signal analysis, and it could present limitations related to important variations in the system (e.g. power flow and voltage map), and therefore, the stability surface could be complement by adding the power flow limits of the system. The latter will not addressed in this work.

From Figure 2.32, it can be can be observed that the critical eigenvalues goes towards the instability with the increase of the PR and the TLL, especially with their simultaneously increase. In order to observe the findings, Figure 2.34 illustrates the variation of active reactive powers of the CCI after a load step ($\Delta P_l = 0.1$ pu) for the different pairs of (PR, TLL) given in Figure 2.33.

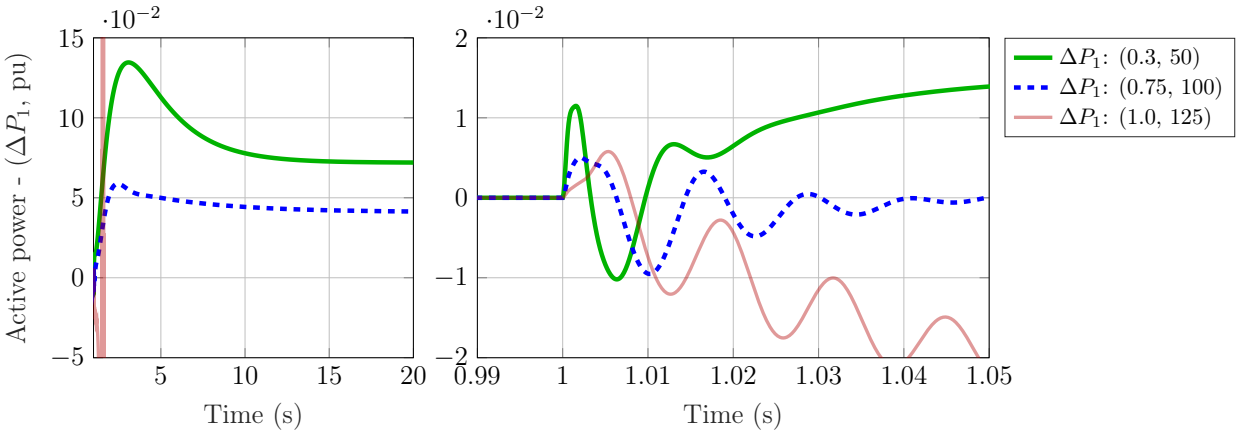

(a) ΔP_1 (pu)

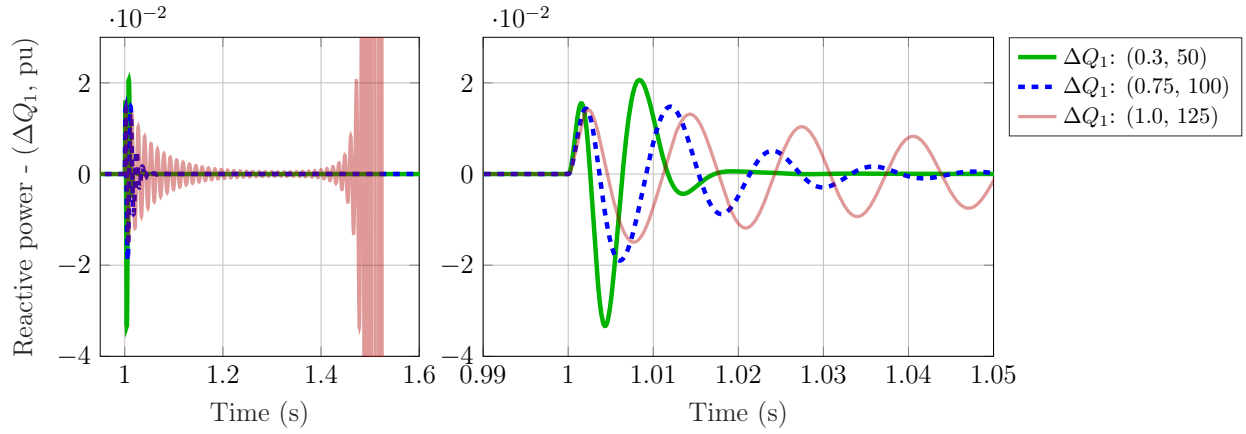

(b) ΔQ_1 (pu)

Figure 2.34 – Variation of active and reactive power of the CCI for different pairs of (PR, TLL).

Reference [102] has shown that the stability limits of a CCI vs SM system presents a high dependency with the operating point of the CCI. With the reduction of the injected active power, the ξ surface related to the differential states of the synchronous machine gets more damped, whereas that related to the differential states of the CCI gets less damped. Figure 2.35 illustrates the ξ surfaces of $\lambda_{7,8}$ and $\lambda_{25,26}$, considering that the active power injected by the CCI (P_1) is equal to 0.3 pu. Despite the topology of this system and the design of its controls being different from those used in [102], it is possible to observe similar phenomena. With the decrease of the active power injected by the CCI, the ξ surface of $\lambda_{7,8}$

becomes more damped and that of $\lambda_{25,26}$ becomes less damped. Globally, the operating area of the system is reduced.

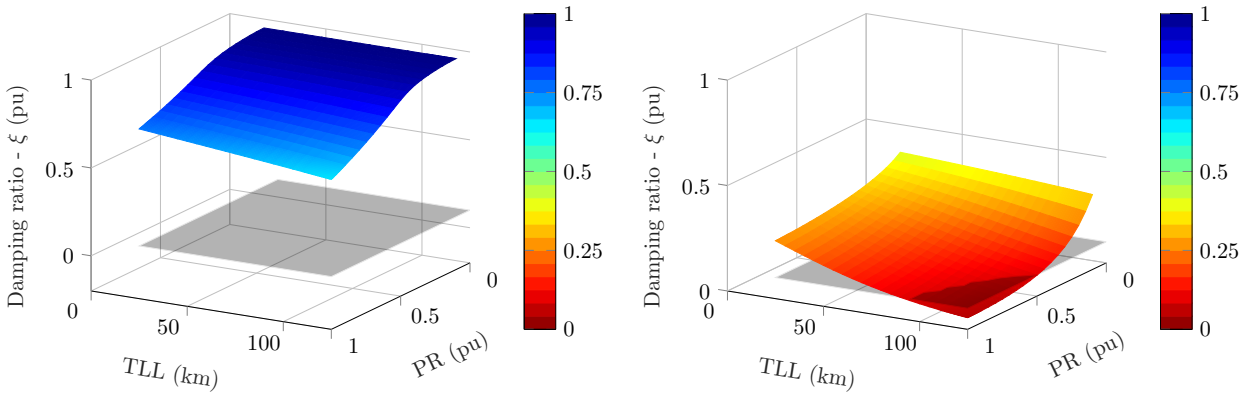

(a) $\lambda_{7,8}$ (b) $\lambda_{25,26}$

Figure 2.35 – ξ surfaces of the critical eigenvalues as a function of PR and TLL ($P_1 = 0.3$ pu).

In summary, it can be observed that the CCI vs SM system is less robust with the increase of the power ratio and the electrical distance between the sources, and less stable than the VCI vs SM system. Regarding the proposed analysis, it should be highlighted that the method of stability surfaces is very flexible, and it can be employed considering different studies, e.g. stability analysis, tuning of controllers, etc.

2.6 Chapter conclusions

This chapter has investigated the stability of a two-source system composed of synchronous machines and PE-based sources in many configurations. The analysis of two-voltage source systems has focused on the frequency stability, considering a gradual replacement of the synchronous machines with inverters operating in VCI mode.

A theoretical approach to evaluate the frequency behaviour of the system was developed using the simplified models of the sources introduced in Chapter 1. With the obtained reduced order models, it was demonstrated that the system with one VCI and one SM shares the same foundations as the system with two synchronous machines, however, due to the flexibility of the VCI control, the VCI vs SM system displays a better frequency behaviour, with less pronounced frequency nadir and more damped oscillations between the sources.

Considering the variation of the principal parameters of the power system, the dynamics of the obtained models were confronted with those observed with their corresponding reference representations, establishing therefore the domain of representativeness of the reduced order models. Furthermore, from the aforementioned analysis, the main tendencies of the frequency to the variation of these parameters were observed and summarised in Table 2.8.

It was shown that the dominant frequency behaviour of the system fundamentally change with the replacement of the second synchronous machine by another VCI. The second order behaviour, which is characteristic of the dynamics of steam turbines, gives rise to first order dynamics in the VCI vs VCI system.

In the case of the CCI vs SM system, it was possible to establish similarities and differences with the VCI vs SM system with its reduced order model. However, since it disregards the grid, the representativeness domain of the model is very limited, and may not be suitable to perform stability analyses. Therefore, a method based on the linearised representation of the system was proposed in order to determine the stability limits of the system. In addition to the reduced flexibility of the CCI control, it was observed that the system is less robust when the inverter operates in this mode than when it operates in VCI mode.

The findings of this chapter will be used in the following chapter to determine the frequency behaviour of more complex systems. The concept of frequency oscillations between the sources will be divided into intra- or inter-area oscillations. However, independently of the classification, it will be demonstrated that the tendencies observed in this chapter are transposable to multi-source systems, regardless their complexity.

Chapter 3

Frequency dynamics assessment of interconnected power systems

Contents

3.1 Introduction

In Chapter 2, the frequency behaviour of a very simple system composed of two sources and one load has been investigated. Based on the classical methodology, it has been possible to establish some reduced order models which have been used to assess the evolution of the dominant and oscillating behaviours of the system in the case of the replacement of synchronous machines with PE-based sources operating either in VCI or CCI mode, and the impact of variations of the principal parameters of the power system.

In the case of large power systems, due to their increased complexity, the notion of dynamic analysis is expanded. In addition to the dominant and oscillatory frequencies already identified in Chapter 2, different groups of sources display different coherent frequency behaviours. These groups of sources compose the different areas of the system, and the coherent behaviour displayed by the sources of one area is called area frequency. The frequency oscillations between sources within a specific area are defined as intra-area oscillations, whereas the oscillations between two area frequencies are defined as inter-area oscillations.

The objective of this chapter is to verify whether or not the general tendencies obtained previously can be extended to larger systems. For this purpose, the well-known 2-area 4-generator system — i.e. the Kundur test system — is adopted, and, as previously, reduced order models of these systems are proposed for the analysis.

In order to facilitate the comprehension of the reader, Figure 3.1 illustrates a diagram of the different representations used in this chapter. For any multi-area multi-source system, a reference EMT model (A) and its linearised form (B), as well as a simplified model (C) are designed. These three models are capable of representing all three different frequency dynamics of the system: the frequencies of sources, areas and the centre of inertia.

Since the analyses of larger systems focus on the frequency behaviour at areas level, disregarding the specific behaviour of each source, from the simplified model, an aggregated model the system (D) is defined considering the aggregation of the coherent sources. It is emphasised that the aggregated model can be designed directly from the EMT model of the system, without passing first by its simplified model.

From the aggregated model, adopting the same hypotheses as in Chapter 2, it could also be possible to establish the dominant (E) and oscillating models (F) of the system. However, in the case of a two-area system, it is demonstrated that its aggregated model is equivalent to the simplified model of two-source systems, and therefore, the findings obtained with the latter are transposable for the former.

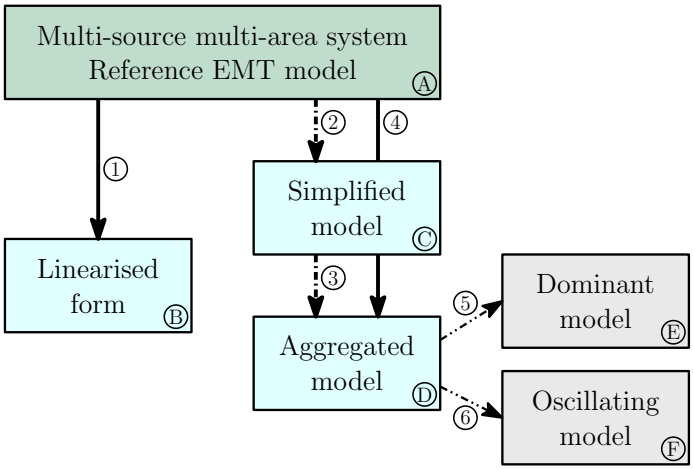

Figure 3.1 – Illustrative diagram of the representations which are used in this chapter.

3.2 The 2-area 4-generator system: the Kundur system with 100% of synchronous machines

The 2-area 4-generator system is chosen as case study in this chapter. According to [103], although small, the topology and parameters of the system are realistic, which make it very useful for some parametric studies. This system, popularly known as the Kundur system [52], is widely employed in the specialised literature, especially for the study of intra- and inter-area oscillations.

3.2.1 Description of the reference model of the system

The single line diagram of the Kundur system is illustrated in Figure 3.2. The network is composed of two symmetrical areas composed of two identical synchronous machines and a generic load, and connected through a weak tie line. As explained in Chapter 1, each synchronous machine is equipped with:

- an IEESGO power frequency governor and steam turbine, Figure 1.8,
- a ST1C static excitation system without transient reduction gain, Figure 1.10c,
- a PSS1A power system stabiliser, Figure 1.11.

The parameters adopted for the synchronous machines and regulators are given in Tables 1.2, 1.5, 1.7 and 1.9. The only difference between the synchronous machines of

both areas is their coefficient of inertia, in which, $H = 6.5$ s and $H = 6.175$ s for the SMs of area 1 and area 2, respectively. The design of the grid elements is realised as described in Section 2.2.1, and the adopted parameters are given in Table 1.1.

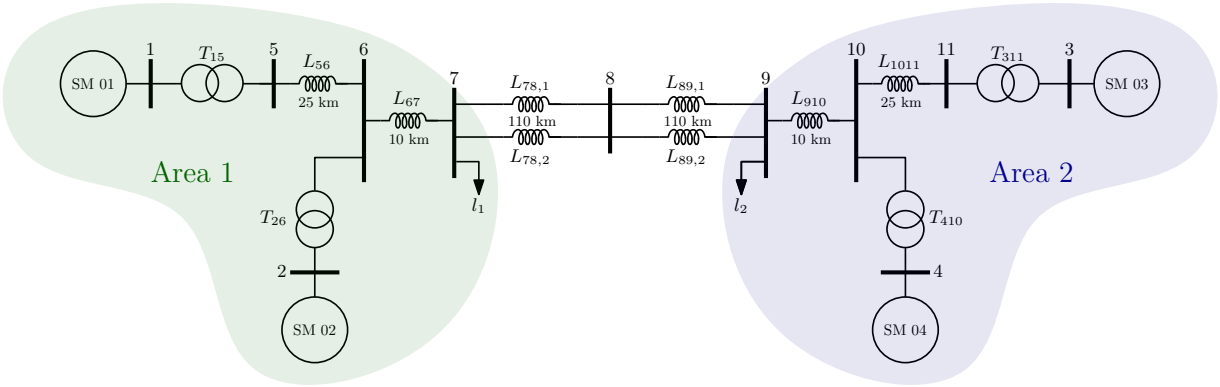

Figure 3.2 – Single line diagram of the Kundur system.

Similarly to the previous chapter, a linearised form of the reference model of the system is proposed to perform the analysis in the frequency domain. The dynamics of the reference representation of the system are described with 94 differential equations, and therefore 94 differential states:

- 22 for the grid:
  - two for $T_{15} + L_{56}$,
  - two for T_{26},
  - two for L_{67},
  - four for the l_1,
  - two for $(L_{78,1} + L_{89,1})//(L_{78,2} + L_{89,2})$,
  - two for $T_{311} + L_{1011}$,
  - two for T_{410},
  - two for L_{910},
  - four for the l_2.
- 18 of each generator:
  - eight of the synchronous machine: eqs. (1.1) to (1.6) and eq. (1.13),
  - five of the IEESGO: Figure 1.8,
  - one of the ST1C: Figure 1.10c,
  - four of the PSS1A: Figure 1.11.

Time domain simulations are performed in order to verify the compliance of the linearised form of the reference model of the system. As operating point, the active power produced in each area is around 1400 MW and their load consumptions are $S_{l1} = -996.7 + j200$ MVA and $S_{l2} = -1766.7 + j300$ MVA, respectively. The net exported power from area 1 to area 2 is $P_{exp} = 400$ MW. The power flow results are given in Table 3.1.

Table 3.1 – Power flow results.

Bus n°	**Bus type**	**V (pu)**	**θ (rad)**	**P (MW)**	**Q (MVar)**
SM n°1 (Bus 1)	Slack	1.03	0.000	722.7	174.6
SM n°2 (Bus 2)	PV	1.01	0.179	700.0	192.6
SM n°3 (Bus 3)	PV	1.03	0.512	700.0	161.1
SM n°4 (Bus 4)	PV	1.01	0.681	700.0	173.7
Load Area 1 (Bus 7)	PQ	0.97	0.443	−966.7	200.0
Load Area 2 (Bus 9)	PQ	0.98	0.942	−1766.7	300.0

As illustrated in Figure 3.3, it can be observed that the dynamics of the four sources obtained with both representations after a variation of the mechanical power of the synchronous machine connected to bus n° 1 ($\Delta P_{m0,1} = 0.05$ pu) are equivalent, validating the linearised representation of the reference model.

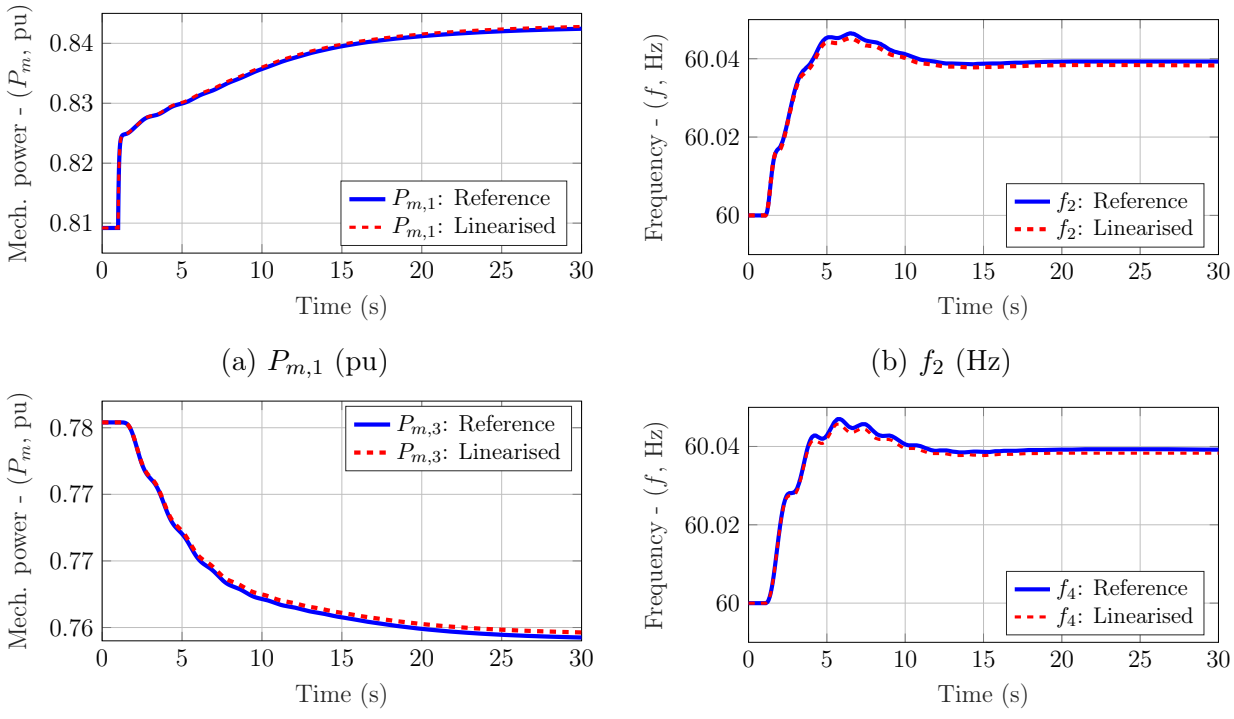

(a) $P_{m,1}$ (pu)

(b) f_2 (Hz)

(c) $P_{m,3}$ (pu)

(d) f_4 (Hz)

Figure 3.3 – Validation of the linearised form of the reference model of the Kundur system with four synchronous machines. Stimulus: $\Delta P_{m0,1} = 0.05$ pu.

3.2.2 Frequency behaviour of the system

In Chapter 2, following a system disturbance, it was observed that, despite the instantaneous frequencies of the voltage sources being different, the frequency behaviours displayed by these sources were coherent. This dominant behaviour displayed by the sources is the frequency of the Centre of Inertia of the system (COI frequency, ω_{coi}).

The same phenomenon can be observed in a multi-source system, however with a supplementary coherence level. Following a system disturbance, different groups of sources display different coherent frequency behaviours. In this case, these groups of sources compose the so-called "system areas", and the dominant behaviour displayed by the sources of one area is the area frequency (ω_a). As expressed in eq. (3.1), the frequency of an area k is computed as a function of the weighted average frequency of its n sources, using their coefficient of inertia (H) and the rated power (S_b) as weighting factor.

$$\omega_{ak} = \frac{\sum_{i=1}^{n} H_i S_i \omega_i}{\sum_{i=1}^{n} H_i S_i} \tag{3.1}$$

Different coherence methods can be employed in order to identify the group of sources composing the different areas of the system; refer to [104] for details on area identification methods. An example of identification of areas based on analysis of the eigenvalues of the system is illustrated further in this section.

Similarly to sources, the instantaneous frequencies of the system areas are different, however, also displaying a coherence between them. The dominant behaviour displayed by the areas — and therefore displayed by all m sources of the system — is the COI frequency, which is computed as expressed in eq. (3.2).

$$\omega_{coi} = \frac{\sum_{i=1}^{m} H_i S_i \omega_i}{\sum_{i=1}^{m} H_i S_i} \tag{3.2}$$

The frequency oscillations between the sources of a specific area are defined as intra-area oscillations, whereas the oscillations between two area frequencies are defined as inter-area oscillations.

In the case of the Kundur system, as described in Section 3.2.1, it is composed of

two areas with two synchronous machines in each area. The frequency behaviour of the system is firstly verified in the frequency domain. The main dependencies between the electromechanical states and the eigenvalues of the Kundur system is illustrated in Figure 3.4, and the eigenvalues related to the frequency behaviour of the system are summarised in Table 3.2. The following can be observed:

- The eigenvalues $\lambda_{13,14}$ have a direct relationship to the frequency of all synchronous machines (all $\Delta\omega$). As already observed in Section 2.2.2.2, the slow dynamics and high damping ratio illustrate the characteristics of steam turbines, indicating that $\lambda_{13,14}$ describe the dominant frequency behaviour of all the system, i.e. the COI frequency. These eigenvalues are hereinafter referred to as λ_{dom}.

- The eigenvalues $\lambda_{19,20}$ are only dependent of the electromechanical states of synchronous machines 1 and 2. Since their damping is around 30%, they are oscillating eigenvalues, illustrating the intra-area oscillations of area 1. The same can be concluded for $\lambda_{21,22}$ for area 2. These eigenvalues are hereinafter referred to as λ_{a1} and λ_{a2}, respectively.

- The eigenvalues $\lambda_{11,12}$ also illustrates the characteristics of an oscillating frequency behaviour, however, they are dependent to all electromechanical states of the system. Therefore they describe the oscillating frequency behaviour between the synchronous machines of areas 1 and 2. These eigenvalues are hereinafter referred to as λ_{osc}.

- From Table 3.2, it can be observed that the frequency of the inter-area oscillations is smaller than those of intra-area oscillations, which is indeed a well-known characteristic of synchronous machine-based systems [52], [103].

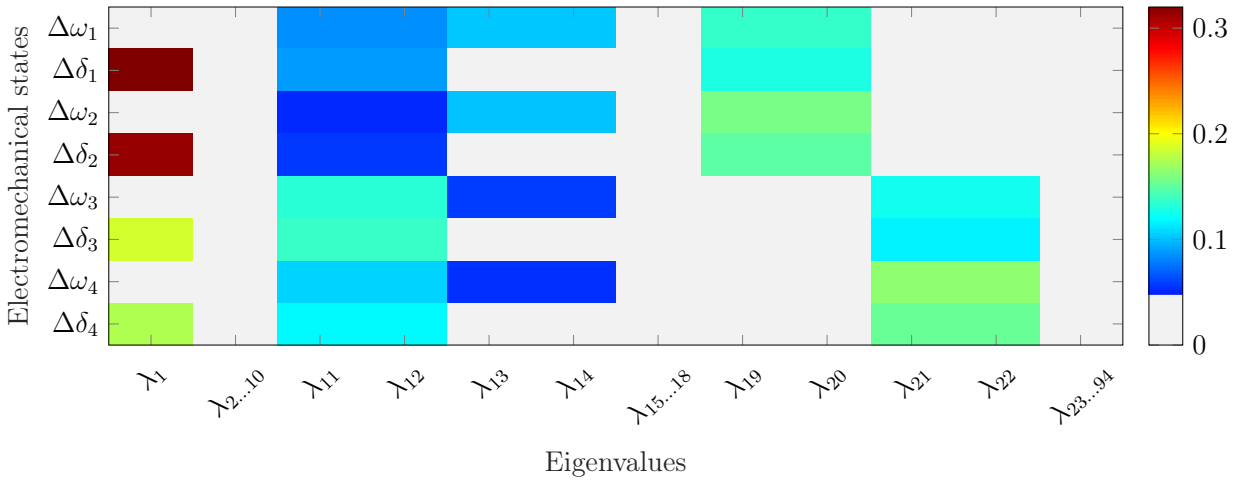

Figure 3.4 – Main dependencies between the electromechanical states and the eigenvalues of the Kundur system (participation factor matrix).

Table 3.2 – Summary of the electromechanical eigenvalues.

	Eigenvalues ($\sigma \pm j\omega_d$)	**Damping ratio** (ξ, %)	**Damped frequency** (f_d, **Hz**)
$\lambda_{\mathbf{11,12}}(\lambda_{\mathbf{osc}})$	$-0.31 \pm j3.70$	8.31	0.59
$\lambda_{\mathbf{13,14}}(\lambda_{\mathbf{dom}})$	$-0.32 \pm j0.39$	62.83	0.06
$\lambda_{\mathbf{19,20}}(\lambda_{\mathbf{a1}})$	$-2.28 \pm j7.22$	30.07	1.15
$\lambda_{\mathbf{21,22}}(\lambda_{\mathbf{a2}})$	$-2.47 \pm j7.49$	31.37	1.19

The frequency behaviour of the system is also illustrated in time domain in Figure 3.5. For this purpose, it is applied a load step at area 1 ($\Delta P_{l1} = 0.1$ pu), considering the same operating point given in Section 3.2.1. Based on these results, the following can be observed:

- A coherence between the frequencies of synchronous machines 1 and 2 is observed in Figure 3.5a. The same is observed between the frequencies of synchronous machines 3 and 4.
- Figure 3.5b illustrates the frequency of each area and the COI frequency, computed using eqs. (3.1) and (3.2), respectively. The frequencies f_{a1} and f_{a2} well represent the dynamics of the sources composing each area, whereas f_{coi} gives the dominant frequency behaviour of the system.
- The oscillations between the sources of each area and the inter-area are observed in Figures 3.5c to 3.5e. However, since the dynamics of the inter-area oscillations are the slowest between the electromechanical eigenvalues, and the damping of the intra-area oscillations is higher, the dynamics of the intra-area oscillations can barely be observed in the first swing of Figures 3.5c and 3.5d.

3.2.3 Methodology employed for the design of reduced order models

In this section, based on Section 2.2.2, reduced order models of the Kundur system are proposed to observe the frequency behaviour of the system. Similarly to the two-voltage source system, the first level of simplification is designed using an association of the $E'X'H$ model of the synchronous machines with their power frequency regulators and a quasi static representation of the grid. From the aggregation of the coherent sources of each area, a second level of simplification is proposed to analyse the frequency behaviour of the system considering the area level. It is demonstrated that this representation is akin to the simplified model of the two-synchronous machine system of Section 2.2.2.1, and therefore, the findings observed with the latter can be applied to the Kundur system.

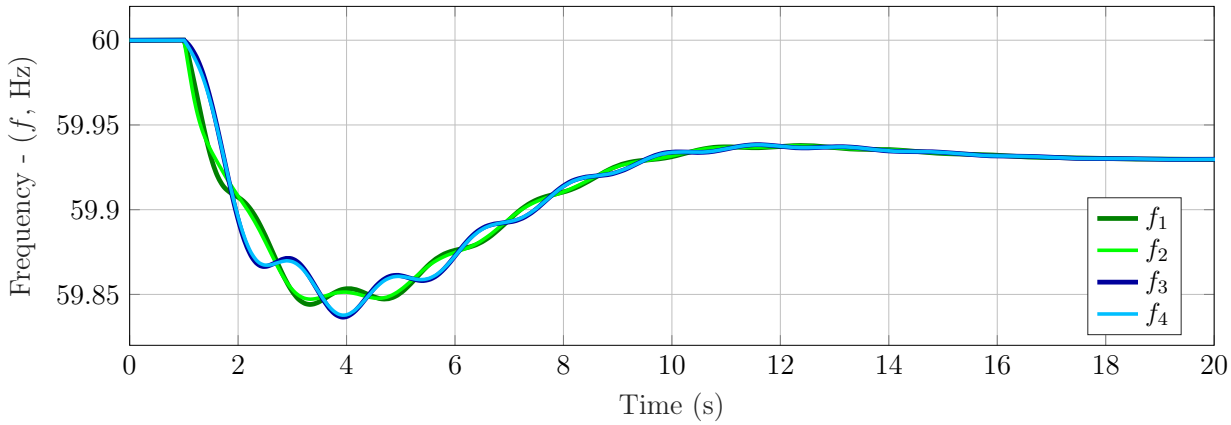

(a) $f_{1...4}$ (Hz)

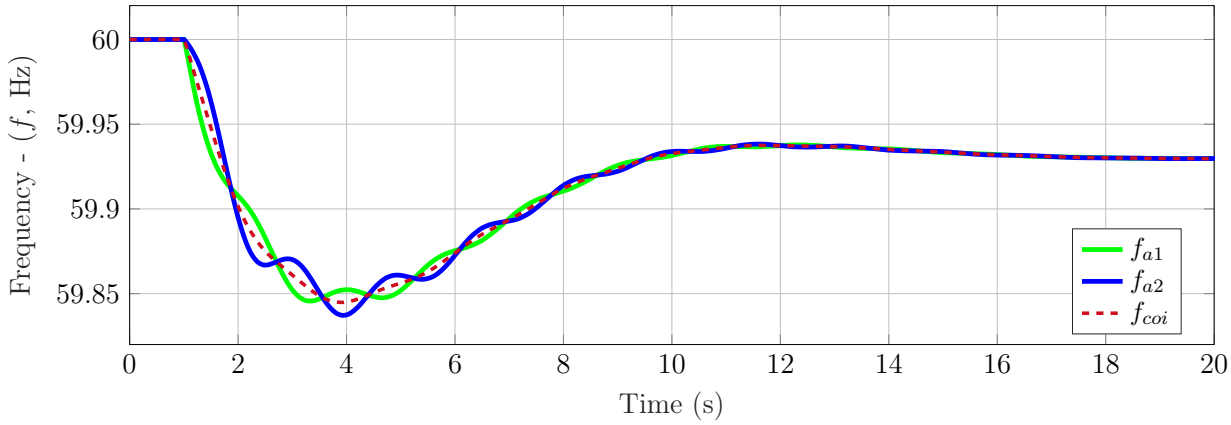

(b) f_{a1}, f_{a2}, f_{coi} (Hz)

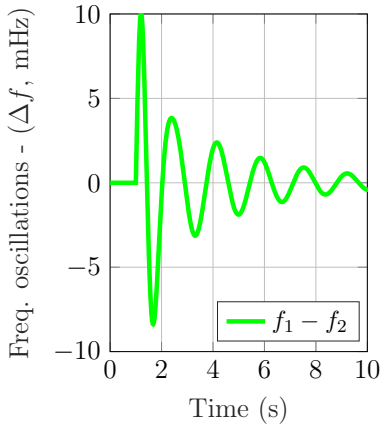

(c) $f_1 - f_2$ (mHz)

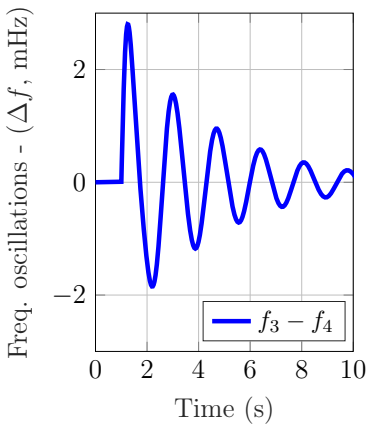

(d) $f_3 - f_4$ (mHz)

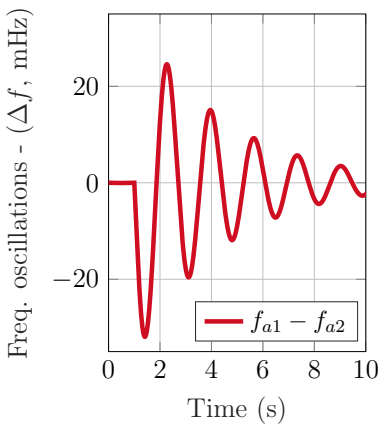

(e) $f_{a1} - f_{a2}$ (mHz)

Figure 3.5 – Frequency behaviour of the Kundur system after a load step $\Delta P_{l1} = 0.1$ pu.

3.2.3.1 The simplified model of the system

As illustrated in Figure 3.6, the simplified model of the reference representation of the Kundur system is designed considering all generators and a quasi static representation of the grid. In this representation, the order of the system is reduced from 96 to 28 — seven differential equations per generator — and yet it is capable of representing all three different frequency dynamics of the system: the frequencies of sources, areas and the centre of inertia.

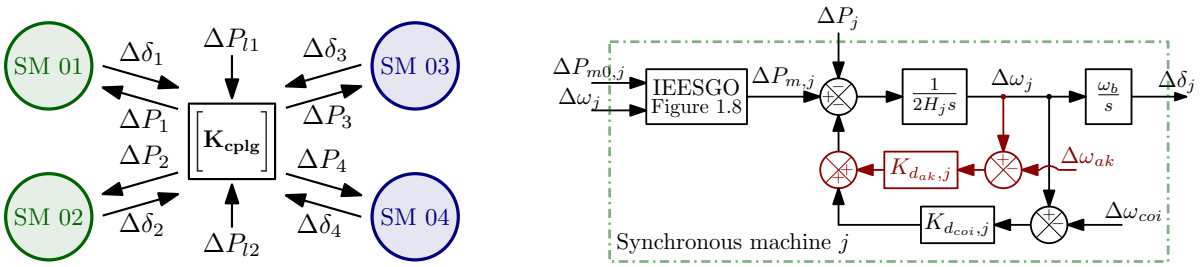

(a) Illustration of the simplified model (b) Modified SM representation

Figure 3.6 – Simplified model of the Kundur system considering all generators.

It can be observed that the construction of this model shares same fundamentals employed in the design of that of the two-voltage source system in Section 2.2.2.1, however, as illustrated in Figure 3.6b, with an important adaptation on the synchronous machine representation.

It has been emphasised in Chapter 1 that, in order to compensate the lack of damping due to simplifying hypotheses, the damping factor of the simplified model of synchronous machines represents a combination of different damping effects of the system. In Chapter 2, since the frequency of the system is variable, the damping power provided by a synchronous machine is proportional to the difference between its frequency and that of the grid (ω_{coi}).

In the case of a multi-area system, a synchronous machine provides a damping power to damp both intra- and inter-area oscillations. As illustrated in Figure 3.6b, a perfect decoupling between intra- and inter-area oscillations is considered. Therefore, a synchronous machine j provides damping powers proportional to $\omega_j - \omega_{ak}$ and to $\omega_j - \omega_{coi}$ to intra- and inter-area oscillations, respectively. The frequencies ω_{ak} and ω_{coi} of the simplified model are also computed using eqs. (3.1) and (3.2).

Similarly to the previous chapter, the parameters $K_{d_{ak}}$ and $K_{d_{coi}}$ are estimated in order to reasonably represent the damping of intra- and inter-area oscillations the system. It is emphasised that the topology of the Kundur system inside an area and between areas is equivalent to that of the two-source system addressed in Chapter 2. Furthermore, the electrical distances between the sources in the same area, and between the sources in different areas are equivalent to those analysed in Section 2.2. Therefore, the values of $K_{d_{ak}}$ and $K_{d_{coi}}$

adopted for the synchronous machines of the Kundur system are equivalent to those of K_d adopted for TLL equal to 25 and 125 km, respectively.

The other parameters adopted for the simplified model are the same as those of the reference model of the system. The quasi static model of the grid is computed as presented in Appendix D. The size of the resulting $\mathbf{K_{cplg}}$ is 4-by-6. The sub-matrices of synchronising torque ($\mathbf{K_s}$) and of initial power sharing between the voltage sources ($\mathbf{K_{ps}}$) are 4-by-4 and 4-by-2, respectively.

A comparison between the eigenvalues obtained with the reference and the simplified representations of the system are illustrated in Figure 3.7, and the eigenvalues related to the frequency behaviour of the system are summarised in Table 3.3. In addition, Figure 3.8 illustrates the three different frequency dynamics which can be obtained with the simplified model.

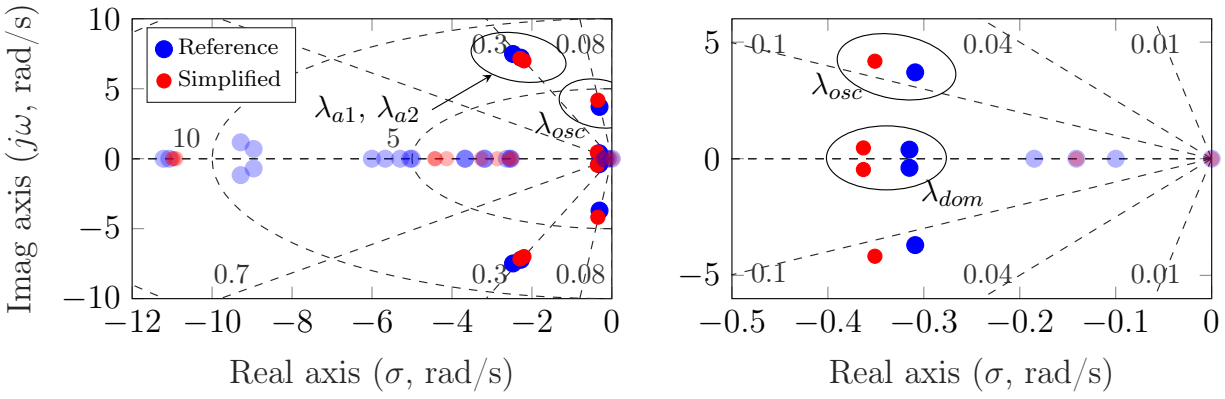

Figure 3.7 – Comparison of the eigenvalues map of the reference and simplified representations of the Kundur system (magnified view at the subject of interest).

Table 3.3 – Summary of the eigenvalues related to the frequency behaviour of the system.

	Reference			**Simplified**		
	Eigenvalues ($\sigma \pm j\omega_d$)	**Damping** (ξ, %)	**Frequency** (f_d, **Hz**)	**Eigenvalues** ($\sigma \pm j\omega_d$)	**Damping** (ξ, %)	**Frequency** (f_d, **Hz**)
$\lambda_{\mathbf{dom}}$	$-0.32 \pm j0.39$	62.83	0.06	$-0.36 \pm j0.46$	61.70	0.07
$\lambda_{\mathbf{a1}}$	$-2.28 \pm j7.22$	30.07	1.15	$-2.20 \pm j6.99$	30.00	1.11
$\lambda_{\mathbf{a2}}$	$-2.47 \pm j7.49$	31.37	1.19	$-2.30 \pm j7.17$	30.55	1.14
$\lambda_{\mathbf{osc}}$	$-0.31 \pm j3.70$	8.31	0.59	$-0.35 \pm j4.18$	8.37	0.67

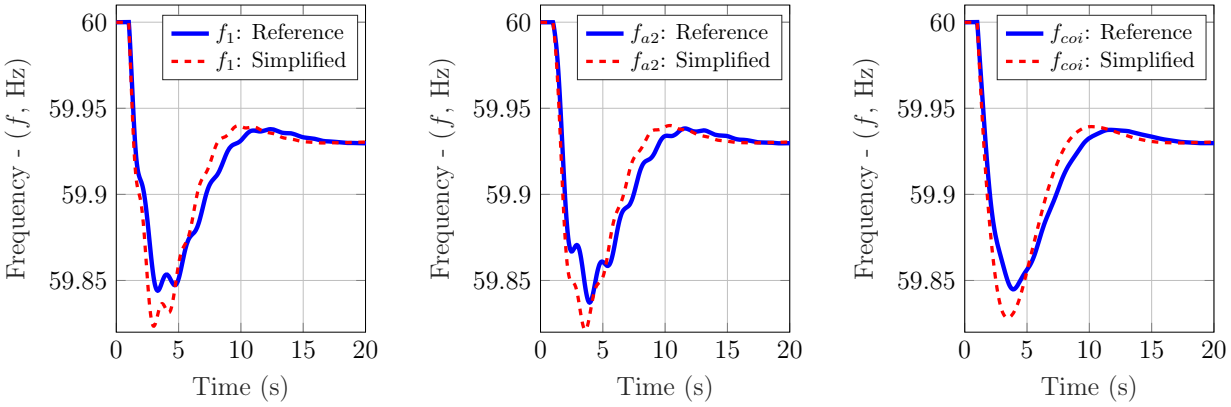

(a) f_1 (Hz) (b) f_{a2} (Hz) (c) f_{coi} (Hz)

Figure 3.8 – Frequency behaviour of the system obtained with both reference and simplified representations after a load step $\Delta P_{l1} = 0.1$ pu.

It can be observed that the simplified model can fairly estimate the eigenvalues related to the frequency behaviour, presenting some deviations when compared with those of the reference model of the system. Despite the deviations, a considerable consistency between the dynamics of both models can be observed in time domain simulations, verifying the capability of the simplified model to provide tendencies about the evolution of the frequency behaviour of the system.

3.2.3.2 Aggregated representation of the synchronous machines of each area

When dealing with the analysis of big systems with many generators, e.g. the European power system, focus is usually applied to the frequency behaviour at areas level, disregarding the specific behaviour of each source in the system. Therefore, despite displaying good accuracy, the simplified model proposed in Section 3.2.3.1 can quickly become inconvenient for this kind of analysis.

Using the reduction techniques introduced in Section 2.2.2, a second level of simplification is proposed in this section. In this representation, each coherent group of generators is aggregated into a single equivalent unit connected to the centre of inertia of the respective area [52], [101], [104]. As result, the system is designed as two areas interconnected through a quasi static representation of the grid, and therefore, it is not capable of representing intra-area dynamics.

As observed in Figure 3.4, the synchronous machines of area 2 do not have a significant impact on the oscillating frequency behaviour inside area 1. Therefore, for the analysis of the intra-area oscillating frequency behaviour of area 1, the original system can be reduced as displayed in Figure 3.9a (similar to Figure 2.1).

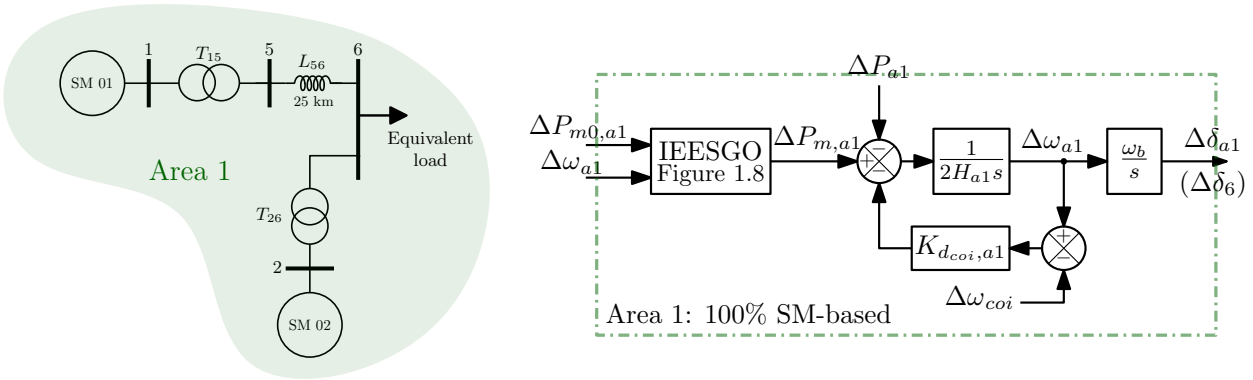

(a) Equivalent of area 1 (b) Simplified area representation

Figure 3.9 – Equivalent single line diagram of area 1 of the Kundur system used to perform intra-area analyses and its simplified aggregated representation employed in inter-area studies.

At the area level, it can be assumed that synchronous machines 1 and 2 display the area frequency (ω_{a1}), neglecting the intra-area oscillations. Therefore, similarly to the model of Figure 2.6, the synchronous machines and their regulators can be aggregated as illustrated in Figure 3.9b. The equivalent inertia (H_{a1}) and power frequency characteristic ($K_{p,a1}$) of the simplified area representation are composites of the parameters of both sources. Regarding the damping, since $\Delta\omega_1 = \Delta\omega_2 = \Delta\omega_{a1}$, $K_{d_{a1},1}$ and $K_{d_{a1},2}$ are neglected, however $K_{d_{coi},1}$ and $K_{d_{coi},2}$ are combined to represent the equivalent damping factor of the area to inter-area oscillations ($K_{d_{coi},a1}$). As a simplifying hypothesis, the asymmetry of the system of Figure 3.9a is neglected, considering that the point of common coupling (bus 6) is the centre of inertia of the area.

The same is made for area 2, resulting into two equivalent areas connected to buses 6 and 9. The quasi static model of the grid is computed as before, however, it is emphasised that, due to the aggregation of the sources into areas, the buses 1 to 5 and 11 have been neglected. The size of the resulting $\mathbf{K}'_{\mathbf{cplg}}$ is 2-by-4. Both sub-matrices of synchronising torque ($\mathbf{K_s}$) and of initial power sharing between the voltage sources ($\mathbf{K_{ps}}$) are 2-by-2.

Figure 3.10 illustrates the simplified model of the Kundur system considering the aggregated representations of the coherent synchronous machines, which is hereinafter referred to as Aggregated Model of the system. In this representation, the order of the system is reduced from 96 to 14, being seven differential equations per area. As mentioned previously, only the frequencies of areas and the centre of inertia are represented with this model.

It is emphasised that the aggregated model of the Kundur system is completely equivalent to the simplified model of a two-synchronous machine system analysed in Section 2.2, and consequently, the observations and findings from the latter are completely transposable to the former.

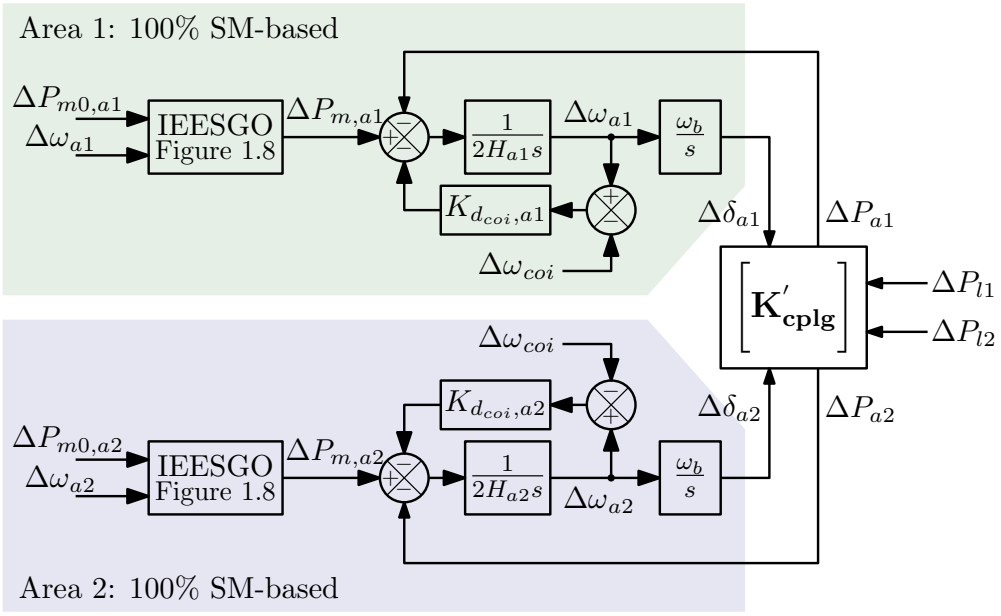

Figure 3.10 – Aggregated model of the Kundur system.

The eigenvalues obtained with all three representations of the system are illustrated in Figure 3.11. Table 3.4 summarises the eigenvalues related to the frequency behaviour of the reference and aggregated models for a detailed comparison.

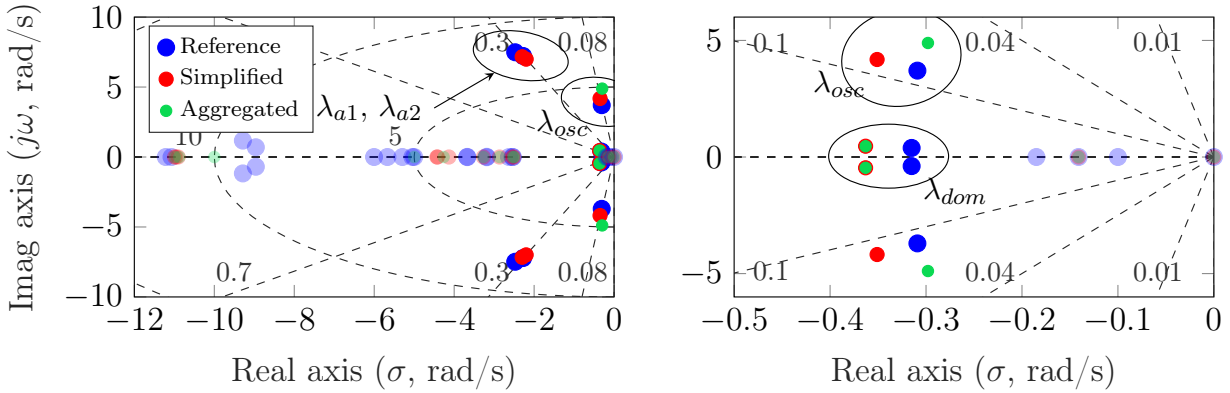

Figure 3.11 – Comparison of the eigenvalues map of all representations of the Kundur system (magnified view at the subject of interest).

It can be observed that λ_{dom} obtained with the aggregated model are same as those obtained with the simplified model, which is a fair representation of the reference model of the system. Regarding λ_{osc}, it can be observed that the damping ratio and frequency of the eigenvalues obtained with the aggregated model respectively are slightly under and overestimated, however they are relatively close to those obtained with other representations, which can be considered as a good estimation given the high level of simplification of the system.

Table 3.4 – Summary of the eigenvalues related to the frequency behaviour of the system.

	Reference			**Aggregated**		
	Eigenvalues ($\sigma \pm j\omega_d$)	**Damping** (ξ, %)	**Frequency** (f_d, **Hz**)	**Eigenvalues** ($\sigma \pm j\omega_d$)	**Damping** (ξ, %)	**Frequency** (f_d, **Hz**)
$\lambda_{\mathbf{dom}}$	$-0.32 \pm j0.39$	62.83	0.06	$-0.36 \pm j0.46$	61.70	0.07
$\lambda_{\mathbf{a1}}$	$-2.28 \pm j7.22$	30.07	1.15	—	—	—
$\lambda_{\mathbf{a2}}$	$-2.47 \pm j7.49$	31.37	1.19	—	—	—
$\lambda_{\mathbf{osc}}$	$-0.31 \pm j3.70$	8.31	0.59	$-0.30 \pm j4.89$	6.08	0.77

As illustrated in Figure 3.12, the frequency dynamics displayed by the aggregated model are similar to those observed with the simplified model. Despite some deviations, both simplified and aggregated model, fairly illustrate the overall frequency behaviour obtained of the reference model of the system, and therefore, they can be employed in many types of preliminary analyses.

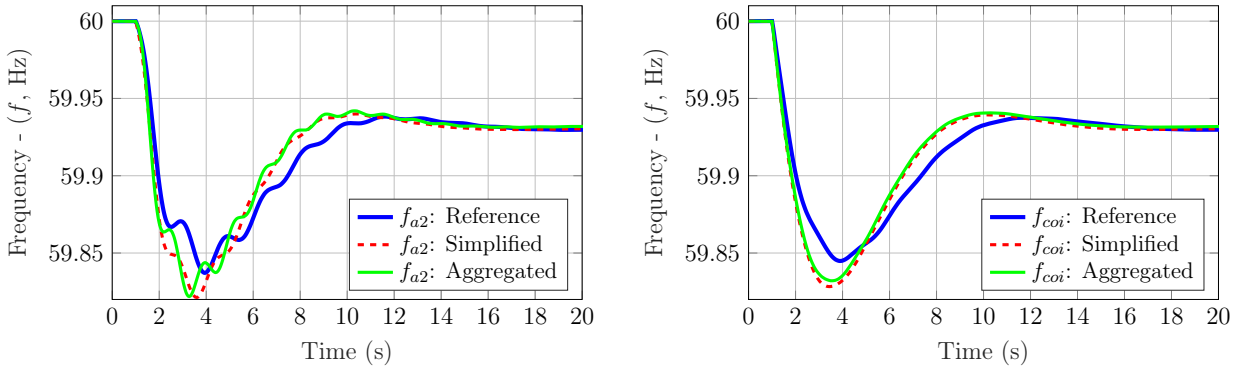

(a) f_{a2} (Hz) (b) f_{coi} (Hz)

Figure 3.12 – Frequency behaviour obtained with all representations of the system after a load step $\Delta P_{l1} = 0.1$ pu.

3.2.4 Considerations about the aggregated model of the system

This section has presented a methodology used to design the Kundur system using the concept of aggregated sources. Using a step-by-approach, a first level of simplification reduced the order of the system from 96 to 28 by representing the synchronous machines as an association of $E'X'H$ models with their power frequency regulators and a quasi static representation of the grid. By aggregating the sources of each area into a single equivalent unit, the order of the system was reduced to 14, and the last level of simplification used in this chapter was obtained: two equivalent areas connected to a quasi static representation of the grid.

It is emphasised that the aggregated model of the Kundur system (Figure 3.10) presents a high similarity with the simplified model of the SM vs SM system of Figure 2.3, and therefore, the findings obtained with the analysis of the dominant and oscillating frequency behaviour of the latter can be used to obtain practical interpretations of the frequency behaviour of the former.

In the next section, it will be demonstrated that the aforementioned analogy is not exclusive of 100% SM-based systems, being valid when one or multiple synchronous machines are replaced with PE-based sources.

3.3 Introduction of PE-based sources in the Kundur system

The following analysis considers that the synchronous machines of area 2 are gradually replaced with PE-based sources either in VCI or CCI mode. At first, only the synchronous machine connected to bus n° 3 is replaced, illustrating the adaptations required to represent the simplified area model. The replacement of the second synchronous machine of area 2 results in a 100% PE-based area. In both cases, it is demonstrated that the resulting system displays similarities with those analysed in Chapter 2, and that the tendencies obtained — and summarised in Table 2.8 — with a two-source system can also be observed in the frequency behaviour of the Kundur system.

In this section, the focus is put on the overall frequency dynamics of the system, observing just the frequency behaviour of the areas and the interactions between them, and therefore, disregarding the frequency behaviour of each source. Therefore, only the reference and aggregated models of the system will be analysed.

3.3.1 Replacement of a SM with a PE-based source: the VCI case

3.3.1.1 Description of the studied system: the reference model

In this configuration, the synchronous machine connected to bus n° 3 is replaced with a PE-based source in VCI mode. As in Section 2.3.1, the inverter is represented with an average model, an ideal voltage source is used to represent the dc side of the source, and an LC filter interfaces it with the ac grid. The controls are implemented using cascaded voltage and current loops, and the VCI-B synchronisation strategy. The parameters of the VCI are given in Table 1.11 and Table 1.12, and the remaining parameters of the system are the

same. The linearised form of the model is described with 90 differential equations, being 14 for the VCI; refer to Section 2.3.1. The linearised form of the system has been validated as previously, and, considering that the principle has been already well established, it will not further be displayed.

3.3.1.2 The aggregated model of the system

As introduced in Section 3.2.3.2, the simplified representation of an area is determined from the aggregation of the coherent sources into an equivalent unit, i.e. designing the dominant model of the area. Similarly to the configuration of Section 2.3.2.2, area 2 is composed of one VCI and one synchronous machine, however, the inter-area damping factor must be considered in this case. Therefore, in order to define the aggregated model of the system, the simplified representation of area 2 might to be re-established.

The simplified representations of the sources composing area 2 are illustrated in Figure 3.13. As explained in Section 3.2.3.1, the simplified model of synchronous machines adapted for multi-area systems is designed with two damping channels to damp intra- and inter-area oscillations.

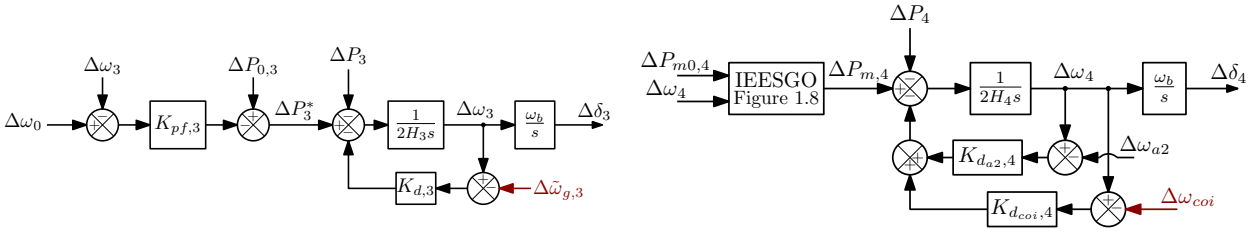

(a) VCI (bus n° 3) (b) SM (bus n° 4)

Figure 3.13 – Simplified representations of the sources of area 2.

As introduced in Section 1.3.1.1, the damping power provided by the VCI is implemented considering the mismatch between its frequency and that of the adjacent bus (bus 11). The latter is estimated as given in eq. (3.3).

$$\Delta\tilde{\omega}_{g,3} = \Delta\omega_3 - \frac{s}{\tau_e s + 1}\frac{\Delta P_3}{\omega_b K_e} \tag{3.3}$$

As in Section 2.3.2.2, in order to aggregate both sources, it is considered that their frequencies are the same, i.e. $\Delta\omega_3 = \Delta\omega_4 = \Delta\omega_{a2}$. The equivalent inertia of the area can be represented as a composite of both sources, and its power frequency control chain can be designed using two parallel channels. However, the damping factor of the area cannot be represented as a composite of $K_{d,3}$ and $K_{d_{coi},4}$.

It is emphasised that $\Delta\tilde{\omega}_{g,3}$ carries a much precise information about the frequency perceived by the VCI than ω_{coi}, and consequently the hypothesis $\Delta\tilde{\omega}_{g,3} = \omega_{coi}$ should not be considered in the design of the simplified area model. Therefore, the equivalent damping power of area 2 is represented as the sum of the damping powers provided by the VCI and the SM, respectively proportional to $\Delta\omega_{a2} - \Delta\tilde{\omega}_{g,3}$ and to $\Delta\omega_{a2} - \Delta\omega_{coi}$.

However, in order to correctly represent the damping power provided by the VCI, since the signal ΔP_3 is not available, it must be replaced with the corresponding initial power sharing fraction of the VCI in eq. (3.3). As a simplifying hypothesis, the asymmetry of the area is neglected, and it is considered an equitable load sharing between the VCI and the synchronous machine. Therefore:

$$\Delta\tilde{\omega}_{g,3} = \Delta\omega_{a2} - \frac{s}{\tau_e s + 1}\frac{0.5\Delta P_{a2}}{\omega_b K_e} \tag{3.4}$$

The aggregated model of the system is illustrated in Figure 3.14. The matrix $\mathbf{K'_{cplg}}$ is computed as previous, and similarly to the representation with 100% of synchronous machines, the system is of 14^{th} order.

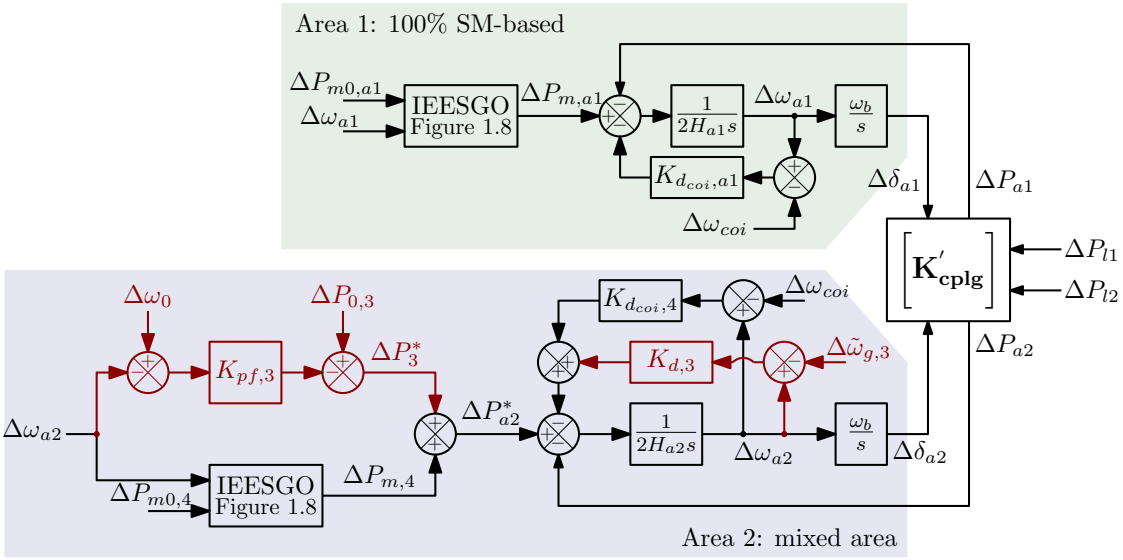

Figure 3.14 – Aggregated model of the Kundur system with mixed areas. Area 2 is composed of one synchronous machine and one VCI.

3.3.1.3 Expected behaviour and comparison with the reference system

In this section, it is observed whether or not the expected tendencies obtained with the analysis of the VCI vs synchronous machine system in Section 2.3 are transposable for

the Kundur system, and whether or not its aggregated model provides good estimations of the frequency behaviour of the system. For this purpose, the same operating point used in Section 3.2.1 is considered. Both the power frequency characteristics and the inertial effect of the VCI are equivalent to those of the replaced synchronous machine, i.e. $K_{pf,3} = -25$ pu and $H_3 = 6.175$ s.

From the observations summarised in Table 2.8, a frequency behaviour enhancement is expected. As explained in Section 2.3.2.2, the power frequency control chain of a VCI is equivalent to the high pressure stage of a steam turbine, increasing the amount of power which is instantaneously released due to frequency variations, and therefore, resulting in a more damped ω_{coi}. Regarding the oscillating frequency behaviour, as explained in Section 2.3.2.3, since the damping factor of the VCI is higher than that of the replaced synchronous machine, the frequency oscillations — both intra- and inter-area — are more damped.

Figure 3.15 compares the frequency behaviour of the VCI case of the Kundur system with that obtained with the original system with 100% of synchronous machines. The aforementioned expected tendencies can be observed in the dominant frequency behaviour of area 2 and the inter-area oscillations. Further analyses about the evolution of the frequency behaviour of the system due to the replacement of synchronous machines by PE-based sources are realised in Section 3.3.3.1.

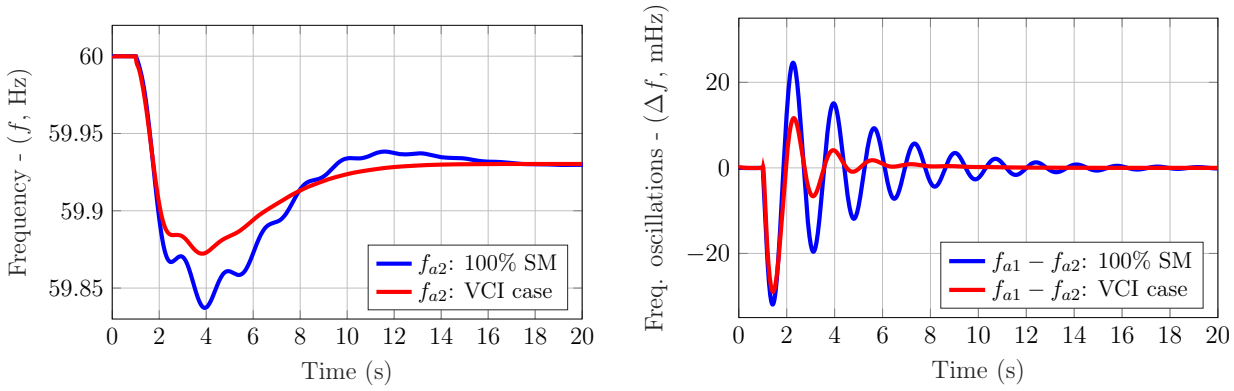

(a) f_{a2} (Hz) (b) $f_{a1} - f_{a2}$ (mHz)

Figure 3.15 – Impact of the replacement of the synchronous machine of bus n° 3 with a VCI on the frequency behaviour of the Kundur system.

The representativeness of the aggregated model of the system is verified in Figure 3.16 by comparing the trajectories of λ_{dom} and λ_{osc} obtained with both reference and aggregated model of the system due to the variation of the inertial effect of the VCI from 0.5 to 6.175 s.

It can be observed that λ_{osc} of both reference and aggregated models display the same tendency, with the increase of H_3, λ_{osc} become more damped. However, these eigenvalues present a higher sensibility to the variation of H_3 in the aggregated model of the system.

Furthermore, the frequency of the inter-area oscillations are slightly overestimated in the aggregated model for all range of H_3.

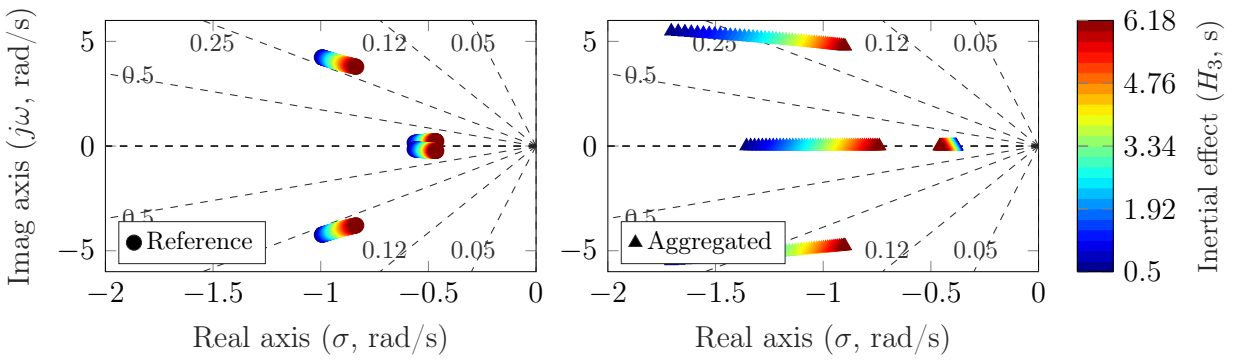

Figure 3.16 – Comparison of the trajectories of the dominant and the oscillating eigenvalues obtained with the reference and aggregated models of the VCI case of the Kundur system. Variation of the inertial effect of the VCI.

Regarding λ_{dom}, it can be observed that the slowest eigenvalue in the aggregated model is at the same surroundings of the eigenvalues of the reference model, however, they display different tendencies. With the increase of H_3, λ_{dom} become continuously slower in the reference model, whereas the slowest eigenvalue in the aggregated model becomes continuously faster, indicating a misrepresentation of the evolution of the dominant frequency behaviour of the system.

In order to observe the impact of this misrepresentation, the frequency behaviour obtained with both reference and aggregated models are compared in Figure 3.17. It can be observed that, despite some deviations, the overall frequency behaviour of the reference model is satisfactorily represented by the aggregated model of the system, and therefore, the latter can be employed on preliminary studies about the impact of the insertion of VCIs on the power system.

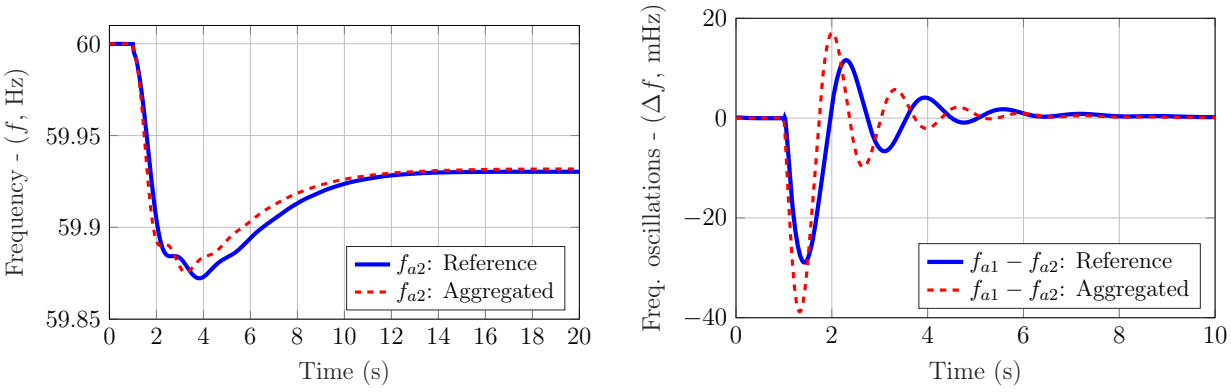

(a) f_{a2} (Hz); $H_3 = 6.175$ s

(b) $f_{a1} - f_{a2}$ (mHz); $H_3 = 6.175$ s

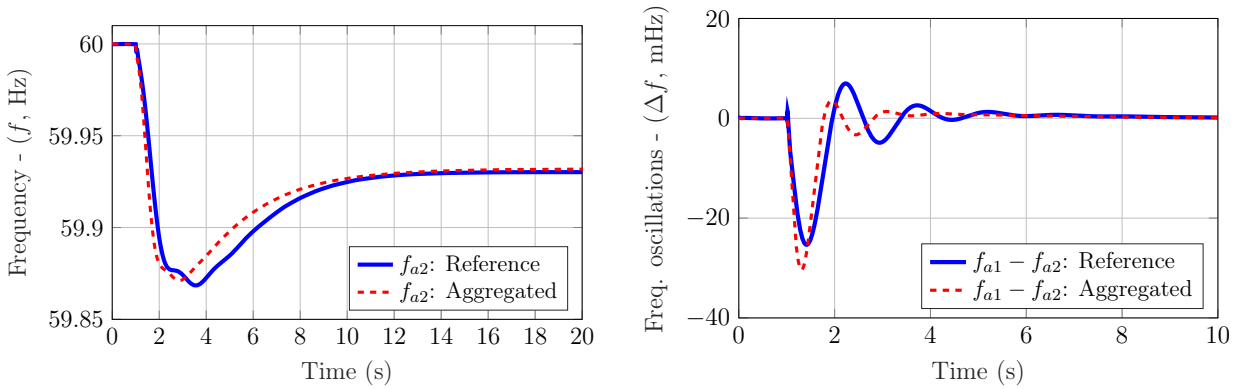

(c) f_{a2} (Hz); $H_3 = 0.5$ s (d) $f_{a1} - f_{a2}$ (mHz); $H_3 = 0.5$ s

Figure 3.17 – Comparison of the frequency behaviour obtained with the reference and aggregated models of the VCI case of the Kundur system.

3.3.2 Replacement of a SM with a PE-based source: the CCI case

3.3.2.1 The reference and aggregated models of the system

The synchronous machine connected to the bus n° 3 can also be replaced with a PE-based source in CCI mode. It is emphasised that, as introduced in Section 1.3.2.3, the power interface of the PE-based source is the same as that used in the previous configuration, and the parameters adopted for the CCI strategy are given in Table 1.15. The linearised form of the reference model of the system is described with 89 differential equations, being 13 for the CCI; refer to Section 2.5.3.

The aggregated model of the system is designed as in previous configurations, aggregating the sources of each area into an equivalent generator. As introduced in Section 2.5.2, the dominant model of the association between a CCI and a synchronous machine is structurally equivalent to that of the association between a VCI and a synchronous machine, although the equivalent inertia of the model is only composed of the coefficient of inertia of the synchronous machine. However, as introduced Section 2.5.3, it is only possible to establish an association between a CCI and a synchronous machine if no stability issue is identified. In this case, the configuration of area 2 is equivalent to the system of Section 2.5 when TLL = 25 km, and, *a priori*, the sources can be aggregated.

The aggregated model of the Kundur system with a CCI is similar to that of Figure 3.14, however, the CCI does not provide any damping power to the frequency oscillations of the system, and the equivalent inertia of area 2 is only composed of the coefficient of inertia of the synchronous machine connected to the bus n° 4, i.e. $H_{a2} = H_4$. The aggregated model is represented as illustrated in Figure 3.18. Similarly to previous representations, the system

is of 14$^{\text{th}}$ order. The parameters of the aggregated model are the same as the reference representation of the system, and the matrix $\mathbf{K}'_{\mathbf{cplg}}$ is the same as that of the VCI case.

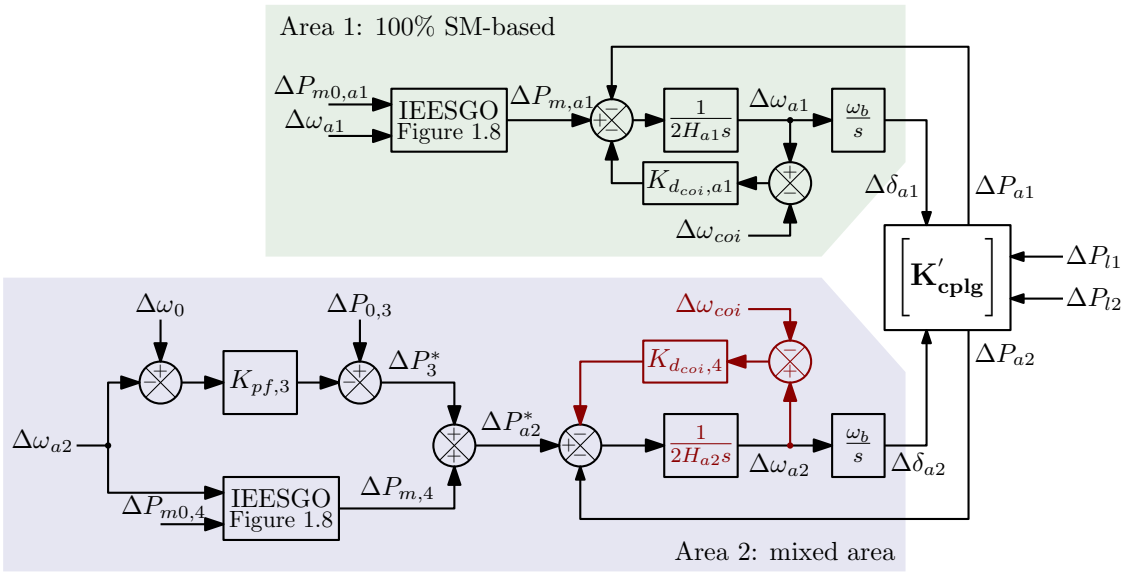

Figure 3.18 – Aggregated model of the Kundur system with mixed areas. Area 2 is composed of one synchronous machine and one CCI.

3.3.2.2 Expected behaviour and comparison with the VCI case

It is undeniable that the behaviour of the sources inside of area 2 is different whether the PE-based source operates in CCI or in VCI mode. However, in a macroscopic view of the system, it is possible to establish some similarities between the structures of Figures 3.14 and 3.18, especially when their parameters are equivalent.

Since the power frequency control chains of Figures 3.14 and 3.18 are equivalents, the dynamics of ω_{a2} displayed in the CCI case of the Kundur system should be similar to that of the VCI case when the inertial effect of the VCI is low. Due to the reduced inertia of area 2, the inter-area oscillations of the CCI case are more damped than those observed with the original Kundur system with 100% of synchronous machines. Furthermore, it has been shown in [33] that the damping power provided by the VCI does not present a consequent impact on the damping of power oscillations when the inertial effect of the VCI is low. Therefore, despite the absence of damping provided by the CCI, the inter-area oscillations observed in the CCI case of the Kundur system should be similar to those of the VCI case when the inertial effect provided by the VCI is low.

The frequency behaviour obtained with the CCI case is compared with that of the VCI case in Figure 3.19. Since the CCI does not provide any inertia to the system, the inertial

effect of the VCI is adjusted to $H_3 = 0.5$ s in order to establish a fair comparison between the configurations. As expected, considering the macroscopic view of the power system, the frequency behaviour obtained with both configurations are equivalent. However, it is emphasised that such equivalency is only true in the case of the parameters of the systems are comparable, and the stability of the CCI is guaranteed.

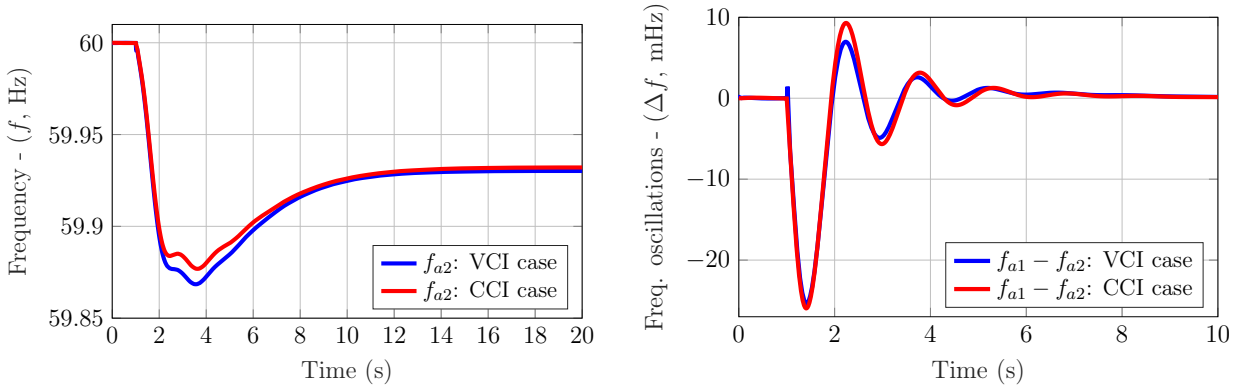

(a) f_{a2} (Hz) (b) $f_{a1} - f_{a2}$ (mHz)

Figure 3.19 – Comparison between the frequency behaviour of the Kundur system with a PE-based source connected to bus n° 3 (reference model). In blue: VCI case ($H_3 = 0.5$ s); In red: CCI case.

Table 3.5 – Comparison of the dominant and oscillating eigenvalues of the VCI and the CCI cases of the Kundur system obtained with their reference and aggregated models.

	VCI case ($H_3 = 0.5$ s)		**CCI case**	
	Reference	**Aggregated**	**Reference**	**Aggregated**
$\lambda_{\mathbf{dom}}$	$-0.56 \pm j0.16$	-0.38 -1.36	$-0.55 \pm j0.10$	-0.38 -1.33
$\lambda_{\mathbf{osc}}$	$-0.99 \pm j4.24$	$-1.71 \pm j5.49$	$-0.95 \pm j4.07$	$-0.92 \pm j5.75$

In addition to the results of Figure 3.19, the eigenvalues λ_{dom} and λ_{osc} obtained with the reference and aggregated models of the VCI and CCI cases are summarised in Table 3.5. In addition to the already observed equivalency between the reference models of the VCI and CCI cases, the coherence between their aggregated models can also be observed, and therefore, the conclusions made in Section 3.3.1.3 are also applicable to this configuration.

3.3.3 Replacement of a synchronous area with a PE-based area

In the following analysis, the second synchronous machine of area 2 is replaced with another PE-based source, resulting in a 100% PE-based area. The frequency behaviour of three different configurations — the VCI-VCI, CCI-VCI and CCI-CCI cases — are analysed in this

section. Similarly to previous configurations, the representativeness of aggregated model of each configuration is investigated. However, for the CCI-CCI case, it is demonstrated that the topology of the system changes, not being possible to establish an aggregated model of the system.

3.3.3.1 100% PE-based area: the VCI-VCI case

The first configuration of a 100% PE-based area to be analysed is the VCI-VCI case. In the reference model of the system, both VCIs are designed and parametrised as described in Section 3.3.1.1. The remainder of the system is designed as in the previous configurations.

The aggregated model of the system is illustrated in Figure 3.20. Since the nature of both sources of area 2 is the same, in addition to the equivalent inertia of the area, the droop control and the damping power of the sources can also be aggregated. The estimation of the grid frequency ($\Delta\tilde{\omega}_{g,a2}$) is implemented as given eq. (3.3), however, replacing ΔP_3 with ΔP_{a2}. The remainder of the aggregated model is equivalent to the previous configuration.

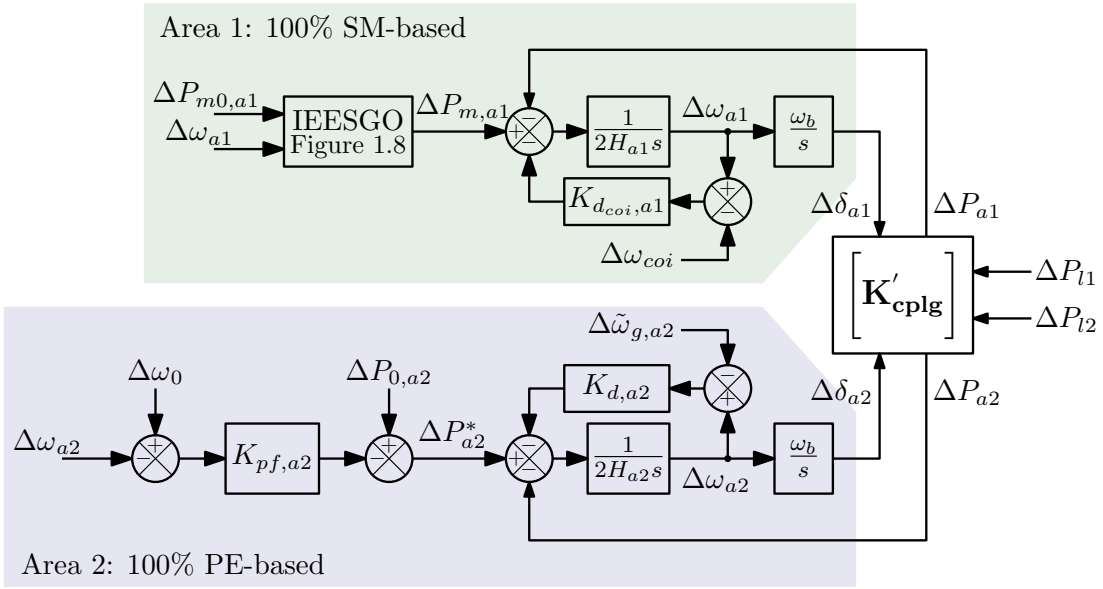

Figure 3.20 – Aggregated model of Kundur system with 100% of PE-based sources in area 2, the VCI-VCI case.

A first analysis proposes to observe the impact of the gradual replacement of the synchronous machines of area 2 with VCIs on the frequency behaviour of the Kundur system. For the purpose of the analysis, three different configurations are analysed, and in order to obtain a fair comparison between the configurations, the power frequency characteristics and the inertial effect of the VCIs are equivalent to those of the replaced synchronous machines, i.e. $K_{pf} = -25$ pu and $H = 6.175$ s.

- **100% SM:** Area 2 is composed only of synchronous machines, Section 3.2;
- **50% SM:** Area 2 is composed of a VCI and a synchronous machine, Section 3.3.1;
- **0% SM:** Area 2 is composed only of VCIs.

The eigenvalues related to the frequency behaviour of the system obtained with the reference models of the three configurations are given in Table 3.6. The following can be observed:

- The eigenvalues λ_{dom} follow the tendencies observed in Section 2.3. With the increase of the contribution of the VCI to FCR, λ_{dom} become more damped, and consequently, the dominant frequency behaviour of the system displays less pronounced nadirs/peaks. Depending on the fraction of VCIs, the dominant eigenvalues become purely real, and the dominant frequency behaviour of the system approaches the first order dynamics.
- Since the eigenvalues λ_{a1} describe the oscillating frequency behaviour between the synchronous machines of area 1, they are not impacted by changes made in area 2.
- The intra-area oscillating eigenvalues of area 2 (λ_{a2}) mainly follow the same tendencies observed in Chapter 2. As introduced in Section 2.3.2.3, the oscillating eigenvalues become more damped when a synchronous machine is replaced with a VCI. In addition, since the electrical distance between the sources decrease, the frequency of the intra-area oscillations increase; refer to Section 2.4.3.
- The inter-area oscillating eigenvalues of the system (λ_{osc}) also illustrate the same tendencies observed in Chapter 2, becoming more damped with the replacement of synchronous machines with VCIs. Differently than λ_{a2}, the variation of frequency of λ_{osc} is almost negligible. Due to the high electrical distance between the areas, the synchronising torque between the areas does not significantly change with the replacement of synchronous machines with VCIs, and consequently, the frequency of the inter-area oscillations is nearly constant.

Table 3.6 – Summary of the eigenvalues related to the frequency behaviour system obtained with the reference models of the analysed configurations.

	100% SM	**VCI case 50% SM**	**VCI-VCI case 0% SM**
$\lambda_{\mathbf{dom}}$	$-0.32 \pm j0.39$	$-0.46 \pm j0.23$	-0.30 -1.09
$\lambda_{\mathbf{a1}}$	$-2.28 \pm j7.22$	$-2.28 \pm j7.24$	$-2.30 \pm j7.24$
$\lambda_{\mathbf{a2}}$	$-2.47 \pm j7.49$	$-7.43 \pm j5.52$	$-17.29 \pm j22.11$
$\lambda_{\mathbf{osc}}$	$-0.31 \pm j3.70$	$-0.83 \pm j3.79$	$-1.45 \pm j3.59$

Figure 3.21 illustrates the dynamics of the frequency of area 2 obtained with the reference and aggregated models of the three configurations, allowing to verify the aforementioned observations about the evolution of the frequency behaviour of the system. Furthermore, it can be observed that the frequency behaviour obtained with aggregated model of the system becomes continuously more representative of the reference model as the synchronous machines of area 2 are replaced with VCIs. This phenomenon can be justified by two reasons: the non-linearities of VCIs are smaller than those of synchronous machines, and, last but not least, the representation of the damping power in the simplified model of VCIs is based on the physical implementation of the control strategy, whereas, in the simplified model of synchronous machines, it is empirically represented.

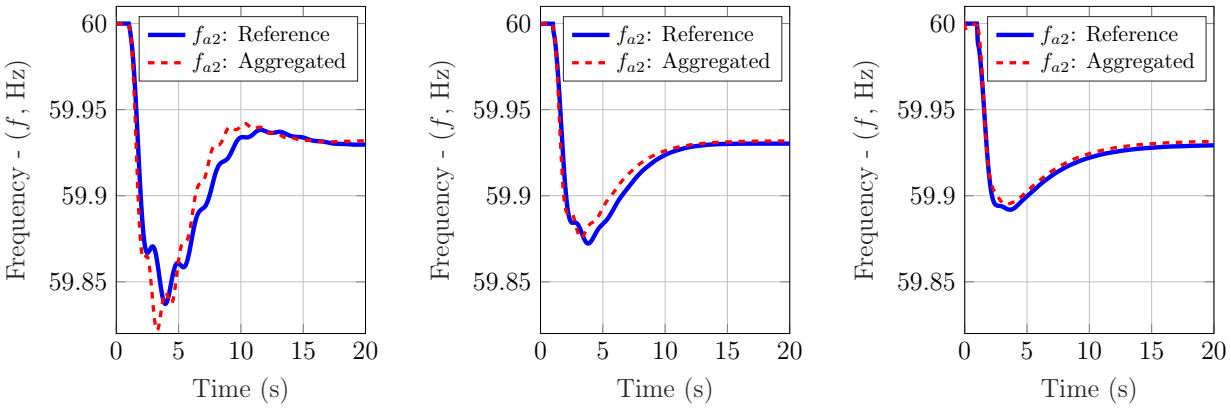

(a) f_{a2} (Hz); 100% SM (b) f_{a2} (Hz); 50% SM (c) f_{a2} (Hz); 0% SM

Figure 3.21 – Evolution of the frequency behaviour of the system due to the gradual replacement of synchronous machines in area 2. Stimulus: $\Delta P_{l1} = 0.1$ pu.

The impact of the equivalent inertia of area 2 is observed in the next analysis. For this purpose, considering that the aggregated model provides a good estimation of the system dynamics, the equivalent inertia of area 2 is varied from 1.0 to 12.35 s. The trajectories of the eigenvalues λ_{dom} and λ_{osc} are illustrated in Figure 3.22.

The dominant eigenvalues of this system display a behaviour similar to that previously observed, where the slowest eigenvalue is almost insensitive to the variation of H, whereas the faster eigenvalue is more sensitive to it. The oscillating eigenvalues describe a "C" shape trajectory. For all range of equivalent inertia, the frequency of the expected inter-area oscillations is between 0.38 and 0.7 Hz, which is still inside the known frequency range for this kind of oscillations, i.e. 0.1 to 0.8 Hz [52], [103]. The expected damping ratio of these oscillations is between 30 and 70%, and the maximum damping ratio does not occurs when the equivalent inertia is minimal, but around 6 s. From Table 3.3, the frequency and damping ratio of the inter-area oscillations of the Kundur system with 100% of synchronous machine are around 0.6 Hz and 8%, respectively. These observations could indicate that, in a multi-area system with massive replacement of synchronous machines with VCIs, the parameters of the remaining PSSs of the system do not imperatively need to be retuned.

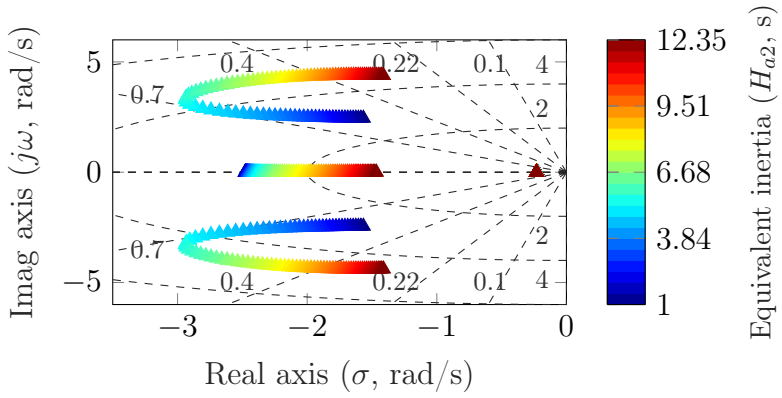

Figure 3.22 – Trajectories of the dominant and the oscillating eigenvalues obtained with the aggregated model of the VCI-VCI case of the Kundur system. Variation of the equivalent inertia of area 2.

Focusing on a specific value of equivalent inertia of area 2 (e.g. $H_{a2} = 6.675$), it is emphasised that many combinations of H_3 and H_4 can result on it. In order to observe whether or not the dispersion of inertial effect impacts on the frequency behaviour of the system, three different scenarios with the same equivalent inertia are proposed. The frequency behaviour of system obtained with the proposed scenarios is illustrated in Figure 3.23, and the comparison of the dominant and oscillating eigenvalues obtained with the aggregated and reference models is given in Table 3.7.

- **First scenario:** $H_3 = 0.5$ s and $H_4 = 6.175$ s;
- **Second scenario:** $H_3 = 3.34$ s and $H_4 = 3.34$ s;
- **Third scenario:** $H_3 = 6.175$ s and $H_4 = 0.5$ s;

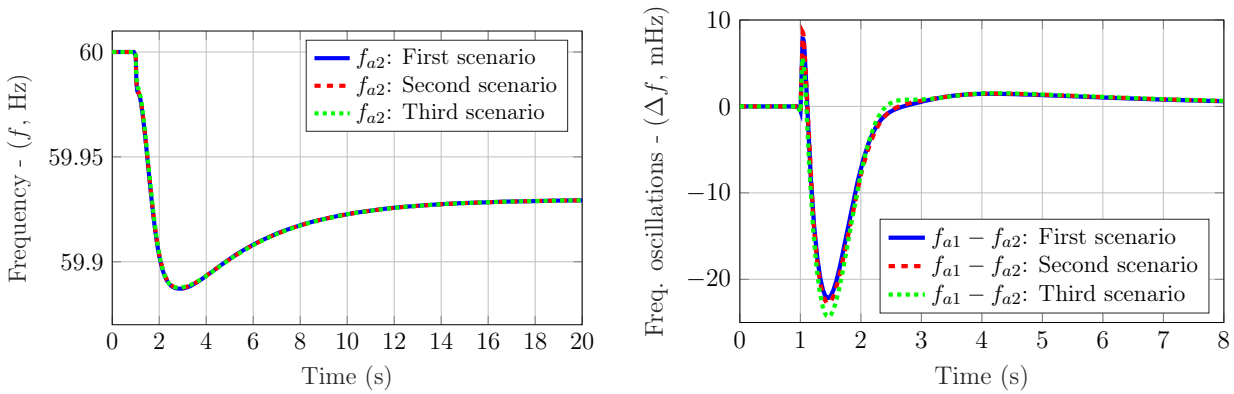

(a) f_{a2} (Hz) (b) $f_{a1} - f_{a2}$ (mHz)

Figure 3.23 – Investigation of the dispersion of inertia inside area 2. Comparison of the frequency behaviour of system obtained with the proposed scenarios.

Table 3.7 – Summary of the dominant and oscillating eigenvalues obtained with the proposed scenarios. Comparison with the expected eigenvalues obtained with the aggregated model of the system.

		Reference model		
	Aggregated model	**First scenario**	**Second scenario**	**Third scenario**
$\lambda_{\mathbf{dom}}$	-0.23 -2.25	-0.29 $-1.37 \pm j0.38$	-0.29 $-1.33 \pm j0.37$	-0.29 $-1.29 \pm j0.37$
$\lambda_{\mathbf{osc}}$	$-2.62 \pm j3.99$	$-3.00 \pm j3.67$	$-2.92 \pm j3.25$	$-2.54 \pm j3.39$

The dynamics observed in Figure 3.23 of all three scenarios are equivalent, inferring that the distribution of inertia inside area 2 does not have a significant impact on the frequency behaviour of the system at the area level. However, it should be emphasised that, in a multi-source system, very dispersed inertias could result in high values of RoCoF displayed by some sources inside the areas, whereas more distributed inertias could limit the magnitude of the RoCoF. In addition, it should also be remembered that, in order to the PE-based source provide such inertial effect, the corresponding amount of energy to be dispatched to the grid should be available in some form, and therefore, the inertial service could have an important impact on the techno-economic aspect of the system. These subjects will not be addressed in work.

3.3.3.2 100% PE-based area: the CCI-VCI case

Instead of operating in VCI mode, one of the PE-based sources of area 2 can operate using the CCI strategy. In this section, the VCI connected to bus n° 3 is replaced with a CCI designed and parametrised as described in Section 3.3.2.1, and consequently, area 2 is composed of one CCI and one VCI. Using the same principles that were outlined in the aforementioned section, the aggregated model of this configuration is the same as that of the VCI-VCI case illustrated in Figure 3.20, however, in this case, the equivalent coefficient of inertia and damping factor of the area is only composed of the parameters of the VCI.

In Section 3.3.2.2, highlighting the equivalency between the aggregated models of the VCI and CCI cases, it has been demonstrated that the frequency behaviour obtained with these configurations are equivalent when the inertial effect of the VCI is low. By extension, since both VCI-VCI and CCI-VCI configurations share the same aggregated model, the frequency behaviour obtained with the CCI-VCI case is expected to be similar to that obtained with the VCI-VCI case with comparable inertial effect. For the purpose of the analysis, two scenarios are proposed in Table 3.8.

Table 3.8 – Proposed scenarios for the comparison between the VCI-VCI and CCI-VCI cases.

	VCI-VCI case		**CCI-VCI case**	
	H_3 (s)	**H_4 (s)**	**H_3 (s)**	**H_4 (s)**
First Scenario:	0.5	6.175	—	6.175
Second Scenario:	0.5	0.5	—	0.5

The simulation results are illustrated in Figure 3.24. As expected, the frequency behaviours observed with the CCI-VCI and the VCI-VCI cases are equivalents for both scenarios. Therefore, by extension, the aggregated model of the system can provide a good estimation of the frequency behaviour of the system for preliminary studies.

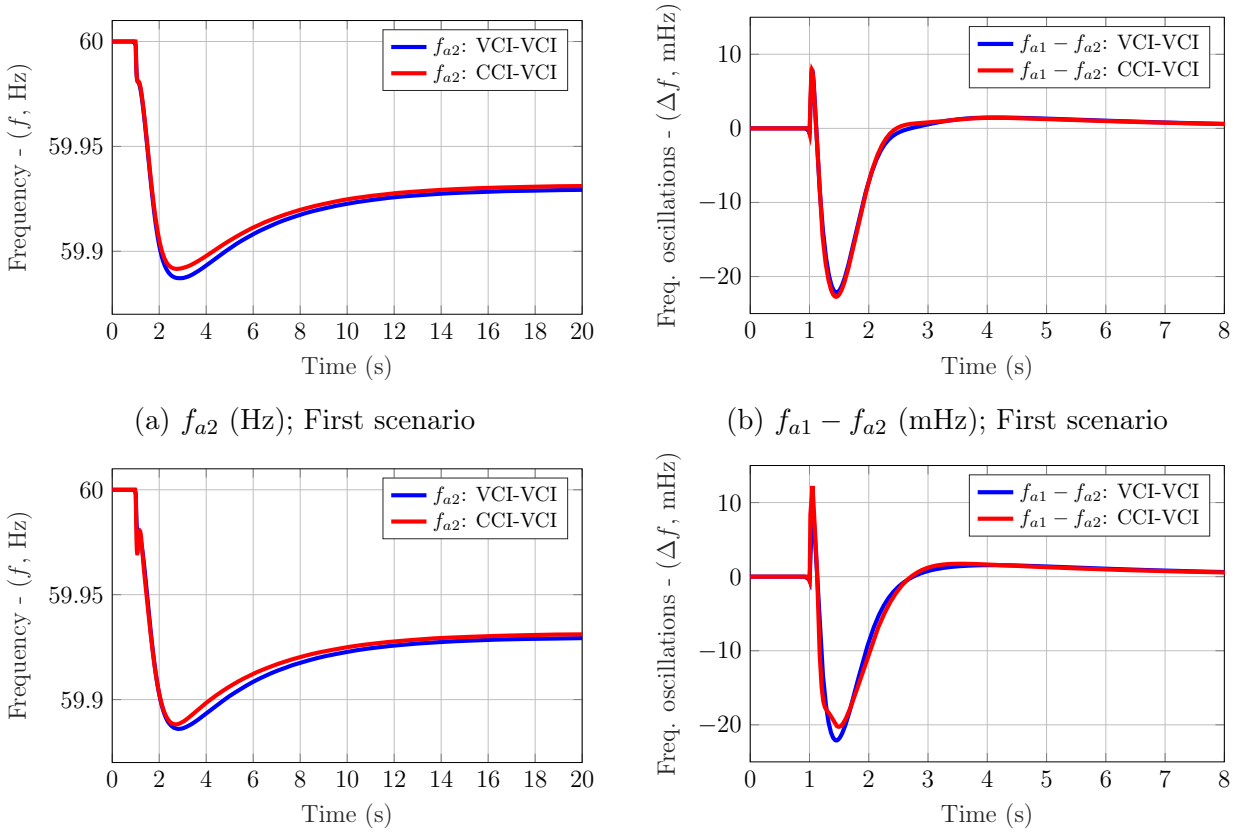

(a) f_{a2} (Hz); First scenario

(b) $f_{a1} - f_{a2}$ (mHz); First scenario

(c) f_{a2} (Hz); Second scenario

(d) $f_{a1} - f_{a2}$ (mHz); Second scenario

Figure 3.24 – Comparison of the frequency behaviours obtained with the reference model of the VCI-VCI and CCI-VCI cases of the Kundur system (comparable parameters).

3.3.3.3 The CCI-CCI case

In this section, both synchronous machines of area 2 are replaced with CCIs designed and parametrised as described in Section 3.3.2.1. In the previous configurations addressed in this chapter, aggregated models of the system have been defined in order to satisfactorily provide the frequency behaviour of the system, simplifying the carried out analysis. It is emphasised that the CCI-CCI case is completely different from the previous configurations addressed in this chapter.

As starting premise, it is considered that, in this configuration, the system is composed of two areas in which areas 1 and 2 are respectively only composed of synchronous machines and of CCIs. However, as introduced in Section 1.3.2, due to their inherent behaviour, CCIs do not generate their own frequency, but estimate the frequency of the grid in order to keep the synchronism with it. Since neither of the sources of area 2 generates the frequency of the area, the starting premise is incorrect, and the system is instead composed of only one area in which the current sources are separated from the voltage sources by a high electrical distance, and therefore, the concept of inter-area oscillations does not apply to this system.

The CCI-CCI case of the Kundur system is similar to that addressed in Section 2.5, however with two sources in each extremity of the network. As introduced in Section 2.5.2, it is not possible to design an aggregated model of this system, only being possible to establish a dominant model which illustrates the dominant frequency behaviour of the system (ω_{coi}). However, as discussed in Section 2.5.3, it is only possible to predetermine the overall dynamics of the system with the using a dominant model when no stability problems are encountered. Furthermore, it has been shown that a CCI may present stability issues when its electrical distance from a voltage source is high. Since this condition is observed in this case, the analysis of the eigenvalues of the reference model of the system is performed. As illustrated in Figure 3.25, no stability issues are detected from this analysis, and therefore, the dominant model could be used to determine the behaviour of ω_{coi}.

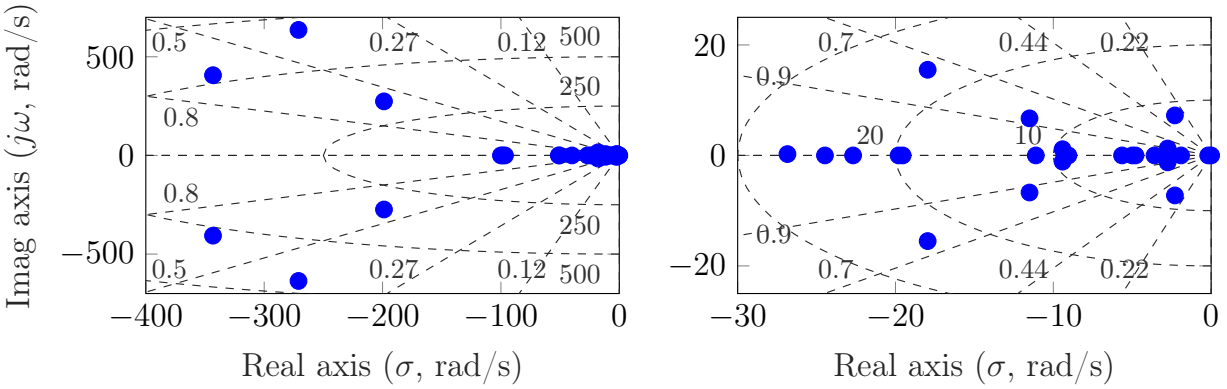

Figure 3.25 – Eigenvalues map of the reference model of the CCI-CCI case of the Kundur system (magnified view at the subject of interest).

The dominant model of this configuration is similar those employed for the VCI vs SM and CCI vs SM systems in Chapter 2. As illustrated in Figure 3.26, the equivalent inertia of the system is a composite of the coefficients of inertia of the synchronous machines (H_{a1}), and the power frequency control chain is designed with two channels, one for the aggregated controls of the synchronous machines and another for the equivalent droop control of the CCIs.

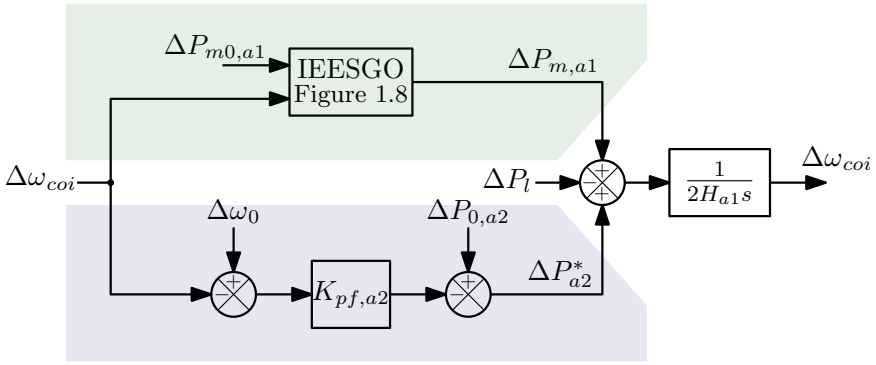

Figure 3.26 – Block diagram representing the dominant frequency behaviour of the CCI-CCI case of the Kundur system.

Figure 3.27 illustrates that the dominant model could indeed fairly represent the dominant frequency behaviour of the CCI-CCI case of the Kundur system obtained with its reference model. However, it is emphasised that, since CCIs are highly dependent of the parameters of the grid, in order to determine whether or not dominant model of a system with massive insertion of CCIs can be representative of the system, a stability study using its detailed model is very often beforehand required, diminishing the convenience and the interest of using a reduced order model.

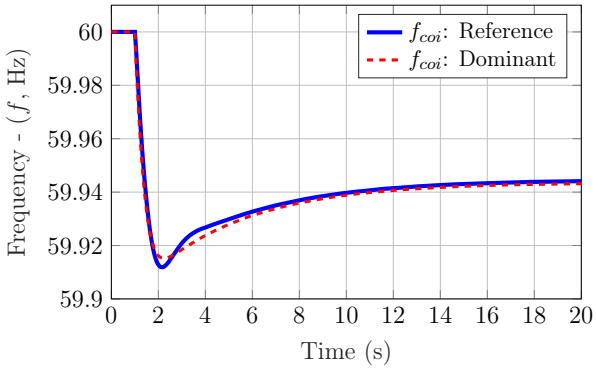

Figure 3.27 – Comparison of the dominant frequency behaviour of the CCI-CCI case of the Kundur system obtained with its reference and dominant models.

3.4 Conclusions

This chapter has investigated the evolution of the frequency behaviour of multi-area multi-source systems due to the replacement of synchronous machines with PE-based sources operating either in VCI or CCI mode.

It has been demonstrated that the simplified model of the Kundur system can be designed using the same approach as introduced in Chapter 2, however, requiring minimal adaptations to the model of the synchronous machine in order to correctly represent the damping power provided to intra- and inter-area oscillations. The eigenvalues and dynamics obtained with this representation are considerably consistent with those obtained with the reference model of the system, indicating its suitability to provide tendencies of the evolution of the frequency behaviour of the system.

Considering an approach more suitable to the analysis of the frequency behaviour of large interconnected power systems, an aggregated model of the Kundur system has been proposed. In this model, each coherent group of sources has been aggregated into a single equivalent unit, resulting in two areas interconnected through a quasi static representation of the system. This representation has also provided consistent results in comparison with the reference model of the system.

It has been demonstrated that the aggregated representation of the Kundur system is similar to the simplified model of the two-source system analysed in Chapter 2, and therefore, the tendencies obtained with the latter should be expected to be observed in the former. Indeed, with the replacement of synchronous machines with PE-based sources operating in VCI mode, it has been shown that the frequency behaviour of the Kundur system obeys the tendencies which were previously observed. The dominant frequency behaviour of the system becomes more damped, displaying less pronounced nadirs/peaks. Likewise, the behaviour of inter-area oscillations is also enhanced, becoming continuously more damped with the insertion of VCIs. It has been observed that the frequency of inter-area oscillations remains inside the known frequency range of these oscillations, which could indicate that in a multi-area system with massive replacement of synchronous machines with VCIs, the parameters of the remaining PSSs of the system do not imperatively need to be retuned. In addition, since the ensemble of physical phenomena is better represented in the simplified model of VCIs than in that of synchronous machines, the dynamics obtained with the aggregated model of the system become continuously more representative of its reference model with the increase of VCIs.

It has been demonstrated that the frequency behaviour displayed by the Kundur system is the same whether one PE-based source of area 2 is a CCI or a VCI with low inertia. However, in the case in which both synchronous machines of area 2 are replaced with CCIs, due to the inherent behaviour of the CCIs, area 2 cease to exist, and consequently, so does

the concept of inter-area oscillations. In this case, the system is composed of only one area in which the current sources are separated from the voltage sources by a high electrical distance, and as introduced in Section 2.5.3, since the stability of a CCI system is highly dependent on the parameters of the grid, a more detailed stability analysis is required to determine whether or not the reduced order model of the system is representative, diminishing the interest of the latter.

Chapter 4

Conclusions and future work

This thesis has treated the evolution of the characteristics of power systems due to the massive replacement of classic generating units — i.e. synchronous machines — with Power Electronics (PE)-based sources operating either as voltage or current sources — i.e. in VCI or CCI mode — until the penetration rate of the former becomes marginal. This work has focused on the evolution of the frequency behaviour considering the normal operation of the system.

Several challenges related to the massive insertion of PE-based sources have been detected in the literature, especially those related to the evolution of the main frequency behaviour of the system and the damping of inter-area oscillations. In the current scenario in which PE-based sources operate in CCI mode, it is expected that the absence of inertial effect increases the rate of change and the nadir of frequency. Furthermore, because of the displacement of synchronous machines and their power system stabilisers, the inter-area oscillations are expected to be less damped. Both phenomena degrade the stability of the system, requiring another control strategy — i.e. VCI mode — to mitigate these issues.

The literature suggests that, since the frequency dynamics of systems with high penetration rate of PE-based sources are not well comprehended, the applicability of the classical methods and tools used for frequency dynamics assessment of systems dominated by synchronous machines in systems dominated by inverters is unknown, and consequently, full electromagnetic transient (EMT) models should be prioritised to perform stability studies. However, the design of EMT models could be unpractical for large power systems such as the European network, and, due to the lack of an analytical interpretation of the phenomena, the findings obtained with a specific system might not be applicable to all configurations.

In this research, in order to deeply understand the impact of the massive insertion of PE-based sources in the power system, the following approach has been adopted. Using systems with incremental complexity, the changes in the frequency behaviour due to the adopted control strategy and parameters of the PE-based sources, and structure of the

grid have been analysed, proposing analytical interpretations of the involved phenomena. For this purpose, the classical methods and tools have been re-evaluated and adapted to be operational for the analysis of power systems with inverters, establishing representative reduced order models of the studied systems. With the proposed methodology, it has been possible to estimate the eigenvalues related to the frequency behaviour of the system, and consequently, to obtain a fair representation of the frequency dynamics of the system. Since the reduced order models are highly representative (in comparison with EMT), it has been possible to summarise a series of tendencies about the evolution of the frequency behaviour of the system.

In general, due to the flexibility of PE-based sources, the frequency behaviour of the system is enhanced with the insertion of these assets. Because of the faster dynamics of the power frequency control chain of PE-based sources compared to that of synchronous machines, the dominant frequency behaviour of the system is more damped, improving the frequency peaks and nadirs. With a massive contribution of the PE-based sources to FCR, the dominant frequency behaviour of the system can resemble the dynamics of a first order system. The oscillations of the system — both intra- and inter-area — become more damped. It has been observed that the frequency of inter-area oscillations remains inside the known frequency range of these oscillations, whereas that of intra-area oscillations has a tendency to increase.

The aforementioned tendencies are obtained when the PE-based sources are operating in either VCI or CCI mode, and it has been demonstrated that, despite the different inherent behaviours of these strategies, the obtained frequency behaviours are equivalent if the parameters of both strategies are comparable. However, it is emphasised that, due to the inherent behaviour of CCIs as current sources, the replacement of synchronous machines with PE-based sources operating with this strategy can modify the repartition of areas throughout the system. Furthermore, since the stability of CCIs is highly dependent of the parameters of the grid, systems with massive insertion of these assets may display stability issues, compromising the employment of reduced order models, and therefore, requiring detailed stability analysis. Therefore, it is suggested, when possible, to favour the VCI strategy.

Despite the fact that the findings have been observed using small systems, since the adopted approach is coherent with that previously used for the analysis of 100% synchronous machine-based systems, the author of this work is confident about the applicability for large systems with massive insertion of PE-based sources.

4.1 Thesis contributions

From the previous paragraphs, the main contribution of this research to the state of the art can be summarised as:

Understanding the frequency behaviour of power systems with high penetration rate of PE-based sources using an oriented approach which allows the re-evaluation of classical methods and tools used for systems based on synchronous machines.

The contributions of each chapter in the totality of this research are summarised in the following paragraphs:

- **Chapter 1:** Presentation of the fundamentals, and design of the reference and simplified models of the sources which were used in the work. A direct comparison between the mechanical structure of synchronous machines and the controls of VCIs have been established, highlighting the flexibility of VCIs, since their parameters can be configurable with any desired values. It has been demonstrated that CCIs behave differently than the other sources, acting as power injectors.

- **Chapter 2:** Investigation of the frequency behaviour of two-source systems with variable frequency. Adaptation of the classical methodology used for 100% synchronous machine-based systems providing compatibility with systems with PE-based sources. Using reduced order models of the systems, it has been possible to analytically interpret the impact of the replacement of synchronous machines with PE-based sources in either VCI or CCI mode on the frequency behaviour of the system, providing tendencies about the evolution of the eigenvalues related to the frequency behaviour to important parametric variations *vis-à-vis* the power system.

- **Chapter 3:** The frequency behaviours obtained with multi-area multi-source systems have been compared with the expected tendencies observed in the previous chapter. It has been demonstrated that it is possible to design reduced order models of systems with mixed sources using the same methodology which was previously employed considering minimal modifications. The frequency behaviour obtained with these models have been proved representative of the reference models of the systems, justifying their usage in preliminary studies about the evolution of the frequency behaviour of systems with massive insertion of PE-based sources.

4.2 Recommendations for future work

Even though this research has clarified some points about the feasibility and operation of power grids with massive insertion of PE-based sources, some questions remain unanswered. A list of proposed subjects which could complement this research is given below.

- The damping coefficients of reduced order models of synchronous machines has been empirically determined in this work. Although many methods found in the current literature have been tested, the dynamics obtained with reduced order models of systems with synchronous machines were only compatible with those obtained with their reference models when the damping coefficients of these sources have been estimated. The methods which attempt to analytically determine the values of the damping coefficient of synchronous machines have not returned satisfactory results. The damping coefficient of the reduced order model of synchronous machines should be further investigated in order to propose an analytical method capable of providing a good representation of the damping power provided by these sources.

- The conclusions from this research have been obtained with academic systems, and, despite being capable of representing the phenomena observed in large interconnected systems, the analysis of an industrial system could sustain these conclusions. The analysis of insular grids could be viable as a case study, since they are sufficiently complex and can still be designed considering a high level of detail. It should be interesting to observe whether or not the massive insertion of PE-based sources can split or merge synchronous areas of the system or even create new ones, and consequently, modify the geographical shape of inter-area modes.

- In this case where the geographical shape of the system areas is modified, a deeper investigation into the performance of PSSs of the remaining synchronous machines might be conducted in order to determine whether or not these devices should be retuned.

- Nevertheless, this research has investigated the impact of the massive insertion of PE-based sources adopting solutions based only on these devices. However, due to the current characteristics of semiconductors, some of the proposed solutions may not be practical, because, in order to limit overloads, the installations must be oversized, increasing the cost of the assets. Hybrid solutions such as CCIs with synchronous compensators providing fast frequency response, inertial effect and voltage support should also be considered in future research.

Bibliography

[1] ENTSO-E, 'European Power System 2040 - Completing the map: The Ten-Year Network Development Plan 2018 System Needs Analysis', Brussels, Tech. Rep., 2018, p. 56.

[2] République Française, 'Décret no 2017-530 du 12 avril 2017 relatif à la programmation pluriannuelle de l'énergie de La Réunion', *Journal Officiel de la République Française*, no. NOR : DEVR1701352D, p. 182, 2017.

[3] ——, 'Décret no 2015-1697 du 18 décembre 2015 relatif à la programmation pluriannuelle de l'énergie de Corse', *Journal Officiel de la République Française*, no. NOR : DEVR1527419D, p. 86, 2015.

[4] A. Yazdani and R. Iravani, *Voltage-Sourced Converters in Power Systems*. Hoboken, NJ, USA: John Wiley & Sons, Inc., 2010, p. 451, ISBN: 9780470551578. DOI: 10.1002/9780470551578.

[5] PROMOTioN, 'Deliverable 1.1: Detailed description of the requirements that can be expected per work package', EU, Tech. Rep., 2016, p. 95.

[6] MIGRATE, 'Deliverable 1.1: Report on Systemic Issues', EU, Tech. Rep. 691800, 2016, p. 137.

[7] RESERVE, 'Deliverable 1.1: Scenarios & architectures for 100% RES and roles of sector actors', EU, Tech. Rep., 2016, p. 98.

[8] N. W. Miller, B. Leonardi, R. D'Aquila and K. Clark, 'Western Wind and Solar Integration Study Phase 3A: Low Levels of Synchronous Generation', National Renewable Energy Laboratory (NREL), Golden, CO (United States), Tech. Rep. November, 2015, p. 110. DOI: 10.2172/1227265.

[9] E. Farantatos and D. Ramasubramanian, 'Program on Technology Innovation: Grid Operation with 100% Inverter-Interfaced Supply Resources', Electric Power Research Institute (EPRI), Palo Alto, CA, Tech. Rep., 2018, p. 66.

[10] EU-SysFlex, 'Deliverable 3.1: Product Definition for Innovative System Services', EU, Tech. Rep., 2019, p. 96.

[11] MIGRATE, 'Deliverable 1.1: Current and arising issues caused by increasing power electronics penetration', EU, Tech. Rep., 2020, p. 6.

[12] ENTSO-E, 'High Penetration of Power Electronic Interfaced Power Sources (HPoPEIPS)', Brussels, Tech. Rep. March, 2017, p. 37.

[13] F. Milano, F. Dorfler, G. Hug, D. J. Hill and G. Verbic, 'Foundations and Challenges of Low-Inertia Systems (Invited Paper)', in *2018 Power Systems Computation Conference (PSCC)*, IEEE, 2018, pp. 1–25, ISBN: 978-1-910963-10-4. DOI: 10.23919/PSCC.2018.8450880.

[14] V. Silva, M. Lopez-Botet-Zulueta and Y. Wang, 'Impact of high penetration of variable renewable generation on frequency dynamics in the continental Europe interconnected system', *IET Renewable Power Generation*, vol. 10, no. 1, pp. 10–16, 2016, ISSN: 1752-1416. DOI: 10.1049/iet-rpg.2015.0141.

[15] U. Tamrakar, D. Shrestha, M. Maharjan, B. Bhattarai, T. Hansen and R. Tonkoski, 'Virtual Inertia: Current Trends and Future Directions', *Applied Sciences*, vol. 7, no. 7, p. 654, 2017, ISSN: 2076-3417. DOI: 10.3390/app7070654.

[16] ENTSO-E, 'High Penetration of Power Electronic Interfaced Power Sources and the Potential Contribution of Grid Forming Converters', Brussels, Tech. Rep., 2020, p. 61.

[17] ——, 'Rate of Change of Frequency (RoCoF) withstand capability', ENTSO-E, Brussels, Tech. Rep., 2017, p. 9.

[18] RTE, *Documentation Technique de Référence*, Paris, 2014.

[19] M. S. Nielsen, 'Allocation of Synchronous Condensers for Low Inertia Systems', M.Sc. Thesis, Technical University of Denmark, 2015, p. 119.

[20] V. Natarajan and G. Weiss, 'Synchronverters With Better Stability Due to Virtual Inductors, Virtual Capacitors, and Anti-Windup', *IEEE Transactions on Industrial Electronics*, vol. 64, no. 7, pp. 5994–6004, 2017, ISSN: 0278-0046. DOI: 10.1109/TIE.2017.2674611.

[21] T. Qoria, F. Gruson, F. Colas, G. Denis, T. Prevost and X. Guillaud, 'Inertia effect and load sharing capability of grid forming converters connected to a transmission grid', in *15th IET International Conference on AC and DC Power Transmission (ACDC 2019)*, vol. 2019, Institution of Engineering and Technology, 2019, 79 (6 pp.)–79 (6 pp.) ISBN: 978-1-83953-007-4. DOI: 10.1049/cp.2019.0079.

[22] O. Mo, S. D'Arco and J. A. Suul, 'Evaluation of Virtual Synchronous Machines With Dynamic or Quasi-Stationary Machine Models', *IEEE Transactions on Industrial Electronics*, vol. 64, no. 7, pp. 5952–5962, 2017, ISSN: 0278-0046. DOI: 10.1109/TIE.2016.2638810.

[23] J. Quintero, V. Vittal, G. T. Heydt and H. Zhang, 'The Impact of Increased Penetration of Converter Control-Based Generators on Power System Modes of Oscillation', *IEEE Transactions on Power Systems*, vol. 29, no. 5, pp. 2248–2256, 2014, ISSN: 0885-8950. DOI: 10.1109/TPWRS.2014.2303293.

[24] E. Grebe, J. Kabouris, S Lopez Barba, W. Sattinger and W. Winter, 'Low frequency oscillations in the interconnected system of Continental Europe', in *IEEE PES General Meeting*, IEEE, 2010, pp. 1–7, ISBN: 978-1-4244-6549-1. DOI: 10.1109/PES.2010.5589932.

[25] H. Weber and S. Al Ali, 'Influence of huge renewable Power Production on Inter Area Oscillations in the European ENTSO-E-System', *IFAC-PapersOnLine*, vol. 49, no. 27, pp. 12–17, 2016, ISSN: 24058963. DOI: 10.1016/j.ifacol.2016.10.692.

[26] J. Renedo, L. Sigrist, A. Garcia-Cerrada and L. Rouco, 'Modelling of VSC-HVDC multi-terminal systems for small-signal angle stability analysis', in *15th IET International Conference on AC and DC Power Transmission (ACDC 2019)*, vol. 2019, Institution of Engineering and Technology, 2019, 46 (7 pp.)–46 (7 pp.) ISBN: 978-1-83953-007-4. DOI: 10.1049/cp.2019.0046.

[27] Y. Pankow, 'Étude de l'intégration de la production décentralisée dans un réseau Basse Tension. Application au générateur photovoltaïque', PhD thesis, École Nationale Supérieure d'Arts et Métiers, 2004, p. 160.

[28] A. Gole and J. Zhou, 'VSC transmission limitations imposed by AC system strength and AC impedance characteristics', in *10th IET International Conference on AC and DC Power Transmission (ACDC 2012)*, vol. 2012, Institution of Engineering and Technology, 2012, pp. 06–06, ISBN: 978-1-84919-700-7. DOI: 10.1049/cp.2012.1986.

[29] J. Z. Zhou, H. Ding, S. Fan, Y. Zhang and A. M. Gole, 'Impact of Short-Circuit Ratio and Phase-Locked-Loop Parameters on the Small-Signal Behavior of a VSC-HVDC Converter', *IEEE Transactions on Power Delivery*, vol. 29, no. 5, pp. 2287–2296, 2014, ISSN: 0885-8977. DOI: 10.1109/TPWRD.2014.2330518.

[30] M. Molinas, J. Suul, S. D'Arco and P. Rodriguez, 'Extended stability range of weak grids with Voltage Source Converters through impedance-conditioned grid synchronization', in *11th IET International Conference on AC and DC Power Transmission*, vol. 2015, Institution of Engineering and Technology, 2015, 064 (10 .)–064 (10 .) ISBN: 978-1-84919-982-7. DOI: 10.1049/cp.2015.0103.

[31] J. A. Suul, S. D'Arco, P. Rodríguez and M. Molinas, 'Impedance-compensated grid synchronisation for extending the stability range of weak grids with voltage source converters', *IET Generation, Transmission & Distribution*, vol. 10, no. 6, pp. 1315–1326, 2016, ISSN: 1751-8687. DOI: 10.1049/iet-gtd.2015.0879.

[32] MIGRATE, 'Deliverable 3.4: New Options in System Operations', EU, Tech. Rep., 2019, p. 114.

[33] ——, 'Deliverable 3.2: Local control and simulation tools for large transmission systems', EU, Tech. Rep., 2018, p. 81.

[34] R. Ofir, U. Markovic, P. Aristidou and G. Hug, 'Droop vs. virtual inertia: Comparison from the perspective of converter operation mode', in *2018 IEEE International Energy Conference (ENERGYCON)*, IEEE, 2018, pp. 1–6, ISBN: 978-1-5386-3669-5. DOI: 10.1109/ENERGYCON.2018.8398752.

[35] C. Arghir, T. Jouini and F. Dörfler, 'Grid-forming control for power converters based on matching of synchronous machines', *Automatica*, vol. 95, pp. 273–282, 2018, ISSN: 00051098. DOI: 10.1016/j.automatica.2018.05.037.

[36] C. Arghir and F. Dorfler, 'The Electronic Realization of Synchronous Machines: Model Matching, Angle Tracking, and Energy Shaping Techniques', *IEEE Transactions on Power Electronics*, vol. 35, no. 4, pp. 4398–4410, 2020, ISSN: 0885-8993. DOI: 10.1109/TPEL.2019.2939710.

[37] A. Tayyebi, D. Groß, A. Anta, F. Kupzog and F. Dörfler, 'Interactions of Grid-Forming Power Converters and Synchronous Machines', pp. 1–14, 2019. arXiv: 1902.10750.

[38] A. Rosse, R. Denis and C. Zakhour, 'Control of parallel inverters using nonlinear oscillators with virtual output impedance', in *2016 18th European Conference on Power Electronics and Applications (EPE'16 ECCE Europe)*, IEEE, 2016, pp. 1–10, ISBN: 978-9-0758-1524-5. DOI: 10.1109/EPE.2016.7695112.

[39] M. Sinha, S. Dhople, B. Johnson, N. Ainsworth and F. Dorfler, 'Nonlinear supersets to droop control', in *2015 IEEE 16th Workshop on Control and Modeling for Power Electronics (COMPEL)*, IEEE, 2015, pp. 1–6, ISBN: 978-1-4673-6847-6. DOI: 10.1109/COMPEL.2015.7236441.

[40] Q.-C. Zhong and G. Weiss, 'Synchronverters: Inverters That Mimic Synchronous Generators', *IEEE Transactions on Industrial Electronics*, vol. 58, no. 4, pp. 1259–1267, 2011, ISSN: 0278-0046. DOI: 10.1109/TIE.2010.2048839.

[41] F. Palombi, L. Piegari, S. D'Arco, A. G. Endegnanew and J. A. Suul, 'Impact on Power System Frequency Dynamics from an HVDC Transmission System With Converter Stations Controlled as Virtual Synchronous Machines', in *2019 IEEE Milan PowerTech*, IEEE, 2019, pp. 1–6, ISBN: 978-1-5386-4722-6. DOI: 10.1109/PTC.2019.8810855.

[42] M. Paolone, T. Gaunt, X. Guillaud, M. Liserre, S. Meliopoulos, A. Monti, T. Van Cutsem, V. Vittal and C. Vournas, 'Fundamentals of power systems modelling in the presence of converter-interfaced generation', *Electric Power Systems Research*, vol. 189, no. April, p. 106 811, 2020, ISSN: 03787796. DOI: 10.1016/j.epsr.2020.106811.

[43] A. Tayyebi, F. Dörfler, Z. Miletic, F. Kupzog and W. Hribernik, 'Grid-Forming Converters – Inevitability, Control Strategies and Challenges in Future Grids Application', *CIRED Workshop*, no. April, pp. 1–5, 2018.

[44] G. Denis, T. Prevost, M.-S. Debry, F. Xavier, X. Guillaud and A. Menze, 'The Migrate project: the challenges of operating a transmission grid with only inverter-based generation. A grid-forming control improvement with transient current-limiting control', *IET Renewable Power Generation*, vol. 12, no. 5, pp. 523–529, 2018, ISSN: 1752-1416. DOI: 10.1049/iet-rpg.2017.0369.

[45] MIGRATE, 'The Massive InteGRATion of power Electronic devices: Enabling the energy transition by providing solutions for the technological challenges', EU, Tech. Rep., 2020, p. 11.

[46] EU-SysFlex, 'Models for Simulating Technical Scarcities on the European Power System with High Levels of Renewable Generation', EU, Tech. Rep., 2018, p. 164.

[47] G. Denis, 'From grid-following to grid-forming: The new strategy to build 100 % power-electronics interfaced transmission system with enhanced transient behavior', PhD thesis, Centrale Lille, 2017, p. 227.

[48] B. N. Gallegos, 'Parametric sensitivity for analysis of dc networks', PhD thesis, Centrale Lille, 2016, p. 120.

[49] Q. Cossart, 'Outils et Méthodes pour l'Analyse et la Simulation de Réseaux de Transport 100% Électronique de Puissance', PhD thesis, École Nationale Supérieure d'Arts et Métiers, 2019, p. 189.

[50] R. H. Park, 'Two-reaction theory of synchronous machines generalized method of analysis-part I', *Transactions of the American Institute of Electrical Engineers*, vol. 48, no. 3, pp. 716–727, 1929, ISSN: 0096-3860. DOI: 10.1109/T-AIEE.1929.5055275.

[51] P. Dandeno, R. Hauth and R. Schulz, 'Effects of Synchronous Machine Modeling in Large Scale System Studies', *IEEE Transactions on Power Apparatus and Systems*, vol. PAS-92, no. 2, pp. 574–582, 1973, ISSN: 0018-9510. DOI: 10.1109/TPAS.1973.293760.

[52] P. Kundur, *Power System Stability and Control*, 1st ed. Palo Alto, CA: McGraw-Hill, Inc., 1994, p. 1176, ISBN: 0-07-035958-X.

[53] 'IEEE Guide for Synchronous Generator Modeling Practices and Parameter Verification with Applications in Power System Stability Analyses', *IEEE Std 1110-2019 (Revision of IEEE Std 1110-2002)*, pp. 1–92, 2020. DOI: 10.1109/IEEESTD.2020.9020274.

[54] J. Machowski, J. W. Bialek and J. R. Bumby, *Power System Dynamics: Stability and Control*, 2nd ed. West Sussex, UK: John Wiley & Sons, Ltd, 2008, p. 629, ISBN: 978-0-470-72558-0.

[55] G. Rogers, *Power System Oscillations*, 1st ed. Norwell, USA: Kluwer Academic Publishers, 2000, p. 332, ISBN: 978-1-4613-7059-8.

[56] I. Boldea, *Synchronous generators*, 1st ed. Boca Raton, FL: Taylor & Francis Group, LLC, 2006, p. 425, ISBN: 9781420037258. DOI: 10.1007/978-94-017-1394-8_11.

[57] M. Eremia and M. Shahidehpour, *Handbook of Electrical Power System Dynamics*, 1st ed., M. Eremia and M. Shahidehpour, Eds. Hoboken, NJ, USA: John Wiley & Sons, Inc., 2013, pp. 1–968, ISBN: 9781118516072. DOI: 10.1002/9781118516072.

[58] A. Blondel, 'Application de la méthode des deux réactions à l'étude des phénomènes oscillatoires des alternateurs accouplés', *Révue Générale de L'Électricité*, vol. XIII, no. Février, pp. 235–251, 1923.

[59] 'IEEE Guide: Test Procedures for Synchronous Machines', *IEEE Std 115-1983 (Revision of IEEE Std 115-1965)*, p. 90, 1983.

[60] M. A. Swidan, 'Study of damping power in interconnected power systems', PhD thesis, Iowa State University, Digital Repository, Ames, 1964. DOI: 10.31274/rtd-180813-2118.

[61] M. Shiroei, B. Mohammadi-Ivatloo and M. Parniani, 'Low-order dynamic equivalent estimation of power systems using data of phasor measurement units', *International Journal of Electrical Power & Energy Systems*, vol. 74, pp. 134–141, 2016, ISSN: 01420615. DOI: 10.1016/j.ijepes.2015.07.015.

[62] IEEE Power & Energy Society, 'Dynamic Models for Turbine-Governors in Power System Studies', Tech. Rep., 2013, p. 117.

[63] The European Commission, 'Commission Regulation (EU) 2017/1485 establishing a guideline on electricity transmission system operation', *Official Journal of the European Union*, vol. L 220, no. August, p. 120, 2017.

[64] C. Roberts, 'Review of International Grid Codes', Lawrence Berkeley National Laboratory, Berkeley, CA, Tech. Rep. February, 2018, p. 64.

[65] 'Analysis and Control of Power System Oscillations', *CIGRE Task Force 38.01.07*, p. 200, 1997.

[66] P. Wetzer, 'Machines synchrones Excitation', *Techniques de l'Ingénieur*, vol. base docum, no. ref. article : d3545, p. 11, 1997.

[67] 'IEEE Recommended Practice for Excitation System Models for Power System Stability Studies', *IEEE Std 421.5-2005 (Revision of IEEE Std 421.5-1992)*, pp. 1–93, 2006. DOI: 10.1109/IEEESTD.2006.99499.

[68] P. W. Sauer and M. A. Pai, *Power system dynamics and stability*, 2nd ed. Illinois: Stipes Pub, Llc., 2007, p. 349, ISBN: 978-1588746733.

[69] R. De Doncker, D. W. Pulle and A. Veltman, *Advanced Electrical Drives*, 1st ed., ser. Power Systems. Dordrecht: Springer Netherlands, 2011, p. 443, ISBN: 978-94-007-0179-3. DOI: 10.1007/978-94-007-0181-6.

[70] A. Gkountaras, 'Modeling techniques and control strategies for inverter dominated microgrids', PhD thesis, Technische Universität Berlin, 2017, p. 169, ISBN: 978-3-7983-2872-3. DOI: 10.14279/depositonce-5520.

[71] A. Paquette, 'Power Quality and Inverter-Generator Interactions in Microgrids', PhD thesis, Georgia Institute of Technology, 2014, p. 177.

[72] B. Kroposki, B. Johnson, Y. Zhang, V. Gevorgian, P. Denholm, B.-M. Hodge and B. Hannegan, 'Achieving a 100% Renewable Grid: Operating Electric Power Systems with Extremely High Levels of Variable Renewable Energy', *IEEE Power and Energy Magazine*, vol. 15, no. 2, pp. 61–73, 2017, ISSN: 1540-7977. DOI: 10.1109/MPE.2016.2637122.

[73] L. L. Grisby, *Electric Power Generation, Transmission and Distribution*, 2nd ed. Taylor & Francis Group, LLC, 2006, p. 503, ISBN: 978-0-8493-9292-4.

[74] F. Salha, 'Microréseaux îlotables : étude et coordination des protections des générateurs et du réseau', PhD thesis, École Centrale de Lille, 2010, p. 165.

[75] M. Ndreko, S. Rüberg and W. Winter, 'Grid Forming Control for Stable Power Systems with up to 100 % Inverter Based Generation: A Paradigm Scenario Using the IEEE 118-Bus System', in *17th International Wind Integration Workshop*, 2018, p. 6.

[76] G. Lancel, B. Deneuville, C. Zakhour, E. Radvanyi, J. Lhermenault, C. Ducharme and S. Ruiz, 'Energy storage systems (ESS) and microgrids in Brittany islands', *CIRED - Open Access Proceedings Journal*, vol. 2017, no. 1, pp. 1741–1744, 2017, ISSN: 2515-0855. DOI: 10.1049/oap-cired.2017.1188.

[77] S. Cherevatskiy, S. Zabihi, R. Korte, H. Klingenberg, S. Sproul, J. Glassmire, B. Buchholz and H. Bitaraf, 'A 30MW Grid Forming BESS Boosting Reliability in South Australia and Providing Market Services on the National Electricity Market', in *18th International Wind Integration Workshop*, Dublin, 2019, p. 8.

[78] K. Ogata, *Modern Control Engineering*, 5th ed. New Jersey: Prentice Hall, 2010, p. 894, ISBN: 978-0-13-615673-4.

[79] E. Rokrok, T. Qoria, A. Bruyere, B. Francois and X. Guillaud, 'Classification and dynamic assessment of droop-based grid-forming control schemes: Application in HVDC systems', *Electric Power Systems Research*, vol. 189, no. 268053, 2020, ISSN: 03787796. DOI: 10.1016/j.epsr.2020.106765.

[80] ——, 'Effect of Using PLL-Based Grid-Forming Control on Active Power Dynamics Under Various SCR', in *IECON 2019 - 45th Annual Conference of the IEEE Industrial Electronics Society*, vol. 2019-Octob, IEEE, 2019, pp. 4799–4804, ISBN: 978-1-7281-4878-6. DOI: 10.1109/IECON.2019.8927648.

[81] A. Monti, F. Milano, E. Bompard and X. Guillaud, *Converter-Based Dynamics and Control of Modern Power Systems*, 1st ed., Elsevier, Ed. Elsevier, 2020, p. 374, ISBN: 9780128184912.

[82] T. Qoria, 'Grid-forming control to achieve a 100% power electronics interfaced power transmission systems', PhD thesis, Centrale Lille, 2020, ?

[83] J. Liu, Y. Miura and T. Ise, 'Comparison of Dynamic Characteristics Between Virtual Synchronous Generator and Droop Control in Inverter-Based Distributed Generators', *IEEE Transactions on Power Electronics*, vol. 31, no. 5, pp. 3600–3611, 2016, ISSN: 0885-8993. DOI: 10.1109/TPEL.2015.2465852.

[84] S. D'Arco, J. A. Suul and O. B. Fosso, 'Small-signal modelling and parametric sensitivity of a Virtual Synchronous Machine', in *2014 Power Systems Computation Conference*, IEEE, 2014, pp. 1–9, ISBN: 978-83-935801-3-2. DOI: 10.1109/PSCC.2014.7038410.

[85] T. Qoria, F. Gruson, F. Colas, X. Guillaud, M.-S. Debry and T. Prevost, 'Tuning of Cascaded Controllers for Robust Grid-Forming Voltage Source Converter', in *2018 Power Systems Computation Conference (PSCC)*, IEEE, 2018, pp. 1–7, ISBN: 978-1-910963-10-4. DOI: 10.23919/PSCC.2018.8443018.

[86] Q.-C. Zhong, G. C. Konstantopoulos, B. Ren and M. Krstic, 'Improved Synchronverters with Bounded Frequency and Voltage for Smart Grid Integration', *IEEE Transactions on Smart Grid*, vol. 9, no. 2, pp. 786–796, 2018, ISSN: 1949-3053. DOI: 10.1109/TSG.2016.2565663.

[87] B. B. Johnson, M. Sinha, N. G. Ainsworth, F. Dorfler and S. V. Dhople, 'Synthesizing Virtual Oscillators to Control Islanded Inverters', *IEEE Transactions on Power Electronics*, vol. 31, no. 8, pp. 6002–6015, 2016, ISSN: 0885-8993. DOI: 10.1109/TPEL.2015.2497217.

[88] M. Colombino, D. Gros and F. Dorfler, 'Global phase and voltage synchronization for power inverters: A decentralized consensus-inspired approach', in *2017 IEEE 56th Annual Conference on Decision and Control (CDC)*, vol. 2018-Janua, IEEE, 2017, pp. 5690–5695, ISBN: 978-1-5090-2873-3. DOI: 10.1109/CDC.2017.8264518.

[89] S. Laudahn, J. Seidel, B. Engel, T. Bulo and D. Premm, 'Substitution of synchronous generator based instantaneous frequency control utilizing inverter-coupled DER', in *2016 IEEE 7th International Symposium on Power Electronics for Distributed Generation Systems (PEDG)*, vol. 00, IEEE, 2016, pp. 1–8, ISBN: 978-1-4673-8617-3. DOI: 10.1109/PEDG.2016.7527020.

[90] R. W. Kenyon, A. Hoke, J. Tan, B. Kroposki and B.-m. Hodge, 'Grid-Following Inverters and Synchronous Condensers: A Grid- Forming Pair?', in *2020 Clemson University Power System Conference*, Clemson, South Carolina, 2020, p. 7.

[91] J. Van de Vyver, 'Support of Grid Frequency Control by Wind Turbines', PhD thesis, Ghent University, 2016, p. 208, ISBN: 978-90-8578-937-6.

[92] D. Pattabiraman, R. H. Lasseter. and T. M. Jahns, 'Comparison of Grid Following and Grid Forming Control for a High Inverter Penetration Power System', in *2018 IEEE Power & Energy Society General Meeting (PESGM)*, vol. 2018-Augus, IEEE, 2018, pp. 1–5, ISBN: 978-1-5386-7703-2. DOI: 10.1109/PESGM.2018.8586162.

[93] S. I. Nanou and S. A. Papathanassiou, 'Grid Code Compatibility of VSC-HVDC Connected Offshore Wind Turbines Employing Power Synchronization Control', *IEEE Transactions on Power Systems*, vol. 31, no. 6, pp. 5042–5050, 2016, ISSN: 0885-8950. DOI: 10.1109/TPWRS.2016.2515504.

[94] B. K. Poolla, D. Gros and F. Dorfler, 'Placement and Implementation of Grid-Forming and Grid-Following Virtual Inertia and Fast Frequency Response', *IEEE Transactions on Power Systems*, vol. 34, no. 4, pp. 3035–3046, 2019, ISSN: 0885-8950. DOI: 10.1109/TPWRS.2019.2892290. arXiv: 1807.01942.

[95] W. Zhong, M. A. A. Murad, M. Liu and F. Milano, 'Impact of Virtual Power Plants on Power System Short-Term Transient Response', *Electric Power Systems Research*, vol. 189, no. February, p. 106 609, 2020, ISSN: 03787796. DOI: 10.1016/j.epsr.2020.106609.

[96] J. Zhu, C. D. Booth, G. P. Adam, A. J. Roscoe and C. G. Bright, 'Inertia Emulation Control Strategy for VSC-HVDC Transmission Systems', *IEEE Transactions on Power Systems*, vol. 28, no. 2, pp. 1277–1287, 2013, ISSN: 0885-8950. DOI: 10.1109/TPWRS.2012.2213101.

[97] J. Renedo, A. Garcia-Cerrada and L. Rouco, 'Active Power Control Strategies for Transient Stability Enhancement of AC/DC Grids With VSC-HVDC Multi-Terminal Systems', *IEEE Transactions on Power Systems*, vol. 31, no. 6, pp. 4595–4604, 2016, ISSN: 0885-8950. DOI: 10.1109/TPWRS.2016.2517215.

[98] B. J. Pierre, H. N. Villegas Pico, R. T. Elliott, J. Flicker, Y. Lin, B. B. Johnson, J. H. Eto, R. H. Lasseter and A. Ellis, 'Bulk Power System Dynamics with Varying Levels of Synchronous Generators and Grid-Forming Power Inverters', in *2019 IEEE 46th Photovoltaic Specialists Conference (PVSC)*, IEEE, 2019, pp. 0880–0886, ISBN: 978-1-7281-0494-2. DOI: 10.1109/PVSC40753.2019.8980733.

[99] G. Geng, S. Abhyankar, X. Wang and V. Dinavahi, 'Solution techniques for transient stability-constrained optimal power flow – Part II', *IET Generation, Transmission & Distribution*, vol. 11, no. 12, pp. 3186–3193, 2017, ISSN: 1751-8687. DOI: 10.1049/iet-gtd.2017.0346.

[100] G. S. Pereira, V. Costan, A. Bruyére and X. Guillaud, 'Simplified approach for frequency dynamics assessment of 100% power electronics-based systems', *Electric Power Systems Research*, vol. 188, no. September 2019, p. 106 551, 2020, ISSN: 03787796. DOI: 10.1016/j.epsr.2020.106551.

[101] P. Anderson and M. Mirheydar, 'A low-order system frequency response model', *IEEE Transactions on Power Systems*, vol. 5, no. 3, pp. 720–729, 1990, ISSN: 08858950. DOI: 10.1109/59.65898.

[102] G. Pereira, V. Costan, A. Bruyère and X. Guillaud, 'Impact of synchronous machine dynamics on the stability of a power grid with high penetration of variable renewable energies', in *15th IET International Conference on AC and DC Power Transmission (ACDC 2019)*, vol. 2019, Institution of Engineering and Technology, 2019, 87 (6 pp.)–87 (6 pp.) ISBN: 978-1-83953-007-4. DOI: 10.1049/cp.2019.0087.

[103] M. Klein, G. Rogers and P. Kundur, 'A fundamental study of inter-area oscillations in power systems', *IEEE Transactions on Power Systems*, vol. 6, no. 3, pp. 914–921, 1991, ISSN: 08858950. DOI: 10.1109/59.119229.

[104] J. H. Chow, *Power System Coherency and Model Reduction*, J. H. Chow, Ed., ser. Power Electronics and Power Systems. New York, NY: Springer New York, 2013, vol. 94, p. 300, ISBN: 978-1-4614-1802-3. DOI: 10.1007/978-1-4614-1803-0.

[105] N. S. Ugwuanyi, X. Kestelyn, B. Marinescu and O. Thomas, 'Power System Nonlinear Modal Analysis Using Computationally Reduced Normal Form Method', *Energies*, vol. 13, no. 5, p. 1249, 2020, ISSN: 1996-1073. DOI: 10.3390/en13051249.

[106] J. Hefferon, *Linear Algebra*, 3dr ed. Colchester, Vermont USA: Open-source, 2017, p. 507, ISBN: 978-1944325114.

[107] W. E. Boyce and R. C. DiPrima, *Elementary Differential Equations and Boundary Value Problems*, 10th ed. USA: JohnWiley & Sons, Inc., 2012, p. 811, ISBN: 978-0-470-45831-0.

[108] I. Perez-arriaga, G. Verghese and F. Schweppe, 'Selective Modal Analysis with Applications to Electric Power Systems, PART I: Heuristic Introduction', *IEEE Transactions on Power Apparatus and Systems*, vol. PAS-101, no. 9, pp. 3117–3125, 1982, ISSN: 0018-9510. DOI: 10.1109/TPAS.1982.317524.

[109] F. L. Pagola, I. J. Perez-Arriaga and G. C. Verghese, 'On Sensitivities, Residues and Participations. Applications to Oscillatory Stability Analysis and Control', *IEEE Power Engineering Review*, vol. 9, no. 2, pp. 61–61, 1989, ISSN: 0272-1724. DOI: 10.1109/MPER.1989.4310488.

[110] J. Freytes, 'Small-signal stability analysis of Modular Multilevel Converters and application to MMC-based Multi-Terminal DC grids', PhD thesis, Centrale Lille, 2017, p. 263.

[111] S. Akkari, 'Control of a multi-terminal HVDC (MTDC) system and study of the interactions between the MTDC and the AC grids', PhD thesis, Université Paris-Saclay, 2016, p. 210.

[112] M. Patino, S. Hohn, R. Dimitrovski and M. Luther, 'Methodology for state-space modelling of power electronic elements in modern electrical energy systems', in *15th IET International Conference on AC and DC Power Transmission (ACDC 2019)*, vol. 2019, Institution of Engineering and Technology, 2019, 48 (6 pp.)–48 (6 pp.) ISBN: 978-1-83953-007-4. DOI: 10.1049/cp.2019.0048.

[113] E. L. Duke, 'Combining and connecting linear, multi-input, multi-output subsystem models', National Aeronautics and Space Administration (NASA), Edwards, CA, Tech. Rep., 1986, p. 38.

[114] A. A. Rockhill, M. Liserre, R. Teodorescu and P. Rodriguez, 'Grid-Filter Design for a Multimegawatt Medium-Voltage Voltage-Source Inverter', *IEEE Transactions on Industrial Electronics*, vol. 58, no. 4, pp. 1205–1217, 2011, ISSN: 0278-0046. DOI: 10.1109/TIE.2010.2087293.

[115] 'IEEE Recommended Practice and Requirements for Harmonic Control in Electric Power Systems', *IEEE Std 519-2014 (Revision of IEEE Std 519-1992)*, pp. 1–29, 2014. DOI: 10.1109/IEEESTD.2014.6826459.

[116] A. M. Cantarellas, E. Rakhshani, D. Remon and P. Rodriguez, 'Design of the LCL with trap filter for the two-level VSC installed in a large-scale wave power plant', in *2013 IEEE Energy Conversion Congress and Exposition*, IEEE, 2013, pp. 707–712, ISBN: 978-1-4799-0336-8. DOI: 10.1109/ECCE.2013.6646771.

[117] K. Ahmed, S. Finney and B. Williams, 'Passive Filter Design for Three-Phase Inverter Interfacing in Distributed Generation', in *2007 Compatibility in Power Electronics*, IEEE, 2007, pp. 1–9, ISBN: 1-4244-1054-1. DOI: 10.1109/CPE.2007.4296511.

[118] T. Wang, Zhihong Ye, Gautam Sinha and Xiaoming Yuan, 'Output filter design for a grid-interconnected three-phase inverter', in *IEEE 34th Annual Conference on Power Electronics Specialist, 2003. PESC '03.*, vol. 2, IEEE, 2003, pp. 779–784, ISBN: 0-7803-7754-0. DOI: 10.1109/PESC.2003.1218154.

[119] D. P. Dorantes, J. L. Monroy Morales and M. Hernandez Angeles, 'A filter design methodology of a VSC-HVDC system', in *2013 IEEE International Autumn Meeting on Power Electronics and Computing (ROPEC)*, IEEE, 2013, pp. 1–6, ISBN: 978-1-4799-2370-0. DOI: 10.1109/ROPEC.2013.6702737.

[120] V. Prasad, D. Borojevic and R. Zhang, 'Analysis and comparison of space vector modulation schemes for a four-leg voltage source inverter', in *Proceedings of APEC 97 - Applied Power Electronics Conference*, Virginia Polytechnic Institute and State University, vol. 2, IEEE, 1997, pp. 864–871, ISBN: 0-7803-3704-2. DOI: 10.1109/APEC.1997.575747.

[121] G. M. A. Delille, 'Contribution du Stockage à la Gestion Avancée des Systèmes Électriques : approches Organisationnelles et Technico-économiques dans les Réseaux de Distribution', PhD thesis, École Centrale de Lille, 2010, p. 314.

[122] A. E Fitzgerald, C. J. Kingsley and S. D. Umans, *Electric Machinery*, 6th ed. Boston, MA: McGraw-Hill, 2005, p. 688, ISBN: 0-07-366009-4.

[123] ABB Power T&D Company Inc., *Electrical Transmission and Distribution Reference Book*, 5th ed., ETI, Ed. 1997, p. 849.

[124] M. El-Shebiny, *Graph Theory and its application in Electrical Power System*, Cairo, Egypt, 2016.

[125] J. C. Das, *Power System Analysis: Short-Circuit Load Flow and Harmonics*, 1st ed. New York, NY: Marcel Dekker, Inc., 2002, p. 844, ISBN: 0-8247-0737-0.

Appendix A

Adopted conventions

The analysis of complex systems composed of many sources and controllers are constantly realised in this work. In order to correctly design these systems, some conventions must be employed. The mathematical tools which are constantly used in the design of these systems are presented in this section.

A.1 Per unit system

In power systems, powers, voltages and currents have different rated levels in different points of the network. The employment of *per unit* values to express the quantities in a power system offers great advantage when compared to usage of SI.

A correct usage of the per unit system facilitate the comprehension of the phenomena involved in the system operation, since a pre-defined level of these quantities will be equal to 1 per unit (pu).

Another great advantage of the per unit system is the application in control systems, where their parameters are usually calculated to meet certain requirements of performance. In the case in which a control system is designed in SI, its parameters must be imperatively recomputed if the rated values of the electrical quantities change. On the contrary, if the control system is designed in per unit, it is just necessary to modify the per unit conversion between the inputs and outputs of the system.

In this work, it is designed many high complexity systems with multi sources and other devices. The equations, parameters and quantities involved with each element of the grid are expressed using the following per unit system.

Base power (S_b):	Three-phase rated power
Base voltage (V_b):	Rated line-to-line voltage (RMS value)
Base frequency (ω_b):	Nominal angular frequency of the grid
Base current (I_b):	Base power/Base voltage
Base impedance (Z_b):	Base voltage/Base current
Base admittance (Y_b):	Base current/Base voltage
Base inductance (L_b):	Base impedance/Base frequency
Base capacitance (C_b):	Base admittance/Base frequency

The synchronous machines are the only elements in this work which are not expressed in aforementioned per unit system. The modelling of these sources follows the approach used in [52], and therefore, the adopted per unit base is given below.

Base power (S_b):	Three-phase rated power
Base voltage (V_b):	Rated line-to-ground voltage (peak value)
Base current (I_b):	Rated line current (peak value)
Base impedance (Z_b):	Base voltage/Base current

A.2 The Park transformation

In the natural frame of electrical quantities — the abc-frame — a balanced three-phase voltage $v(t)$ is expressed as given in eq. (A.1), where, $\hat{V}$ is amplitude of the voltage, ω is the angular frequency of the signal and φ the initial phase of $v_a(t)$ in relation to a given reference.

$$\begin{cases} v_a(t) = \hat{V}\cos\left(\omega t + \varphi\right) \\ v_b(t) = \hat{V}\cos\left(\omega t - \dfrac{2\pi}{3} + \varphi\right) \\ v_c(t) = \hat{V}\cos\left(\omega t + \dfrac{2\pi}{3} + \varphi\right) \end{cases} \tag{A.1}$$

The same voltage $v(t)$ can be expressed in the rotating dq0-frame, presenting a main advantage over abc-frame: at nominal frequency and under balanced conditions, dq-components are constants and the zero sequence is null.

Considering these properties, it is preferable to design control systems using the latter, since simple PI controllers using dq-components can provide performances as good as complex controllers in abc-frame. Likewise, the interpretation of quantities expressed in dq0-frame is easier than that in abc-frame.

The transposition from the abc to the dq0-frame is made by using the Park transformation. It is possible to find two variants of this transformation in the literature: amplitude and power invariant [52]. In this document, the merit of using one or another variant will not be addressed. Excepting on the modelling of synchronous machines, the transformation adopted in this work is the power invariant.

The power invariant Park transformation is expressed in eq. (A.2). The three-phase voltage $v(t)$ is multiplied by the transformation matrix $P(\theta)$, where θ the angular position considered in the transformation.

$$\begin{bmatrix} v_d(t) \\ v_q(t) \\ v_0(t) \end{bmatrix} = \underbrace{\sqrt{\frac{2}{3}} \begin{bmatrix} \cos(\theta) & \cos\left(\theta - \frac{2\pi}{3}\right) & \cos\left(\theta + \frac{2\pi}{3}\right) \\ -\sin(\theta) & -\sin\left(\theta - \frac{2\pi}{3}\right) & -\sin\left(\theta + \frac{2\pi}{3}\right) \\ \frac{1}{\sqrt{2}} & \frac{1}{\sqrt{2}} & \frac{1}{\sqrt{2}} \end{bmatrix}}_{P(\theta)} \times \begin{bmatrix} v_a(t) \\ v_b(t) \\ v_c(t) \end{bmatrix} \tag{A.2}$$

Substituting eq. (A.1) into eq. (A.2), and considering that $\theta = \omega t + \theta_0$ and $\varphi = 0$, the voltage $v(t)$ is expressed in dq0-frame as:

$$\begin{cases} v_d(t) = \sqrt{\frac{3}{2}}\hat{V}\cos(\theta_0) \\ \\ v_q(t) = \sqrt{\frac{3}{2}}\hat{V}\sin(\theta_0) \end{cases} \tag{A.3}$$

where θ_0 represents the alignment of the d-axis (dq0-frame) in relation to the a-axis (abc-frame). The Park transformation can be applied for other quantities, *mutatis mutandis*.

Likewise, the transposition from the dq0-frame to the abc-frame is made by applying the inverse Park transformation. The three-phase voltage $v(t)$ is computed by multiplying $v_{dq0}(t)$ by the inverse transformation matrix $P(\theta)^{-1}$ as given in eq. (A.4).

$$\begin{bmatrix} v_a(t) \\ v_b(t) \\ v_c(t) \end{bmatrix} = \underbrace{\sqrt{\frac{2}{3}} \begin{bmatrix} \cos(\theta) & -\sin(\theta) & \frac{1}{\sqrt{2}} \\ \cos\left(\theta - \frac{2\pi}{3}\right) & -\sin\left(\theta - \frac{2\pi}{3}\right) & \frac{1}{\sqrt{2}} \\ \cos\left(\theta + \frac{2\pi}{3}\right) & -\sin\left(\theta + \frac{2\pi}{3}\right) & \frac{1}{\sqrt{2}} \end{bmatrix}}_{P(\theta)^{-1}} \times \begin{bmatrix} v_d(t) \\ v_q(t) \\ v_0(t) \end{bmatrix} \tag{A.4}$$

Appendix B

Small-signal stability analysis

Many systems of any nature, as the power systems, display non-linear physical relationship, where the principle of superposition does not apply. However, in normal operation, where the behaviour of the non-linear system can be fairly reproduced using its linearised representation around an equilibrium point [52], [54], [78]. In this work, the carried out studies consider the normal operation of the systems, and consequently, small-signal stability analysis is suitable to model these systems in mathematical terms and to analyse their dynamic characteristics.

B.1 Linearisation of non-linear system

The linear representation of a non-linear system is obtained expanding its mathematical functions into a Taylor series, and neglecting the high order terms. Equation (B.1) illustrates the Taylor expansion of a generic function $y = f(x)$, where x_0 and y_0 are, respectively, the input and output equilibrium point, and y_{lin} is the linearised function.

$$\begin{aligned} y &= f(x) \\ &= \underbrace{\underbrace{f(x_0)}_{y_0} + \frac{df}{dx}(x - x_0)}_{y_{lin}} + \underbrace{\sum_{n=2}^{\infty} \frac{1}{n!}\frac{d^n f}{dx^n}(x - x_0)^n}_{\text{High order terms}} \end{aligned} \tag{B.1}$$

Figure B.1 gives a visual representation of the eq. (B.1). It can be observed that compliance between the non-linear system and its linearised representation depends both on the non-linearity level of the function and the magnitude of the input variation, i.e. the function is more linear around A than B, and the deviation between the non-linear and linearised functions is small as the input variation is lower. In the case where the linearised

representation is not capable of providing a good compliance with the non-linear system, an alternative non-linear modal analysis can be employed [105].

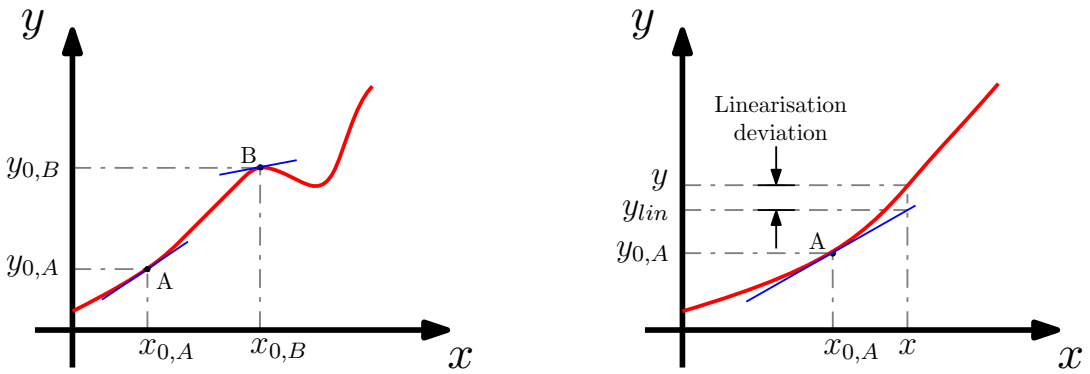

(a) General view (b) Magnified view around A

Figure B.1 – Illustration a generic non-linear function and its linearised representation.

B.2 State-space from differential-algebraic equations

The aforementioned approach can be generalised for a non-linear system composed of a set of differential-algebraic equations with multiple inputs and outputs as expressed in eq. (B.2).

$$\begin{cases} \dot{\mathbf{x}} = \mathbf{f}(\mathbf{x}, \mathbf{z}, \mathbf{u}) \\ 0 = \mathbf{g}(\mathbf{x}, \mathbf{z}, \mathbf{u}) \\ \mathbf{y} = \mathbf{h}(\mathbf{x}, \mathbf{z}, \mathbf{u}) \end{cases} \tag{B.2}$$

where $\mathbf{x}$, $\mathbf{z}$, $\mathbf{u}$ and $\mathbf{y}$ are the column vectors of differential states and algebraic variables, system inputs and outputs. Linearising eq. (B.2) around an equilibrium point $\gamma = (\mathbf{x_0}, \mathbf{z_0}, \mathbf{u_0})$:

$$\begin{cases} \Delta\dot{\mathbf{x}} = \left.\dfrac{\partial \mathbf{f}}{\partial \mathbf{x}}\right|_\gamma \Delta\mathbf{x} + \left.\dfrac{\partial \mathbf{f}}{\partial \mathbf{z}}\right|_\gamma \Delta\mathbf{z} + \left.\dfrac{\partial \mathbf{f}}{\partial \mathbf{u}}\right|_\gamma \Delta\mathbf{u} \\ 0 = \left.\dfrac{\partial \mathbf{g}}{\partial \mathbf{x}}\right|_\gamma \Delta\mathbf{x} + \left.\dfrac{\partial \mathbf{g}}{\partial \mathbf{z}}\right|_\gamma \Delta\mathbf{z} + \left.\dfrac{\partial \mathbf{g}}{\partial \mathbf{u}}\right|_\gamma \Delta\mathbf{u} \\ \Delta\mathbf{y} = \left.\dfrac{\partial \mathbf{h}}{\partial \mathbf{x}}\right|_\gamma \Delta\mathbf{x} + \left.\dfrac{\partial \mathbf{h}}{\partial \mathbf{z}}\right|_\gamma \Delta\mathbf{z} + \left.\dfrac{\partial \mathbf{h}}{\partial \mathbf{u}}\right|_\gamma \Delta\mathbf{u} \end{cases} \tag{B.3}$$

From this point, the dependencies on the equilibrium point γ are omitted to simplify the notations. If $\dfrac{\partial \mathbf{g}}{\partial z}$ is non-singular, it is possible to isolate $\Delta\mathbf{z}$ in the second line of eq. (B.3) and substitute it in the first and third lines:

$$\begin{cases} \Delta\dot{\mathbf{x}} = \underbrace{\left[\dfrac{\partial \mathbf{f}}{\partial \mathbf{x}} - \dfrac{\partial \mathbf{f}}{\partial \mathbf{z}}\left(\dfrac{\partial \mathbf{g}}{\partial \mathbf{z}}\right)^{-1}\dfrac{\partial \mathbf{g}}{\partial \mathbf{x}}\right]}_{\mathbf{A}}\Delta\mathbf{x} + \underbrace{\left[\dfrac{\partial \mathbf{f}}{\partial \mathbf{u}} - \dfrac{\partial \mathbf{f}}{\partial \mathbf{z}}\left(\dfrac{\partial \mathbf{g}}{\partial \mathbf{z}}\right)^{-1}\dfrac{\partial \mathbf{g}}{\partial \mathbf{u}}\right]}_{\mathbf{B}}\Delta\mathbf{u} \\ \Delta\mathbf{y} = \underbrace{\left[\dfrac{\partial \mathbf{h}}{\partial \mathbf{x}} - \dfrac{\partial \mathbf{h}}{\partial \mathbf{z}}\left(\dfrac{\partial \mathbf{g}}{\partial \mathbf{z}}\right)^{-1}\dfrac{\partial \mathbf{g}}{\partial \mathbf{x}}\right]}_{\mathbf{C}}\Delta\mathbf{x} + \underbrace{\left[\dfrac{\partial \mathbf{h}}{\partial \mathbf{u}} - \dfrac{\partial \mathbf{h}}{\partial \mathbf{z}}\left(\dfrac{\partial \mathbf{g}}{\partial \mathbf{z}}\right)^{-1}\dfrac{\partial \mathbf{g}}{\partial \mathbf{u}}\right]}_{\mathbf{D}}\Delta\mathbf{u} \end{cases} \tag{B.4}$$

where $\mathbf{A}$, $\mathbf{B}$, $\mathbf{C}$ and $\mathbf{D}$ are the state matrix, the input matrix, the output matrix, and the direct transmission matrix. The form of eq. (B.4) is known as state-space representation of a system. In order to simplify the notation, Δ is usually omitted, and the system is rewritten as given in eq. (B.5).

$$\begin{cases} \dot{\mathbf{x}} = \mathbf{A}\mathbf{x} + \mathbf{B}\mathbf{u} \\ \mathbf{y} = \mathbf{C}\mathbf{x} + \mathbf{D}\mathbf{u} \end{cases} \tag{B.5}$$

B.3 Stability and dynamic behaviour of linear systems

The state matrix of a linear system can be used to identify the eigenvalues and eigenvectors of the system, which are very useful to determine the stability of the system. The state matrix can be seen as a linear transformation, and, in linear algebra, an eigenvector is defined as the vector that remains in its own span during the transformation, only being scaled by a factor λ [106], as indicated in eq. (B.6).

$$\begin{cases} \upsilon\mathbf{A} = \lambda\upsilon \\ \mathbf{A}\nu = \lambda\nu \end{cases} \tag{B.6}$$

where υ and ν are known as left and right eigenvectors due to their relative position regarding the linear transformation. It should be highlighted that, in order to satisfy eq. (B.6), υ and

ν are row and column vectors, respectively. Rearranging the second line of eq. (B.6):

$$(\mathbf{A} - \lambda\mathbf{I})\,\nu = 0 \tag{B.7}$$

Since it is required that ν be non-null, the matrix $(\mathbf{A} - \lambda\mathbf{I})$ must be singular to solve eq. (B.7). Therefore:

$$\det(\mathbf{A} - \lambda\mathbf{I}) = 0 \tag{B.8}$$

The expansion of eq. (B.8) is also known as characteristic polynomial of the system, and the scalars λ which solve this equation are known as the eigenvalues of the linear transformation. For a generic linear system with n differential states, and therefore, n eigenvalues, the time response of a differential state m can be expressed as a linear combination of the solutions of the differential equations [52], [78], [106], [107], as given in eq. (B.9).

$$\Delta x_m(t) = \sum_{i=1}^{n} \nu_{mi} \left(\sum_{k=1}^{n} \upsilon_{ik} \Delta x_{k,0} \right) e^{\lambda_i t} \tag{B.9}$$

It is emphasised that the necessary condition to the system be stable, the solution of all differential equations must achieve the equilibrium, i.e.:

$$\lim_{t\to\infty} e^{\lambda_i t} = 0 \tag{B.10}$$

The condition expressed in eq. (B.10) is satisfied if all $\Re\{\lambda_i\} < 0$. As illustrated in Figure B.2, if any λ_i does not satisfy the necessary condition, all differential states diverge, and the system is unstable.

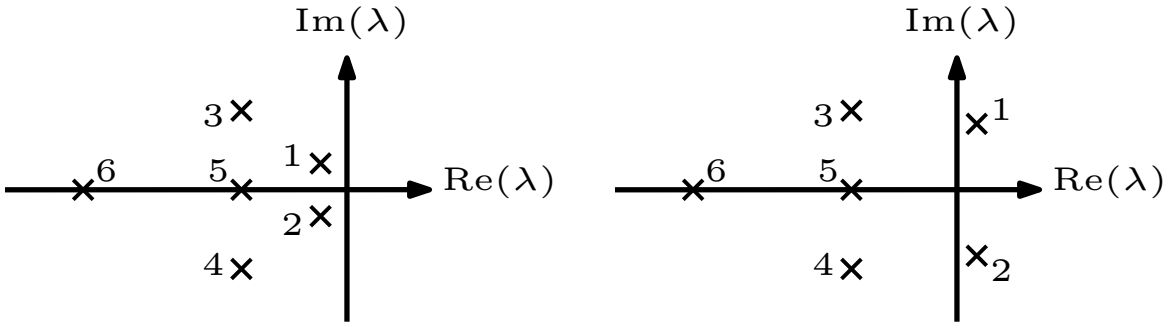

(a) Stable (b) Unstable

Figure B.2 – Illustration of the necessary condition to the stability of a linear system.

The aforementioned condition guarantees that any transient response of the system eventually reaches the equilibrium, however, it does not guarantee a satisfactory transient response characteristics. Depending on the nature of λ_i, the solution a differential equation ($y_i(t)$) can or cannot present an oscillatory behaviour with frequency equal to ω_i rad/s during the decay. Note that, despite $y_i(t)$ being a complex solution for $\lambda_i = \sigma_i + j\omega_i$, since each complex λ_i has a conjugate pair, the final solution is a real function.

$$\begin{cases} y_i(t) \propto e^{\sigma_i t} & \text{if } \lambda_i = \sigma_i \\ y_i(t) \propto e^{\sigma_i t}\left(\cos\omega_i t + j\sin\omega_i t\right) & \text{if } \lambda_i = \sigma_i + j\omega_i \end{cases} \tag{B.11}$$

The speed of decay of each $y_i(t)$ depends on the value of the time constant $-1/\sigma_i$. For purely real eigenvalues, adopting a 2% criterion for the settling time, it is considered that the transient response of $y_i(t)$ completely decays in approximately $-4/\sigma_i$, i.e. the solution reaches 98% of the equilibrium value after $-4/\sigma_i$. For complex conjugate eigenvalues, the settling time of $y_i(t)$ depends on the damping ratio of the eigenvalues, however, the value $-4/\sigma_i$ can still be considered for $0 < \xi < 0.9$ [78]. The ξ_i of an eigenvalue λ_i is computed as given in eq. (B.12).

$$\xi_i = \frac{-\sigma_i}{\sqrt{\sigma_i^2 + \omega_i^2}} \tag{B.12}$$

Since the transient response of a signal $y(t)$ is a linear combination of all $y_i(t)$, it cannot be satisfactory if the dominant eigenvalues related to $y(t)$ are poorly damped and/or too slow [78].

The stability and/or the transient response of the system can be enhanced by displacing the responsible eigenvalue(s) to a more convenient position in the complex plane. It can be achieved by tuning the parameters which have a direct link with the differential states displaying important relationship with the target eigenvalues. However, despite the position of the eigenvalues in the complex plane indicates about the stability and the dynamic response of the system, it does not indicate which states/parameters have influence on the instability or unacceptable transient response.

B.4 Matrix of participation factors

The matrix of participation factors can be used to identify the influence of the states in each eigenvalues of the system [52], [54], [108], [109]. This matrix is computed considering the left and right eigenvalues matrices of the system. The solution of eq. (B.6) for a given

eigenvalue λ_i results in two eigenvectors of dimensions $1 \times n$ and $n \times 1$ for the left and the right eigenvectors, respectively, where n indicates the number of differential states.

$$\upsilon_{\mathbf{i}} = \begin{bmatrix} \upsilon_{i1} & \upsilon_{i2} & \dots & \upsilon_{in} \end{bmatrix} \qquad \nu_{\mathbf{i}} = \begin{bmatrix} \nu_{1i} \\ \nu_{2i} \\ \vdots \\ \nu_{ni} \end{bmatrix} \tag{B.13}$$

It is convenient to normalise the eigenvectors such as $\upsilon_{\mathbf{i}}\nu_{\mathbf{i}} = 1$. Repeating the process to all eigenvalues of the system, and concatenating the respective eigenvectors together, it is obtained the matrices of eigenvectors:

$$\Upsilon = \begin{bmatrix} \upsilon_{11} & \upsilon_{12} & \dots & \upsilon_{1n} \\ \upsilon_{21} & \upsilon_{22} & \dots & \upsilon_{2n} \\ \vdots & \vdots & \ddots & \vdots \\ \upsilon_{i1} & \upsilon_{i2} & \dots & \upsilon_{in} \end{bmatrix} \qquad \Lambda = \begin{bmatrix} \nu_{11} & \nu_{12} & \dots & \nu_{1i} \\ \nu_{21} & \nu_{22} & \dots & \nu_{2i} \\ \vdots & \vdots & \ddots & \vdots \\ \nu_{n1} & \nu_{n2} & \dots & \nu_{ni} \end{bmatrix} \tag{B.14}$$

where Υ and Λ are the matrices of left and right eigenvectors, respectively. It should be highlighted that, since the number of eigenvalues is imperatively equal to the number of differential states, $i = n$, and both Υ and Λ are square matrices. The rows and columns of Υ represent, respectively, the eigenvalues and the differential states, whereas those of Λ, the differential states and the eigenvalues. Since the matrices are normalised, $\Upsilon\Lambda = \mathbf{I}$.

The matrix of participation factors ($\mathbf{P}$) is computed as the element-wise product between the transposed matrix of left eigenvectors and the matrix of right eigenvectors, as given in eq. (B.15). Since the eigenvector matrices are normalised, the sum of each row or each column of P is equal to 1. The same does not apply to the sum of the magnitudes of the elements of P.

$$\mathbf{P} = \Upsilon^T \odot \Lambda$$

$$= \begin{array}{c} \\ \\ \text{Diff. states} \\ \downarrow \end{array} \begin{array}{c} \\ \\ \mathrm{x}_1 \\ \mathrm{x}_2 \\ \vdots \\ \mathrm{x}_n \end{array} \begin{array}{c} \overset{\text{Eigenvalues}}{\longrightarrow} \\ \lambda_1 \quad \lambda_2 \quad \dots \quad \lambda_i \\ \begin{bmatrix} \upsilon_{11}\nu_{11} & \upsilon_{21}\nu_{12} & \dots & \upsilon_{i1}\nu_{1i} \\ \upsilon_{12}\nu_{21} & \upsilon_{22}\nu_{22} & \dots & \upsilon_{i2}\nu_{2i} \\ \vdots & \vdots & \ddots & \vdots \\ \upsilon_{1n}\nu_{n1} & \upsilon_{2n}\nu_{n2} & \dots & \upsilon_{in}\nu_{ni} \end{bmatrix} \end{array} \tag{B.15}$$

The magnitude of each element P_{ni} indicates the relative participation of the differential state x_n in the eigenvalue λ_i and *vice versa*. As bigger is the magnitude of P_{ni}, higher is the relationship between x_n and λ_i. Therefore, in order to displace an eigenvalue, it is necessary to identify the differential states the most related to it, and perform a variation in the parameters which are, in turn, the most related to these states.

B.5 Dynamic analysis with stability surfaces

As illustrated in Figure B.3, many stability studies are conducted observing the trajectory of the eigenvalues of the system as a function of 1-D parametric variation [52], [55], [78]. Very often, even 2-D parametric variations are performed in some studies, where the second parameter is discretely varied, resulting in multiple side-by-side eigenvalues trajectories, which demands an important effort in the analysis.

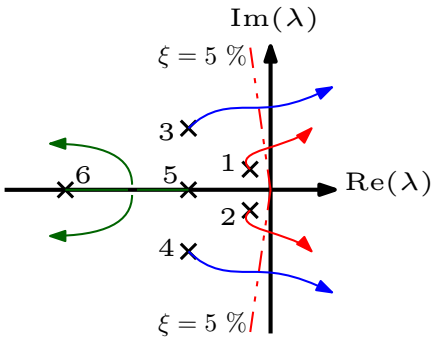

Figure B.3 – Illustration of eigenvalues trajectory.

Stability surface [102] is a variant of the eigenvalues analysis which allows the simultaneous variation of any two parameters of the system and provides an easy interpretation of the findings. Considering the p_1p_2-plane representing the 2-D space of the parameters p_1 and p_2, the stability surface is a template indicating the regions where the system can satisfactorily operates as a function of both parameters according to the established criteria.

In eigenvalues analysis, the standard criterion to determine the stability of a system is that the real part of all eigenvalues must be negative. However this criterion does not analyse whether or not the dynamics of the system are acceptable. In power systems, poorly damped oscillating phenomena can jeopardise the stability of the grid, and the integrity of its elements.

The method of stability surfaces uses the damping ratio (ξ) of the eigenvalues of the system as the criterion to determine whether or not the system is stable and it can acceptably operates. For this purpose, a critical damping ratio (ξ_{cr}) is defined as minimal threshold.

The threshold of ξ is any positive real value, and it can be adapted to the envisaged study (e.g. multiple criteria can be adopted for different eigenvalues). It can be observed that the standard stability criterion is embedded into eq. (B.12), since if $\sigma < 0$, ξ is negative.

The key idea of the proposed method is to compute the ξ value of the eigenvalues of the system for all (p_1, p_2) of the parametric variation, and to construct the ξ surfaces as a function of these parameters, as illustrated in Figure B.4. It is defined as critical eigenvalues, those going towards, and eventually crossing, the critical damping ratio (ξ_{cr}) adopted as threshold for the study. Since the method separately evaluates the surface of each eigenvalue, an algorithm to track the movement the eigenvalues as a function of the parametric variation is envisaged in order to prevent their misclassification, and therefore, to prevent the loss of consistency in the analysis.

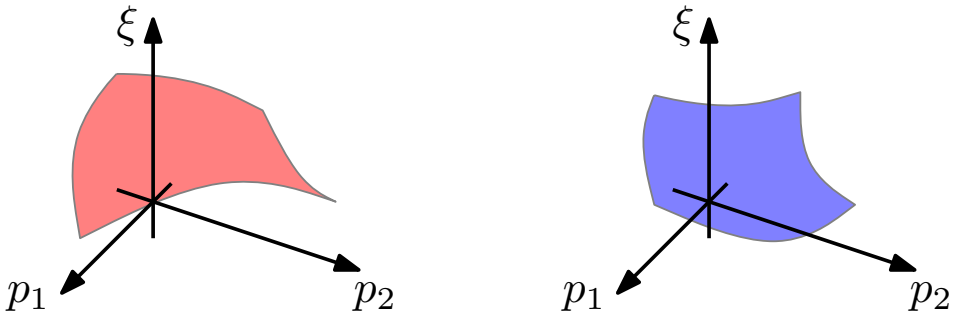

(a) ξ surface of $\lambda_{1,2}$ (b) ξ surface of $\lambda_{3,4}$

Figure B.4 – Illustration of ξ surfaces related to the critical eigenvalues of the system.

A dedicated algorithm identifies in each 3-D surface the points of (p_1, p_2) where ξ do not meet the established criterion, and projects them into the p_1p_2-plane. The projection of each 3-D surface corresponds to the non-conformity zone of each critical eigenvalue. As illustrated in Figure B.5, the superposition of all projections gives the template indicating the global instability zone, where the system is not in compliance to operate or even unstable. As in classic small-signal stability analysis, seeking stability enhancement, the participation factor matrix can be used to identify the states most related to the critical eigenvalues of the system.

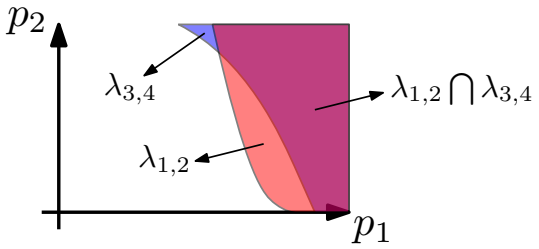

Figure B.5 – Illustration of a template indicating the pairs p_1p_2 where the system does not satisfactorily operates according to the established criteria.

B.6 Association of multiple local state-space systems into a global system

In this section, it is developed the principle of the association of multiple state-space representations, which is a handful technique in the design of high complexity systems with multiple sources and other elements as those designed in this work. The following development is based on [110]–[113].

Considering n state-space models in which each one is expressed as in eq. (B.5). As expressed in eq. (B.16), the first step of the approach is to concatenate all state-spaces together, creating an intermediary representation — open-loop state-space — identified with the subscript "ol". An illustrative representation of the first step to associate multiple state-spaces is given in Figure B.6.

$$\begin{cases} \dot{\mathbf{x}}_{\mathbf{ol}} = \mathbf{A}_{\mathbf{ol}}\mathbf{x}_{\mathbf{ol}} + \mathbf{B}_{\mathbf{ol}}\mathbf{u}_{\mathbf{ol}} \\ \mathbf{y}_{\mathbf{ol}} = \mathbf{C}_{\mathbf{ol}}\mathbf{x}_{\mathbf{ol}} + \mathbf{D}_{\mathbf{ol}}\mathbf{u}_{\mathbf{ol}} \end{cases} \tag{B.16}$$

where the vectors $\mathbf{x_{ol}}$, $\mathbf{u_{ol}}$ and $\mathbf{y_{ol}}$, and the matrices $\mathbf{A_{ol}}$, $\mathbf{B_{ol}}$, $\mathbf{C_{ol}}$ and $\mathbf{D_{ol}}$ are expressed respectively as in eqs. (B.17) and (B.18).

$$\mathbf{x_{ol}} = \begin{bmatrix} \mathbf{x_1} \\ \mathbf{x_2} \\ \vdots \\ \mathbf{x_{n-1}} \\ \mathbf{x_n} \end{bmatrix} \qquad \mathbf{u_{ol}} = \begin{bmatrix} \mathbf{u_1} \\ \mathbf{u_2} \\ \vdots \\ \mathbf{u_{n-1}} \\ \mathbf{u_n} \end{bmatrix} \qquad \mathbf{y_{ol}} = \begin{bmatrix} \mathbf{y_1} \\ \mathbf{y_2} \\ \vdots \\ \mathbf{y_{n-1}} \\ \mathbf{y_n} \end{bmatrix} \tag{B.17}$$

$$\mathbf{A_{ol}} = \begin{bmatrix} \mathbf{A_1} & 0 & \dots & 0 & 0 \\ 0 & \mathbf{A_2} & \dots & 0 & 0 \\ \vdots & \vdots & \ddots & \vdots & \vdots \\ 0 & 0 & \dots & \mathbf{A_{n-1}} & 0 \\ 0 & 0 & \dots & 0 & \mathbf{A_n} \end{bmatrix} \qquad \mathbf{B_{ol}} = \begin{bmatrix} \mathbf{B_1} & 0 & \dots & 0 & 0 \\ 0 & \mathbf{B_2} & \dots & 0 & 0 \\ \vdots & \vdots & \ddots & \vdots & \vdots \\ 0 & 0 & \dots & \mathbf{B_{n-1}} & 0 \\ 0 & 0 & \dots & 0 & \mathbf{B_n} \end{bmatrix}$$

$$\mathbf{C_{ol}} = \begin{bmatrix} \mathbf{C_1} & 0 & \dots & 0 & 0 \\ 0 & \mathbf{C_2} & \dots & 0 & 0 \\ \vdots & \vdots & \ddots & \vdots & \vdots \\ 0 & 0 & \dots & \mathbf{C_{n-1}} & 0 \\ 0 & 0 & \dots & 0 & \mathbf{C_n} \end{bmatrix} \qquad \mathbf{D_{ol}} = \begin{bmatrix} \mathbf{D_1} & 0 & \dots & 0 & 0 \\ 0 & \mathbf{D_2} & \dots & 0 & 0 \\ \vdots & \vdots & \ddots & \vdots & \vdots \\ 0 & 0 & \dots & \mathbf{D_{n-1}} & 0 \\ 0 & 0 & \dots & 0 & \mathbf{D_n} \end{bmatrix} \tag{B.18}$$

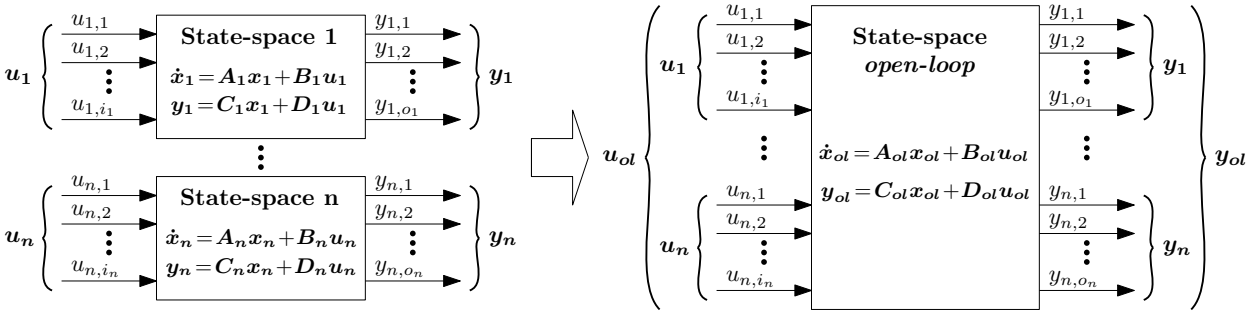

Figure B.6 – Illustrative representation of the concatenation of n state-space models.

The second step of the process is to define the connection between the inputs and outputs of the n state-spaces and to define the so-called global inputs and outputs of the system, i.e. inputs and outputs of the desired closed-loop state-space model, identified with the subscript "cl". Figure B.7 illustrates the second step to associate multiple state-space models.

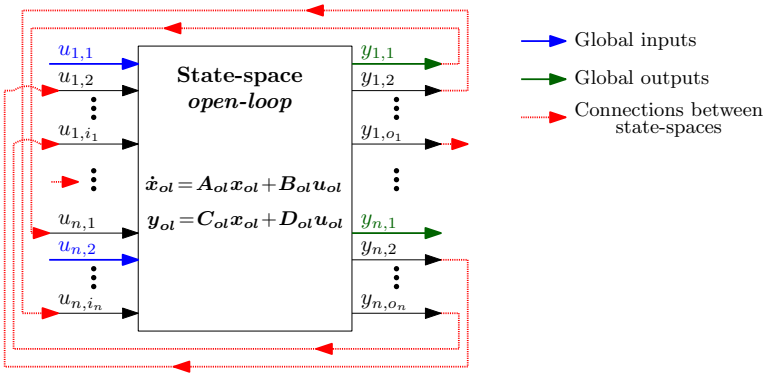

Figure B.7 – Connections between state-spaces and definition of global inputs and outputs of the system.

As expressed in eq. (B.19), the ensemble of open-loop inputs ($\mathbf{u_{ol}}$) can be expressed a combination of open-loop outputs ($\mathbf{y_{ol}}$) and closed-loop inputs of the system ($\mathbf{u_{cl}}$). Likewise, the closed-loop outputs of the system ($\mathbf{y_{cl}}$) can also be expressed as a combination of the same variables. The aforementioned relationships are indicated with the matrices $\mathbf{M_{11}}$, $\mathbf{M_{12}}$, $\mathbf{M_{21}}$ and $\mathbf{M_{11}}$.

$$\begin{cases} \mathbf{u_{ol}} = \mathbf{M_{11}}\mathbf{y_{ol}} + \mathbf{M_{12}}\mathbf{u_{cl}} \\ \mathbf{y_{cl}} = \mathbf{M_{21}}\mathbf{y_{ol}} + \mathbf{M_{22}}\mathbf{u_{cl}} \end{cases} \tag{B.19}$$

The closed-loop state-space representation of the composite system is expressed as in eq. (B.20), and the third step of the algorithm is to compute the matrices $\mathbf{A_{cl}}$, $\mathbf{B_{cl}}$, $\mathbf{C_{cl}}$ and $\mathbf{D_{cl}}$ of this representation. Note that $\mathbf{x_{cl}}$ is equal to $\mathbf{x_{ol}}$.

$$\begin{cases} \dot{\mathbf{x}}_{\mathbf{cl}} = \mathbf{A}_{\mathbf{cl}}\mathbf{x}_{\mathbf{cl}} + \mathbf{B}_{\mathbf{cl}}\mathbf{u}_{\mathbf{cl}} \\ \mathbf{y}_{\mathbf{cl}} = \mathbf{C}_{\mathbf{cl}}\mathbf{x}_{\mathbf{cl}} + \mathbf{D}_{\mathbf{cl}}\mathbf{u}_{\mathbf{cl}} \end{cases} \tag{B.20}$$

In order to compute the aforementioned matrices, some algebraic manipulations are required. Replacing $\mathbf{u}_{\mathbf{ol}}$ of eq. (B.16) by the first line of eq. (B.19):

$$\begin{cases} \dot{\mathbf{x}}_{\mathbf{ol}} = \mathbf{A}_{\mathbf{ol}}\mathbf{x}_{\mathbf{ol}} + \mathbf{B}_{\mathbf{ol}}\big(\mathbf{M}_{\mathbf{11}}\mathbf{y}_{\mathbf{ol}} + \mathbf{M}_{\mathbf{12}}\mathbf{u}_{\mathbf{cl}}\big) \\ \mathbf{y}_{\mathbf{ol}} = \mathbf{C}_{\mathbf{ol}}\mathbf{x}_{\mathbf{ol}} + \mathbf{D}_{\mathbf{ol}}\big(\mathbf{M}_{\mathbf{11}}\mathbf{y}_{\mathbf{ol}} + \mathbf{M}_{\mathbf{12}}\mathbf{u}_{\mathbf{cl}}\big) \end{cases} \tag{B.21}$$

Expanding the second line of eq. (B.21):

$$\begin{aligned} \mathbf{y}_{\mathbf{ol}} &= \mathbf{C}_{\mathbf{ol}}\mathbf{x}_{\mathbf{ol}} + \mathbf{D}_{\mathbf{ol}}\big(\mathbf{M}_{\mathbf{11}}\mathbf{y}_{\mathbf{ol}} + \mathbf{M}_{\mathbf{12}}\mathbf{u}_{\mathbf{cl}}\big) \\ (I - \mathbf{D}_{\mathbf{ol}}\mathbf{M}_{\mathbf{11}})\,\mathbf{y}_{\mathbf{ol}} &= \mathbf{C}_{\mathbf{ol}}\mathbf{x}_{\mathbf{ol}} + \mathbf{D}_{\mathbf{ol}}\mathbf{M}_{\mathbf{12}}\mathbf{u}_{\mathbf{cl}} \\ \mathbf{y}_{\mathbf{ol}} &= \underbrace{(\mathbf{I} - \mathbf{D}_{\mathbf{ol}}\mathbf{M}_{\mathbf{11}})^{-1}}_{\mathbf{E}_{\mathbf{ol}}}\big(\mathbf{C}_{\mathbf{ol}}\mathbf{x}_{\mathbf{ol}} + \mathbf{D}_{\mathbf{ol}}\mathbf{M}_{\mathbf{12}}\mathbf{u}_{\mathbf{cl}}\big) \end{aligned} \tag{B.22}$$

Replacing $\mathbf{y}_{\mathbf{ol}}$ in the first line of eq. (B.21) by eq. (B.22):

$$\begin{aligned} \dot{\mathbf{x}}_{\mathbf{ol}} &= \mathbf{A}_{\mathbf{ol}}\mathbf{x}_{\mathbf{ol}} + \mathbf{B}_{\mathbf{ol}}\big(\mathbf{M}_{\mathbf{11}}\mathbf{E}_{\mathbf{ol}}\big(\mathbf{C}_{\mathbf{ol}}\mathbf{x}_{\mathbf{ol}} + \mathbf{D}_{\mathbf{ol}}\mathbf{M}_{\mathbf{12}}\mathbf{u}_{\mathbf{cl}}\big) + \mathbf{M}_{\mathbf{12}}\mathbf{u}_{\mathbf{cl}}\big) \\ &= \mathbf{A}_{\mathbf{ol}}\mathbf{x}_{\mathbf{ol}} + \mathbf{B}_{\mathbf{ol}}\mathbf{M}_{\mathbf{11}}\mathbf{E}_{\mathbf{ol}}\mathbf{C}_{\mathbf{ol}}\mathbf{x}_{\mathbf{ol}} + \mathbf{B}_{\mathbf{ol}}\mathbf{M}_{\mathbf{11}}\mathbf{E}_{\mathbf{ol}}\mathbf{D}_{\mathbf{ol}}\mathbf{M}_{\mathbf{12}}\mathbf{u}_{\mathbf{cl}} + \mathbf{B}_{\mathbf{ol}}\mathbf{M}_{\mathbf{12}}\mathbf{u}_{\mathbf{cl}} \\ &= \big(\mathbf{A}_{\mathbf{ol}} + \mathbf{B}_{\mathbf{ol}}\mathbf{M}_{\mathbf{11}}\mathbf{E}_{\mathbf{ol}}\mathbf{C}_{\mathbf{ol}}\big)\mathbf{x}_{\mathbf{ol}} + \big(\mathbf{B}_{\mathbf{ol}}\mathbf{M}_{\mathbf{11}}\mathbf{E}_{\mathbf{ol}}\mathbf{D}_{\mathbf{ol}} + \mathbf{B}_{\mathbf{ol}}\big)\mathbf{M}_{\mathbf{12}}\mathbf{u}_{\mathbf{cl}} \end{aligned} \tag{B.23}$$

Replacing $\mathbf{y}_{\mathbf{ol}}$ in the second line of eq. (B.19) by eq. (B.22):

$$\begin{aligned} \mathbf{y}_{\mathbf{cl}} &= \mathbf{M}_{\mathbf{21}}\mathbf{E}_{\mathbf{ol}}\big(\mathbf{C}_{\mathbf{ol}}\mathbf{x}_{\mathbf{ol}} + \mathbf{D}_{\mathbf{ol}}\mathbf{M}_{\mathbf{12}}\mathbf{u}_{\mathbf{cl}}\big) + \mathbf{M}_{\mathbf{22}}\mathbf{u}_{\mathbf{cl}} \\ &= \mathbf{M}_{\mathbf{21}}\mathbf{E}_{\mathbf{ol}}\mathbf{C}_{\mathbf{ol}}\mathbf{x}_{\mathbf{ol}} + \mathbf{M}_{\mathbf{21}}\mathbf{E}_{\mathbf{ol}}\mathbf{D}_{\mathbf{ol}}\mathbf{M}_{\mathbf{12}}\mathbf{u}_{\mathbf{cl}} + \mathbf{M}_{\mathbf{22}}\mathbf{u}_{\mathbf{cl}} \\ &= \mathbf{M}_{\mathbf{21}}\mathbf{E}_{\mathbf{ol}}\mathbf{C}_{\mathbf{ol}}\mathbf{x}_{\mathbf{ol}} + \big(\mathbf{M}_{\mathbf{21}}\mathbf{E}_{\mathbf{ol}}\mathbf{D}_{\mathbf{ol}}\mathbf{M}_{\mathbf{12}} + \mathbf{M}_{\mathbf{22}}\big)\,\mathbf{u}_{\mathbf{cl}} \end{aligned} \tag{B.24}$$

Since $\mathbf{x_{ol}} = \mathbf{x_{cl}}$, from the comparison of eq. (B.23) and eq. (B.24) with eq. (B.20), the matrices $\mathbf{A_{cl}}$, $\mathbf{B_{cl}}$, $\mathbf{C_{cl}}$ and $\mathbf{D_{cl}}$ are expressed as in eq. (B.25). A illustration of the resulting closed-loop state-space representation of the system is given in Figure B.8.

$$\begin{cases} \mathbf{A_{cl}} = \mathbf{A_{ol}} + \mathbf{B_{ol}}\mathbf{M_{11}}\mathbf{E_{ol}}\mathbf{C_{ol}} \\ \mathbf{B_{cl}} = \left(\mathbf{B_{ol}}\mathbf{M_{11}}\mathbf{E_{ol}}\mathbf{D_{ol}} + \mathbf{B_{ol}}\right)\mathbf{M_{12}} \\ \mathbf{C_{cl}} = \mathbf{M_{21}}\mathbf{E_{ol}}\mathbf{C_{ol}} \\ \mathbf{D_{cl}} = \mathbf{M_{21}}\mathbf{E_{ol}}\mathbf{D_{ol}}\mathbf{M_{12}} + \mathbf{M_{22}} \end{cases} \tag{B.25}$$

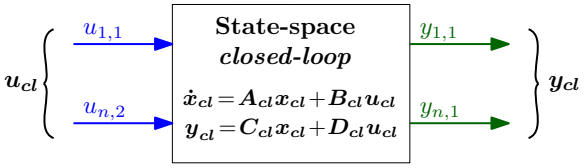

Figure B.8 – Illustration of the resulting closed-loop state-space representation of the system

Appendix C

Design of LCL Filters for VSCs

Variable Renewable Energies (VREs) — i.e. wind and photovoltaic — are usually interfaced via Power Electronics (PE) devices. In the case of a two-level Voltage Source Converter (VSC), the power width modulation generates large voltage and current harmonic spectra [114], [115]. The harmonics flow causes distortions in the sinusoidal shape of voltage and current, which can inflict interference with communication circuits and higher losses in electromagnetic devices [115]. In order to mitigate these issues, IEEE519/2014 [115] specifies limits for harmonic-current injection at the point of common coupling of generators as a function of their short circuit ratio. For VSC applications, L, LC and LCL filters, with or without trap, are found in the literature as solutions to mitigate harmonic current injection [114], [116]–[119]. Based on the literature, this chapter presents an algorithm for the design of LCL filters satisfying the requirements of IEEE519.

The basic structure of an LCL filter is illustrated in Figure C.1. It is composed of two inductances, L_s and L_t, and a shunt capacitor, C_s, between them. The resistances of the inductors are represented with R_s and R_t, and the parasite resistance of the capacitor is neglected.

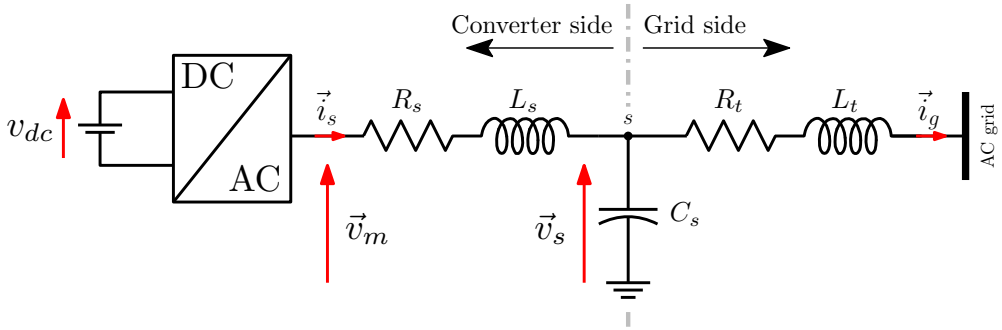

Figure C.1 – Single line diagram of an inverter connected to the grid via an LCL filter.

Since the objective of the filter is to mitigate the harmonic-current injection generated by the modulation of the output voltage of the inverter, the transfer functions $H_1(s) = i_s/v_m$

and $H_2(s) = i_g/v_m$ given in eq. (C.1) are employed for the design of the parameters of the filter. The resonance frequency of $H_1(s)$ and $H_2(s)$, ω_r and $\omega_{r'}$, given in eq. (C.2).

$$H_1(s) = \frac{i_s}{v_m} = \frac{1}{L_s} \frac{s^2 + \frac{R_t}{L_t} s + {\omega_{r'}}^2}{s^3 + \left(\frac{R_s}{L_s} + \frac{R_t}{L_t}\right) s^2 + \left({\omega_r}^2 + \frac{R_s R_t}{L_s L_t}\right) s + \left(\frac{R_s + R_t}{L_s}\right) {\omega_{r'}}^2}$$
$$H_2(s) = \frac{i_g}{v_m} = \frac{1}{L_s} \frac{{\omega_{r'}}^2}{s^3 + \left(\frac{R_s}{L_s} + \frac{R_t}{L_t}\right) s^2 + \left({\omega_r}^2 + \frac{R_s R_t}{L_s L_t}\right) s + \left(\frac{R_s + R_t}{L_s}\right) {\omega_{r'}}^2} \tag{C.1}$$

$$\omega_r = \frac{1}{\sqrt{C_s L'}}, \qquad \text{where: } L' = \frac{L_s L_t}{L_s + L_t}$$
$$\omega_{r'} = \frac{1}{\sqrt{C_s L_t}} \tag{C.2}$$

Figure C.2 illustrates the Bode diagram of $H_1(s)$ and $H_2(s)$ and their relevant asymptotes. It can be observed that, for high frequencies — i.e. those above the resonance — $H_1(s)$ can be approached considering just the inductance of the converter side. Therefore, the switching ripple of i_s is attenuated as function of L_s. The value of L_s is described as a function of the dc rated voltage, v_{dc}, the switching frequency, f_{sw}, and the maximum accepted current ripple, $\Delta i_{s,max}$, in eq. (C.3) [47], [120], [121]. The value of R_s usually represents active losses in the inductor, and therefore, can be computed using a constant R_s/X_s ratio.

$$L_s \geq \frac{1}{8} \frac{v_{dc}}{\Delta i_{s,max} f_{sw}} \tag{C.3}$$

In many grid applications, a step-up transformers are used to connect generators to the grid, and consequently, the grid side inductance can be represented by the leakage inductance of the transformer. The value of L_t is often not dimensioned considering the passive filter, but to limit the magnitude of short-circuit currents. Depending on the power level application, the leakage inductances of transformers vary between 5 and 15 % [122], and, due to the high performance of these devices ($\approx$ 98 %), their resistances (R_t) are often very small or even neglected [122], [123].

Regarding the shunt capacitor, two methods of design can be found in the literature. In [114], [116], [117], C_s is designed as a function of the resonance frequency of the filter, given that L_s and L_t are already fixed. A trade-off between L_s and C_s can be considered in order to optimise the physical volume of the filter. In [118], C_s is sized considering the reactive power balance between the filter elements. In this work, the former method is employed. In order to obtain a good quality of injected current, i_g, f_r, should be 10 times lower than f_{sw}, guaranteeing an attenuation of 60 dB, i.e. 1000 times. Therefore, from eq. (C.2), C_s is expressed as in eq. (C.4).

$$C_s \geq \frac{25}{(\pi f_{sw})^2 L'} \tag{C.4}$$

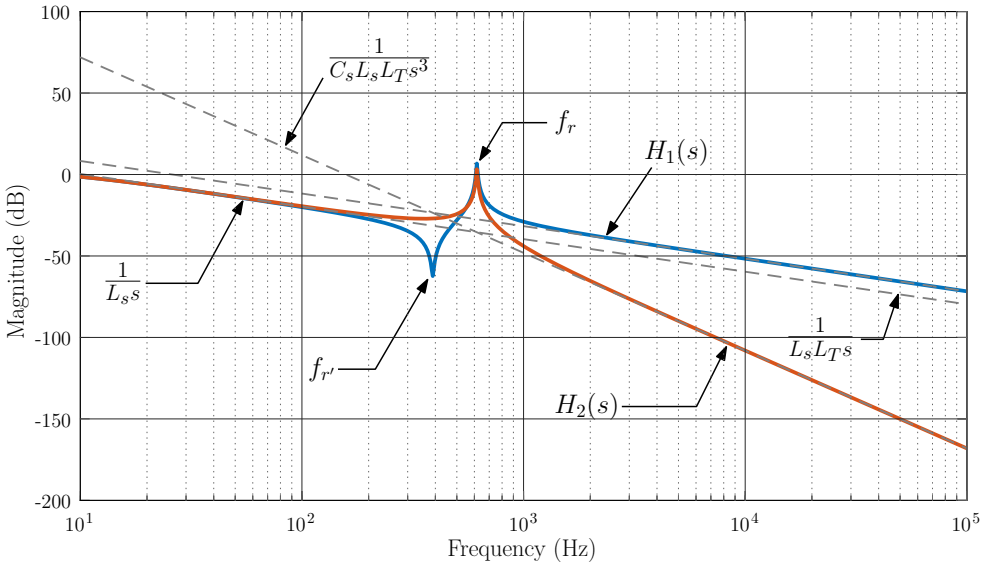

Figure C.2 – Illustration of the design of an LCL filter using the Bode diagram of $H_1(s)$ and $H_2(s)$ and their relevant asymptotes (magnitude only; reproduction from [114]).

Appendix D

Coupling of simplified models of voltage and current sources

In order to evaluate the frequency behaviour of power systems, simplified models of are extensively used in this work. These models are design using simplified representations of each source and a quasi static representation of the grid. This chapter presents the methodology used to design the quasi static representation of the grid, coupling the simplified models of the voltage and current sources connected to it.

D.1 The generic approach

In order to be as general as possible, the simplified models of voltage and current sources of any nature are represented with the blocks of Figure D.1. The active power flow between voltage sources (ΔP) and the grid is depends on the angle of the source ($\Delta\delta$). On the contrary, when the source displays the behaviour of a current source, the active power flow is imposed by the source, and the angle of the grid is a consequence of the power flow.

(a) Voltage source (b) Current source

Figure D.1 – Generic representation of the simplified models of voltage and current sources connected to the grid.

The coupling of voltage and current sources in a multi-source system is based on the active power flow of the grid. The active power flow through a generic system bus k is

expressed in eq. (D.1).

$$P_k = V_k \sum_{m \in \mathbf{K}} V_m \left(G_{km} \cos \delta_{km} + B_{km} \sin \delta_{km} \right) \tag{D.1}$$

where $\mathbf{K}$ is the subset of buses m which are connected to the bus k, V_k and V_m are the voltages of the analysed bus and its adjacent, G_{km} and B_{km} are the conductance and susceptance of the admittance matrix ($\mathbf{Y}$) of the system [52], [57] and δ_{km} is the difference between the voltage angles of the concerning buses. The matrix $\mathbf{Y}$ of any system can be represented using the graph theory [124], [125].

As expressed in eq. (D.2), Jacobian matrix ($\mathbf{J}$) of the active power of the buses with respect to their angles is obtained by linearising the set of eq. (D.1) around the equilibrium points of δ_1 to δ_k.

$$\begin{bmatrix} \Delta P_1 \\ \Delta P_2 \\ \vdots \\ \Delta P_k \end{bmatrix} = \underbrace{\begin{bmatrix} \frac{\partial P_1}{\partial \delta_1} & \frac{\partial P_1}{\partial \delta_2} & \cdots & \frac{\partial P_1}{\partial \delta_k} \\ \frac{\partial P_2}{\partial \delta_1} & \frac{\partial P_2}{\partial \delta_2} & \cdots & \frac{\partial P_2}{\partial \delta_k} \\ \vdots & \vdots & \ddots & \vdots \\ \frac{\partial P_k}{\partial \delta_1} & \frac{\partial P_n}{\partial \delta_2} & \cdots & \frac{\partial P_k}{\partial \delta_k} \end{bmatrix}}_{\mathbf{J}} \times \begin{bmatrix} \Delta \delta_1 \\ \Delta \delta_2 \\ \vdots \\ \Delta \delta_k \end{bmatrix} \tag{D.2}$$

It is emphasised that, in eq. (D.2), the active powers flow of the nodes are treated as functions of the angles of the buses, which, as mentioned previously, is true only when voltage sources are connected to these nodes. In the case where current sources or loads are connected to these nodes, the angles are function of the powers. The same is valid for the transition buses, i.e. buses without sources and loads. Therefore, as given in eq. (D.3), eq. (D.2) is rearranged in two different set of equations, those in which their active powers are dependent variable and those which their angles are dependent variable.

$$\begin{cases} \Delta \mathbf{P_d} = \dfrac{\partial \mathbf{P_d}}{\partial \delta_\mathbf{i}} \Delta \delta_\mathbf{i} + \dfrac{\partial \mathbf{P_d}}{\partial \delta_\mathbf{d}} \Delta \delta_\mathbf{d} \\ \Delta \mathbf{P_i} = \dfrac{\partial \mathbf{P_i}}{\partial \delta_\mathbf{i}} \Delta \delta_\mathbf{i} + \dfrac{\partial \mathbf{P_i}}{\partial \delta_\mathbf{d}} \Delta \delta_\mathbf{d} \end{cases} \tag{D.3}$$

where the subscriptions **d** and **i** indicates, respectively, the dependent and independent elements. Isolating $\Delta\delta_{\mathbf{d}}$ in the second line of eq. (D.3):

$$\Delta\delta_{\mathbf{d}} = -\left(\frac{\partial \mathbf{P_i}}{\partial \delta_{\mathbf{d}}}\right)^{-1} \frac{\partial \mathbf{P_i}}{\partial \delta_{\mathbf{i}}} \Delta\delta_{\mathbf{i}} + \left(\frac{\partial \mathbf{P_i}}{\partial \delta_{\mathbf{d}}}\right)^{-1} \mathbf{I} \Delta \mathbf{P_i} \tag{D.4}$$

Substituting eq. (D.4) in the first line of eq. (D.3):

$$\Delta \mathbf{P_d} = \underbrace{\left[\frac{\partial \mathbf{P_d}}{\partial \delta_{\mathbf{i}}} - \frac{\partial \mathbf{P_d}}{\partial \delta_{\mathbf{d}}}\left(\frac{\partial \mathbf{P_i}}{\partial \delta_{\mathbf{d}}}\right)^{-1} \frac{\partial \mathbf{P_i}}{\partial \delta_{\mathbf{i}}}\right]}_{\mathbf{K_s}} \Delta\delta_{\mathbf{i}} + \underbrace{\left[\frac{\partial \mathbf{P_d}}{\partial \delta_{\mathbf{d}}}\left(\frac{\partial \mathbf{P_i}}{\partial \delta_{\mathbf{d}}}\right)^{-1} \mathbf{I}\right]}_{\mathbf{K_{ps}}} \Delta \mathbf{P_i} \tag{D.5}$$

The matrix representation of eq. (D.5) is:

$$\begin{bmatrix} \Delta P_1 \\ \vdots \\ \Delta P_k \end{bmatrix} = \underbrace{\begin{bmatrix} \mathbf{K_s} & \mathbf{K_{ps}} \end{bmatrix}}_{\mathbf{K_{cplg}}} \begin{bmatrix} \Delta\delta_1 \\ \vdots \\ \Delta\delta_k \\ \Delta P_m \\ \vdots \\ \Delta P_n \end{bmatrix} \tag{D.6}$$

where the subscriptions $1 \ldots k$ represent the voltage sources and the subscriptions $m \ldots n$, the current sources, loads and transition buses. From eq. (D.6), it can be observed that the active power flows of the voltage sources are a function of their angle and the power of the other elements.

The matrix of coupling ($\mathbf{K_{cplg}}$) is the quasi static representation of the grid, and it is composed of two sub-matrices. The matrix $\mathbf{K_s}$ indicates the synchronising torque between the voltage sources. The matrix $\mathbf{K_{ps}}$ gives the ratio of instantaneous load sharing between the voltage sources due to the variation of the active power of the current sources, loads and transition buses, and therefore, the sum of the magnitude of the column elements of $\mathbf{K_{ps}}$ is unitary (if active grid losses are neglected). It is emphasised that, in normal operating conditions, the active power flow of transition buses do not vary, and therefore, their respective columns in $\mathbf{K_{ps}}$ can be disregarded, reducing the order of $\mathbf{K_{cplg}}$.

D.2 Numerical application: the SM vs SM system

A numerical application of the aforementioned generic approach is realised to determine the matrix $\mathbf{K_{cplg}}$ of the simplified model of the SM vs SM system of Section 2.2. Considering the given topology and parameters, the admittance matrix of the system ($\mathbf{Y}$) is computed using the equivalent admittance of the elements of the grid, including X'_d of the synchronous machines.

$$\begin{bmatrix} 0.055 - j1.479 & 0 & -0.055 + j1.479 \\ 0 & 0.012 - j2.222 & -0.012 + j2.222 \\ -0.055 + j1.479 & -0.012 + j2.222 & 0.067 - j3.702 \end{bmatrix} \tag{D.7}$$

From the power flow given in Table 2.1, it is possible to compute $\vec{e'}$ of the synchronous machines:

$$\begin{cases} \vec{e'_1} = 1.06\angle 0.35 \text{ pu} \\ \vec{e'_2} = 1.03\angle 0.21 \text{ pu} \end{cases} \tag{D.8}$$

Using the values of eqs. (D.7) and (D.8), the active power flows of the buses are determined as expressed in eq. (D.1). The matrix $\mathbf{J}$ of the system is found from the derivative of the active power of the buses with respect of their angles as given in eq. (D.2):

$$\begin{bmatrix} 1.460 & 0 & -1.460 \\ 0 & 2.218 & -2.218 \\ -1.408 & -2.210 & 3.618 \end{bmatrix} \tag{D.9}$$

Since a load is connected to node 3, δ_3 is a depend variable, and, to compute $\mathbf{K_{cplg}}$, this variable should be eliminated using eq. (D.5). The matrix $\mathbf{K_{cplg}}$ is given in is eq. (D.10).

$$\begin{bmatrix} \Delta P_1 \\ \Delta P_2 \end{bmatrix} = \begin{bmatrix} 0.892 & -0.892 & -0.403 \\ -0.863 & 0.863 & -0.613 \end{bmatrix} \begin{bmatrix} \Delta\delta_1 \\ \Delta\delta_2 \\ \Delta P_3 \end{bmatrix} \tag{D.10}$$

Stability of power systems with high penetration of sources interfaced by power electronics

The massive insertion of Power Electronics (PE)-based sources into the grid is creating some technical challenges which must be overcome in order to guarantee the stability of the power system. One of the main concerns is due to the characteristics of these sources, which are different to those of Synchronous Machines (SMs). This research intends to provide a supplementary insight into the massive insertion of PE-based sources into the power system, more specifically the evolution of the frequency behaviour of these systems. For this purpose, a set of methods and tools already used on classical SM-based systems is proposed. Reduced order models of PE-based sources behaving as voltage or current sources are proposed, and, since the obtained representations share the same theoretical approach as that employed for SMs, they can be employed together to analyse any power system, regardless its complexity. The reduced order model of the systems can either be designed by representing each source of the original system or using the concept of synchronous areas, providing flexibility in the analysis. Using a step-by-step approach, the frequency behaviours observed with academic systems are deeply analysed with the proposed methodology, and validated with those obtained with detailed EMT models. The proposed approach developed in this work can be used to determine the impact of the penetration rate of PE-based sources on the overall frequency behaviour, and on the intra- and inter-area oscillations of different power systems.

Keywords: "Stability of power systems"; "synchronous machines"; "power electronics-based sources"; "Voltage Control mode Inverters (VCIs)"; "Current Control mode Inverters (CCIs)"; "small-signal stability"; "reduced order models".

Stabilité des systèmes électriques comportant une forte proportion de sources interfacées par électronique de puissance

L'insertion massive de sources interfacées par Électronique de Puissance (EP) dans le réseau va induire de grands défis techniques à surmonter pour garantir la stabilité du système électrique. L'une des principales préoccupations tient aux caractéristiques de ces sources, qui sont différentes de celles des Machines Synchrones (MS). Ce travail apporte un éclairage supplémentaire sur l'effet de l'insertion massive des sources interfacées par EP dans le système électrique, plus spécifiquement sur l'évolution du comportement de la fréquence de ces systèmes. Pour y répondre, un ensemble d'outils et de méthodes s'inspirant des fondamentaux des systèmes basés sur la production d'électricité avec les MSs a été développé. Des modèles d'ordre réduit des sources interfacées par EP se comportant comme sources de tension ou de courant sont proposés. Comme ces représentations partagent la même approche théorique que les modèles de MSs, il est ensuite possible de les fusionner en vue de l'analyse des systèmes électriques quelconques, indépendamment leur complexité. Les systèmes d'ordre réduit peuvent soit être modélisés en représentant chaque source ou bien en utilisant le concept des zones synchrones, ce qui offre une grande flexibilité d'analyse. Avec une approche progressive, le comportement de la fréquence des systèmes académiques relevé avec la méthodologie proposée est analysé en profondeur et comparé avec celui obtenu avec des modèles détaillés. L'approche développée dans ce travail peut être utilisée pour déterminer l'impact du ratio de pénétration des sources interfacées par EP sur le comportement global de la fréquence, mais aussi pour évaluer les oscillations intra et interzones des différents systèmes électriques.

Mots clés: « Stabilité des systèmes électriques »; « machines synchrones »; « sources interfacées par électronique de puissance »; « convertisseurs en mode source de tension »; « convertisseurs en mode source de courant »; « stabilité aux petits signaux »; « modèles d'ordre réduit ».